UNDERSTANDING LUNAR VOLCANIC PROCESSES AND MARE SURFACE AGE-DATING VIA REMOTE SENSING

A DISSERTATION SUBMITTED TO THE GRADUATE DIVISON OF THE UNIVERSITY OF HAWAIʻI AT MĀNOA IN PARTIAL FULFILLMENT OF THE REQUIREMENTS FOR THE DEGREE OF

DOCTOR OF PHILOSOPHY
IN
GEOLOGY AND GEOPHYSICS
May 2023

By
Thomas A. Giguere

Dissertation committee:

Jeffrey J. Gillis-Davis, Chairperson
Paul G. Lucey
G. Jeffrey Taylor
Scott Rowland
Kim Binsted

Keywords: Moon, Lunar remote sensing, Cratering, Volcanism, Impact processes, Surface

ACKNOWLEDGMENTS

Heartfelt thanks to everyone in HIGP, Earth Sciences and the greater SOEST family for many great years! Thanks to all co-authors, collaborators, TA's, and professors, and all who have engaged in interesting conversation along the way!

I thank the administrative experts: Vi Nakahara, Leona Anthony, Grace Furuya, Rena Lefevre, Susan Van Gorder, Sharisse Nakasone, Jason McCartney, Kitty Hino, and Anela Nishimoto for their vital support. Thank you Lily Shao for your knowledge, guidance, and patience and for answering my endless questions about the process. Thanks to Ethan Kastner (late nights) and Eric Pilger for all of the technical support.

Thanks to G. Jeff Taylor for the invitation in the MS program that was the beginning of my journey and the contant flow of enthusiasm, new ideas, and a unique type of humor that never ceases to make me laugh.

Many formative evenings were spent with B. Ray Hawke as my available time coincided with his overnight work schedule. I truly appreciate the literal years of mentorship and for sharing his love of all things Moon (from cryptomare to Sailor Moon). His influence is felt everytime I examine a backwater location on the Moon, hoist a marguerita, or enjoy barbeque. This is treasured time.

Much appreciation goes to Joe Boyce for stepping up when truly needed and for guiding me on the nuances of crater counting. This career move into planetary surface age dating was both unexpected and rewarding at the same time.

Thanks to Barb Bruno for advice, friendship and encouragement at key moments along this voyage of discovery. Your fresh perspective was a welcome change from my linear thinking.

Well deserved thanks to my committee: Jeffrey J. Gillis-Davis, Paul G. Lucey, G. Jeffrey Taylor, Scott Rowland, and Kim Binsted who are appreciated for their patience and guidance throughout my dissertation. Many thanks to Paul Lucey for sharing his wealth of knowledge and enthusiasm, plus his out of the box approach to everything to do with science, not just the Moon. Jeff Taylor, support from beginning to end, hard to top that. Scott Rowland provided a welcome source of independent volcanic knowledge, along with a crucial, objective perspective on the two final papers. Kim Binsted maintained the team balance with a touch of Mars.

A special shoutout to Jeff G-D for taking the lead and wearing many hats for all of the critical steps along the road to my dissertation. All this while effectively working in two places at once. Thank you (!) for the all of the extra time spent as my advisor, co-author on three manuscripts and numerous abstracts and recently as my PhD committee chairperson. Jeff always provided the most thorough review of whatever we were working on. Impressive and a very excellent role-model.

Parental thanks are in order for influences and inspiration that began early and lasted a lifetime. I owe a tremendous amount to my father (Arthur Giguere) , a chemical engineer, and his infectious curiousity about all things natural including flora and fauna, geology, astronomy, and of course macro economics and mother (Susan) who was supportive at every step. I can trace my interest in the Moon, planets, and space back to the discovery of a small telescope found in a closet in the family home. It's amazing how a simple object, unused for a dozen years, can create such a lasting spark.

Huge thanks go out to my family! Love to Glenda and the kids, Emma and Elizabeth, who have been along for the entire ride, and very often supportive. I appreciate all that you have done, very much. I know you believed it would never end… but here we are, now what! The younger version of the kids spent quite a bit of time at HIGP and I promise to replace the defaced Data Center log book if requested (a recent discovery).

Thank you!

ABSTRACT

The Moon has a long and complex history of volcanism, which shapes the face that we see from Earth to this day. In this dissertation, we use remote sensing to examine multiple locations on the Moon to understand the regional volcanic processes along with their eruption ages.

We begin (chapter 2) with the lunar floor-fractured crater Gassendi and surrounding area, which were examined with high-resolution Lunar Reconnaissance Orbiter Camera imagery and other remote-sensing data to characterize and understand the volcanism in the southwestern region. This region exhibits a variety of volcanic features (e.g., cryptomaria deposits, pyroclastic deposits, maria, lava lakes). We confirm the existence of a previously identified cryptomare deposit, identify an additional cryptomare deposit west of Gassendi crater, and a pyroclastic northeast of Gassendi. Spectral and geochemical anomalies associated with dark-haloed impact craters reveal cryptomaria deposits in the western Gassendi crater floor and previously unmapped mare basalt within northeastern Gassendi. We identified three separate lava lakes on the northeast, northwest, and southwest floor of Gassendi crater based on morphology analogous to terrestrial lava lakes, geochemical signatures, and digital terrain data. Crater count (model) age data suggest the lava lakes were active at ~3.6 Ga (300 Ma after floor emplacement). Criteria used to identify lava lakes in Gassendi were applied globally to locate candidate lava lakes within floor-fractured craters. With the identification of lava lake morphology, both in Gassendi crater and in other floor-fractured craters, the current ascent and eruption models should be revised to allow for at least short-term connection between magma supply at depth and surface lava lakes. Hence, this integration of multiple perspectives afforded by recent remote data sets reveals new views about lunar volcanic processes.

Next (chapter 3), we examine Northeastern Oceanus Procellarum (NE-OP) study area, which is a patchwork of lava flows that range in model age from 1.4 – 3.5 Ga (average age for all count areas is 2.3 Ga), but whose FeO and TiO_2 contents deviate little. The intermediate TiO_2 content values (4.0–6.8 wt.%) exhibited by the mare in this region represent material that is underrepresented in the current lunar sample collection. The model ages in the study region are bimodal (~2.2 Ga and ~3.0+ Ga), with eruption of lava flows at the Chang‘E-5 landing site occurring at ~3.0 Ga. By comparison, other investigators estimate the model age of the Chang‘E-5 site to be ~1.2 to 1.6 Ga. We find preliminary evidence that differences in measurement

methodology may lead to disparate model ages and explain the difference in predicted model age of the Chang‘E-5 site.

We finish (chapter 4) with an examination of three NASA CLPS landing sites in the lunar maria (i.e., Reiner Gamma, Mare Crisium, and Lacus Mortis) and used crater counting techniques to determine the age of the mare (absolute model age). We compare differences in researcher measurement techniques and place the sites in regional context with regards to their lava flow ages. Two researchers performed crater density measurements at the three sites, using identical imagery with the same illumination conditions, and the same software tools. The uniform nature of the analysis environment allowed researchers to use accepted crater counting techniques to determine absolute model ages (AMA), while subsequently allowing the examination of the variations in the personal approaches used by the researchers. Comparisons revealed variations in researcher methodology and resulting AMAs. Landing sites were subdivided into two or more smaller count areas and we determined that all areas have mare basalts that are Imbrian in age. Variations in AMAs between researchers were the result of differences in the number of secondary and degraded craters identified and to a lesser extent crater diameter measurements. Building on the legacy work of the crater counting community, we recommend rigorous secondary crater identification and exclusion, DTM aspect-based diameters to calibrate measurements, high-resolution orbital imagery to improve rimcrest location measurements, and surface imagery to verify rimcrest condition.

TABLE OF CONTENTS

LIST OF TABLES

LIST OF FIGURES

LIST OF ABBREVIATIONS

An	Anorthite
APL	Applied Physics Laboratory
C	Continuum
CLPS	NASA Commercial Lunar Payloads Services
cm	Centimeter
cm-1	Wavenumber
CPX	Clinopyroxene
D	Grain size
DEC	Declination
DN	Digital Number
DR	Regolith reworking depth
e	Emission angle
E	Emission
e	Emissivity
En	Enstatite
EVA	Extra Vehicular Activity
FHT	Feldspathic Highlands Terrane
F	Flux
Fo	Forsterite
FOV	Field of view
Fs	Ferrosilite
FUV	Far Ultra-Violet
FWHM	Full width at half maximum
g	Phase angle
Ga	One billion years ago
GHz	Gigahertz
GRAIL	Gravity Recovery and Interior Laboratory
GRS	Gamma-ray spectrometer

HCP	High-Ca pyroxene
HSI	HyperSpectral Imaging
Hz	Hertz
i	Incidence angle
IR	Infrared
JHU	Johns Hopkins University
JPL	Jet Propulsion Laboratory
K	Kelvin
kg	Kilogram
km	Kilometer
KREEP	Potassium, rare earth elements and phosphorus
LADEE	Lunar Atmosphere and Dust Environment Explorer
LAMP	Lyman Alpha Mapping Project
LCP	Low-Ca pyroxene
LKFM	Low Potassium Fra Mauro
LM	Lunar Module
LOLA	Lunar Orbiter Laser Altimeter
LP	Lunar Prospector
LRO	Lunar Reconnaissance Orbiter
LROC	Lunar Reconnaissance Orbiter Camera
LRV	Lunar Roving Vehicle
LSCC	Lunar Soil Characterization Consortium
L_{solar}	Solar Radiance
LWIR	Long-Wave Infrared
m	Meter
Ma	One million years ago
M^3	Moon Mineralogy Mapper
mbar	Millibar
MI	Multi-band Imager
min	Minute
mm	Millimeter

mrad	Milliradian
NAC	Narrow Angle Camera
NIR	Near-infrared
NIST	National Institute of Standards and Technology
nm	Nanometer
ns	Nanosecond
OL	Olivine
OMAT	Optical Maturity
OPX	Orthopyroxene
PKT	Procellarum KREEP Terrane
PLG	Plagioclase
ppm	Parts Per Million
R	Reflectance
RA	Right Ascension
RELAB	Reflectance Experiment LABoratory
RMS	Root-Mean-Square
sec	Second
SMFe	Submicroscopic iron
SNR	Signal-to-Noise Ratio
SP	Kaguya Spectral Profiler
SPA	South Pole-Aitken
SSA	Single Scattering Albedo
TC	Kaguya Terrain Camera
μm	Micrometer
USGS	U.S. Geological Survey
UTC	Coordinated Universal Time
UV	Ultraviolet
UVVIS	Ultra violet and visible bands
VIS	Visible
VLT	Very low titanium
VNIR	Visible to near-infrared

vol%	Volume percent
WAC	Wide Angle Camera
λ	Wavelength
wt.%	Weight Percent
x	Band Depth
yr	Year

CHAPTER 1: INTRODUCTION

1.1 The Moon

The Moon has a complex history of volcanism and is the target of our research. As Earth's constant companion, the Moon likely formed as a result of the impact of a Mars-sized planet and the proto-Earth (Hartmann and Davis, 1975; Origin of the Moon conference (Kona Hawaii), 1984). The volitile-poor ejecta from the impact coalesced to form the Moon. A molten layer of rock may have resulted from the rapid formation of the Moon after the collision due to the energy of the collision and gravitational collapse. This Lunar Magma Ocean (LMO) crystallized, with the dense minerals (olivine, pyroxene) settling to the bottom and a less dense anorthositic crust forming the top layer. Subsequently, volcanic eruptions created the morphology that we observe on the Moon. These volcanic products have low viscosities and higher iron abundances that their terrestrial counterparts. Volcanism on the Moon was active for an extended period of time (~1.1-4.0 Ga), with the major activity occurring between 3.4 and 3.7 Ga (Head, 1976; Hiesinger et al., 2011). The timing and processes that created these volcanic products (e.g., basalt flows, cryptomaria, pyroclastic deposits, and lava lakes) is the focus of chapters 2, 3 and 4.

1.2 Remote sensing/regional studies

We use remote sensing to examine multiple mare locations, to characterize their geochemistry and eruption ages, and to place them in local and regional volcanic context. We focus on selected regions of the Moon for each study, so as to understand in detail the specific volcanic and impact processes that occurred in the area. These processes leave tell-tail signs involving impact craters, lava flows, burial, a subsequent excavation, which is dicernible for eons and serve to tell a detailed story of the areas' formation. The knowledge gained from each regional assessment may then be applied to the global picture.

The remote sensing techniques used to gather data about volcanism in our regional study areas can be defined as "reconnaissance at a distance" (Colwell, 1966) and further refined as the science and art of obtaining information about an object, area or phenomenon through the analysis of data acquired by a device that is not in direct contact with the target (Lillesand and Kiefer, 1979).

A variety of spacecraft-based (and some earth-based) instruments are used to observe a range of frequencies of the electromagnetic spectrum for our lunar targets. Observing at different

wavelengths and absorption bands provides information about the surface being studied, e.g. mineralogy, chemical composition, roughness, age, morphology, etc.

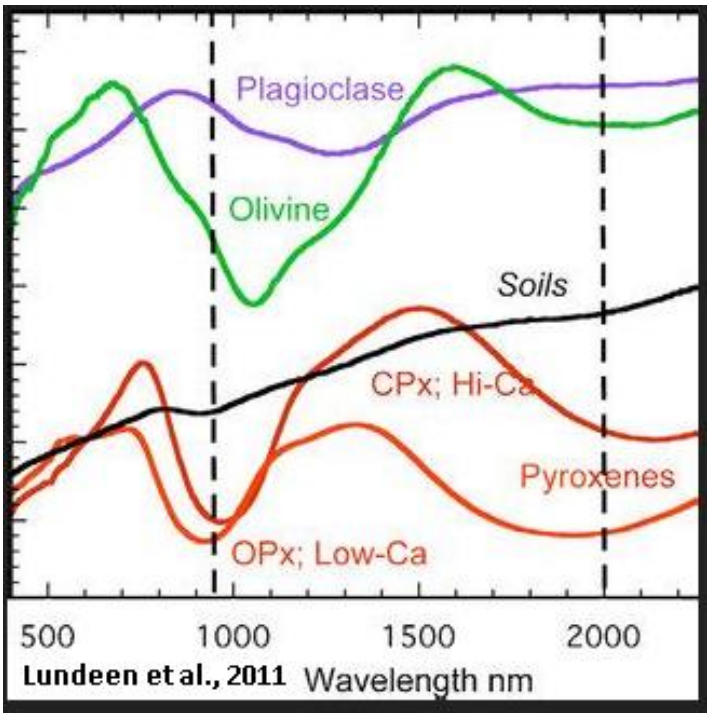

Figure 1.1. Lab spectra for major lunar minerals, including clinopyroxene (CPx), which are used for comparison to remotely acquired spectra.

1.3 Instruments and data

Our research uses multiple passive and active instruments, resolution, and spectral coverage from various spacecraft missions, which are categorized as remote or derived data products.

- Remote sensing products
    - Single-band (LRO/LROC NAC, Clementine 750 nm, Kaguya 750 nm), resolution 0.5 – 100 m/px
    - Multi-band (Clem, LRO/LROC WAC, Kaguya MI), resolution of ~100-200 m/pix, band passes, 320 nm – 1550 m
    - Hyperspectral (M3) – Moon Mineralogy Mapper (M3), Chandrayaan-1, 82 bands, wavelengths 400-3000 nm
    - Lunar Prospector (LP) gamma-ray spectrometer (GRS) for Th and K
- Derived data products (FeO, TiO_2, OMAT)

- Clementine five-color UV-VIS (Isbell et al., 1999; Eliason et al., 1999; Robinson et al., 1999) data products: optical maturity (OMAT) images and FeO and TiO_2 maps (Lucey et al., 2000a, 2000b; Gillis et al., 2003, 2004)
- Kaguya Multi-band Imager (MI) used to derive OMAT (Lemelin et al., 2019) and FeO (Lemelin et al., 2015)
- LROC WAC used for 643 nm, TiO_2 (Sato et al., 2017)
- Kaguya Multi-band Imager (MI) - mineralogy (opx, cpx, olv & glass maps), 62-m/px (Lemelin et al., 2015; Trang et al., 2017)

1.4 Key concepts

We use two key concepts in our work when determining the age of an exposed lava flow and locating buried lava flows.

Lava flow age - The general process for determining the relative and absolute model ages of planetary surfaces begins with the assumption that the flux of impacting meteoroids is relatively constant and spatially stochastic, and that crater size is primarily a function of impactor mass and velocity which also influences size, is assumed constant for a given planetary body. Hence, a surface with fewer impact craters is younger than a surface with more craters, which is logical as the older surface accumulates more craters over time. An age relationship is established when the surface with a specific number of craters, in a given size range, has an absolute age-dated sample from the same surface (e.g., the Apollo landing sites). This crater size frequency versus sample age relationship is performed for multiple surfaces. Thus, we extrapolate this age-crater relation to estimate the absolute age of other locations, even though the location has not been directly sampled.

Cryptomare deposits - aka “hidden mare basalts”, are vital to identify as these eruptions products contribute to the overall inventory of this major form of lunar volcanism. Schultz and Spudis (1979) originally described the obscuration of mare deposits by highland material and later Head and Wilson (1992) coined the term “cryptomare”. We use the criteria for cryptomare deposit identification based on Antonenko et al. (1995), namely:

- Low albedo surface
- Presence of dark-haloed impact craters, which are exogenic craters that have excavated mare basalt from depth (Hawke and Bell, 1983; Bell and Hawke, 1984),
- Association with mafic geochemical anomalies, and

- Presence of a significant component of mare basalt in the high-albedo surface unit as identified by spectral band identification (Head et al., 1993; Blewett et al., 1995)

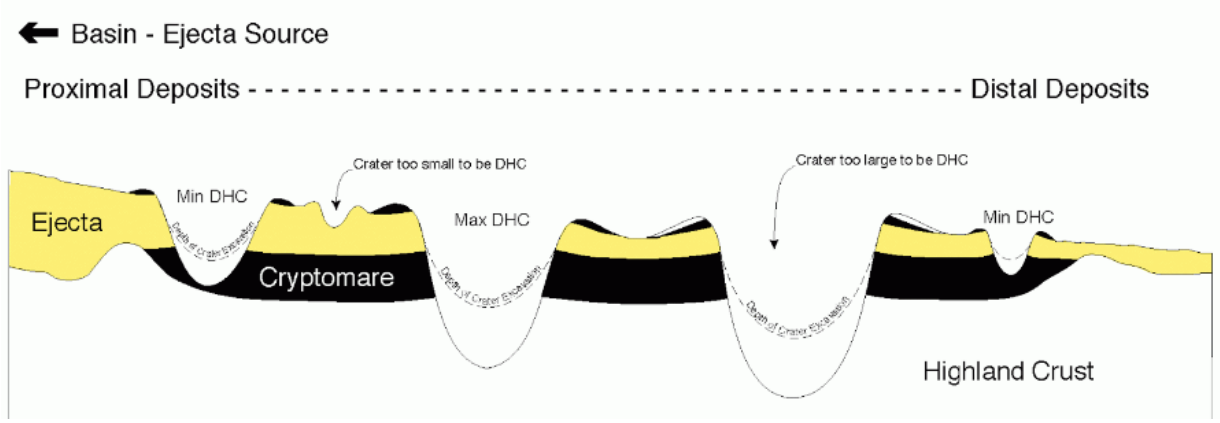

Figure 1.2. Proximal/Distal basin ejecta cryptomare with Dark Halo Craters (DHC) impacting the regolith and excavating low-albedo ejecta (side view). Credit: Irene Antonenko.

1.5 Dissertation Goals

Our investigation into regional volcanism begins with Gassendi crater on the southwestern nearside (chapter 2), then to northeastern Oceanus Procellarum (chapter 3), and concludes with an examination of CLPS landing sites (chapter 4), which is comprised of three distinct locations. Our remote sensing tools and analysis improve with each chapter as the instruments and data keep pace with technology advances, allowing us to better tell the stories that the Moon reveals.

CHAPTER 2: VOLCANIC PROCESSES IN THE GASSENDI REGION OF THE MOON

[Published in 2020: Journal of Geophysical Research: Planets, 125(9), p.e2019JE006034.]

Thomas A. Giguere[a*], B. Ray Hawke[a], Jeffrey J. Gillis-Davis[b], Myriam Lemelin[c], Joseph M. Boyce[a], David Trang[a], Samuel J. Lawrence[d], Julie D. Stopar[e], Bruce A. Campbell[f], Lisa R. Gaddis[g], David T. Blewett[h], J. Olaf Gustafson[i], Chris A. Peterson[a], Cassandra R. Runyon[j]

[a]Hawai'i Institute of Geophysics and Planetology, Department of Earth Sciences, University of Hawai'i at Manoa, 1680 East-West Road, Honolulu, HI, 96822, United States, [b]Washington University, Department of Physics, One Brookings Drive, St. Louis, MO 63130, [c]Department of Earth and Space Science and Engineering, York University, Toronto, CAN M3J 1P3, [d]NASA Johnson Space Center, 2101 NASA Pkwy, Houston, TX 77058, [e]Lunar and Planetary Institute, 3600 Bay Area Boulevard, Houston, TX 77058, [f]Smithsonian Institution, Center for Earth and Planetary Studies, MRC 315, PO Box 37012, Washington, DC 20013, [g]U.S. Geological Survey, Astrogeology Science Center, Flagstaff, AZ 86001, [h]Planetary Exploration Group, Johns Hopkins University Applied Physics Laboratory, 11100 Johns Hopkins Rd., Laurel, MD 20723, [i]Department Earth and Atmospheric Sciences, Cornell University, Ithaca, NY 14853, [j]College of Charleston, Charleston, SC.

Abstract

The lunar floor-fractured crater Gassendi and surrounding area were examined with high-resolution Lunar Reconnaissance Orbiter imagery and other remote-sensing data to characterize and understand the volcanic processes in the southwestern region of the Moon. This study was selected because the Gassendi region exhibits a variety of volcanic features (e.g., cryptomaria deposits, pyroclastic deposits, maria, lava lakes) and team participants have studied this region for thirty years (Hawke et al., 1991). This study confirms the existence of a previously identified cryptomare deposit, identifies an additional cryptomare deposit west of Gassendi crater, and a pyroclastic northeast of Gassendi. Spectral and geochemical anomalies associated with dark-haloed impact craters reveal cryptomaria deposits in the western Gassendi crater floor and previously unmapped mare basalt within northeastern Gassendi. We identified three separate lava lakes on the northeast, northwest, and southwest floor of Gassendi crater based on morphology analogous to terrestrial lava lakes, geochemical signatures, and digital terrain data. Crater count

(model) age data suggest the lava lakes were active at ~3.6 Ga (300 Ma after floor emplacement). Criteria used to identify lava lakes in Gassendi were applied globally to locate candidate lava lakes within floor-fractured craters. With the identification of lava lake morphology, both in Gassendi crater and in other floor-fractured craters, the current ascent and eruption models should be revised to allow for at least short-term connection between magma supply at depth and surface lava lakes. Hence, this integration of multiple perspectives afforded by recent remote data sets reveals new views about lunar volcanic processes.

2.1.0 Introduction

The Gassendi crater and surrounding area (Figure 2.1), with a diversity of volcanic features and multiple unanswered questions, demand a thorough investigation. This region is at the crossroads of major lunar terranes including the mare/highlands boundary of southern Oceanus Procellarum, the southeast periphery of the PKT region (Jolliff et al., 2000), and the boundary between the thicker highlands crust to the south and the thinner crust associated with the mare region to the north (Zuber et al., 2013). We leverage recent spacecraft data to increase the inventory of volcanic deposits (mare, cryptomare, pyroclastic) and focus on the existence of lava lakes within Gassendi: first described by Schultz (1976a, 1976b). The information gained through mapping and morphologic study of Gassendi-region volcanic features will reveal insights into eruption models and the thermal/eruptive history of the Moon.

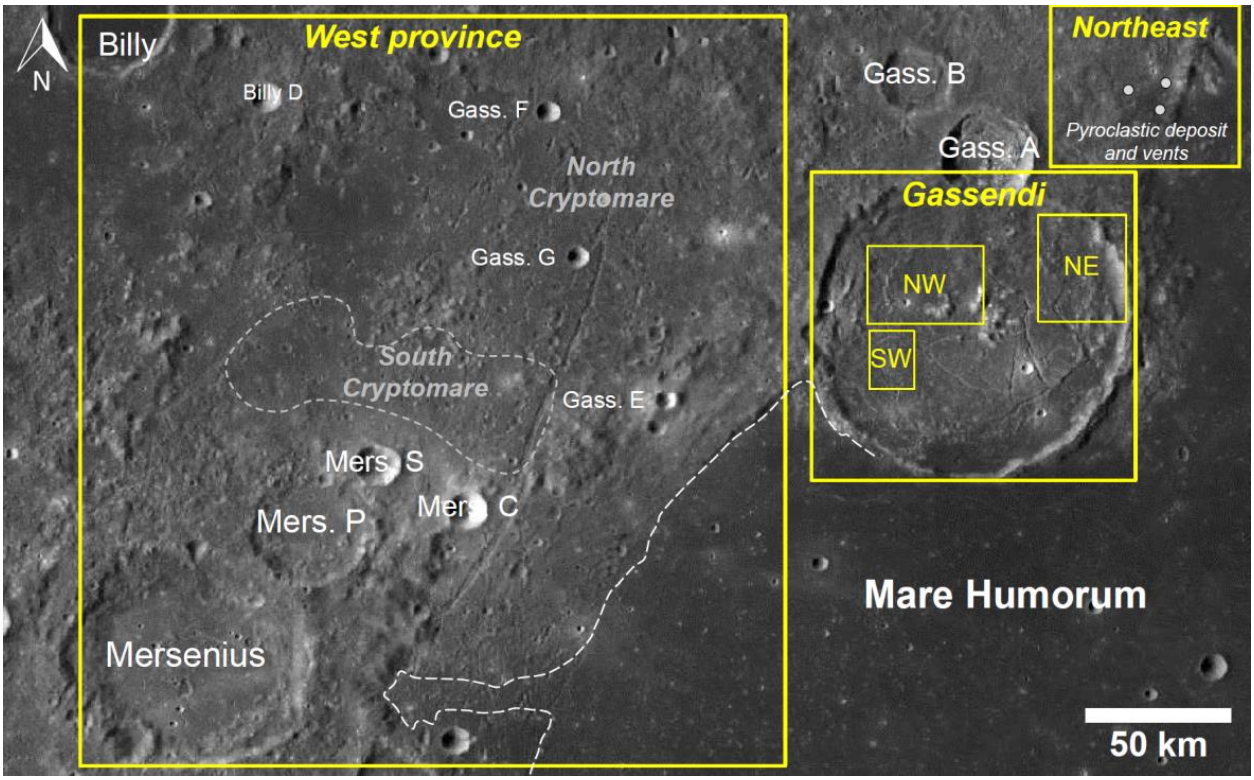

Figure 2.1: Gassendi crater (110 km in diameter) and region of study is located to the north and northwest of Mare Humorum on the nearside of the Moon. The "Gassendi region" is defined as the area surrounding Gassendi crater and includes the Gassendi satellite craters (A through Y); excludes Mare Humorum. The area extends to the south and west to include Mersenius crater, and to the north and east of Gassendi A and B. Three provinces are defined for the Gassendi Region: West, Northeast, and Gassendi. The north and south cryptomare (white dashed boundary) are located in the West province, the pyroclastic vents and deposits (white dots) are shown in the Northeast province, and three subsided lava lakes are indicated by the NE, NW, and SW labels in the Gassendi province. The western boundary of Mare Humorum is highlighted with white long dashes. WAC Global Morphologic basemap (100 m/pixel), Equidistant cylindrical projection.

This region has triggered numerous investigations. Beginning over a century ago, multiple researchers observed and documented wall slumps, floor fractures, and depressions in Gassendi crater (Mee and Brenner, 1895; Elger, 1895; Hallowes, 1916). More recently studied features include: a large radar anomaly west of the crater, which exhibits low depolarized 3.8 cm radar returns (Hawke et al., 1993); pyroclastic deposits in Mersenius crater; a cryptomare deposit (buried or obscured mare basalt) in the highlands to the west of Gassendi crater (Hawke et al., 1993); smooth plains, volcanic constructs (Schultz, 1976a, 1976b) and floor fractures (Schultz, 1976a; Dombard and Gillis, 2001; Jozwiak et al., 2012) on the floor of Gassendi crater (Figure 2.1). Schultz (1976a) describes the southeast portion of the floor of Gassendi as rejuvenated with mare flooding both from within the crater and from a breach on the south wall, which resulted in an

influx of lava from Mare Humorum. Volcanic units in the region range in age from the oldest Nectarian (3.85–3.92 Ga; Wilhelms, 1987) cryptomare deposits located to the west of Gassendi to the youngest Upper Imbrian-aged (3.20 – 3.80 Ga; Wilhelms, 1987) flows in the southeast part of Gassendi crater (3.45 Ga, Hiesinger et al., 2000).

Remote sensing data available at the time of previous studies limited earlier geologic interpretations. Spacecraft images had lower resolution, less consistent viewing geometry and lighting, and fewer spectral bands. We extend the current state of knowledge by integrating the latest remote sensing data to study geomorphology, composition, and origin of geologic units in the Gassendi region. Data we draw from are Lunar Reconnaissance Orbiter (LRO) Camera (LROC) Wide Angle Camera (WAC) and Narrow Angle Camera (NAC) images, Diviner Lunar Radiometer Experiment rock abundance, Digital Terrain Models (DTMs) derived from LRO and Kaguya instruments, Moon Mineralogy Mapper spectral data, Earth-based Radar, Clementine UV-VIS and Kaguya Multiband Imager images and derived data products (e.g., FeO, TiO_2, and mineral maps), and Lunar Prospector based elemental abundance maps.

The study area designated "*Gassendi region*" after the prominent crater Gassendi (located at 17.55°S, 39.96°W; diameter = 110 km), is located directly north and northwest of Mare Humorum on the lunar nearside. The area includes the region surrounding Gassendi crater and the Gassendi satellite craters (A through Y) but excludes Mare Humorum. We subdivide the region into three provinces: West, Gassendi, and Northeast (Figure 2.1). The West province is mapped as the Vitello Formation (plv), which consists of ejecta from the Humorum basin; the Gassendi province is mapped as the Gassendi Group (Iplg) post-Humorum crater material (Titley, 1967); and the Northeast province is mapped as Regional material (Ir) material derived from Mare Imbrium (Marshall, 1963).

The goals of this study include: 1) Identify and determine the composition of unmapped mare basalts in the interior of Gassendi crater; 2) Investigate the distribution and composition of pyroclastic deposits in the region; 3) Identify and map the distribution of exogenic dark-haloed craters (DHCs) in the region, which are used for the identification of cryptomare deposits; 4) Determine the compositions, ages, and processes responsible for cryptomare deposit formation; 5) Locate and characterize volcanic features on the floor of Gassendi including the identification of lava lakes, and; 6) Determine if lava lakes or similar features exist in floor-fractured craters elsewhere on the Moon. Through these goals, we aim to understand the timing and sequence of

volcanic events that led to our current view of the Gassendi region and whether the features that we observe are unique to that region or occur elsewhere on the Moon.

2.2.0 Data and Methods

This investigation used LROC Narrow Angle Camera (NAC) and Wide-Angle Camera (WAC) images (Robinson et al., 2010). The LROC NAC acquires two adjacent frames simultaneously covering an area 5 km wide by up to 26 km long, with a pixel scale of 0.5 m (Robinson et al., 2010) during the initial nominal orbit at an altitude of 50 km. The high resolution and moderate to low Sun angles of the NAC data make it invaluable for mapping morphology (Wilhelms, 1987). The LRO has undergone a number of orbital adjustments since December 2011 with a periapsis as low as 40 km and an apoapsis as high as 185 km. Hence, the resulting NAC pixel widths range from 0.3 m to 2.2 m. When available for our study area, the higher resolution NAC images provided fine details of the smallest geologic features (Speyerer et al., 2016).

LROC WAC imaged the Moon at seven band passes (Table 2.1). A single-band (643 nm) WAC mosaic at 100 m/pixel served as the base map for this investigation. It was cropped from the global WAC morphological mosaic, which was constructed from more than 15,000 individual map-projected images acquired between 2009 and 2011 (Speyerer et al., 2011) with improved geometric accuracy and photometric correction in July 2013. This mosaic, available through the Planetary Data System (PDS), was acquired over a narrow solar incidence range (55-80°) in order to accentuate morphology. Additional single-band WAC imagery with very low-Sun angles (high incidence) at 100 m/pixel, was used to identify subtle topography. WAC imagery with high-Sun angles (solar incidence <40°) emphasizing albedo differences, together with NAC imagery, was used to locate and characterize pyroclastic deposits.

Table 2.1: Instrument Band Passes: LROC/WAC, Clementine, Kaguya/MI, Moon Mineralogy Mapper (M^3).

LROC/WAC			Clementine			Kaguya/MI			Moon Mineralogy Mapper (M^3)		
Band (nm)	FWHM (nm)	Resolution (m/px)	Band (nm)	FWHM (nm)	Resolution (m/px)	Band (nm)	FWHM (nm)	Resolution (m/px)	Band (nm)[1]	FWHM (nm)	Resolution (m/px)
320	32	384	415	40	100	415	20	20	430	10	140
360	15	384	750	10	100	750	10	20	|	10	140
415	36	100	900	30	100	900	20	20	|	10	140

565	20	100	950	30	100	950	30	20	|	10	140
605	20	100	1000	30	100	1000	40	20	|	10	140
645	23	100				1000	30	62	|	10	140
690	39	100				1050	30	62	|	10	140
						1250	30	62	|	10	140
						1550	50	62	3000	10	140

[1]The Chandraayan-1 M^3 has 82 bands, range 430-3000 nm (Pieters et al., 2009).

The LRO Diviner Lunar Radiometer Experiment data was employed to identify surface rock abundance in pyroclastic deposits. The radiometer has seven bands ranging from 8-300 μm (Paige et al., 2010). The 128 m/pixel rock abundance map provided by the Diviner team (Bandfield et al., 2011) reveals blocks >1 m on the surface.

General topographic data and morphology information were collected for features in the Gassendi region using the global WAC 100 m/pixel topographic model, called the LROC GLD100 (Scholten et al., 2012). Higher resolution topographic data were obtained for the depression in the northeast portion of Gassendi crater, centered at latitude, longitude: 17.13°S, 38.89°W, based on a NAC-derived Digital Terrain Model (DTM). The 3-m/pixel resolution DTM provided by the LROC team was created from radiometrically calibrated stereo image pairs (M1213319041, M1213326073) and processed using tie-points, sensor position, and camera pointing to find a least root mean square solution in SOCET SET (Tran et al., 2010; Burns et al., 2011; Mattson et al., 2012, Henriksen et al., 2017). The absolute accuracy of the stereo image pairs was improved by defining the geodetic reference frame using Lunar Orbiter Laser Altimeter (LOLA) elevation profiles (Burns et al., 2011; Mattson et al., 2012). NAC-derived DTMs could not be used for the whole study region because NAC stereo pairs currently only cover the northeast part of Gassendi crater.

High resolution DTM data were obtained from the SLDEM2015 (Barker et al., 2016) and the Japanese Space Agency (JAXA) SELENE "Kaguya" monochromatic Terrain Camera. This data set permits more precise elevation measurements to be made on small features. Kaguya DTMs were produced from geometrically rectified Level-2A data Terrain Camera (TC) images (Haruyama et al., 2008b). The DTMs were then map-projected and mosaicked (Isbell et al., 2014) to bring the data to MAP-form (similar to the PDS archives) and made available from the SELENE online archive (http://l2db.selene.darts.isas.jaxa.jp/, Okumura et al., 2009). The TC DTM has a

pixel scale of ~7.4 m (4096 pixel/degree) and a predicted vertical error of 17 m (Haruyama et al., 2008a, 2014).

Mineral and glass maps were produced for pyroclastic deposits with Kaguya Multiband Imager (MI) data at level 2 MAP processing (Table 2.1). This processing level includes radiometric, geometric, and topographic corrections as well as the projection of the data (simple cylindrical) onto a map (Ohtake et al., 2008). The 62-m/pixel maps for the Gassendi region were produced by applying Hapke's radiative transfer equations to the continuum removed MI data (Lemelin et al., 2015; Trang et al., 2017). Map production assumptions include: regolith grain size is 17um, glass grain size is 60um, and the Mg number is 65. The abundance of olivine, orthopyroxene, clinopyroxene, plagioclase, and pyroclastic glass is determined for each map pixel. The model has been validated against observations and samples from Apollo 17 Taurus-Littrow Valley region by Trang et al. (2017).

A Clementine five-color UV-VIS digital image model (DIM) for the Moon was used (Isbell et al., 1999; Eliason et al., 1999; Robinson et al., 1999). This image product has moderately high spatial resolution of ~100-200 m/pixel, with multi-spectral band passes from 415 to 1000 nm (Table 2.1). The band centers were selected specifically for lunar study by the Clementine science team (Nozette et al., 1994). This calibrated image cube served as the basis for the production of a number of derived data products, including optical maturity (OMAT) images and FeO and TiO2 maps (Lucey et al., 2000a, 2000b; Gillis et al., 2003, 2004). Algorithms that allow us to derive OMAT (Lemelin et al., 2019) and FeO (Lemelin et al., 2015) from the Kaguya Multiband Imager VIS data (20 m/pixel), as well as TiO2 (Sato et al., 2017) from LROC WAC UV-VIS reflectance data (400 m/pixel) have been recently published. Here we choose to focus on the Clementine algorithms to rely on a single dataset for the analysis of the derived data products and the spectral interpretation. Indeed, we also extracted five-point spectra from the calibrated and registered Clementine UV-VIS image cube. Clementine color ratios were used for the initial identification and mineralogical assessment of pyroclastic deposits. This dataset minimizes brightness variations in multispectral scenes caused by albedo variations and topographic shading and isolates the color variations related to mineralogy or maturity (e.g., Pieters et al., 1994; McEwen et al., 1994).

The Moon Mineralogy Mapper (M3) imaging spectrometer on the Chandrayaan-1 spacecraft (Pieters et al., 2009) collected spectral images in 2009 (82 bands) over a broad wavelength range (400-3000 nm) and with pixel dimensions of 140 m/pixel (Table 2.1). The M3 spectra (Level 2

V1.0) provided to the PDS (Malaret et al., 2011) served to verify the Clementine 5-band spectral results (Table 2.2). The version of M3 data we used have topographic, radiometric, thermal, photometric, and instrumental corrections (Boardman et al., 2011; Clark et al., 2011; Green et al., 2011; Hicks et al., 2011; Besse et al., 2013). Continuum removal was applied to aid characterization of the 1- and 2-μm bands for identifying mineralogy (Pieters et al., 2009; Besse et al., 2014).

Table 2.2: Dark Halo Crater Spectra (Moon Mineralogy Mapper).

Province	Feature Name	Latitude, Longitude (Feature)	Spectrum Number	Image	Average Resolution (m/pixel)	Optical Period
West	Gassendi F	-14.8982, -44.9032	1	M3G20090209T014431_V03_L1B.LBL	140	OP1B
West	Unnamed	-18.2389, -46.4792	5	M3G20090209T033051_V03_L1B.LBL	140	OP1B
Gassendi	Unnamed	-17.0602, -40.2360	10	M3G20090208T175211_V03_L1B.LBL	140	OP1B
Gassendi	Unnamed	-17.9175, -41.0085	11	M3G20090208T175211_V03_L1B.LBL	140	OP1B
Humorum	Doppelmayer K	-23.9314, -40.7620	19	M3G20090208T175211_V03_L1B.LBL	140	OP1B

Three Lunar Prospector (LP) gamma-ray spectrometer (GRS) and neutron spectrometer (NS) elemental abundance data sets were used for FeO, TiO2, and Th compositions. The half-degree (~15 km/pixel) iron abundance data product contains data from the LP-GRS acquired during the low-altitude portion of the mission. Data reduction of this data set was given by Lawrence et al. (2002), with improved calibration by Prettyman et al. (2006). The half-degree titanium abundance values were derived from LP-NS measurements acquired during the low-altitude portion of the mission (for data reduction of this imagery, see Elphic et al., 2002). The half-degree thorium data is described by Lawrence et al. (2003).

Radar data presented here were collected using Earth-based telescopes at the Arecibo Observatory (transmitted) and the Green Bank Observatory (received). The radar wavelengths are 12.6 (S-band) and 70 cm (P-band) (Campbell et al., 2007; Campbell et al., 2010). Spatial resolution on the lunar surface is about 80 m for the 12.6-cm data and about 200 m for the 70-cm images. Of primary interest are the reflections collected in the same sense of circular polarization (SCP), which are sensitive to wavelength-scale surface rocks and those buried from a meter or two (for S-band) to 5-10 m (for P-band) below the surface. The S-band data can also be compared with LRO Diviner Lunar Radiometer Experiment data. Images at both wavelengths have played a key role in mapping smooth, rock-poor pyroclastic deposits (e.g., Campbell et al., 2008) and the changes in regolith loss associated with cryptomare deposit units (e.g., Campbell and Hawke, 2005).

Impact crater size-frequency density-based techniques provide model ages of the surface of units in our study area. Crater count data provide a means of determining relative age, and with assumptions, a means of estimating absolute (model) age (Michael and Neukum, 2010). LROC NAC images were used for crater counts and crater diameter measurements. Cumulative size-frequency distribution (CSFD) curves were constructed from the crater count data collected for each area. Crater model ages were calculated based on the CSFD curve using the Craterstats2 program (Michael and Neukum, 2010). The statistical error was calculated for the craters in each diameter bin (N) based on a Poisson distribution and is represented as error bars on the CSFD. The lunar production function and lunar chronology of Neukum et al. (2001) was used to estimate model crater age for the CSFD curves.

The criteria for cryptomare deposit identification in the Gassendi region are based on Antonenko et al. (1995) and references therein. Schultz and Spudis (1979) originally described the obscuration of mare deposits by highland material and later Head and Wilson (1992) coined the term “cryptomare”. The major criteria are 1) the presence of dark-haloed impact craters, which are exogenic craters that have excavated mare basalt from depth (Hawke and Bell, 1983; Bell and Hawke, 1984), 2) association with mafic geochemical anomalies, and 3) the presence of a significant component of mare basalt in the high-albedo surface unit as identified by either spectral band identification or mixing analysis (Head et al., 1993; Blewett et al., 1995). Cryptomaria emplacement ages are estimated by comparing the ages of nearby craters and determining superposition relationships. This approach is used when the cryptomare deposit is deeply buried

(greater than hundreds of meters). Basin and craters ages are based on the time-stratigraphic system of Wilhelms (Wilhelms, 1987; Wilhelms and Byrne, 2009).

Geochemical signatures (LROC WAC, Clementine, M3, LP-GRS, LP-NS) were used to verify both surface and buried mare basalt areas. Iron and titanium values for mare basalts exposed on the surface were acquired from level, uncontaminated areas of the maria. Values for buried basalts were extracted as an average of a 3x3 pixel matrix from the ejecta blanket of the dark-haloed impact craters that penetrated into the basalt layer (Table 2.3).

Table 2.3: Clementine Iron and Titanium abundance for dark-haloed craters in the Gassendi region.

Province	Crater	Latitude, Longitude	Diameter (km)	Description	FeO wt %[1]	TiO_2 wt %[1]
West	1	-14.8982, -44.9032	8.0	Gassendi F	14.5 ± 0.1	2.6 ± 0.1
West	2	-16.5793, -44.7583	8.0	Gassendi G	13.8 ± 0.2	2.4 ± 0.1
West	3	-17.8760, -48.0500	2.1	Unnamed DHC	14.0 ± 0.8	1.4 ± 0.1
West	4	-18.4273, -46.7980	1.6	Unnamed DHC	13.9 ± 1.2	1.3 ± 0.2
West	5	-18.2389, -46.4792	1.4	Unnamed faint DHC	14.0 ± 0.8	1.3 ± 0.1
West	6	-19.1297, -45.4624	3.4	Unnamed DHC	11.7 ± 0.5	1.7 ± 0.2
West	7	-18.1310, -43.6895	1.0	Unnamed DHC	13.3 ± 0.4	4.7 ± 0.3
Gassendi	8	-18.0179, -40.9718	1.2	Unnamed faint DHC	14.8 ± 0.0	1.7 ± 0.3
Gassendi	9	-16.9818, -40.4959	1.3	Unnamed faint DHC	14.7 ± 0.1	1.4 ± 0.1
Gassendi	10	-17.0602, -40.2360	1.0	Unnamed faint DHC	14.6 ± 0.1	2.4 ± 0.4
Gassendi	11	-17.9460, -41.0388	1.4	Unnamed faint DHC	14.8 ± 0.0	2.0 ± 0.2
Gassendi	12	-18.2377, -40.5315	1.0	Unnamed faint DHC	14.3 ± 0.1	1.8 ± 0.1

[1] These are the maximum value for the dark halos and were obtained by averaging a 3x3 pixel matrix in the area of the highest chemical concentration.

Multiple identifying characteristics were used as criteria to confirm the existence of lava lakes, including geochemical, geological, and morphological evidence. Elevated levels of FeO and TiO2 reveal the presence of mare basalt. The basalt may either be exposed or obscured, as a cryptomare deposit. The geologic criteria for discerning lunar lava lakes were devised by comparing lunar geologic structures to the morphology of terrestrial lava lakes. The lava lakes examined in other studies were located in the Andes (Witter et al., 2004), Antarctica (Harris et al., 1999), Ethiopia (Harris et al., 1999), and Hawaii (Swanson et al., 1979; Harris et al., 1999; Witham and Llewellin, 2006; Stovall et al., 2009a, 2009b). Lava lake morphology ranges from small-scale to large-scale features (Witter, 2004; Stovall et al., 2009a, 2009b). Identification of small-scale features

identified in terrestrial lava lakes (e.g., lava drips, lava textures, splash features, lava islands), is impractical given that they are either below the NAC camera resolution or are eroded and obscured over time by the regolith formation process (Gault et al., 1974). Priority was placed on identifying large-scale features (crustal foundering, vertical rinds, scarps, drain-back features, depressions, floor morphology) as seen on terrestrial lava lakes (Stovall et al., 2009a, 2009b) as these larger features may be preserved in the lunar environment.

2.3.0 Results

2.3.1 West province - Cryptomare Deposits

We discovered a new cryptomare deposit and confirmed the presence of a previously identified cryptomare deposit (Hawke et al., 1985; Lucey et al., 1991) (Figure 2.2B and 2.2C). Previous radar (Gaddis et al., 1985; Hawke et al., 1993) and spectral studies (Hawke et al., 1985; Lucey et al., 1991) concluded that Eratosthenian-aged (1.10-3.20 Ga; Wilhelms, 1987) craters Gassendi F and Gassendi G excavated mare material from beneath a highland-rich surface unit that was emplaced as ejecta from Gassendi, Mersenius, Mersenius P, Letronne, and other impact events. These craters are Nectarian in age, with the exception of Letronne (10.6°S, 42.4°W), which is Lower Imbrian in age (3.80 – 3.85 Ga; Wilhelms, 1987; Wilhelms and Byrne, 2009). This ancient buried basalt unit was emplaced after the formation of the Humorum basin (Nectarian) but prior to the aforementioned Nectarian-aged craters, and thus is Nectarian in age (3.92-3.85 Ga). Our geochemical and spectral data clearly indicate that craters Gassendi F and G excavated FeO-rich basaltic material (FeO ~14-15 wt. %; Figure 2.2B, 2.3A and 2.3C; Table 2.3), with an average TiO_2 value of 2.5 wt. % (Figure 2.2C; Table 2.3). Mare basalts with 2-2.5 wt. % TiO_2 are the most abundant on the lunar nearside (Giguere et al., 2000). Craters Gassendi F and G are both under 8 km in diameter and excavated mare material from depths of up to 700 m. Excavation depths for simple craters are calculated using $H_{exc}=0.1Dt$ (H_{exc} is the depth of excavation, D_t is the transient crater diameter). The transient crater diameter is derived using the relationship $D_t=0.84D$, where D is the observed crater diameter (Melosh, 1989).

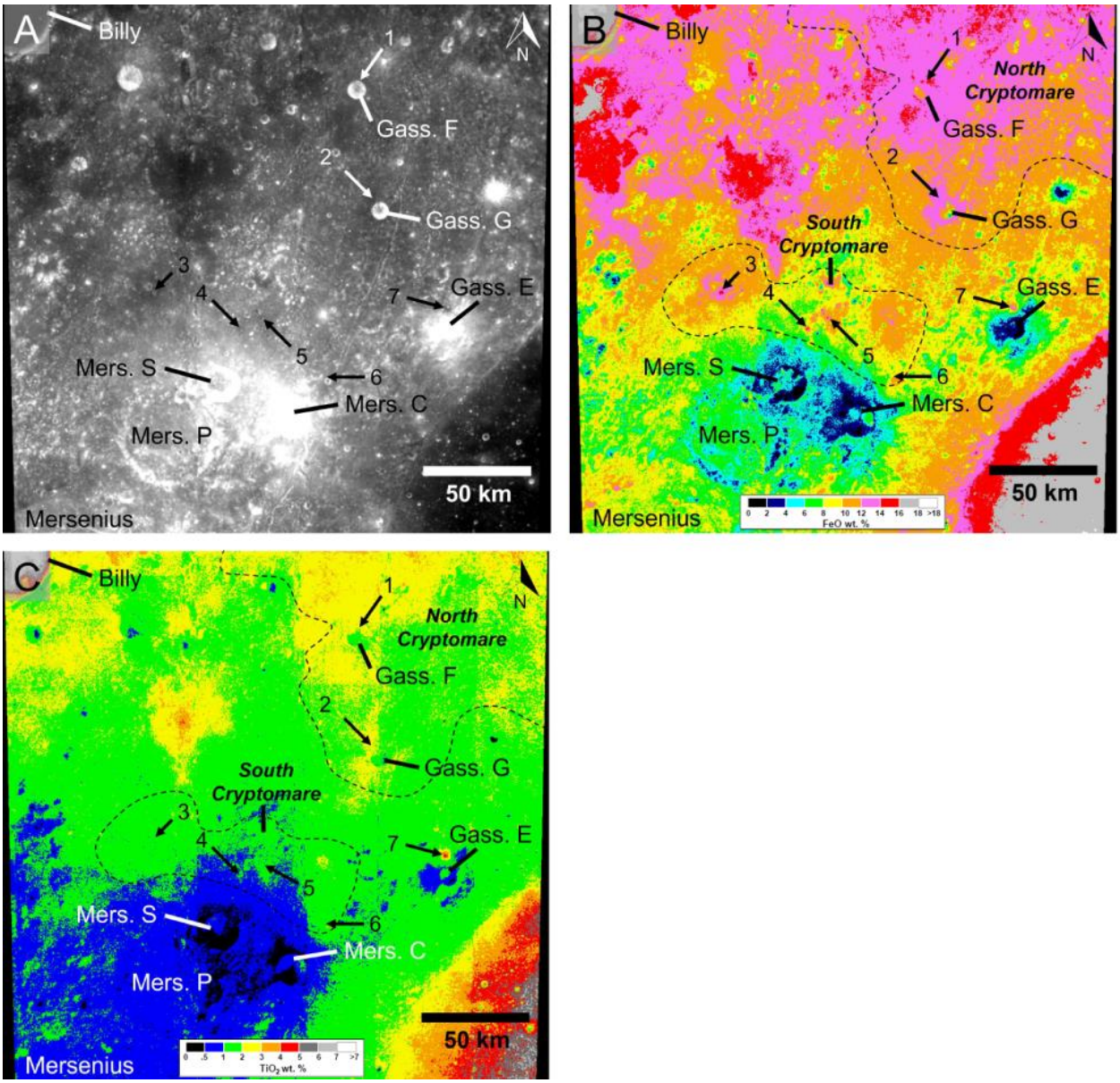

Figure 2.2: A) Clementine 750 nm image mosaic of the west province of the Gassendi region. Five-point spectra locations (numbered arrows, Table 2.4). B) FeO map derived from Clementine UV-VIS images. Northern and southern cryptomare (black dotted line). DHC FeO and TiO_2 values (numbered arrows, Table 2.3). C) TiO_2 map derived from Clementine UV-VIS images. Each image mosaic has a spatial resolution of 100 m/pixel and is centered at 46°W, 17.5°S (42-50°W, 14-21°S).

Small dark-haloed craters revealed a previously unidentified cryptomare deposit around craters Gassendi E, Mersinius C, and Mersinius S, south of Gassendi F and G ("South Cryptomare" in Figure 2.2B and 2.2C). The DHCs labeled 3-7 range in diameter from 1 km to 3.4 km; each crater exposes dark material from much shallower depths (~80-290 m) than Gassendi F and G. The crater ejecta FeO values range from 12.2-15.5 wt. % and their five-point spectra, by presence of a 1-µm

absorption, indicate that the dark material is dominated by mare basalt (Figure 2.3A; Table 2.4). Clinopyroxene was confirmed in the ejecta of DHC 5 (1.4 km) based on the observed absorption band centers at 0.985 μm and 2.200 μm (Spectrum 5 in Figure 2.3C). These mare flows were obscured by the compound effect of discontinuous, distal ejecta deposits of nearby Copernican-age (Present – 1.1 Ga; Wilhelms, 1987) craters Gassendi E, Mersinius C, Mersinius S and other craters. With one exception, the southern cryptomare deposit exhibits lower TiO_2 abundances (1.3-1.7 wt. %) than the values (~2.5 wt. %) determined for the northern cryptomare deposits exposed by Gassendi F and G. The exception, crater 7 in Figure 2.2 and Table 2.3, has an average TiO_2 concentration of 4.7 wt. %.

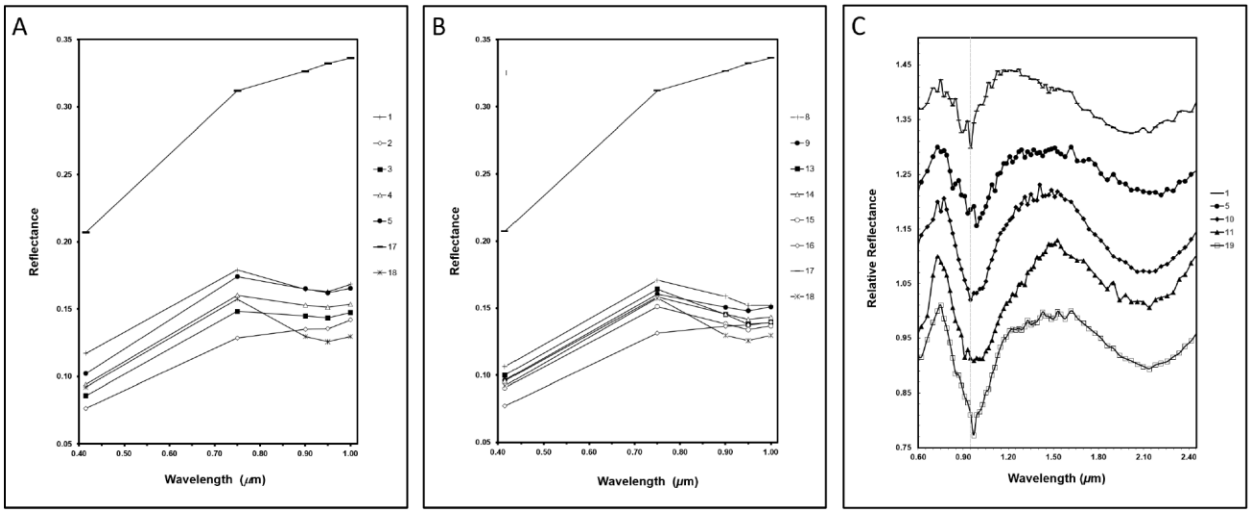

Figure 2.3: Five-point Clementine UV-VIS spectra for features in the Gassendi region A) West province of the Gassendi region. Spectra locations (Figure 2.2) are described in Table 2.4. B) Gassendi province crater interior. Spectra locations (Figure 2.4) are described in Table 2.4. Comparison spectra for fresh highlands (spectrum 17) and for fresh mare (spectrum 18) are shown on both A) and B). Spectra are an average of a 3x3 pixel matrix. C) Representative Moon Mineralogy Mapper (M3) dark halo crater spectra for the Gassendi region. Spectra 1 and 5 (Figure 2.2 and 2.3A), are for the West province. Spectra 10 and 11 (Figure 2.4), are for the Gassendi province. Spectrum 19 is a fresh mare crater (Doppelmayer K) in Mare Humorum. Continuum-removed spectra are offset for clarity. Spectra collected during optical period OP1B. Vertical gray dotted line at 0.95 μm.

Table 2.4: Clementine spectra locations for the Gassendi region. Spectrum are shown in Figures 2.4 and 2.6.

Province	Spectrum Number	Latitude, Longitude	Description of Area
West	1	-14.8982, -44.9032	Gassendi F rim crest
West	2	-16.5793, -44.7583	Gassendi G dark ejecta
West	3	-17.8760, -48.0500	Dark-haloed impact crater

West	4	-18.4273, -46.7980	Dark-haloed impact crater
West	5	-18.2389, -46.47920	Dark-haloed impact crater
Gassendi	8	-18.0179, -40.9718	Small crater with FeO-rich ejecta
Gassendi	9	-16.9818, -40.4959	Small crater with FeO-rich ejecta
Gassendi	13	-17.4517, -38.8962	Immature fracture wall
Gassendi	14	-17.4821, -38.9625	Immature fracture wall
Gassendi	15	-16.9941, -38.7843	Lava terrace scarp
Gassendi	16	-17.4897, -38.7717	FeO-rich plains material on NE Gassendi floor
Gassendi	17	-17.3601, -41.7505	Fresh crater on west wall of Gassendi
Mare Humorum	18	-19.6800, -41.9461	Mare Humorum crater 1

The two cryptomare deposits in the West province exhibit enhanced FeO values (9-13 wt. %) on the Lunar Prospector-Gamma Ray Spectrometer map. These deposits also show slightly enhanced TiO_2 abundances on the Lunar Prospector Neutron Spectrometer TiO_2 image. Letronne crater, rimcrest located 30 km north of the Gassendi region, has relatively high-thorium (Th) values (6-7 ppm) associated with the ejecta south of the crater (Lawrence et al., 2002; Elphic et al., 2002; Lawrence et al., 2003). These independent data sources, although lower in resolution, confirms the elevated geochemical values of the cryptomare deposit surfaces above average highlands in the area.

2.3.2 Gassendi Province – Gassendi Crater Interior

Our investigation of the Gassendi crater interior (Figure 2.1 and 2.4) focused on evidence for maria, cryptomaria, pyroclastic deposits, and lava lake morphology. Mare basalt deposits were mapped in the south and southeastern portions of the Gassendi interior near the crater wall (Titley, 1967; Schultz, 1976a, 1976b; Chevrel and Pinet, 1990, 1992; Hiesinger et al., 2000; Hackwill et al., 2006); however, no mare units have been mapped in the southwestern, northeastern, or northwestern sections of the crater floor. Large parts of the southwestern and northwestern floor exhibit elevated FeO values (12-14 wt. %) relative to those of the surrounding floor material (10-12 wt. %) suggesting the presence of cryptomaria (Figure 2.4B).

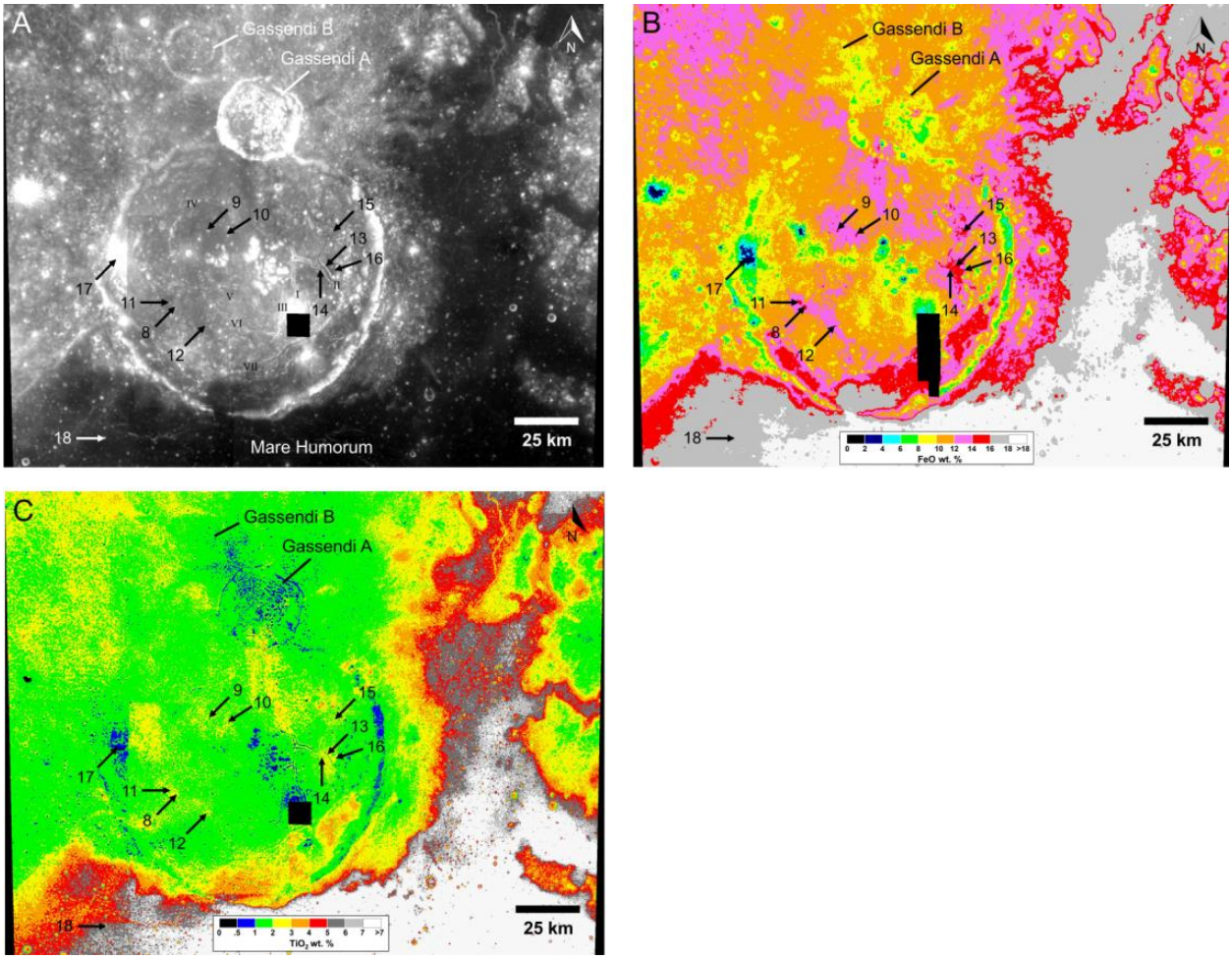

Figure 2.4: A) Clementine 750 nm image mosaic of Gassendi crater. Five-point spectra locations (numbered arrows, Table 2.4). Roman numerals (I – VII) indicate "Rimae Gassendi" floor fractures. B) FeO map derived from Clementine UV-VIS images. DHC FeO and TiO_2 values (numbered arrows, Table 2.3). C) TiO_2 map derived from Clementine UV-VIS images. Each image mosaic has a spatial resolution of 100 m/pixel and is centered at 39°W, 17°S (35-43°W, 14-20°S).

2.3.2.1 Cryptomare Deposits in Gassendi Crater

We identified cryptomare deposits on the floor of Gassendi crater based on the presence of dark-haloed impact craters with FeO-rich ejecta. The iron values range from 14.3 to 14.8 wt. % FeO (Figure 2.4B, Table 2.3: craters 8-12). These values were compared to the FeO abundances of the surface mare deposits mapped (Titley, 1967) in the southern and southeastern portion of the crater. The values fall within the range (14-18 wt. %) of the mapped deposits. The Clementine (Figure 2.4A and 2.3B, spectra 8, 9; Table 2.4) and M^3 (Figure 2.3C) spectra collected on immature surfaces exhibit strong "1 μm" bands centered at or longward of 0.95 μm, thus indicating high-Ca pyroxene. Clinopyroxene, elevated FeO contents, and low albedo are diagnostic features of mare

basalt (Antonenko et al., 1995). An additional cryptomare deposit on the northeastern floor was characterized in a similar manner to the western deposits. Spectra were collected for the walls of floor fractures, plains material, and lava scarps (spectra 13, 14, 15, 16; Table 2.4). Previous studies (Schultz, 1976a, 1976b; Chevrel and Pinet, 1990, 1992), as well as the iron and spectral data presented here, point to the occurrence of mare volcanism in this area.

2.3.2.2 Depressions in Gassendi Crater

Observations of molten material that was presumed to drain into fractures (Schultz, 1976b) led us to reexamine the floor of Gassendi crater for evidence of lava lakes. The geologic map of the Mare Humorum region (I-495, Titley, 1967) shows mare in the topographic low to the southeast and two depressions on the floor of Gassendi (Figure 2.5A). These depressions on the floor of Gassendi are labeled "NW" and "NE", and represent the northwestern and northeastern depressions. In addition, Hawke et al. (2013) identified a depression on the southwestern ("SW") floor of Gassendi. The LROC GLD100 elevation map confirms that these three areas are topographic lows when compared to the surrounding floor (Figure 2.5B). The northeast depression has the lowest elevation of the three depressions. We observed unique features in each of the three depressions.

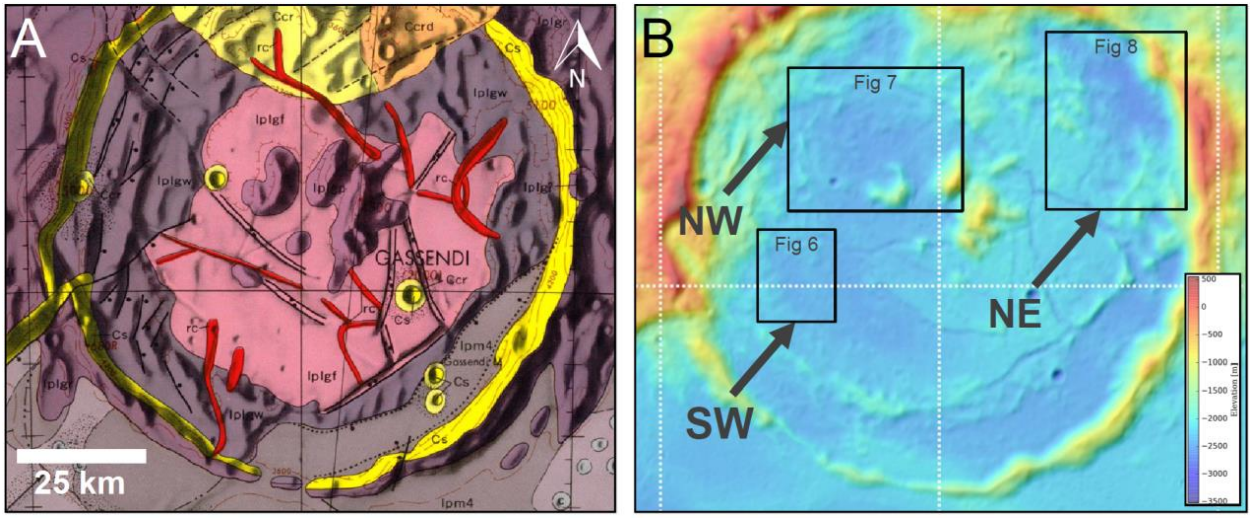

Figure 2.5: A) Three depressions on the floor of Gassendi crater. The northeast ("NE") and northwest ("NW") depressions are indicated on the map with contour lines that have interior tick marks (Titley, 1967). The southwest ("SW") depression was identified by Hawke et al., 2013. The pre-Imbrian wall (lplgw), floor (lplgf), and peak (lplgp) units from the Gassendi Group are the most extensive units within Gassendi crater. The Imbrian-aged mare material (Ipm4) is located in the southeast. For additional unit information, refer to the Geologic Map of the Mare Humorum Region of the Moon, I-495 (LAC-93). B) LROC elevation map of the Gassendi crater region derived from the GLD100 DTM. The southwest ("SW", Figure 2.6), northwest

("NW", Figure 2.7), and northeast ("NE", Figure 2.8) depressions are indicated on the map (black arrows). Elevation values on the map may be determined from the legend on the right side of the figure. The maximum depth below the (average scarp elevation) for each depression: southwest: 60 m (-2384 m); northwest: 120 m (-2386 m); and northeast: 300 m (-2311 m).

Previously we identified a scarp around the southwest depression (Hawke et al., 2013, 2015) (Figure 2.6). The western scarp is well defined, the eastern boundary is less defined, and the southern boundary is not visible. We note multiple layers of curvilinear scarps on the west side (Figure 2.6C and 2.6D). The scarp at the highest elevation is continuous and uniform in elevation. The elevation along the 200 m long west scarp is -2361 ± 2 m (Barker et al., 2016). The southern boundary is disrupted by several impact craters that modified the depression after it formed (Figure 2.6A and 2.6B). Mapping the boundary scarp (Figure 2.6B) reveals that the depression is 60 m below the average scarp elevation and has an area of ~50 km^2, which makes it smaller than the northwest and northeast depressions. The surface material in the depression exhibits enhanced FeO (12 to 14 wt. %) and TiO_2 (2-3 wt. %) values, and together with the spectral data (Figure 2.3B, spectrum 8) suggest the presence of mare basalt material (Figures 2.4B and 2.4C). A fracture in the floor of Gassendi runs from south-southeast to north-northwest under the western floor of this depression. A second floor-fracture traverses the northern part of the depression from the southwest to the northeast (Figure 2.6A). The morphology of both fractures is subdued within the depression due to obscuration by mare basalts (Figure 2.6).

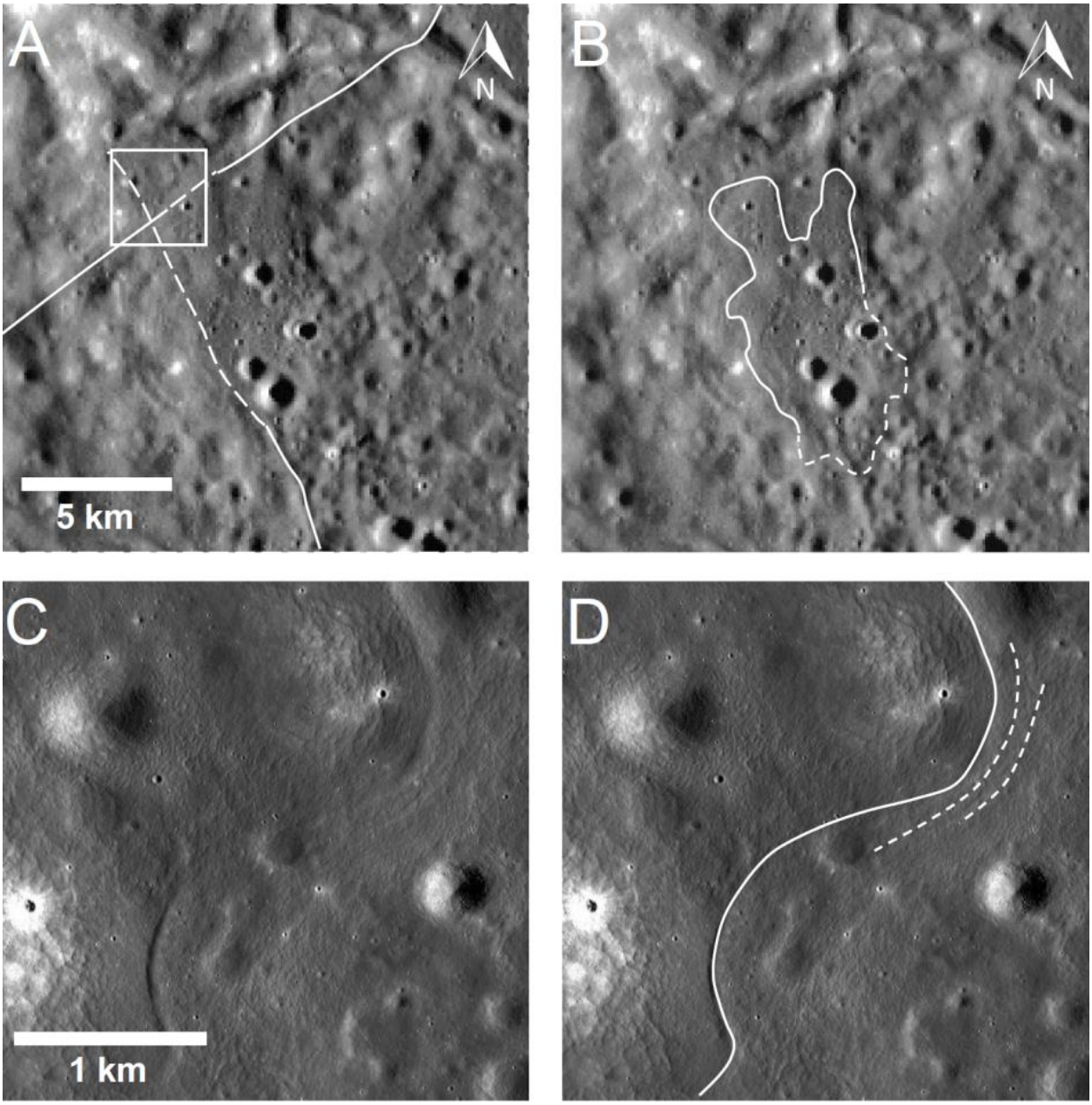

Figure 2.6: Two identical views of the small (~50 sq km) southwestern lava lake depression located 30 km from the center of Gassendi crater. A) Low relief scarps interpreted as lava terraces are visible on the west and east sides of the depression. The white box indicates the location of C) and D). Two fractures (south-southeast to north-northwest under the western floor; southwest to northeast under the northern floor) are dashed where the fracture is buried by mare basalt and indistinct. B) The inner scarp is outlined with a white solid line (dashed line indicates the scarp is not visible or indistinct). WAC near side mosaic, composed of high incidence angle frames (643 nm, 100 m/pixel) (Speyerer et al., 2011). C) Curved lava scarps on the west side of the southwestern depression. D) The scarp is outlined with a white solid line (dashed line where the scarps are indistinct); the depression is in the lower right of the image. NAC M1200404178R, 1.24 m/pixel, incidence 70 degrees.

Several features of possible endogenic origin, including an irregular depression partly surrounded by a scarp, were documented on the northwest floor by Schultz (1976b, see Figure 2.13). The floor of the northwest depression is flat in the south and is undulatory to the north, which may be due to the presence of floor fractures and slumping wall material (Figure 2.7). There are two north-south oriented floor fractures 12 kilometers apart on the east and west sides of the depression. The depression has a ~22 km scarp that traverses its southeastern edge. No scarp is visible on the north side; thus, the area of this depression is difficult to determine. We used a Kaguya DTM (Haruyama et al., 2008a; 2008b) to determine that the southern scarp is nearly constant in elevation (-2386 ± 16 m) along its exposed length (Figure 2.7) with the exception of the western edge, which is higher due to the incursion of Copernican-aged crater Gassendi P. The maximum depth of this depression is 120 m below the average scarp elevation. The FeO abundance of the floor is mafic, in the range of 12 to 14 wt. %; the TiO_2 abundance is 2 to 3 wt. % (Figure 2.4B, 2.4C), which is higher than the surrounding highlands.

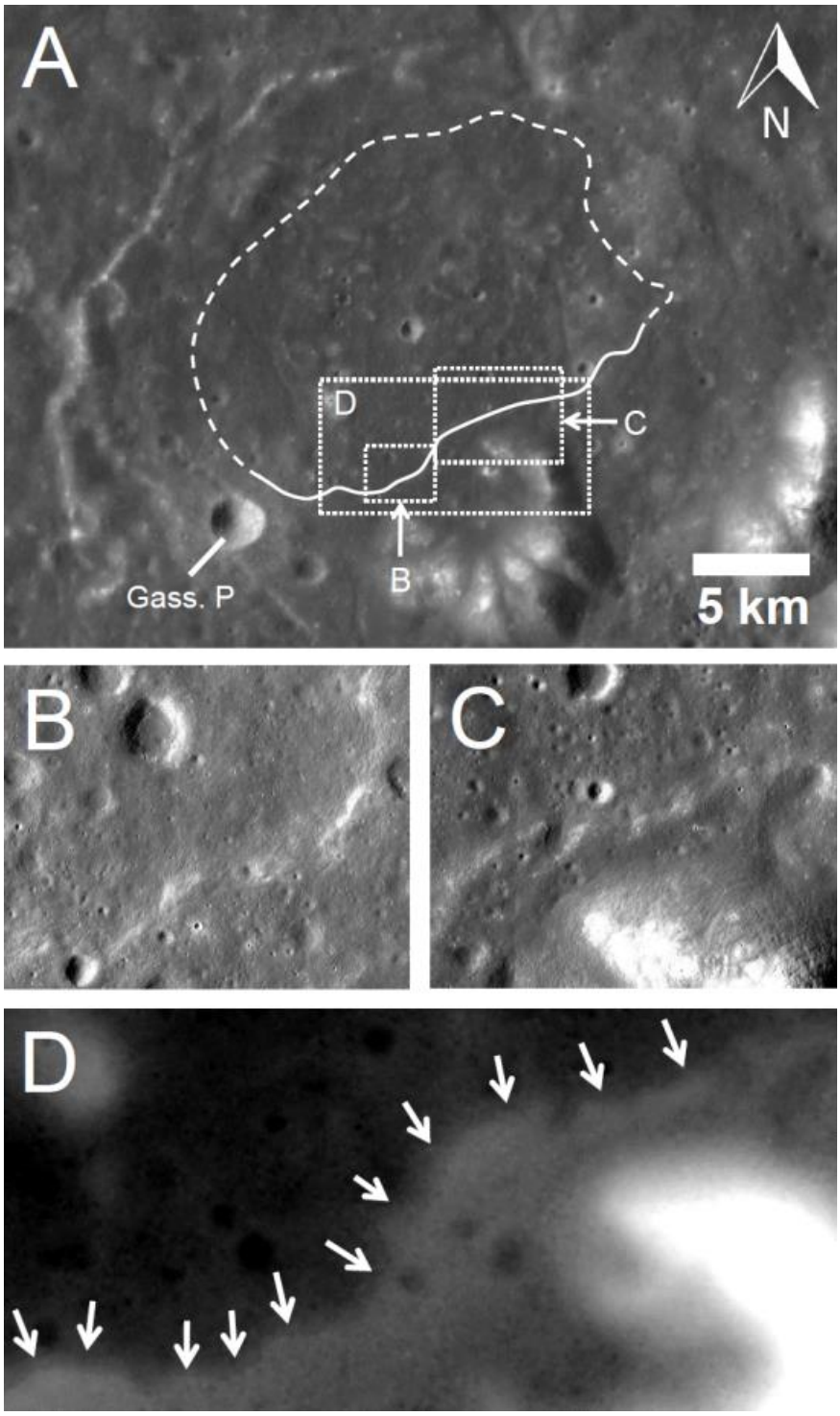

Figure 2.7: A) The northwest depression features a prominent scarp on the south side of the depression (white solid line); the boundary is less distinct to the north (white dotted line). High resolution NAC views, B) and C), show the irregular scarp. B) Western portion of the scarp. C) Eastern portion of the scarp. NAC M1112075088, 0.9 m/pixel, incidence 68 degrees. D) The southern scarp has a constant elevation (white arrows), Kaguya DTM.

We confirm the existence of the volcanic features previously reported by Schultz (1976a, 1976b) on the northeastern floor of Gassendi (Figure 2.1). LROC NAC images reveal floor fractures, wall scarps elevated above the fractured floor, perched mare-like plains units, and distinct scarps bounding the northeast depression (Figure 2.8). We identified scarps interior to the bounding scarp. The scarps have an irregular boundary in the plan view and a stair-step appearance in the NAC profile. We processed high-resolution NAC images of the scarp for comparison to terrestrial scarps (Figure 2.8B-8E). The morphology of the floor, while subdued at the meter scale, has complex topography at a decameter and larger scale. There are topographic highs and lows, which span 200-300 meters within the extents of the depression. Two elevated circular features, each just under 2 km in diameter (Figure 2.8B), are depicted as perched plains in Figure 2.9A. The lowest elevation in the depression is in the northeast (Figure 2.8A) and is 300 m below the average elevation of the bounding scarp. Topographic data (SLDEM2015, NAC DTM) show the top of the scarp around the depression tilts up to the southwest, which is towards the center of Gassendi. Two major floor fractures exit the depression on the southwest side and widen as the distance from the depression increases (Figures 2.8A and 2.9A). The depression exhibits enhanced FeO and TiO_2 values (Figure 2.4B and 2.4C), relative to the average Gassendi floor values. The FeO abundances range from 12 to 16 wt. %. The highest FeO concentrations (15-16 wt. %) are associated with perched plains deposits NE and SW of Rima Gassendi II (Figure 2.4A). There are enhanced TiO_2 abundances (2-4 wt. %) to the north of the circular features within the depression and also associated with the low albedo perched plains. This location corresponds to the Rima Gassendi II ST ("spectral trough") unit defined by Chevrel and Pinet (1990, 1992) using Earth-based telescopic multispectral images. The authors determined that clinopyroxene (spectral absorption centered at 0.98 μm) was a major component in the ST material.

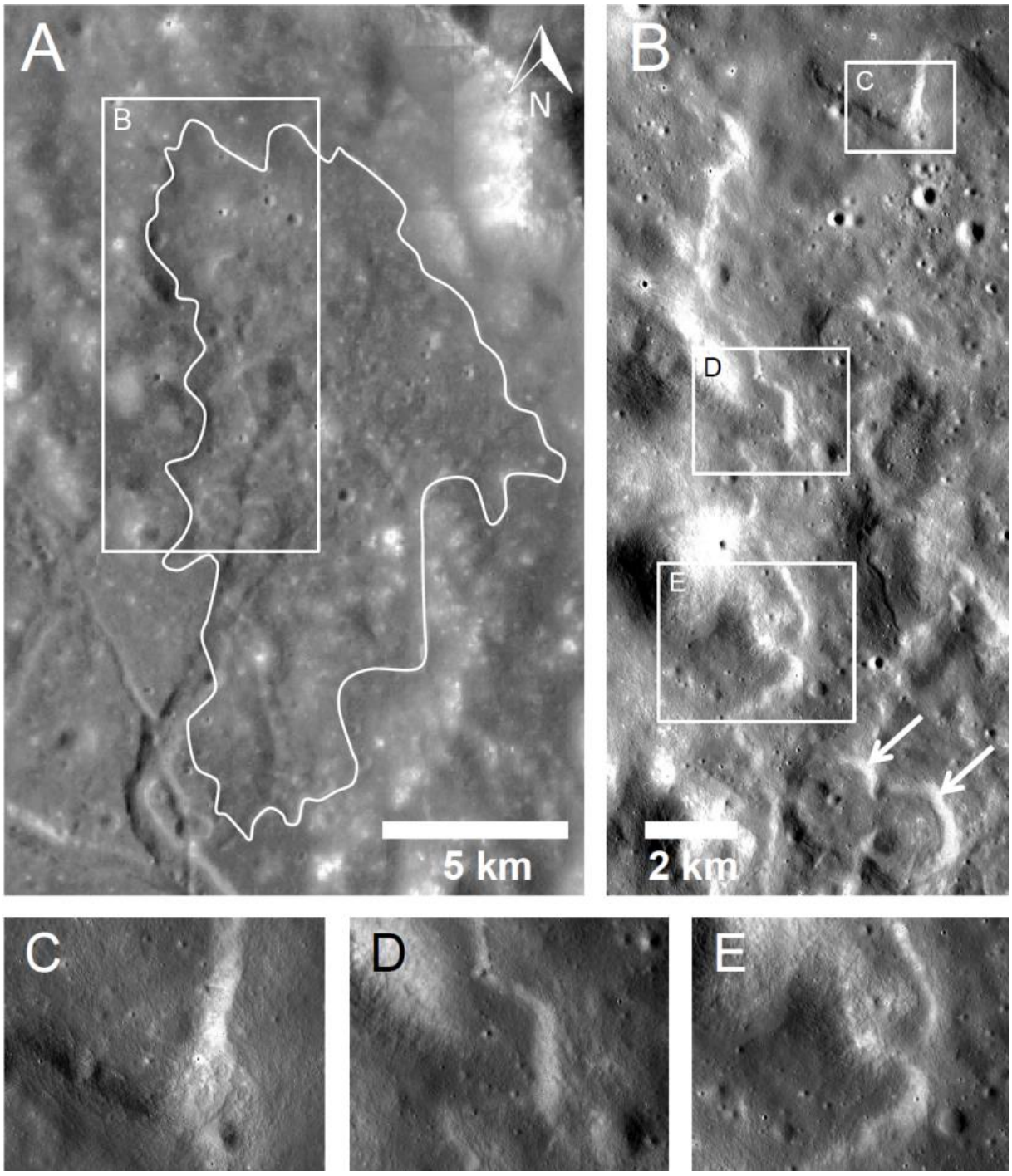

Figure 2.8: The northeast depression has a prominent scarp which is visible on all sides of the depression (white solid line encloses the depression). The white box outlines the detailed image shown in B). WAC Global Morphologic basemap (100 m/pixel). B) Western margin of the northeastern depression. This portion of the scarp trends north and south. Two elevated circular features, 2 km in diameter, are marked with white arrows. The white boxes outline the detailed NAC images shown in C, D, and E. M193210370, resolution 1.9 m, incidence angle 74.9 degrees. North is up in all images.

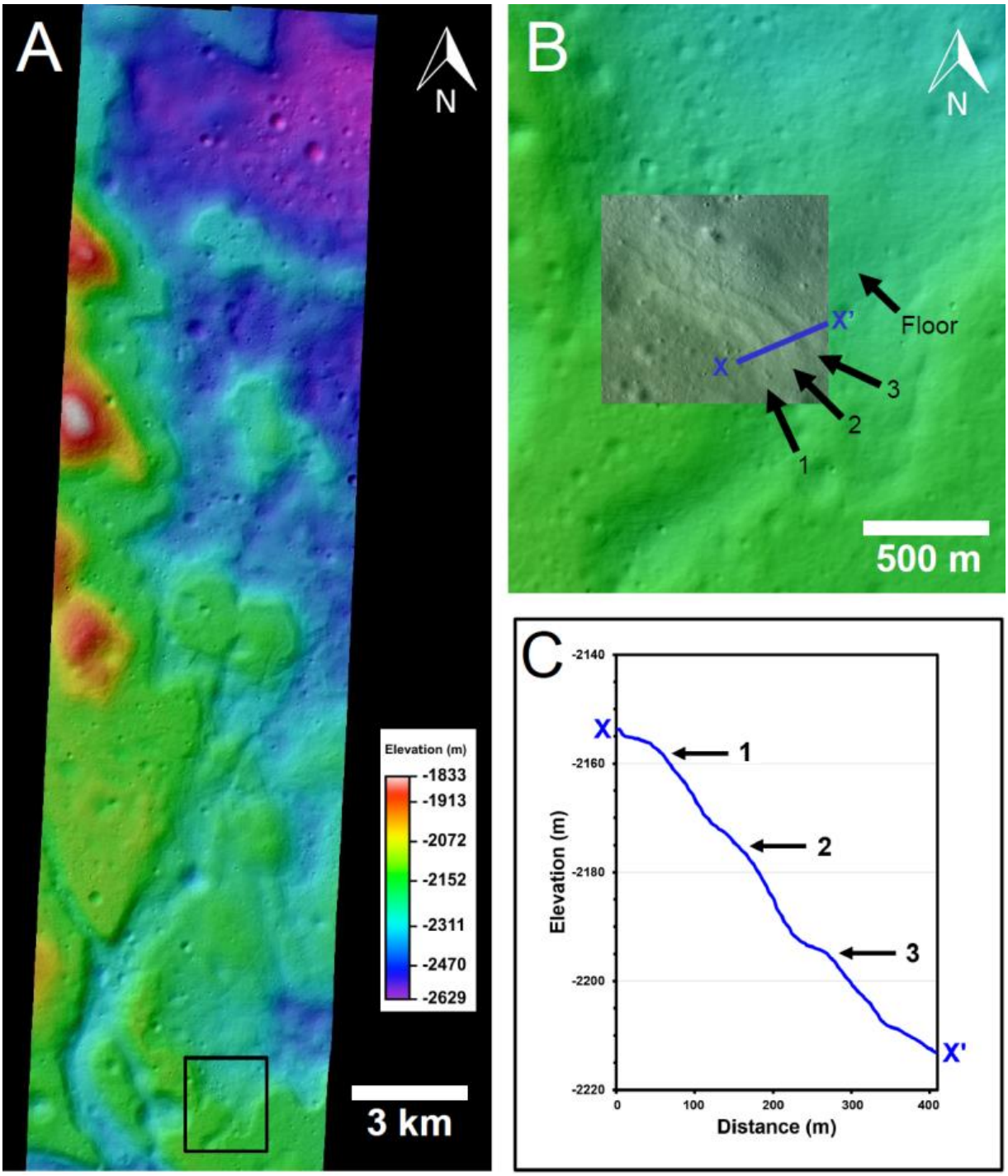

Figure 2.9: A) Depression in the northeast portion of Gassendi crater. Image centered at lat,lon: -17.13°, 321.11°. This view overlaps 8B and extends the view to the south. Multiple scarps at the south end of the NE depression (black box) refer to image B). DTM is 3 m/pix resolution, derived from NAC stereo image pairs (M1213319041, M1213326073). B) Multiple scarps on the southeast side of the NE lava lake in Gassendi crater. Scarp elevations (m) are 1: -2158, 2: -2175, 3: -2194, mean floor elevation: -2232. Vertical profile from X to X' (blue line). NAC DTM (background, 3 m/pix, stereo pairs M1213319041, M1213326073); inset NAC image (M1123846148R, incidence angle 72.4, resolution 1.8 m/pix). C) Vertical profile (X to X') of the three scarps on the southeast side of the NE lava lake.

2.3.3 Northeast Province - Pyroclastic Deposits

A previously unrecognized pyroclastic deposit was identified using high-Sun WAC imagery, P-band and S-band radar. The deposit is in the highlands west of Rimae Herigonius, approximately 45 km to the northeast of Gassendi (Figure 2.1). This area is mapped as Imbrium ejecta and upper Imbrian-aged mare material on the Letronne geologic map (Marshall, 1963). Pyroclastic deposits are a potential resource (Hawke et al., 1990) and provide compositional information on the lunar mantle (Delano, 1986; Shearer and Papike, 1993). The low-albedo and spectrally red deposit has an area of ~250 km^2 and blankets hills and depressions (Figure 2.10). The S-band same sense circular polarization (SCP) radar (Figure 2.10D) shows the deposit to be smooth, rock-poor to a meter or two in depth based on low reflections for this area (Campbell et al., 2008). A possible source vent (15.0°S, 37.7°W) has been identified using LROC images (Figure 2.11). This depression ("south vent") is roughly rectangular in shape (2 × 3 km), has a depth of ~120 m, and is associated with an unnamed north-south oriented lineament, interpreted as a fault or fracture (Marshall, 1963). The pyroclastic deposit (white dashed area in Figure 2.10A) exhibits FeO values averaging 14-16 wt. %, with the highest values approaching 17 wt. % (Figure 2.4B), and TiO_2 values between 3 and 4 wt. % (Figure 2.4C) in the Kaguya (Ohtake et al., 2008) and Clementine (Lucey et al., 2000a, 2000b; Gillis et al., 2003, 2004) data. A second possible vent is located 8 km to the north at 14.7°S, 37.7°W (Figure 2.10). This "northeast" vent resides on the same lineament as the south vent, which suggests the two vents were possibly part of a fissure eruption. A possible third vent, 13 km to the northwest, is on a northwest-southeast trending rille. Located at 14.8°S, 38.1°W, this smaller vent (500 × 800m) exhibits a subtle dark mantle around the vent (Figure 2.10A).

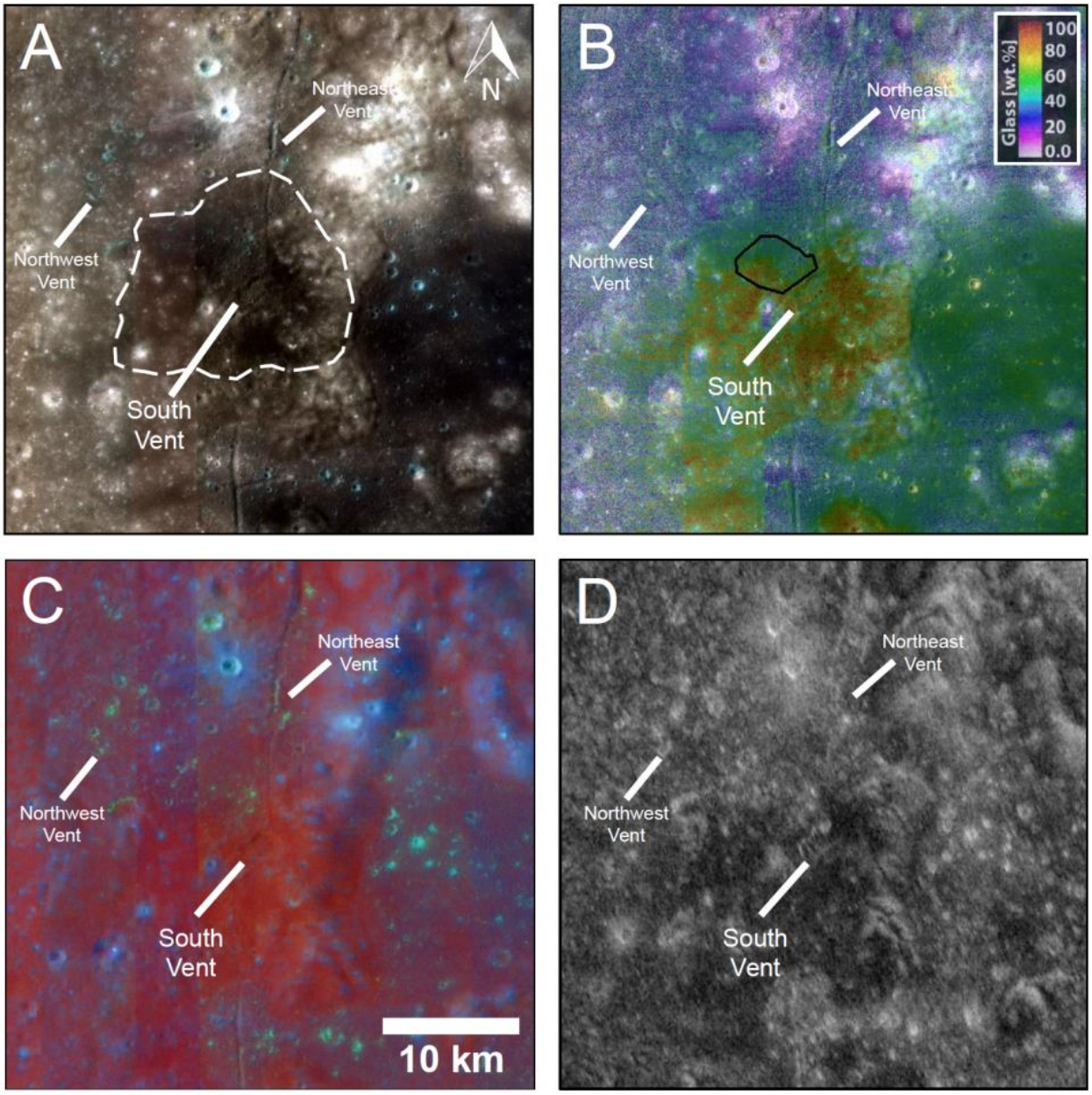

Figure 2.10: A) Pyroclastic deposit to the NE of Gassendi crater. The white-dashed outlines the primary deposit. The large south vent, as well as the northeast and northwest vents are highlighted. Kaguya Multiband Imager, spatial resolution of ~20 m/pixel; false-color view (red= 900 nm; green=750 nm; blue= 415 nm). B) Glass abundance map over Kaguya MI Band 2 image. Produced by applying Hapke's radiative transfer equations to the continuum removed MI data. Assumptions: regolith grain size is 17um, glass grain size is 60um, and the Mg number is 65 (Lemelin et al., 2015; Trang et al., 2017). Rock abundance (Bandfield et al., 2011) calculated on region of interest (black outline). Resolution: 62 m/pixel. C) Kaguya Color Ratio image (red=750/415 nm; green=750/950 nm; blue=415/750 nm) showing glassy Fe2+-rich pyroclastics (deep red) around the south vent. D) Smooth, rock-poor pyroclastic deposit shown around the south vent. S-band radar, same sense of circular polarization (SCP) (Campbell et al., 2010).

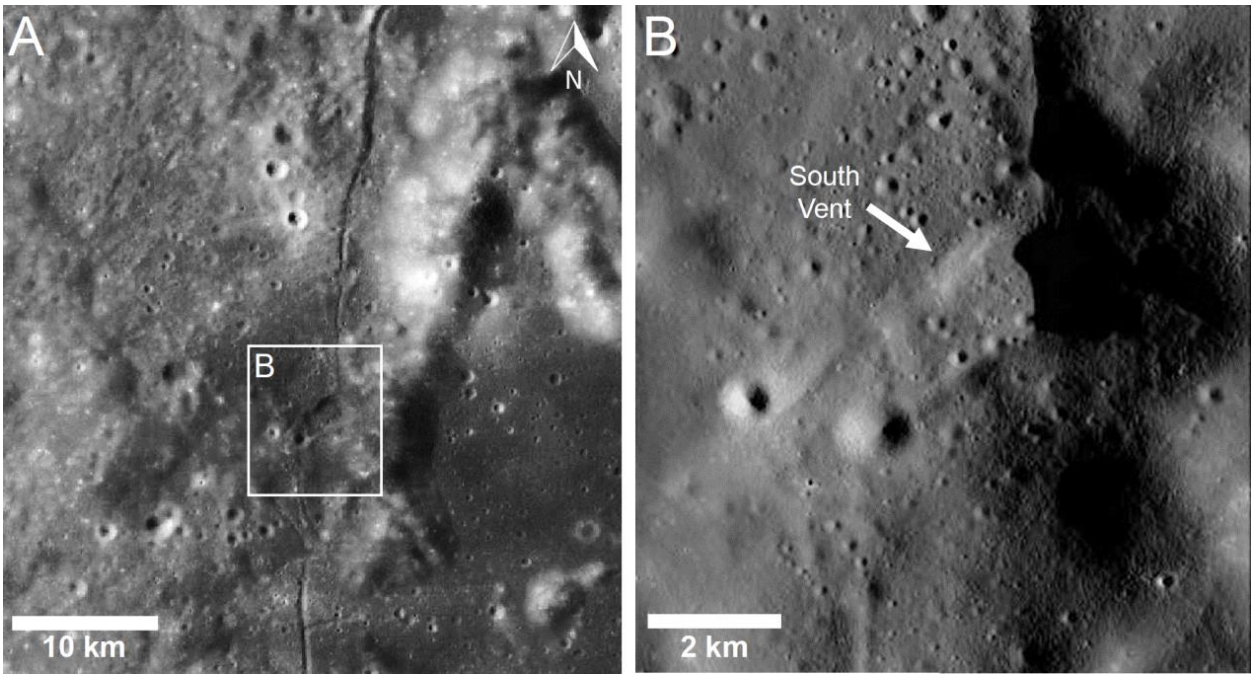

Figure 2.11: A) South pyroclastic vent and deposit to the northeast of Gassendi crater. WAC near side mosaic (643 nm, 100 m/pixel) (Speyerer, 2011). B) Portion of a mosaic of NAC frames M193203275L&R. The south pyroclastic vent is indicated by the white arrow.

We determined the rock abundance (Diviner map based on Bandfield et al., 2011) of the south pyroclastic deposit to be 0.3 ± 0.1%. The rock abundance is similar (0.32%) to an Alphonsus-type localized deposit (Trang et al., 2017). Modal rock abundances for regional pyroclastic deposits are 0.3% while highlands and maria exhibit higher surface rock abundance values of 0.4, and 0.5%, respectively (Bandfield et al., 2011). We determined the mineralogy with two instruments and methods. The Kaguya color ratio image, using previously defined band ratios (Pieters et al., 1994; McEwen et al., 1994), shows the deposit as deep red, i.e., as having a steep continuum, (Figure 2.10C) which is indicative of glassy Fe^{2+}-rich pyroclasts (McEwen et al., 1994; Pieters et al., 1994). Kaguya mineral maps that we derived (Lemelin et al., 2015; Trang et al., 2017) show the mean abundances to be: glass (67 ± 11%), clinopyroxene (19 ± 6%), and plagioclase (13 ± 5%). Evidence for olivine and orthopyroxene in the spectra is non-existent (Figure 2.10B). On the basis of Kaguya data, we conclude this is a glass-rich deposit that includes small amounts of basaltic material. Some highland contamination has occurred based on the abundance of plagioclase. Identifying a new pyroclastic deposit in the northeast province adds to the previously identified inventory (e.g., Mersenius crater, Hawke et al., 1993; Gaddis et al., 2003; Gustafson et al., 2014; Trang et al., 2017).

2.4.0 Discussion

Volcanism on the Moon was active for an extended period of time (~1.1-4.0 Ga), with the major activity occurring between 3.4 and 3.7 Ga (Head, 1976; Hiesinger et al., 2003, 2011). Volcanism in the Gassendi region (e.g., basalt flows, cryptomaria, pyroclastic deposits, and lava lakes), discussed below, was active prior to and during this peak (~3.6-3.9 Ga).

2.4.1 West Province - Cryptomaria

The newly identified cryptomare deposit located to the south in the West province (Figure 2.2B and 2.2C), together with the previously identified cryptomare deposit to the north (Hawke et al., 1985; Lucey et al., 1991), provide insights into the stratigraphy and evolution of volcanism in the West province (Figure 2.1 and 2.2). The northern cryptomare deposit (excavated by crater Gassendi F and G) has a maximum burial depth of ~700 m and is likely Nectarian in age. The southern cryptomare deposit has a maximum burial depth of ~80-290 m, based on the shallower excavation depth of DHCs 3–6 (Table 2.3). The southern cryptomare deposit, like the northern cryptomare deposit, was obscured by ejecta from craters (Gassendi, Mersenius, Mersenius P), thus is also likely Nectarian in age. Subsequent impacts (Copernican-aged Gassendi E, Mersinius C, Mersinius S) further obscured the southern cryptomare deposit with additional distal ejecta. These are "Balmer-type" cryptomare deposits (Giguere et al., 2003; Hawke et al., 2005). Balmer-type cryptomare deposits are formed by burial from distal crater ejecta deposits, and often by multiple craters. The type location is Balmer basin (Hawke and Spudis, 1980; Hawke et al., 1985; Giguere et al., 2003; Hawke et al., 2005).

Compositional data of the two cryptomare deposits suggests that either the source region changed or the composition of the source evolved between eruptions. The average composition of the southern cryptomare deposit is 1.4 wt. % TiO_2 (craters 3-6, Table 2.3). Dark-halo crater 7 (Table 2.3), 60 km to the east, is higher in TiO_2 (4.7 wt. %). The difference in TiO_2 composition is greater than the +/- 1 wt. % uncertainty of the technique (Lucey et al., 2000a). We infer from these data that the southern cryptomare deposit consists of low-Ti mare and that the northern cryptomare deposit has a different composition, medium-Ti. The classification of Ti basalts into low and medium is based on Pieters et al. (1993) and Taylor et al (1991).

The geochemical evidence suggests two episodes of mare volcanism in the West province. Humorum basin impact ejecta was overlain with a layer of medium-Ti basalt in the northern

Gassendi region and low-Ti basalt was erupted to the south. Subsequently, multiple Nectarian and Imbrium-aged craters buried the two basalt units with highland material. Lastly, the southern deposit was partially obscured by Copernican-aged crater (Gassendi E, Mersinius C, Mersinius S) material. The TiO_2 content of material excavated by crater 7 is higher than the average values of either the northern or southern cryptomare. The basalt near Gassendi E may not be related to the other deposits and could represent a dike or pond from a different source region (Table 2.3).

The identification of a new cryptomare deposit (Figure 2.2B and 2.2C) in the West province increases the overall cryptomare deposit surface area in the Gassendi region by 20-25%. Furthermore, the composition of the basalt differed for the two eruption episodes, indicating that either the basalts came from two different mantle source regions, or a single mantle source region evolved between the eruptions.

2.4.2 Gassendi Province – Lava Lakes on Gassendi Floor

The Moon likely hosted two types of lava lakes: active and inactive (Swanson et al., 1979; Harris et al., 1999). Active lava lakes can be considered as the exposed upper surface of a convecting magma column and may be subdivided into two categories: sustained or cyclical (Witham and Llewellin, 2006). Inactive lakes are rootless and stagnant, and do not form directly on top of the magma column but instead represent lava that pooled in a topographic low to form a lake. An inactive lake may be referred to as a "mare pond" or "mare patch", however, this terminology is most often applied to exposed mare surfaces that are not part of a named mare. Identifying and categorizing once active lava lakes on the Moon has important implications with regard to models of lunar volcanism.

Within the Gassendi Province, lava was confined and remained resident in three depressions; thus, forming lava lakes (Figures 2.6, 2.7 and 2.8). Evidence for lava lakes in Gassendi relies on the identification of a mafic signature and observing the present-day morphology (e.g. scarps, depressions, level floor) of the preserved last stages of lava lake activity (Gillis and Spudis, 2000). The three lava lakes we investigated showed elevated surface FeO values (12-16 wt. %) relative to the average Gassendi floor values (Figure 2.4; Table 2.5). The mafic signature may take the form of exposed mare basalts or a cryptomare. Confinement allows the lava to collect, cool, and form scarps by the cyclical buildup of a lava crust around the margins of each lake. Each fill and drainage episode leaves additional material behind, enlarging the scarp (Richter, 1970; Witham and Llewellin, 2006). A flat surface indicates a level lake surface where no drainage occurred,

whereas a depression with surrounding scarps suggests the previous existence of a lava lake that drained and left a mafic signature and residual ring of material behind. The lava may have drained back through the floor fracture conduit into the source magma chamber or may have been siphoned off laterally via a mechanically or thermally eroded breach in the topography (Hurwitz et al., 2010). Tectonism is an unlikely explanation for the scarps as they tend to be curvilinear in plan view and follow topographic contours. Although the three lava lakes have similar volcanic origins, each lake has a unique history.

Table 2.5. Summary of Gassendi Depressions Characteristics

Depression	Area (sq km)	Scarp Length[1] (km)	Depth – Max[2] (m)	Scarp Height (m)	FeO (wt. %)		TiO_2 (wt. %)	
					Max	Surface[3]	Max	Surface[3]
Southwest (SW)	45	15	60	16	15	12-14	3	2-3
Northwest (NW)	244	22	120	53	15	12-14	4	2-3
Northeast (NE)	262	93	300	136	16	12-15	4	2-3

[1]Total length of all bounding scarps, not including interior scarps.
[2]Average scarp elevation to maximum depth of the depression.
[3]Range of values for the surface of the depression.

The southwest depression (SW) contains basaltic material. The surface material excavated by small impact craters from the depression span FeO 12-15 wt. % (Table 2.5). These FeO values are lowered due to obscuration by highland-rich ejecta from Copernican-aged Gassendi A (32 km, 15.55°S, 39.80°W) and other craters. The topography surrounding the SW depression is lowest on the east and southeast sides. The lowest point of the depression is 60 m lower than the bounding wall. The lake level may have risen over these low elevation points in the bounding wall, causing lava to flow out of the depression and downslope to the southeast. There is evidence for mare basalts to the southeast (Figure 2.4B). The mafic signature from the depression extends to the southeast for a distance of 22 km. The FeO values of this feature range from 12-14 wt. % with the width of the mafic signature on the surface narrowing as the distance from the SW depression increases. A small fracture (200 m width) is an alternate source for the basalts outside of the depression. An alternative path for the overflow is the fracture running south-southeast to north-

northwest under the western floor of the depression. This fracture, as well as the southwest-northeast fracture, have degraded morphology at the lowest elevation within the depression, as they were likely covered by the mare infill. With multiple layers of scarps on the walls of the depression (Figure 2.6C and 2.6D), we postulate that this was an active cyclical lava lake with multiple fill and/or drainage episodes. Alternatively, a single fill episode, followed by slow, sporadic drainage may have produced the observed morphology. The resulting morphology would be indistinguishable between the two processes. The flat floor of the depression, with the exception of secondary craters, suggests that the southwest lava lake did not undergo complete drainage.

The northwest (NW) depression, like the SW depression, is a cryptomare deposit and is enclosed on all sides by higher terrain restricting the outflow of lava. The single lava scarp on the southern boundary is well developed (Figure 2.7). The Clementine geochemical data confirms the presence of mare basalts confined to the depression on the west side. The surface and excavated basaltic material from these deposits range from 12-15 wt. % FeO (Table 2.5), which is higher than the surrounding surface FeO values (10-12 wt. %). The highest FeO values are located in the ejecta excavated by small craters. The area is bounded to the south by the Gassendi central peaks and encircled to the west and north by floor fractures. On the eastern side is a large set of fractures, which are more than a kilometer wide in some areas. There are two smaller north-south trending floor fractures; widths average about 200 meters. The fractures are ~6 km from the center of the depression and are the most likely location of mare basalt entering and draining from the depression. The continuous scarp on the south boundary suggests a single influx of lava, followed by a lengthy residence period allowing the scarp to grow in size. This event was followed by lava lake drainage.

The northeast (NE) depression is more complex than either the SW or NW depressions, as it exhibits large floor-fractures (Figure 2.8), is larger in spatial extent, and has the greatest elevation difference between floor and rim (Table 2.5). The morphology matches a Class 3 floor-fractured crater (Schultz, 1976b; Jozwiak et al., 2012), which typically has a wide moat between the base of the crater wall and the crater interior, and radial and concentric (polygonal) fractures. A prominent scarp is nearly continuous around the northeast depression (Figure 2.8A). The scarp is partially obscured on the northeast side by mass wasting of the nearby crater wall. The scarp is sinuous, unlike a linear tectonic feature that crosscuts terrain. The elevation of the scarp is remarkably uniform, varying only a few hundred meters over the ~90 km length. The scarp elevation is higher

on the inside boundary (Figure 2.9A), closest to the center of the crater; a modeled 1.9 km thick intrusion producing a Bouguer gravity anomaly of ~40 mGal (Jozwiak et al., 2015) could have produced the observed central uplift tilting the floor and bounding scarp. We identified three levels of scarps above the floor (Figure 2.9B and 2.9C, Table 2.6). The NE lake had a sustained residence period, which created the wide main scarp 1. The lava lake appears to have had multiple fill/drain episodes or simply drained in three stages, with a sustained level of lava between each intervening period that allowed scarp formation. Finally, the lava drained leaving a thin veneer on the floor.

Table 2.6: Multi-layered scarp on the Gassendi NE lava lake. DTM is 3 m/pix resolution, derived from NAC stereo image pairs (M1213319041, M1213326073).

Scarp	Elevation (m)	Height (m)	Width (m)
1	-2158	17	100's m
2	-2175	19	108
3	-2194	38	70
Floor	-2232	0	NA

The morphology of the pair of raised features, each 2 km in diameter (Figure 2.8 and 2.9), is similar to a basaltic butte. We suggest that these buttes formed in a multi-step process: First, rising mare lava filled the main depression (outlined in white in Fig 7A) to a level that was even with the mare outside of the crater rim crest; subsequent drainage of the lava, when the main depression's rim was breached, left the basalt-filled craters as perched inactive lava ponds, which when solidified created a positive relief feature. High-iron material was excavated by the 300 m crater on the north butte. This butte morphology is also seen at: Yerkes (36 km; 14.6°N, 51.7°E), Jansen (23 km; 13.5°N, 28.7°E; Moore, 2001); an unnamed crater located north of Euler H in an Imbrium lava flow (1.2 km; 26.6°N, 28.7°W; Schaber et al., 1975), and Le Monnier (61 km; 26.6°N, 30.6°E; Florenskii et al., 1978) in a mare setting and also with the unusual interior morphology of Wargentin crater (84 km; 49.6°S, 60.2°W; Hawke and Bell, 1981; Whitten and Head, 2015).

With the greater areal exposure of mafic material, the basalt surface and maximum excavated FeO values (12-16 wt. %) in the NE depression (Table 2.5) are higher than the background FeO

level of the Gassendi floor (10-12 wt. %) and has higher peak iron values than either the southwest or northwest depressions. The large floor fractures on the southwest side of the depression are probable conduits for the ingress and egress of mare basalt onto the floor of the depression. The lava lake was likely sustained at a high level for an extended period of time, creating the large continuous scarp bounding the depression. Later, drainage lowered the level of the lake, which created scarps at lower elevations interior to the bounding scarp.

2.4.2.1 Model Ages

The morphology and geochemical data have provided evidence for lava lakes; however, absolute age data are needed to understand the timing and sequence of eruption events within Gassendi. Seven count areas were identified on the floor of Gassendi: three lava lakes, three areas representing the floor, and one mare area (Figure 2.12). The CSFDs for the lava lakes (SW, NW, and NE) are plotted in Figure 2.12B, along with the CSFDs for the floor and mare areas (Figure 2.12C). The NE lava lake surface falls along the lunar production function with a model age of ~3.6 ± 0.02 Ga. The NW and SW lava lake surfaces have model ages of ~3.9 ± 0.1 Ga and ~3.6 ± 0.03 Ga (Figure 2.12B). The three floor areas (central, south, east) plot on the lunar production function with a model age of ~3.9 ± 0.1 Ga and the mare area counts (south east floor) show a model age of ~3.6 ± 0.03 Ga (Figure 2.12C). The age data shows that the three lava lakes (SW, NW, and NE) were contemporary eruption events occurring ~300 Ma after the floor was emplaced. The NE lava lake inundated the floor in our count area. The SW and NW lava lakes have the same model age as the NE, but also have a second older model age that matches the age of the floor. Thin lava lake deposits would have only partially buried some of the preexisting larger craters. Alternatively, the lakes only partially covered the floor, leaving the original floor exposed in some areas. A third possibility involves relatively large secondary craters influencing the count area; the SW depression has at least one large secondary crater identified in NAC images. The mare in the southern part of the crater has a model age (~3.6 ± 0.04 Ga), which is the same as the lava lake ages and is in agreement with previous work for the floor of Gassendi (Shylaja, 2005; ~3.6 ± 0.7). Volcanism within Gassendi crater was widespread, occurred over a short duration, and peaked at approximately the same time as the peak of all nearside lunar volcanism (Hiesinger et al., 2011).

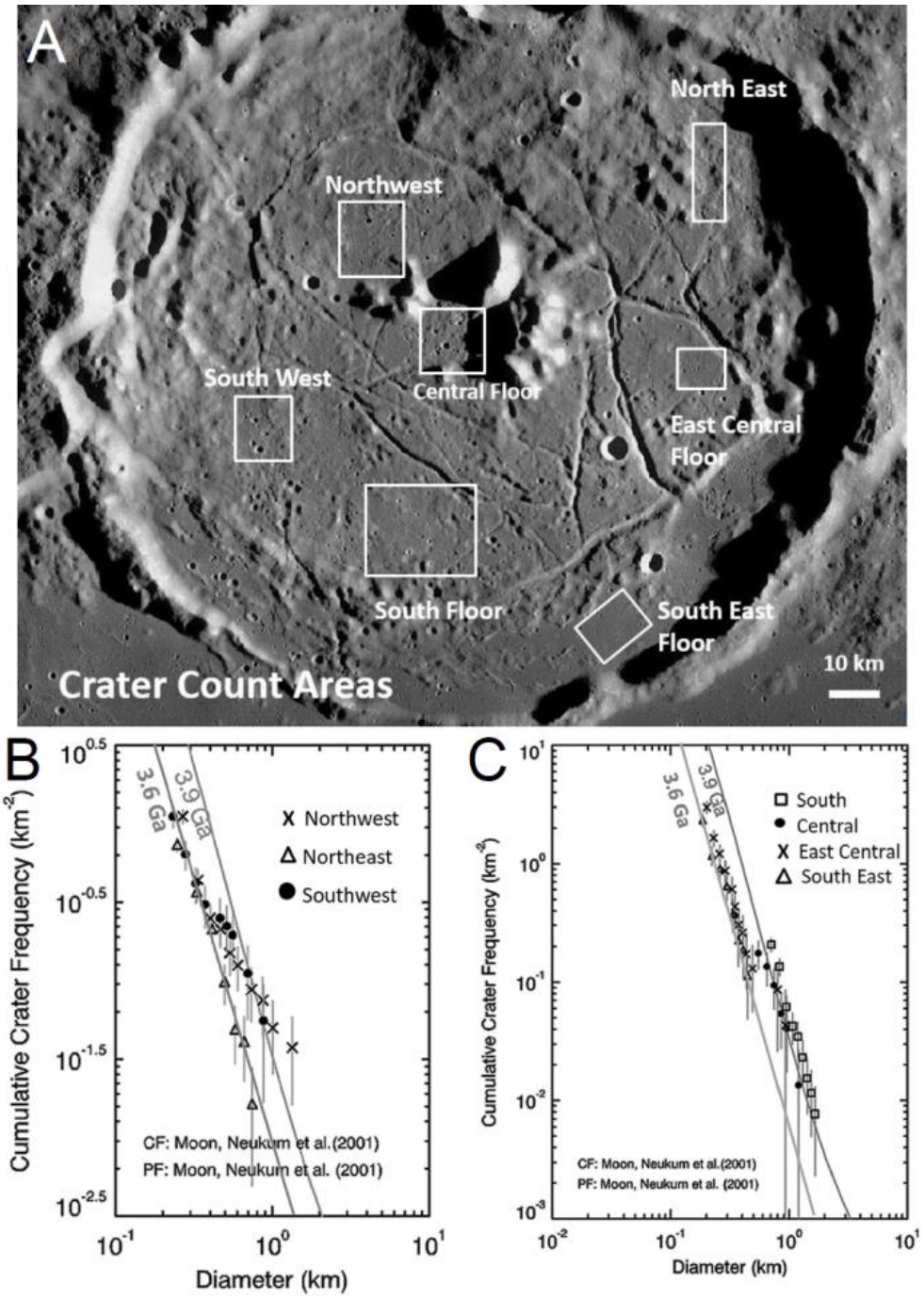

Figure 2.12. Crater count data for the Gassendi province. A) Crater count areas. The cumulative size frequency distributions of craters counted are plotted in diagrams B and C. Low Sun WAC Near Side mosaic (643 nm, 100 meters/pixel). B) The CSFD for lava lake areas Northwest (N = 42, area = 80 km^2), Northeast (N = 92, area = 22 km^2), and Southwest (N = 42, area = 36 km^2). C) The CSFD for floor areas South Floor (N = 55, area = 260 km^2), Central Floor (N = 24, area = 74 km^2), East Central Floor (N = 69, area = 23 km^2), and South East Floor (N = 62, area = 26.5 km^2). N is the number of craters (N) counted in each area, and area is the surface area counted in square kilometers. Error bars were calculated for N in each diameter bin based on the statistical error inherent to the number of craters counted, assuming a Poisson distribution of values. CSFD plots generated with methods of Michael and Neukum (2010).

2.4.2.2 Emplacement and Occurrences

The presence of sustained or cyclic lava lakes on the Moon may change our understanding of how magma is delivered to the surface. The Gassendi impact crater formed between the first (325 km diameter) and second (440 km diameter) rings of the Humorum basin. The crust was heavily fractured by the Humorum basin-forming event, then further fractured by the Gassendi impact (Melosh, 1984). The deep crustal fractures created pathways for magma to propagate to the surface. When magma following in these conduits encountered the lower density breccia zone of the Gassendi crater floor, its upward migration was inhibited and, as a result, magma began to form sills beneath the crater (Schultz, 1976b; Head and Wilson, 1992). The sill inflates as the intrusion persists but was confined to the boundary of the crater floor by the lithostatic overburden pressure of the crater wall (Thorey and Michaut, 2014; Jozwiak et al., 2015). The inflated sill may become dome shaped initially (e.g., lopolith), transitioning to a laccolith with a piston-like effect. The result of the inflation was the crater floor lifted, dilated, and subsequently fractured. If magma intrusion continued, the floor fractures would have allowed lava/pyroclastics to erupt onto the surface (Schultz, 1976b; Thorey and Michaut, 2014; Jozwiak et al., 2015; Trang et al., 2016). Modeling suggests that intrusive, not extrusive, bodies would form in an impact basin rim setting (crustal setting 2, Jozwiak et al., 2015). However, at Gassendi other physical factors (crust density, specific fractures) as well as proximity to the heat producing PKT region (Jolliff et al., 2000) may raise magma temperatures to superliquidus (heated above liquidus), which increase the melt/eruption volume and the driving pressure of the magma (Wieczorek et al., 2001) and permit the eruptive products that we see on the floor of Gassendi. A magma reservoir below the Gassendi crater substructure (Thorey and Michaut, 2014; Jozwiak et al., 2015) provides a source for the observed eruption products.

Gassendi, however, is not the only location with lava lake related morphology. The processes that create lava scarps occurs in other forms elsewhere on the Moon. Locations exist where mare flows have risen rapidly during large effusion eruptions (Hulme and Fielder, 1977), then subsequently lowered, leaving "bathtub ring" scarps. Previous workers have identified these scarps as a thin, horizontal layer of lava on a topographically high feature: e.g., near Herigonius crater (Greeley and Spudis, 1978), on the flanks of a dome adjacent to Maskelyne D in SE Mare Tranquillitatis and South of Gruithuisen **δ** (Schultz, 1976a). Many of these areas may not involve

cyclic behavior, but instead are either caused by a bottleneck that restricts flow advancement or a temporary barrier that is later breached. “Fill and Spill” lava flows (Hamilton et al., 2015) can create “bathtub ring” scarps. Other workers have identified areas within the maria where subsidence and drainage have taken place: e.g., near crater Lubiniezky (Holcomb, 1971), Bowditch crater (25.0°S, 103.1°E) (West, 1972; Wilhelms and El-Baz, 1977) and at Montes Harbinger in southeast Mare Imbrium (Schultz, 1976a). Recent work (Needham, et al., 2017; Stopar et al., 2018; Qiao et al., 2017) invoke lava lake processes. Generally, the residence time is longer in a confined area, such as a crater floor, providing more time to develop scarp morphology.

2.4.3 Terrestrial and Lunar Lava Lake Comparison

Terrestrial lava lake morphology provides a comparative analog for Gassendi lava lakes. The 1959 eruption of Kilauea Iki crater (0.9 × 1.6 km) on the island of Hawaii USA, was a short-lived event (November 14 - December 20, 1959). Although Kilauea Iki experienced multiple separate eruption events during this time period, the morphology that we see today reflects only the last few events (Stovall et al., 2009b). The morphology of the cooled lava around the margins of the Kilauea Iki include rounded and irregular scarps (Figure 2.13A). These lava lake scarps and horizontal lava shelves record multiple fill-drain events within the active lava lake (Figure 2.13B). Measurements of lava scarps that remained after the eruption provide insight into the magma reservoir system, and lava lake formation and fluctuation. Hawaiian basaltic lavas are useful for comparison to lunar lavas because they are less viscous than other terrestrial lavas due to lower silica content and higher eruption temperatures (Francis, 1993). While basaltic lavas are among the best analogs to lunar flows, there are major differences in viscosity (lunar lava is about a factor of 10 more fluid than terrestrial lava; Murase and McBirney, 1970; Greeley, 1971) and temperature (1150°C vs. 1500°C) (Flynn and Mouginis-Mark, 1992; Kesson and Ringwood, 1976).

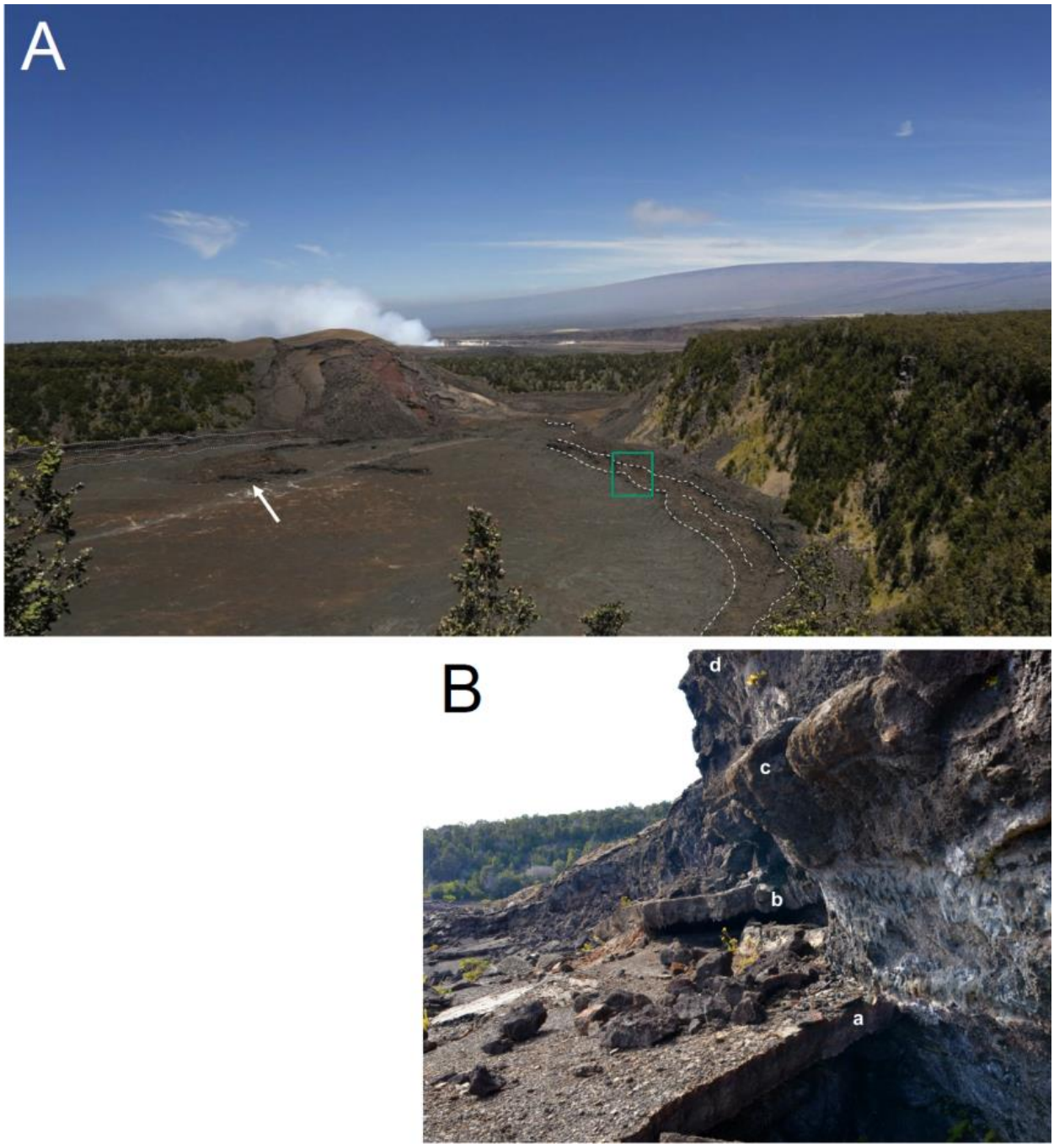

Figure 2.13: A) Oblique photograph of Kilauea Iki pit (0.9 × 1.6 km) looking toward the southwest, Island of Hawaii. The dotted white lines outline the major scarps on both sides of the pit. At this scale, the right side shows two scarps, indicating separate drainage events. The white arrow points to part of the dislodged, submerged eruption cone. The green box, north side of Kilauea Iki pit, is the approximate location of photograph B). Photo credit: Michael Szoenyi, NPS. B) Kilauea Iki lava lake levels. Multiple levels of the lava lake are preserved as horizontal lava shelves (a – d) in this view looking to the west. This wall is on the north side of the lava lake, opposite the vent. The levels are not labeled in emplacement order. Lava shelf "a" is ~20 cm thick. Photo credit: Thomas Giguere.

Seventeen eruptions from a vent on the wall of the pre-existing Kilauea Iki crater formed a cinder cone called Pu‘u Pua‘i and a lava lake. The eruptions began with fountaining, driven by gas-rich magma (Eaton et. al., 1987), that varied from a few meters to 580 m in height (Eaton and Murata, 1960). Lava fountaining produced a massive volume of lava in a short period of time, which partially filled Kilauea Iki and continued to rise until the height of the vent was reached. When fountaining ceased some of the lava remained in the lake. The remainder of the degassed lava drained back into the magma chamber (See Figure 2 in Richter et al., 1970).

The first eruption phase was followed by sixteen smaller eruptions. As a result, the cyclical active lava lake in Kilauea Iki crater rose and fell with each eruption (Table 2.7; Figure 2.14) (Stovall et al., 2009b). Kilauea Iki crater developed a scarp, described as a “black ledge” (Richter et al., 1970) throughout the series of eruptions. Each cycle of draining and filling caused the ledge to grow in width as new lava accreted to the already cooled margins. The width and height of the ledge varied around the lake during the eruption process. The raised feature on the west side of the lake has the appearance of a scarp (Figure 2.13A); however, eyewitness accounts identify it as part of the eruption cone that broke off, was carried down flow, and submerged in the lake. Hence, not all scarps are formed by lava accretion along lake margins.

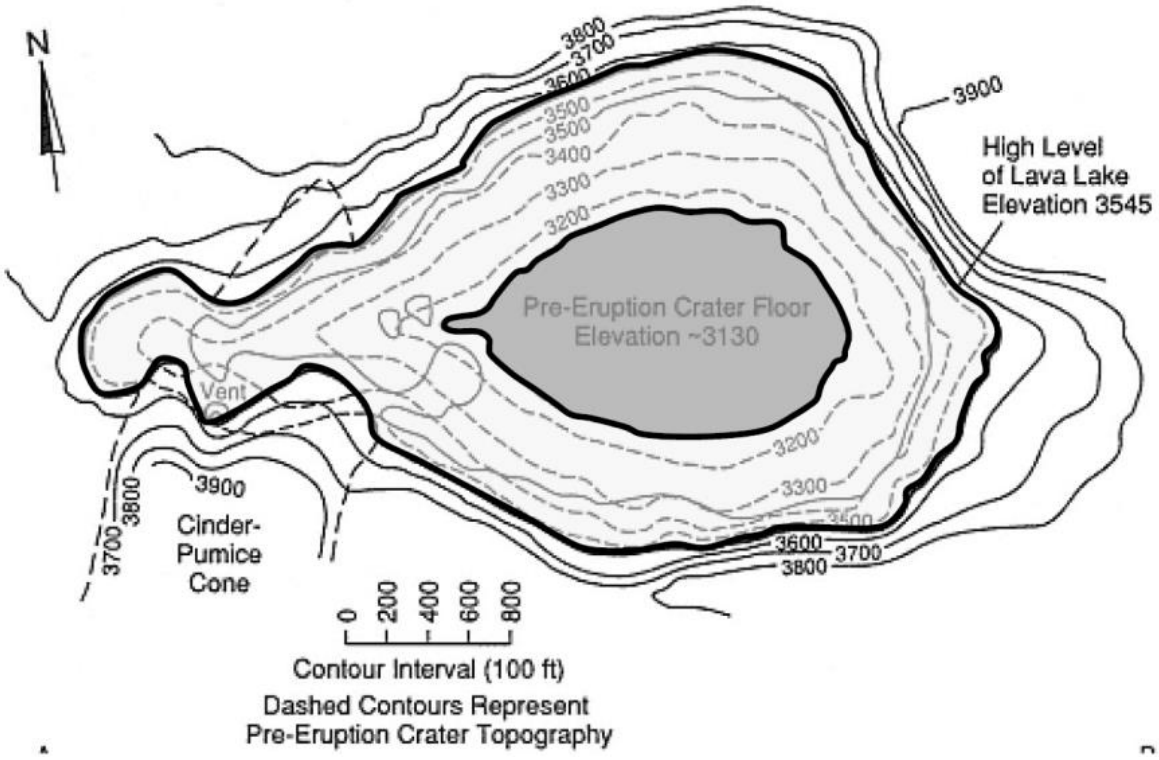

Figure 2.14: Plan sketch of Kilauea Iki pit, Island of Hawaii. The plan shows the various lava levels within Kilauea Iki during the 1959 eruption. Initial level: 3130 ft (dark gray), High level: 3545 ft (light gray); delta of 126 meters). Adapted from Richter and Moore, 1966.

Table 2.7: Rapid rise of the lava lake within Kilauea Iki. (adapted from Richter et al., 1970).

Kilauea Iki - Lava lake levels, 1959 Eruption		
Eruption Episode	**Lava Lake Level**	**Height Delta**
Nov. 16	7 m	NA
Nov. 17	17 m	10 m
Nov. 18	34 m	17 m
Nov. 19	60 m	26 m
Nov. 20	82 m	22 m
Nov. 21	98 m	26 m

Differences in properties between the Earth and Moon (e.g., gravity, atmosphere, crust density, volatile content, magma composition, temperature, etc.) can affect the scale of lava eruptions and in turn their lava lakes (Whitford-Stark, 1982). A comparison of the ledge width for Kilauea Iki (second eruption 8-25 m; final eruption 15-60 m) to the Gassendi northeast depression (150-300 m), show that the widths are different by a factor of ten. The northeast depression (12 × 24 km) is more than ten times larger than Kilauea Iki (0.9 × 1.6 km). However, the width difference between the analogs is more likely attributable to two factors: lava lake volume and lava residence time at the surface before draining. We base this conclusion on the correlation between eruption observations and scarp morphology in Kilauea Iki, and draw inferences to morphologic characteristics of the scarp in the Gassendi lava lakes. The ledge grew in width as the short-lived Kilauea Iki eruption proceeded, the same as would have occurred for the Gassendi eruption. The Kilauea Iki eruption was especially vigorous in the early days of the eruption, which caused the lake level to rise and fall rapidly (Figure 2.14, Table 2.7). The lake level was at 98 meters in height on November 21, 1959. This terrestrial height is comparable to the depths that we have measured for the three Gassendi depressions after drainage (SW, 60 m; NW, 120 m; NE, 300 m) (Barker et al., 2016). Ledges comparable in lateral extent to Gassendi are not found in Kilauea Iki, perhaps due to its short-lived eruption. Halemaumau, on the other hand, represents a longer-lived active

lava lake (Tilling, 1987). As part of the 1955 Kilauea eruption, ledges formed similar in size to those in Gassendi. During the early stages of the eruption, a ledge formed that was 50 meters wide. By the end of the eruption, the ledge extended out 350 meters (Macdonald and Eaton, 1955). The scarp morphology is similar to the Gassendi depressions (Figures 2.6 - 2.9). The bounding scarp of the Gassendi northeast lake varies with peninsular shaped prominences on the north side, inlets and prominences on the west side, and a smoothly undulating margin on the east side. These inlets and prominences are created when the lake surface cools unevenly along the boundaries and material collects. Mass wasting around the lake margins causes material to build up and protrude into the lake, as in the case of the eruption cone for Kilauea Iki. Based on concentric ledges in the southwest lava lake and scarps in the northeast lava lake, we conclude that the Gassendi lava lakes either had cyclical eruption/drain episodes, or a single eruption event that drained slowly/episodically.

2.4.4 Northeast Province - Pyroclastic Deposits

The composition, mineralogy, rock abundance, and rock type were ascertained for the NE pyroclastic deposit. These characteristics are useful for determining the eruptive behavior of this deposit. The northeast deposit is in the "Glassy" pyroclastic group, based on values determined for glass, clinopyroxene, plagioclase, and rock abundance (Figure 2.15). The Glassy group has mean values as follows: glass (73%), clinopyroxene (16%), and plagioclase (11%) (see Table 4 in Trang et al., 2017). Other members in this glassy group include deposits found in: Alphonsus, Birt E, Gauss, and Oppenheimer N and E (see Figure 15 in Trang et al., 2017). The Glassy group deposit erupted in a vulcanian-style eruption manner similar to that described by Head and Wilson (1979) with the assumption that the glass material is juvenile, and the large amount of glass suggests that the erupted material cooled quickly in an optically thin gas cloud (see Figure 19 in Trang et al., 2017). The clinopyroxene component may be derived from basaltic fragments entrained during the eruption; lateral transport likely contributed the small amount of plagioclase from the adjacent highlands to the east. Lunar localized pyroclastic deposits lie along a gabbroic to gabbroic-anorthosite trend (Trang et al., 2017); the northeast pyroclastic rock type is gabbroic, which is typical of pyroclastic deposits due to the low amounts of orthopyroxene present. The presence of minor amounts of plagioclase (11%) suggest that the eruption incorporated wall rock, or the deposit was contaminated with highland material. Overall, observations suggest that the deposit to the NE of Gassendi crater is a block-poor and glass-rich deposit composed of small fragments. In contrast,

the Mersenius pyroclastic deposits located in the West province (Hawke et al., 1993; Gaddis et al., 2003; Gustafson et al., 2014; Trang et al., 2017) are block-rich and glass-poor (Figure 2.15). Mersenius has twice the clinopyroxene (~40 wt. %) and four times the plagioclase (~56 wt. %) than the northeast deposit. The northeast pyroclastic deposit had a different eruption style and source region from the Mersenius eruptions.

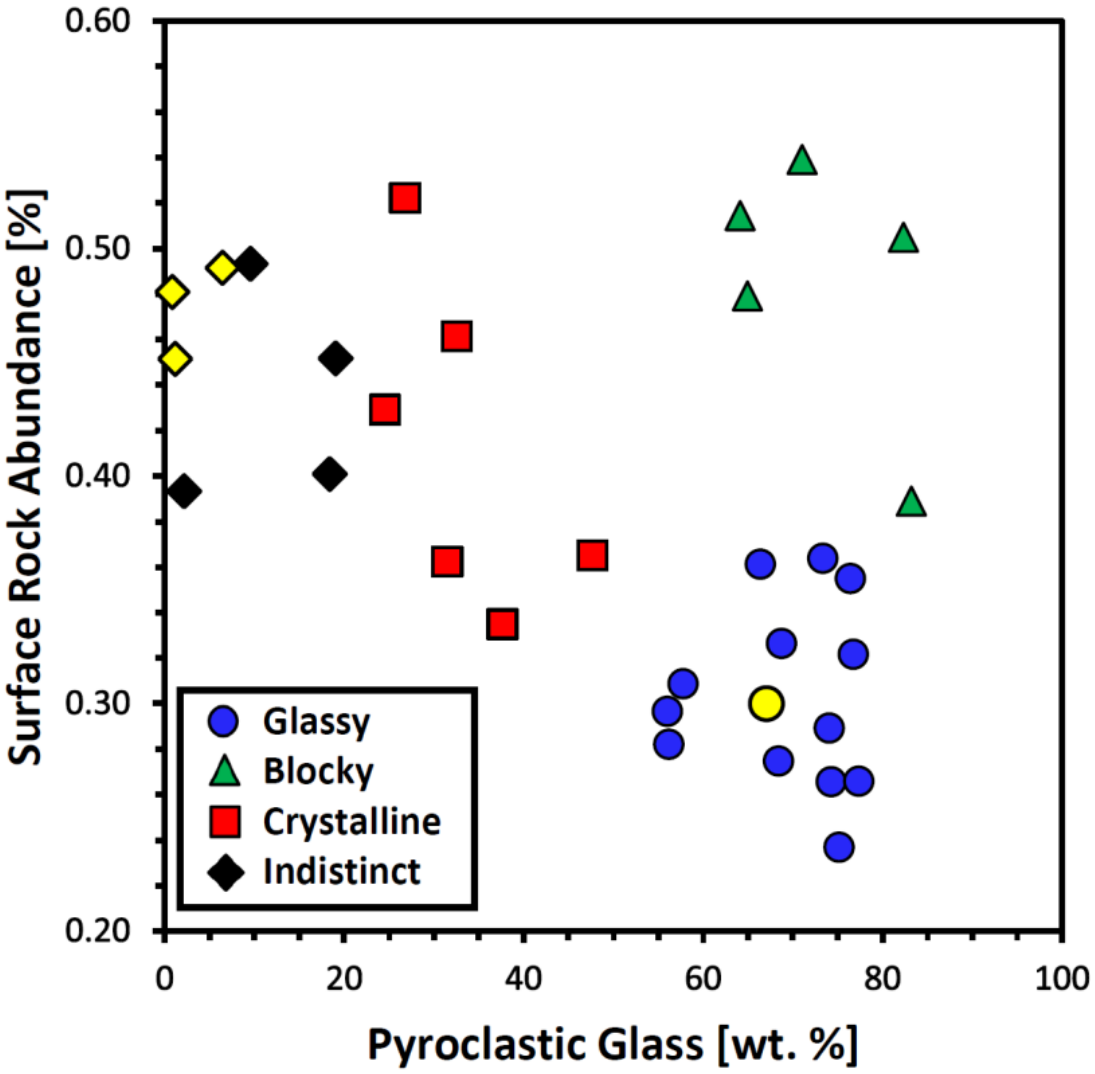

Figure 2.15: The Northeast pyroclastic deposit is in the "glassy" group (yellow circle). Mersenius pyroclastic deposits located in the West province (Hawke et al., 1993; Gaddis et al., 2003; Gustafson et al., 2014; Trang et al., 2017) are block-rich and glass-poor (yellow diamond). Figure modified after Trang et al., 2017.

2.4.5 Lava Lakes Beyond Gassendi

The focus of this work is on the floor-fractured crater Gassendi; however, Gassendi is actually on a continuum of craters from small to large in size that contain mare basalts on the floor. There are approximately 170 floor-fractured craters described by multiple workers (Schultz 1976a, 1976b; Hall et al., 1981; Wichman and Schultz, 1995; Dombard and Gillis, 2001; Jozwiak et al., 2012, 2015). These shallow floored craters exhibit morphologies similar to Gassendi and in some cases may have had lava lakes. Of the total number of floor-fractured craters, 27 craters were examined with WAC and high-resolution NAC imagery. Nine craters had mare basalt present on the crater floor; six craters exhibited possible lava lake depressions (Table 2.8). Several craters exhibit more than one depression (e.g., Doppelmayer, Gassendi, and Humboldt).

Table 2.8: Lunar floor-fractured craters that exhibit lava lake-like depressions.

Crater Name	Location (Lat/Lon)	FFC Dia (km)	Source Image	Description
Unnamed	19.6827 N, 86.4950 E	10.6	WAC (low-Sun), NAC images	Unnamed crater NE of Hubble C. Possible scarp on the SW floor. Mare present
Hansteen	11.5872 S, 51.9335 W	45	WAC (low-Sun)	Possible high-lava scarp, west side of central mare pond
Doppelmayer	28.4712 S, 41.5147 W	63	WAC (low-Sun), NAC images	Possible scarp on west side
Isaev	17.5 S, 147.0 E	90	WAC (low-Sun), NAC images	Mare pond north of the center of the crater has a north-south oriented irregularly shaped depression
Gassendi	17.4349 S, 40.032 W	110	Multiple	Three lava lakes
Humboldt	27.1440 S, 81.1541 E	207	WAC (low-Sun), NAC images	Mare pond to the northeast has two depressions

Representative floor-fractured crater Humboldt (25.6°S, 82.9°W) at 207 km in diameter, has four mare deposits on the floor. The mare pond to the northeast has two depressions (Figure 2.16), indicated by arrows in Figure 2.16C. The pond superposes the fractures in this area of the floor indicating a younger age for the basalts and in turn the depressions. The westernmost of these two depressions is 5.5 km long and 4 km wide with a depth below the surrounding scarp of 25-40 meters. The western depression in the mare equates to nearly one million cubic meters of basalt that has been removed or drained. Humboldt and other floor-fractured craters are evidence that lava lakes may be present elsewhere on the Moon.

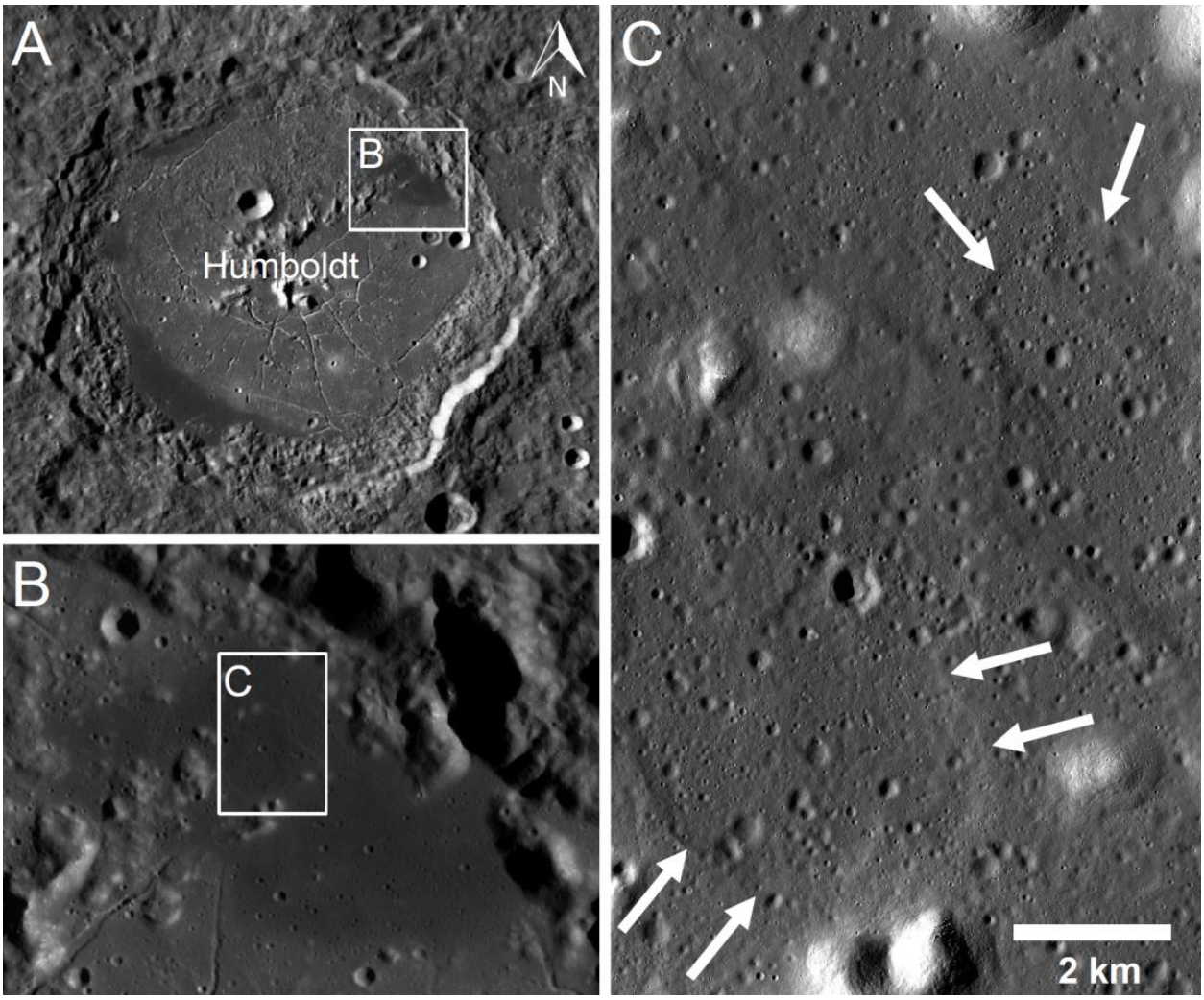

Figure 2.16: A) Humboldt crater, 25.6°S, 82.9°W, is 207 km in diameter and has a fractured floor and four mare intrusions. The white box indicates the location of B). B) The northeast mare pond has two depressions. The white box indicates the location of C). C) The two depressions are indicated with white arrows. The western most depression is 5.5 km long and 4 km wide with a depth below the surrounding scarp of 25-40 meters. LROC NAC image M180622344R/LE.IMG, incidence angle 75°, resolution 1.61 m. North is up in all images.

The lava lakes we identified are listed in Table 2.8. Data show that lava lakes are most often found in floor-fractured craters and may, with dedicated mapping, be found to occur globally. Their lack of identification in lunar volcanic history to date may be due to the subtleness of their appearance. In fact, with the increasing availability of high-resolution remote-sensing data coupled with the criteria for identifying lava lakes, their documented prevalence may increase. Lava lakes may have formed frequently in lunar history; however, it is likely that the most recognizable lake

phases in the overall eruption sequence are later buried by subsequent mare basalt layers or destroyed by cratering. We see a similar effect with source vents for mare and pyroclastic deposits. Vents are rarely visible, having been obscured by later eruptions of fluid lava and gradational crater erosion (Greeley, 1976; Wilhelms, 1987). In the future, high-resolution gravity or radar data may shed light on the extent of this rare phenomenon.

2.5.0 Summary and Conclusions

The diverse Gassendi region was examined to understand and characterize the range of volcanic landforms and processes in this area of the Moon. The current inventory of known mare volcanism was expanded and provides a better understanding of the morphology, emplacement processes, and inventory of these features. The proximity of these deposits to Humorum basin, the large floor-fractured crater Gassendi, and the Procellarum-KREEP terrain (Jolliff et al., 2000) are the likely drivers for the abundant volcanic landforms. In addition to the previously mapped mare basalts on the floor of Gassendi crater we identified new volcanic features in the form of cryptomaria, pyroclastic deposits, mare basalts, and lava lake structures.

- In the highlands to the west of Gassendi crater (West Province) we confirmed the existence of a previously identified Nectarian-aged cryptomare deposit and identified a new cryptomare deposit to the south at a shallower depth. The evidence indicates two episodes of mare emplacement from two different sources or a single source that evolved in composition between eruptions formed these deposits.
- Cryptomaria were identified and characterized on the western and northeastern portions of the Gassendi crater floor based on the spectral and geochemical data for small dark-haloed impact craters and surrounding surfaces. The identification of cryptomare deposits increases the global cryptomaria deposit inventory. This increase in the total mare basalt volume has implications for the volcanic and thermal processes of the Moon.
- Three lava lakes were identified on the northeast, northwest, and southwest floor of Gassendi crater. The constructs are depressions with bounding curvilinear scarps of uniform elevations. Interior scarps were formed as lake levels lowered. The lava lakes occurred over floor fractures, which allowed lava to enter and drain. The northeast lake

completely drained, whereas the southwest and southeast lakes have residual lava on their floors. The morphology of the lunar lava lakes is similar to terrestrial lava lakes.

- The surfaces of the lava lakes exhibit higher mafic values (FeO 12-15 wt. %) than the floor of Gassendi (10-12 wt. %). The spectral data confirm mare basalt mineral assemblages (i.e., high-Ca pyroxene). These surfaces show enhanced TiO_2 abundances (2-3 wt. %) over the background (1-2 wt. %).
- Volcanism within Gassendi crater was widespread and of short duration. These eruption events have a model age of ~3.6 ± 0.03 Ga and occurred ~300 Ma after the floor was emplaced. The NE lava lake inundated the floor depression, whereas the SW and NW lava lakes partially covered the floor or did not superpose large floor craters. The volcanism within Gassendi crater post-dates the mare emplacement in the highlands to the west of Gassendi crater (West Province).
- The criteria developed to identify lava lakes in the Gassendi region were used to search for lava lakes within floor-fractured craters. After studying just 16% of all known floor-fractured craters, we located subsidence morphology in mare basalts on the floors of multiple floor-fractured craters.
- Initial mapping suggests that lava lakes occur globally but preferentially occur in floor-fractured craters. As a result, lava lakes may signal a unique class of floor-fractured crater.
- The presence of lava lakes suggests that, at least in some instances, magmas stall near the surface. The relation between lava lakes and floor-fractured craters may result from the crustal structure (e.g., an impervious or a low-density layer beneath the crater) and lack of mare flooding that floor-fractured craters provide.
- A previously unmapped pyroclastic was identified in the highlands northeast of Gassendi crater. The deposit is in the glassy pyroclastic group and erupted in a vulcanian-style eruption where the juvenile glass material cooled quickly in an optically thin gas cloud. The deposit had a different eruption style (more glass, less blocks), mineralogy, and source region than the Mersenius eruptions.

The lava lakes, cryptomaria and pyroclastic deposits point to dynamic mare basalt emplacement processes that occurred on the floor of Gassendi crater and in the surrounding area. The presence of lava lakes on the Moon requires the adjustment of current eruption models, in

order to incorporate the observation that magmas can stall near the surface and also maintain a cyclical connection to the surface.

2.6.0 Acknowledgements

Special thanks to Dr. B. Ray Hawke for his interest in and the original idea of performing a thorough study of the Gassendi region. We also each thank him for his unwavering support for our work and our careers, and we sincerely hope that this paper does justice to his initial work on the subject and his memory. The authors would also like to thank an anonymous reviewer and Brad Thomson for their constructive comments. The lunar remote sensing datasets used in this article is publicly available in the PDS. All data to reproduce the results and figures in this work can be accessed online DOI 10.17605/OSF.IO/256E4 (https://osf.io/256E4/). We would like to acknowledge support from NASA through the LRO/LROC Contract ASU 11 - 599 with Arizona State University (Mark Robinson, PI) and SSERVI award NNA80NSSC20M0027 (Jeffrey Gillis - Davis, PI). This paper is SOEST Contribution 11084 and HIGP Contribution 2417 and SSERVI - 2020 - 048.

CHAPTER 3: LAVA FLOW AGES IN NORTHEASTERN OCEANUS PROCELLARUM- THE NEED FOR CALIBRATING CRATER COUNTING PROCEDURES

[Published in 2022: Icarus, 375, p.114838]

Thomas A. Giguere[a*], Joseph M. Boyce[a], Jeffrey J. Gillis-Davis[b], David Trang[a], and Julie D. Stopar[c]

[a]Hawai‘i Institute of Geophysics and Planetology, Department of Earth Sciences, University of Hawai‘i at Manoa, 1680 East-West Road, Honolulu, HI, 96822, United States, [b]Washington University, Department of Physics, One Brookings Drive, St. Louis, MO 63130, [c]Lunar and Planetary Institute, 3600 Bay Area Boulevard, Houston, TX 77058.

Abstract

The Northeastern Oceanus Procellarum (NE-OP) study area is a patchwork of lava flows that range in model age from 1.4 – 3.5 Ga (average age for all count areas is 2.3 Ga), but whose FeO and TiO_2 contents deviate little. The intermediate TiO_2 content values (4.0–6.8 wt.%) exhibited by the mare in this region represent material that is underrepresented in the current lunar sample collection. The model ages in the study region are bimodal (~2.2 Ga and ~3.0+ Ga), with eruption of lava flows at the Chang‘E-5 landing site occurring at ~3.0 Ga. By comparison, other investigators estimate the model age of the Chang‘E-5 site to be ~1.2 to 1.6 Ga. We find preliminary evidence that differences in measurement methodology may lead to disparate model ages and explain the difference in predicted model age of the Chang‘E-5 site.

3.1.0 Introduction

In this study, we investigated the Northeastern Oceanus Procellarum (NE-OP) region with the goal of understanding and characterizing the mare volcanic history in this region of the Moon, and estimated the model age of the Chang‘E-5 landing site based on crater count data. The NE-OP region lies between Mare Imbrium to the east and Mons Rümker and NW Oceanus Procellarum to the west and includes the P58 spectral unit (Hiesinger et al., 2003) (Figure 3.1). Results from this overview study help to place China National Space Administration (CNSA) Chang‘E-5 sample results into a broader geologic context. In addition, we find that model ages obtained by different researchers for this region, and the Chang‘E-5 landing site in particular, range significantly. The disparity of model ages suggests that the method used by all workers practicing crater age dating

needs to be revaluated before any of the model ages can be accepted as accurate. We address this issue in this paper and recommend an action.

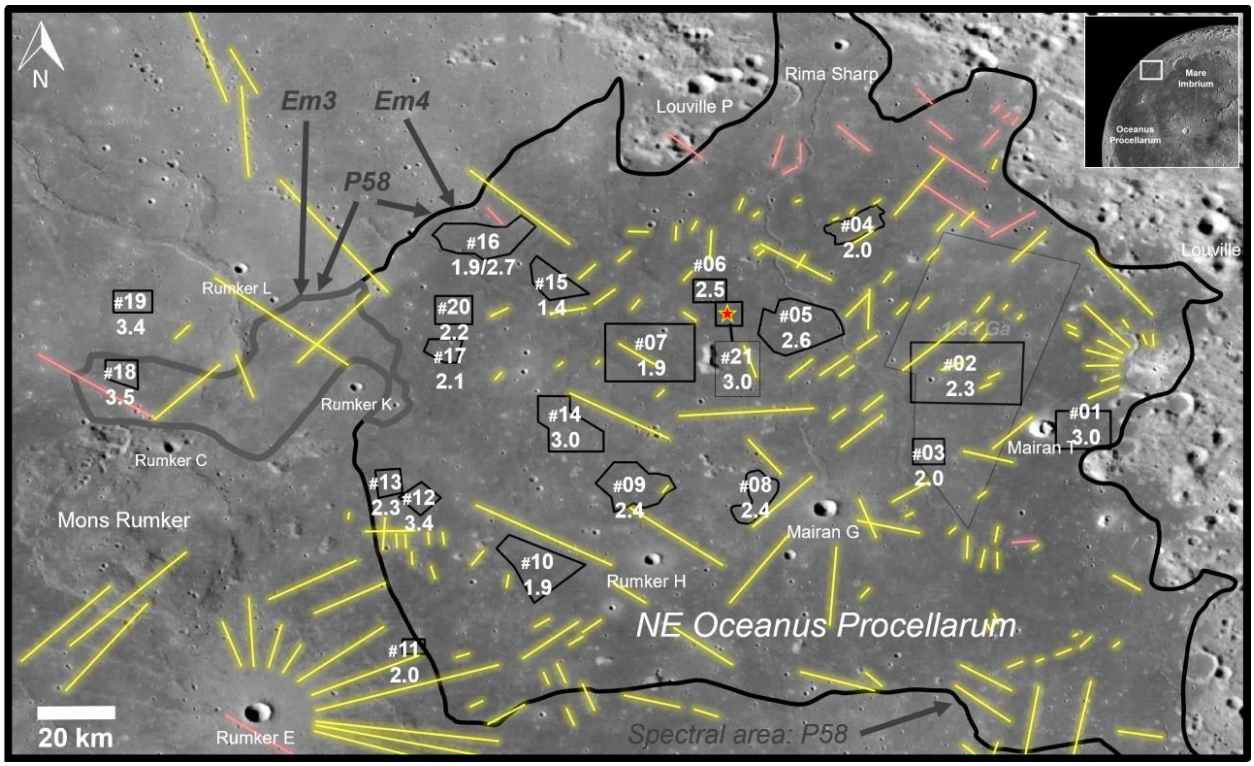

Figure 3.1. NE-OP study area on the NW quadrant on the nearside of the Moon (inset) with multiple numbered count areas (black outlines) that display average model age (Ga) (white text) and the "CE-5" (Chang'E-5) landing location (red/yellow star). The Hiesinger et al. (2003) mare age unit P58 (black outline) and crater count area (light gray) are overlaid. The approximate location of major secondary crater rays (yellow) are identified via morphology and lower geochemical values. Count areas are located to avoid major rays. Some secondary crater rays were identified by morphology only (pink). Background: LROC WAC basemap (Speyerer et al., 2011; cylindrical projection).

Based on its spectral characteristics, P58 was mapped as compositionally uniform by Hiesinger et al. (2003) and later researchers (e.g., Qian et al., 2018) used SELENE (Kaguya) MI imagery to refine the spectral unit of Hiesinger et al. (2003), dividing it into geologic/spectral unit Em3 and Em4 (Figure 3.1). Giguere et al. (Figure 3, 2000) found that the lava flows in this region exhibit intermediate TiO_2 abundances.

The region was age dated by Hiesinger et al. (2003) where the model age was extrapolated from a smaller count area located on the east side to the rest of the region (Figure 3.1). This extrapolation was based on the assumption that the uniformity of spectral values indicated that the

surface of this region was covered by only one large flow unit. However, the variations in crater model ages for mare surfaces in different locations within this region suggest a complex emplacement history, not detectable from the surface morphology or reflectance spectra, which may have lasted for ~2.1 Gyr (Boyce, 1976; Boroughs and Spudis, 2001; Hiesinger et al., 2003; Morota et al., 2011; Qian et al., 2018; Wu et al., 2018; Jia et al., 2020; Qian et al., 2021a, 2021c; Xu et al., 2021).

The Chang'E-5 sample return mission landed on the lava flows of NE-OP, and returned samples to the Earth on December 16, 2020 (Wang et al., 2021) (Figure 3.1). NE-OP was selected as the Chang'E-5 landing site because previous crater model ages suggested the mare material could be as young as 1.21 Ga (Qian et al., 2018). A young sample would serve to calibrate the crater flux for younger mare surfaces. The current impact crater flux curve is calibrated against radiometrically determined crystallization ages (e.g., 3.15 ± 0.04 – 3.85 ± 0.04 Ga) of returned samples from known locations at the Apollo and Luna landing sites (Table 5.8, Stöffler et al., 2006). A segment of the current impact crater flux curve is described by a crystallization age of 3.92 Ga (Table 5.10, Stöffler et al., 2006). A limitation of these sample ages is that they span a narrow distribution of older ages. Hence, substantially younger, radiometric measurements of the Chang'E-5 samples would provide insight that would help decipher 1) the timing of mare basalt emplacement, 2) the thermal and eruptive history of the NE-OP volcanic province, and 3) whether the rate of meteoroids striking the Moon has changed or remained the same between 3+ Ga and the present day.

Multiple researchers (Hiesinger et al., 2003; Morota et al., 2011; Qian et al., 2018; Jia et al., 2020; Qian et al., 2021a, 2021c; Xu et al., 2021) determined model ages for NE-OP, which commonly disagree with each other (i.e., 1.21, 1.33, 1.41, 1.49, 1.53, 1.6, 2.07, 2.2, 3.2, 3.46 Ga) (Figure 3.2, Table 3.1A). However, we find this wide model age range disconcerting, as have others (Xu et al., 2021), because the count areas were comparable and the methods used similar. In addition, most of these model age studies (including this study) use the same Chronology Function (CF, Neukum et al., 2001) and Production Function (PF, Neukum et al., 2001), processing software (Craterstats2, Michael and Neukum, 2010), and methodology (eliminating secondaries, accurately measuring crater diameters, identifying degraded craters, etc.). The scatter in model ages from these studies is significant. This spread of model ages might indicate that dating a surface by crater

counting has a high degree of uncertainty (e.g., ±0.5 Ga) and low-level of reproducibility. Even if a model age is consistent with the radiometric age of the Chang'E-5 samples, the similarity might be coincidence rather than causation. The currently accepted lunar impact flux in this age range is model dependent and poorly constrained for moderately young model ages. Identifying deviations in methodology will serve to converge determined model ages.

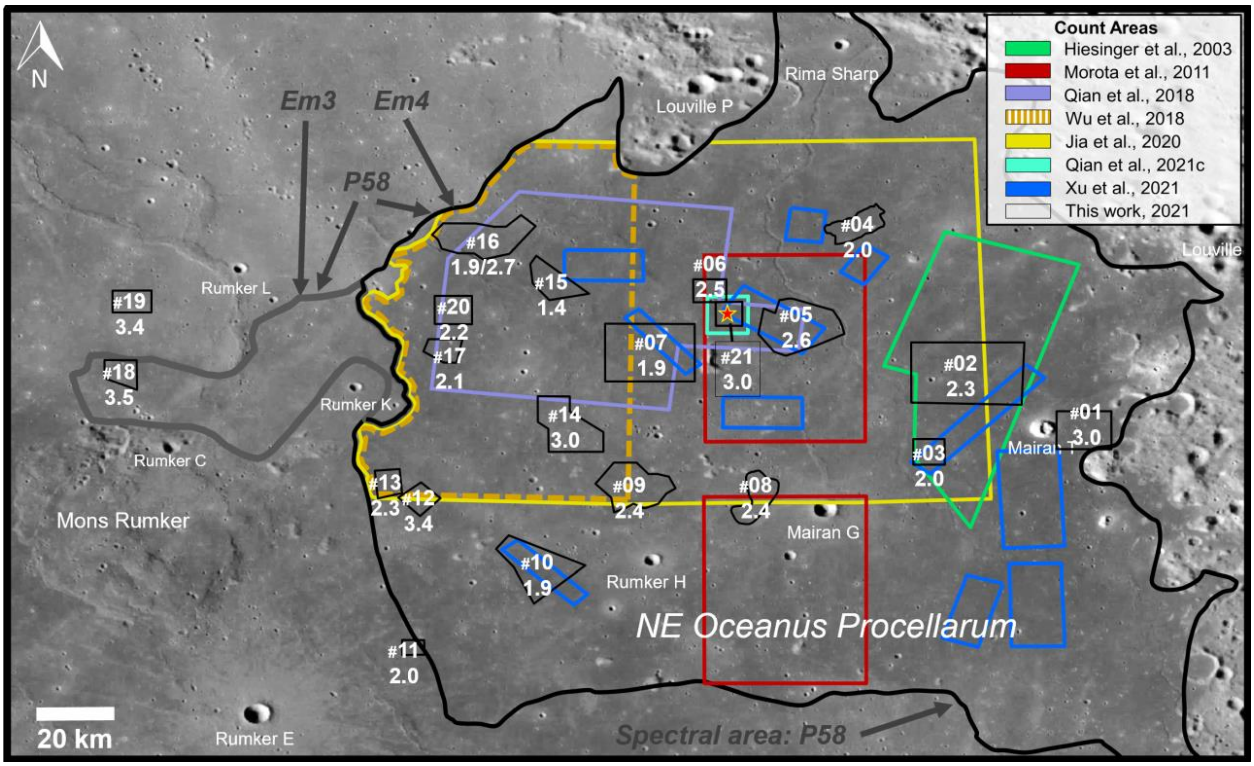

Figure 3.2. Count area boundary comparison in the NE-OP (P58) study area. The multiple count areas and average model ages (Ga) from this study (black outlines) are mapped over the count boundaries from previous researchers (Hiesinger et al., 2003; Morota et al., 2011; Qian et al., 2018; Wu et al., 2018; Jia et al., 2020; Qian et al., 2021a, 2021c; Xu et al., 2021). The earliest authors counted sub areas in P58 (Hiesinger et al., 2003; Morota et al., 2011), whereas Qian et al. (2018) divided P58 into Em3 (small area north of Mons Rümker, gray outline) and Em4 (eastern NE-OP, black outline), in which sub areas were counted (Qian et al., 2018; Wu et al., 2018; Jia et al., 2020; Qian et al., 2021a, 2021c; Xu et al., 2021). Generally, one or more count areas from this study are located within the larger boundaries defined by previous researchers (Figure 3.6, Table 3.2). Our count areas #05 and #21, #07, #10 overlie count areas c, b, and f (blue rectangles; Xu et al., 2021), respectively. CE-5 landing location (red/yellow star) is located in count area #21. Background: LROC WAC basemap (Speyerer et al., 2011; cylindrical projection).

Table 3.1: Model age and composition for locations in Northeast Oceanus Procellarum/unit P58 (Hiesinger et al., 2003). A) Previous studies, B) This study.

A. Previous studies - Model age and Composition

Author/Year	Location[1]	Area (sq km^2)	Model Age (Ga)[3]	Avg FeO (wt%)	Avg TiO_2 (wt%)	Count Location includes the CE-5 Landing Site
Boyce, 1976	P58	1600	3.2			Yes
Boroughs and Spudis, 2001	P58	37,000[2]	1.5	18.9	2.6	Yes
Hiesinger et al., 2003, 2011	Eastern P58	2551	1.33 +0.19/-0.25			No
Morota et al., 2011 (Model A)	Central P58	2801.2	1.91 ±0.11; 3.46 +0.11/-0.44			Yes
Morota et al., 2011 (Model B)	Central P58	2801.2	2.20 ±0.13; 3.46 +0.11/-0.26			Yes
Qian et al., 2018	Em3	1167	1.51 ±0.07	16.2±0.7	3.6±0.9	No
	Northwest Em4	4742	1.21 ±0.03	16.7±0.7	4.8±1.2	Yes
Wu et al., 2018	Em3	2961	2.06 ±0.24			No
	Northwest Em4	5607	1.49 ±0.17			No
Jia et al., 2020	Em3	2823	2.54 +0.41/-0.50			No
	Northern Em4	17,074	2.07 +0.026/-0.027			Yes
Qian et al., 2021a	Em4	37,000[2]	1.53 ±0.027	~16-18	~6	Yes (Subunit 13)
Qian et al., 2021c (Area 5)	CE-5	99.4	1.60 ±0.16 (Area 5)	16.5-17.5	5-8	Yes
Xu et al., 2021	Em4	2361	1.41 +0.027/-0.028	17.3	4.7	Yes
Xu et al., 2021 (Area a)	Northwest Em4		1.10 +0.079/-0.079			No
Xu et al., 2021 (Area b)	Northwest Em4		1.23 +0.087/-0.087			No
Xu et al., 2021 (Area c)	CE-5		1.49 +0.084/-0.084			Yes
Xu et al., 2021 (Area d)	NorthCentral Em4		1.34 +0.011/-			No

			0.011			
Xu et al., 2021 (Area e)	NorthCentral Em4		1.01 +0.012/-0.012			No
Xu et al., 2021 (Area f)	Southwest Em4		1.45 +0.010/-0.010			No
Xu et al., 2021 (Area g)	Southeast Em4		1.54 +0.081/-0.081			No
Xu et al., 2021 (Area h)	Southeast Em4		1.71 +0.065/-0.065			No
Xu et al., 2021 (Area i)	Southeast Em4		1.22 +0.070/-0.070			No
Xu et al., 2021 (Area j)	Southeast Em4		1.40 +0.080/-0.080			No

B. This Study - Model age and Composition

#	Location[4]	Lat/Lon (Center)	#[5]	Area (sq km^2)	Age (Ga)[3]	Avg FeO (wt%)	Avg TiO_2 (wt%)	Max FeO (wt%)	Max TiO_2 (wt%)
1	10 km E of Mairan T Dome	41.78, -47.95	9	174.92	3.0 +0.3/-0.9	17.2±1.2	6.2±1.2	18.0±0.3	7.3±0.7
2	28 km NW of Mairan T Dome	42.38, -49.20	11	570.55	2.3 +0.6/-0.7	17.4±1.0	6.4±1.0	18.4±0.3	7.7±0.7
3	32 km NE of Mairan G	41.53, -49.68	71	66.74	2.0 +0.2/-0.2	17.4±0.6	6.2±0.7	17.6±0.4	6.6±0.7
4	83 km NW of Mairan T Dome	44.03, -50.49	64	98.27	2.0 +0.3/-0.3	17.3±0.7	6.0±0.8	17.8±0.5	6.7±0.8
5	60 km NNW of Mairan G	42.89, -51.22	100	272.07	2.6 +0.2/-0.3	17.4±0.8	6.5±0.9	18.0±0.3	7.2±0.7
6	69 km S of Louville P	43.33, -52.13	44	61.63	2.5 +0.4/-0.4	17.5±0.9	6.8±0.9	17.9±0.3	7.2±0.7
7	70 km NNW of Mairan G	42.66, -52.80	48	353.40	1.9 +0.3/-0.3	17.2±0.8	6.3±0.9	17.8±0.8	7.2±1.1

8	18 km W of Mairan G	40.99, -51.62	37	112.75	2.4 +0.4/-0.4	17.0±0.5	5.8±0.7	17.4±0.3	6.5±0.5
9	25 km NNW of Rumker H	41.13, -52.99	37	210.07	2.4 +0.4/-0.4	17.2±0.6	6.2±0.8	17.7±0.3	6.9±0.8
10	30 km W of Rumker H	40.26, -54.03	64	236.72	1.9 +0.2/-0.2	17.6±0.7	6.8±0.9	18.4±0.2	7.7±0.7
11	45 km ENE of Rumker E	39.35, -55.43	19	27.42	2.0 +0.4/-0.4	17.6±0.5	6.6±0.8	18.2±0.3	7.5±0.6
12	44 km SSE of Rumker K	41.01, -55.34	33	61.52	3.4 +0.1/-0.2	17.3±0.7	6.4±0.8	17.8±0.5	7.1±0.8
13	34 km SSE of Rumker K	41.17, -55.71	69	59.96	2.3 +0.3/-0.3	17.5±0.5	6.5±0.8	17.7±0.4	6.9±0.8
14	50 km NW of Rumker H	41.79, -53.74	86	190.84	3.0 +0.2/-0.3	16.8±0.7	5.8±0.8	17.4±0.4	6.5±0.7
15	73 km NE of Rumker K	43.53, -53.652	73	103.94	1.4 +0.2/-0.2	17.4±0.6	6.2±0.8	17.8±0.5	6.7±0.7
16	58 km NNE of Rumker K	43.90, -54.65	61	215.99	1.9 +0.2/-0.2; 2.7 +0.7/-1.5	16.7±0.7	5.3±0.8	17.5±0.3	6.4±0.6
17	25 km ENE of Rumker K	42.66, -55.10	95	57.70	2.1 +0.2/-0.2	17.3±0.6	6.1±0.9	17.9±0.4	6.9±0.8
18	29 km NNW of Rumker C	42.42, -58.67	10	63.52	3.5 +0.1/-0.2	16.4±0.7	4.0±0.8	16.9±0.3	4.6±0.6
19	29 km WSW of Rumker L (P10)	43.20, -58.57	41	70.13	3.4 +0.1/-0.1	15.4±0.6	1.6±0.4	15.9±0.5	1.8±0.3

20	35 km NE of Rumker K	43.11, -54.99	102	85.73	2.2 +0.2/-0.2	16.9±0.5	5.6±0.7	17.5±0.6	6.5±0.9
21	**CE-5 Landing Site** 70 km NNW of Mairan G	43.06, -51.92	81	50.06	3.0 +0.2/-0.3	17.4±0.9	6.7±0.9	17.9±0.4	7.3±0.7

[1]Location within region P58 (Hiesinger et al., 2003) or Em3/Em4 (Qian et al., 2018). See Figure 3.2.
[2]Area estimated.
[3]Model age for each count area. Two model ages indicate possible mare resurfacing.
[4]Crater center to the center of each count area.
[5]Number of craters in CSFD.

While the overall process of determining absolute model age is well established (Ostrach et al., 2011; Michael and Neukum, 2010; Xiao and Strom, 2012; Xiao and Werner, 2015; Fassett, 2016; Robbins et al., 2018; Wang et al., 2020), there may be steps in the process that are less rigorously defined and open to subjectivity. We have made a preliminary assessment of crater counting done by different workers and find that differences in methodologies are likely the reason for the varying estimates of crater density in NE-OP and at the Chang'E-5 site. Until counting procedures are cross-calibrated between research groups, crater model ages should be recognized as having large uncertainties.

3.2.0 Data and Methods

This investigation used Lunar Reconnaissance Orbiter (LRO) Wide-Angle Camera (WAC) images for figures, orientation and derived data products and LRO Narrow Angle Camera (NAC) images (Robinson et al., 2010; Speyerer et al., 2011) were used for crater counts and crater diameter measurements. A high spatial resolution NAC Digital Terrain Model (DTM) (reported precision error from SOCET SET (SOftCopy Exploitation Toolkit developed and published by BAE Systems) is 1.89 m based on a measure of the horizontal and vertical accuracy of LOLA points and the DTM) was created by the LROC Team at Arizona State University (Henriksen et al., 2017), and was used for diameter measurements in the Chang'E-5 landing area. The NAC DTM has a post spacing of 3.0 m and was created from NAC pairs: M1374407232LE and M1374421274LE. Moderate spatial resolution Digital Elevation Model (DEM) data, ~59 m/pixel

at the equator, were obtained from the SLDEM2015 (Barker et al., 2016), which was constructed from geodetically-accurate topographic heights from the LRO Lunar Orbiter Laser Altimeter (LOLA) and co-registered stereo-derived DEMs from the Kaguya monochromatic Terrain Camera (TC) (Haruyama et al., 2008a; 2008b). This data was used to perform initial crater diameter measurement, similar to an approach used to measure larger scale craters (Fassett et al., 2012).

Image data from the Japanese lunar orbiter spacecraft SELENE (Selenological and Engineering Explorer; also known as "Kaguya") TC (Haruyama et al., 2008a; 2008b) and the Multi-band Imager (MI) (Ohtake et al., 2008) visible and near-infrared multispectral camera were used for detailed morphologic and geochemical analyses. Imagery resolution for the MI VIS (visible) data is 30 m/pixel, and is 10 m/pixel for the TC. Lemelin et al. (2015) produced a conversion for the 750 and 950 nm bands in the Kaguya MI data to match Clementine ultraviolet-visible (UV-VIS) data allowing for the algorithm developed by Lucey et al. (2000a,b) to be used on Kaguya data. This allowed us to derive the optical maturity parameter (OMAT) (Lemelin et al., 2019) and FeO (Figure 3.3A). In addition, following the steps in Lemelin et al. (2015), we converted the Kaguya MI 415 nm band to match Clementine UVVIS data and used Lucey et al. (2000a) to also calculate TiO_2 (Figure 3.3B) (see supplementary materials). The standard deviation for the fit are 0.43 wt.% for titanium content and 0.81 wt.% for iron content (Otake et al., 2012). Average maximum FeO and TiO_2 values were determined for each location by averaging 30 m/pixels over a 1 km^2 area. LROC WAC UV-VIS derived TiO_2 abundances (Sato et al., 2017) at 400 m/pixel were also used in this study as an independent check on TiO_2 abundances derived with the SELENE MI imagery (Ohtake et al., 2008).

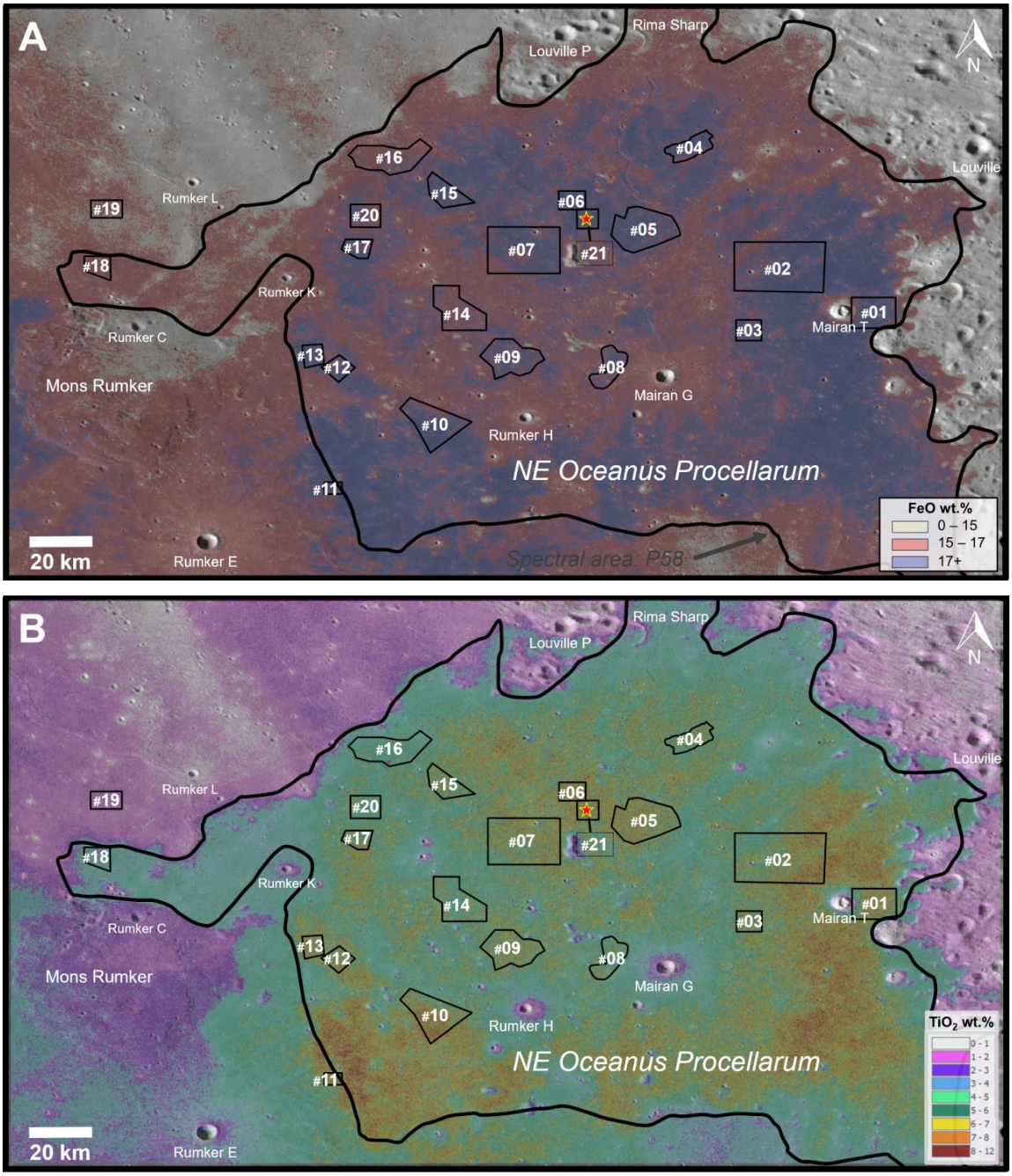

Figure 3.3. NE-OP study area numbered count areas (white text, black outlines) with geochemical values for mare basalts. Average model age (Ga) for each count area available in Figure 3.1 and 3.2. A) SELENE (Kaguya) FeO abundance (Lemelin et al., 2015). B) SELENE (Kaguya) TiO_2 abundance (method based on Otake et al., 2012; Lemelin et al., 2015; Lucey et al., 2000a). Count area boundaries are irregular in shape and designed to maximize the crater counting statistics, while minimizing the inclusion of secondary impact crater chains by avoiding the portions of the mare with reduced FeO and TiO_2 values (Giguere et al., 2020; 2021). CE-5 landing location (red/yellow star). Hiesinger et al. (2003) mare age unit P58 (black outline). Background: LROC WAC basemap (Speyerer et al., 2011; cylindrical projection).

Count areas were distributed in NE-OP to capture both the age and geochemistry of individual regions within the spectral unit P58 (Figures 3.1 and 3.2). Count area boundaries are expressed as irregular polygons. Their area chosen to maximize the crater counting statistics, while minimizing the inclusion of secondary impact crater chains identified by their morphology, which were confirmed as portions of the mare with reduced FeO and TiO_2 values, and relatively higher OMAT values (i.e., less mature) (Giguere et al., 2020; 2021). Crater size-frequency distribution (CSFD) curves were constructed from the crater count data collected for each of the count areas (Figure 3.4). Crater absolute model ages (AMA) were calculated based on the CSFD curve using the Craterstats2 program (Michael and Neukum, 2010) and rounded to 0.1 Ga due to crater measurement/primary crater identification issues discussed in section 3.4.2. The statistical error was calculated for the craters in each diameter bin based on a Poisson distribution and is represented as error bars on the CSFD (Michael and Neukum, 2010). The lunar chronology function of Neukum et al. (2001) was used to estimate model ages from the CSFD curves. The model age of each of the count areas is plotted in Figure 3.4 and given in Table 3.1B.

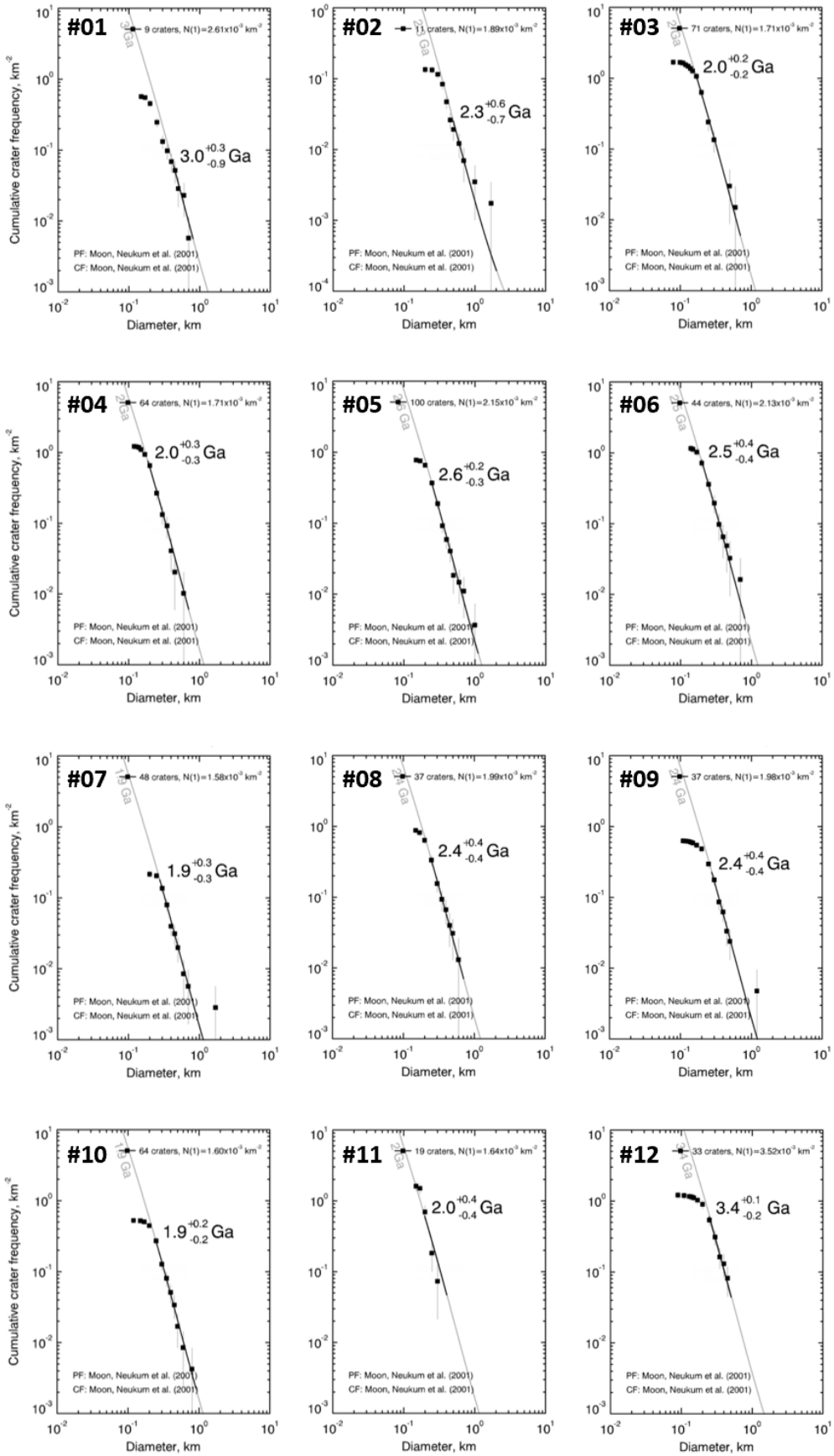
#01
9 craters, N(1)=2.61x10⁻³ km⁻²
3.0 +0.3 -0.9 Ga
#02
11 craters, N(1)=1.89x10⁻³ km⁻²
2.3 +0.6 -0.7 Ga
#03
71 craters, N(1)=1.71x10⁻³ km⁻²
2.0 +0.2 -0.2 Ga
#04
64 craters, N(1)=1.71x10⁻³ km⁻²
2.0 +0.3 -0.3 Ga
#05
100 craters, N(1)=2.15x10⁻³ km⁻²
2.6 +0.2 -0.3 Ga
#06
44 craters, N(1)=2.13x10⁻³ km⁻²
2.5 +0.4 -0.4 Ga
#07
48 craters, N(1)=1.58x10⁻³ km⁻²
1.9 +0.3 -0.3 Ga
#08
37 craters, N(1)=1.99x10⁻³ km⁻²
2.4 +0.4 -0.4 Ga
#09
37 craters, N(1)=1.98x10⁻³ km⁻²
2.4 +0.4 -0.4 Ga
#10
64 craters, N(1)=1.60x10⁻³ km⁻²
1.9 +0.2 -0.2 Ga
#11
19 craters, N(1)=1.64x10⁻³ km⁻²
2.0 +0.4 -0.4 Ga
#12
33 craters, N(1)=3.52x10⁻³ km⁻²
3.4 +0.1 -0.2 Ga
PF: Moon, Neukum et al. (2001)
CF: Moon, Neukum et al. (2001)
Cumulative crater frequency, km⁻²
Diameter, km

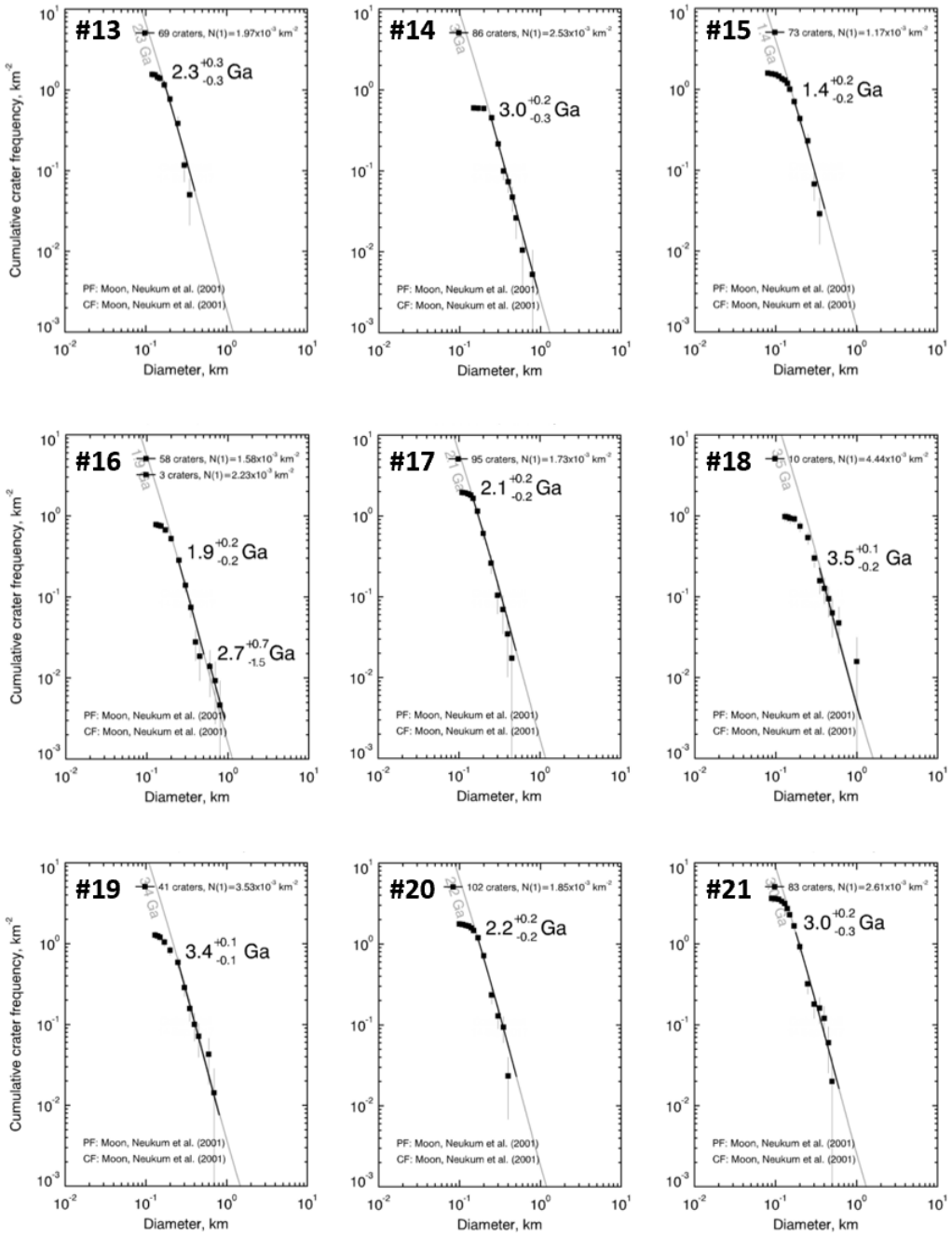

Figure 3.4. Crater size frequency diagrams (CSFDs) for count areas #01 through #21 in NE-OP determined using methods of Michael and Neukum (2010). CSFD #15 is the youngest count area, the oldest surface is at count area #18, #16 exhibits possible resurfacing, and the Chang'E-5 landing site is #21. The numbers of craters counted is listed at the top of each plot; details (location, lat/lon, size, age, etc) for each count area are available in the Supplementary data.

Updated crater counting approaches that take into account issues cited by multiple researchers (Ostrach et al., 2011; Xiao and Strom, 2012; Robbins et al., 2018) and high-resolution imagery (Robinson et al., 2010; Haruyama et al., 2008b; Ohtake et al., 2008) used in this study allowed

relatively smaller areas than those used by previous workers to be counted (Stadermann et al., 2018; Hon and Stopar, 2020); thus providing a more detailed characterization of the basalts and flows in the study area. Our typical minimum crater diameter measure is ~200 m; some count areas used crater diameters down to 170 m. The count areas range in area from 27.4 km^2 to 570.6 km^2. Smaller count areas were avoided as AMA accuracy decreases for smaller count areas (van der Bogert et al., 2015) and the likelihood of identifying secondary craters as primary craters increases (Xiao and Strom, 2012). We used a wide range of incidence angles (Ostrach et al., 2011) to help identify craters, while a single incidence angle was used for diameter measurements. All measured craters within each count area had diameters higher than the minimum conservative pixel threshold diameter, D_{min}; the threshold at which crater population can be completely included in the count (diameter > 10 base image pixels) (Wang et al., 2020). In order to exclude obvious secondary craters from contaminating the crater counts, we inspected the TC and LROC WAC/NAC images to identify such craters (see Oberbeck and Morrison, 1974; Pike and Wilhelms, 1978; McEwen and Bierhaus, 2006). Two mechanisms were used to remove secondary craters from the count population; 1) exclusion areas were defined and craters within the area were not counted and the area was subtracted from the overall count area; and, 2) individual craters were identified as secondary and were excluded.

3.3.0 Results

We have estimated model ages in the study region from crater counts in 21 individual areas, as well as FeO and TiO_2 abundance (Table 3.1B). The count areas were distributed within the eastern portion (east of Mons Rümker) of the originally proposed (180 km x 120 km) Chang'E-5 landing area, (Zeng et al., 2017; see Figure 3 in Qian et al., 2018; Yue et al., 2019; Zhong et al., 2020).

The craters measured at each count area were used to produce individual CSFDs (Figure 3.4), and determine model ages (Table 3.1B). The count areas were examined to identify model age variations between the mare surfaces (Figure 3.1). Of the 21 count areas, six date at 3 Ga or older (including the Chang'E-5 landing site), 11 areas are between 2 and 3 Ga, and four areas are younger than 2 Ga. Hence, based on these data, the mare surfaces within NE-OP range from Upper Imbrian (i.e., #18 at 3.5 +0.1/-0.2 Ga) to Eratosthenian (Wilhelms, 1987) in model age (i.e., #15 at 1.4 +0.2/-0.2 Ga), and suggest that the duration of eruptions in NE-OP was active for at least ~2.1 Gyr. The average age for all count areas is 2.3 Ga.

The NE-OP mare display relatively uniform FeO and TiO_2 abundance. The average maximum FeO abundance for our count areas ranges from 16.9 to 18.4 wt.%; TiO_2 varies from 4.6 to 7.7 wt.%. Averages of FeO and TiO_2 values for each count area show a narrow range in FeO (16.4 to 17.6 wt.% with a median value of 17.2 wt.%) and TiO_2 (4.0 to 6.8 wt.% with a median value of 6.2 wt.%) (Table 3.1B). The highest-FeO areas in each count area are co-located with the highest-TiO_2 areas. Count area #10 has the highest FeO (18.4 wt.%) and TiO_2 (7.7 wt.%) values, and area #18 the lowest FeO (16.9 wt.%) and TiO_2 (4.6 wt.%) values.

3.4.0 Discussion

In this section, we discuss two important points: 1) That compositional uniformity does not equate to model age uniformity; and, 2) That model ages for similar locations can vary by researcher.

3.4.1 Model Ages

Our model age data shows that the maria in NE-OP is comprised of a patchwork of individual flows, which can be as young as 1.4 +0.2/-0.2 Ga (#15) to as old as 3.5 +0.1/-0.2 Ga (#18). Our smaller count areas are more likely to record the model age of individual eruption episodes than larger count areas, however, individual count areas could contain multiple eruption episodes and their associated model ages. Our minimum crater diameter measurement (~170 – 200 m) allowed more areas in NE-OP to be counted to gain an overall view of the age distribution, while still gaining insights into resurfacing events.

Crater counting can detect resurfacing that has occurred by either lateral or vertical processes. For instance, count area #14 (3.0 +0.2/-0.3 Ga) has an older AMA than adjacent count areas and lies on an elevated Oceanus Procellarum wrinkle ridge (Thompson et al., 2017; Yue et al., 2017) 150 m higher in elevation than count area #17 (2.1 +0.2/-0.2 Ga), 40 km to the northwest. The older age may be a relic caused by mare resurfacing that was limited to adjacent areas of lower elevation. Some CSFD curves, like that of area #16, exhibits a “knee” in the CSFD slope, which along with the subdued appearance of craters suggests that the small crater population (<350 m) is more sparsely distributed and hence younger (i.e., 1.9 +0.2/-0.2 Ga) than the larger crater population (i.e., 2.7 +0.7/-1.5 Ga) (Figure 3.4). This characteristic is generally regarded as evidence of the partial resurfacing of a mare area where a thin young lava flow superposes an older

cratered surface (Basaltic Volcanism Study Project (BVSP), 1981, Figure 8.1.1; Baldwin, 1985; Wilhelms, 1987, Hiesinger et al., 2002).

Based on the 21 distinct model ages, we observe two general peaks in eruption periodicity, one at ~2.2 Ga and the other at ~3.0+ Ga (Figure 3.5). We do not observe strong spatial trends in mare unit model age, however, the average model age is slightly younger to the west of the Chang'E-5 count area. The average age for all count areas in NE-OP is 2.3 Ga. The youngest basalt model age (#15) is located in northwest NE-OP. Although no flow morphology (Schaber et al., 1976; Campbell et al., 2007) or vent has been identified, the young basalts may indicate that the eruptive source region is at or near this count area. Adding additional count areas within NE-OP could refine the volcanic history of NE-OP in space and time.

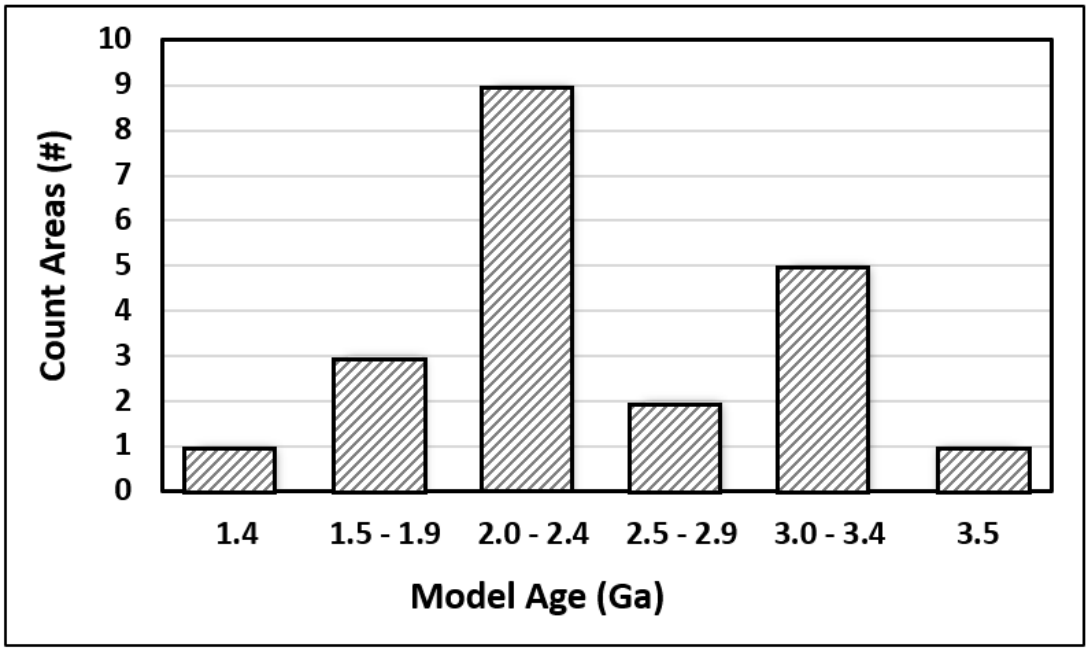

Figure 3.5. NE-OP lava flow eruption frequency. Two eruption peaks are observed at ~2.0 -2.4 Ga and 3.0+ Ga.

A comparison of the model ages in our study area (Table 3.1B) to the model ages of previous studies (Table 3.1A) shows major differences. The reason for these discrepancies is multifaceted. An evaluation of the suspected cause for this incongruity is discussed in section 3.4.2.

As a first step in understanding the mismatch between model ages for the P58/EM4 count areas we examined the geographic count areas established in previous studies. Researchers' (e.g. Morota et al., 2011; Wu et al., 2018, etc.) count areas have different sizes, boundaries and occupy different

locations within P58 (see Figure 3.2 and the Count Area legend (upper right corner)). Count areas from this study are either partially or fully contained within the other researchers count areas. The number of our count areas contained by larger count areas varied with each researcher (Figure 3.6, Table 3.2). These spatial relationship variations make direct comparison of the model ages challenging, however, systematic trends were observed. As illustrated in multiple examples, our count areas are smaller and the determined model ages are older than the model age for the larger surrounding count area (Table 3.1, 3.2; Figure 3.2, 3.6). For instance, our model ages for two count areas within the Hiesinger et al. (2003) count area (1.33 Ga) are older (2.0 Ga, 2.3 Ga). Morota et al. (2011) published two model ages (2.20/3.46 Ga) for their P58 count areas, suggesting that the area was resurfaced, whereas our three model ages are between their model ages (2.4 - 3.0 Ga). The Qian et al. (2018) model age for the northwest portion of Em4 is 1.21 Ga. Our nine count areas within the same area ranged in model age from 1.4 to 3.2 Ga (Figure 3.6, Table 3.2). Similar discrepancies were observed when our model ages were compared to those of other researchers (Wu et al., 2018; Jia et al., 2020; Xu et al., 2021). Qian et al. (2021a) subdivided the EM4 unit into 52 1°x1° count area tiles and determined a model age for each tile that range from 1.1 Ga to 2.9 Ga; Our 19 count areas in P58/EM4 range from 1.4 Ga to 3.4 Ga. Our model ages are systematically older than the model ages determined by previous authors despite counting craters in uniform geochemical areas and avoiding secondary craters (Table 3.1).

Table 3.2: Spatial comparison of count areas and model ages. Count areas (this study) are partially or fully contained within previously defined count areas (Figure 3.2 and 3.6).

Spatial comparison of count areas					
Previous Study		**This Study**			
Author/Year	**Model Age (Ga)**	**Number of Count Areas**	**Count Areas**	**Model Age (Ga)**	**Count Area Relationship**
Hiesinger et al., 2003, 2011	1.33	2	02	2.3	Fully
			03	2.0	Fully
Morota et al., 2011	2.20; 3.46	4	05	2.6	Fully
			06	2.5	Partial
			08	2.4	Partial
			21	3.0	Fully
Qian et al., 2018	1.21	9	05	2.6	Partial
			06	2.5	Partial
			07	1.9	Partial
			14	3.0	Partial
			15	1.4	Fully

			16	1.9/2.7	Partial
			17	2.1	Partial
			20	2.2	Partial
			21	3.0	Fully
Wu et al., 2018	1.49	9	07	1.9	Partial
			09	2.4	Partial
			12	3.4	Partial
			13	2.3	Fully
			14	3.0	Fully
			15	1.4	Fully
			16	1.9/2.7	Fully
			17	2.1	Fully
			20	2.2	Fully
Jia et al., 2020	2.07	16	02	2.3	Partial
			03	2.0	Fully
			04	2.0	Fully
			05	2.6	Fully
			06	2.5	Fully
			07	1.9	Fully
			08	2.4	Partial
			09	2.4	Partial
			12	3.4	Partial
			13	2.3	Fully
			14	3.0	Fully
			15	1.4	Fully
			16	1.9/2.7	Fully
			17	2.1	Fully
			20	2.2	Fully
			21	3.0	Fully
Qian et al., 2021a	1.53	19	01	3.0	Fully
			02	2.3	Fully
			03	2.0	Fully
			04	2.0	Fully
			05	2.6	Fully
			06	2.5	Fully
			07	1.9	Fully
			08	2.4	Fully
			09	2.4	Fully
			10	1.9	Fully
			11	2.0	Partial
			12	3.4	Fully
			13	2.3	Fully
			14	3.0	Fully
			15	1.4	Fully
			16	1.9/2.7	Fully
			17	2.1	Fully

			20	2.2	Fully
			21	3.0	Fully
Qian et al., 2021c	1.60	1	21	3.0	Fully
Xu et al., 2021; Area b	1.23	1	07	1.90	Partial
Xu et al., 2021; Area c	1.49	2	05	2.6	Partial
			21	3.0	Partial
Xu et al., 2021; Area f	1.45	1	10	1.9	Partial

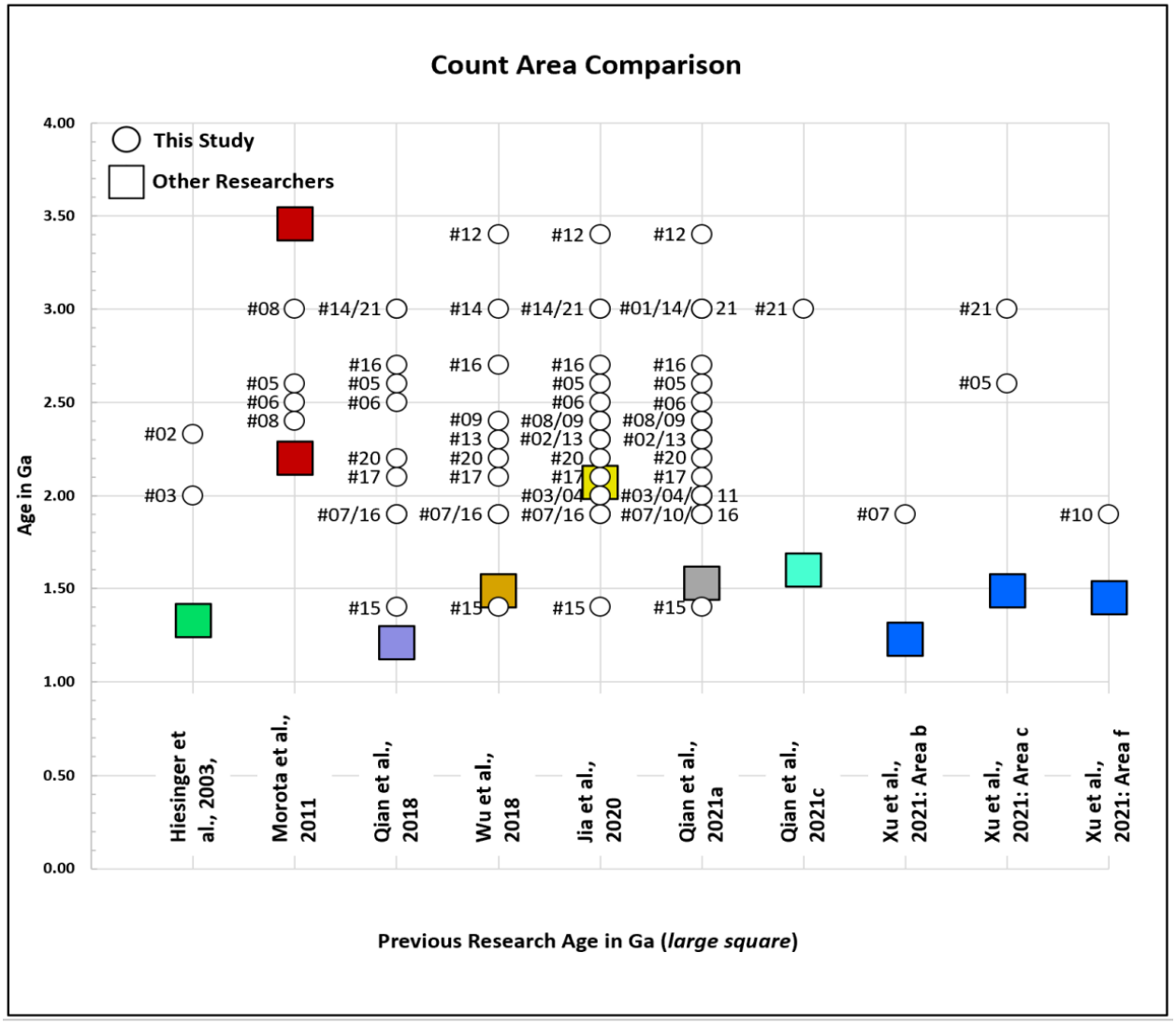

Figure 3.6. Count area comparison. We compare each count area and model age in this study (small white dots with black borders) to the model age determined by previous researchers (Hiesinger et al., 2003; Morota et al., 2011; Qian et al., 2018; Wu et al., 2018; Jia et al., 2020; Qian et al., 2021a, 2021c; Xu et al., 2021) (large colored squares). AMA error bars (Table 3.1) omitted for clarity. Our smaller count areas are compared if they are partially or fully contained within previously defined count areas (Table 3.2). Our model ages are generally older than that of previous researchers.

3.4.2 Crater Measurement Inconsistencies

Our preliminary assessment of, at least, some of the measurement inconsistencies is that rimcrest-to-rimcrest crater diameter measurements vary, identification of primary versus secondary craters is inconsistent, and the detection of degraded craters is sporadic.

We suggest that the actual crater density at the Chang'E-5 landing site is currently unknown for the following reasons: (1) The crater densities (on which the published model ages are based) vary greatly from researcher to researcher; and (2) Without a calibration standard, it is difficult to determine which is the most accurate. Examining identified craters versus missed craters and the metrics of physical crater attributes will begin to divulge the cause for model age inconsistencies between crater counting groups. For such an analyses to be possible researchers need to make their ancillary crater count data publically available. The goal in comparing information across works is to devise a system of standard and reproducible crater measurements.

Qian et al. (2018) included crater count information (latitude, longitude, diameter) in the supplemental section, which is an excellent information sharing model for the community to follow and an example that we follow in our supplemental data. We conducted a comparison of our crater count results for the area around the Chang'E-5 landing site (count area #21) with the identical area extracted from the larger count area used by Qian et al. (2018) (Figure 3.2). We used LROC NAC imagery with multiple incidence angles to count 46 craters > 200 m in the 50 km^2 area, whereas in the same area Qian et al. (2018) used Kaguya imagery with a single incidence angle (morning) and counted 14 craters > 200 m (Figure 3.7). This difference in the total number of counted craters caused the two model age estimates to be substantially different, i.e., 2.45 +0.8/-1.1 Ga for Qian et al. (2018) compared with 3.03 +0.2/-0.3 Ga for our data. We found that the uncounted craters are generally older and degraded (i.e., eroded rim crests, encroached by adjacent and superposed smaller craters). A previous study showed similar results, where the number of craters identified by multiple crater experts varied by a significant percentage (Robbins et al., 2014). In addition, we compared the reported rimcrest-to-rimcrest diameters of the 14 craters measured by Qian et al. (2018) with our data. Overall, we found that our crater diameters measurements range from 2 to 27 % larger, with an average of ~13% larger (Figure 3.7C).

As a second check, we compared the rim crest diameters that we determined for craters at the Chang'E-5 site measured from LROC NAC images to measurements of these craters from topographic data (i.e., the SLDEM2015 topographic dataset) where the rim crest and crater bottom

were determined from four profiles (E-W, N-S, SW-NE, NW-SE lines) across each crater (Figure 3.7D). Typically, our NAC-based diameters measurements were systematically ~9% smaller than the diameters measured in this moderate resolution (59 m/pixel) topographic dataset.

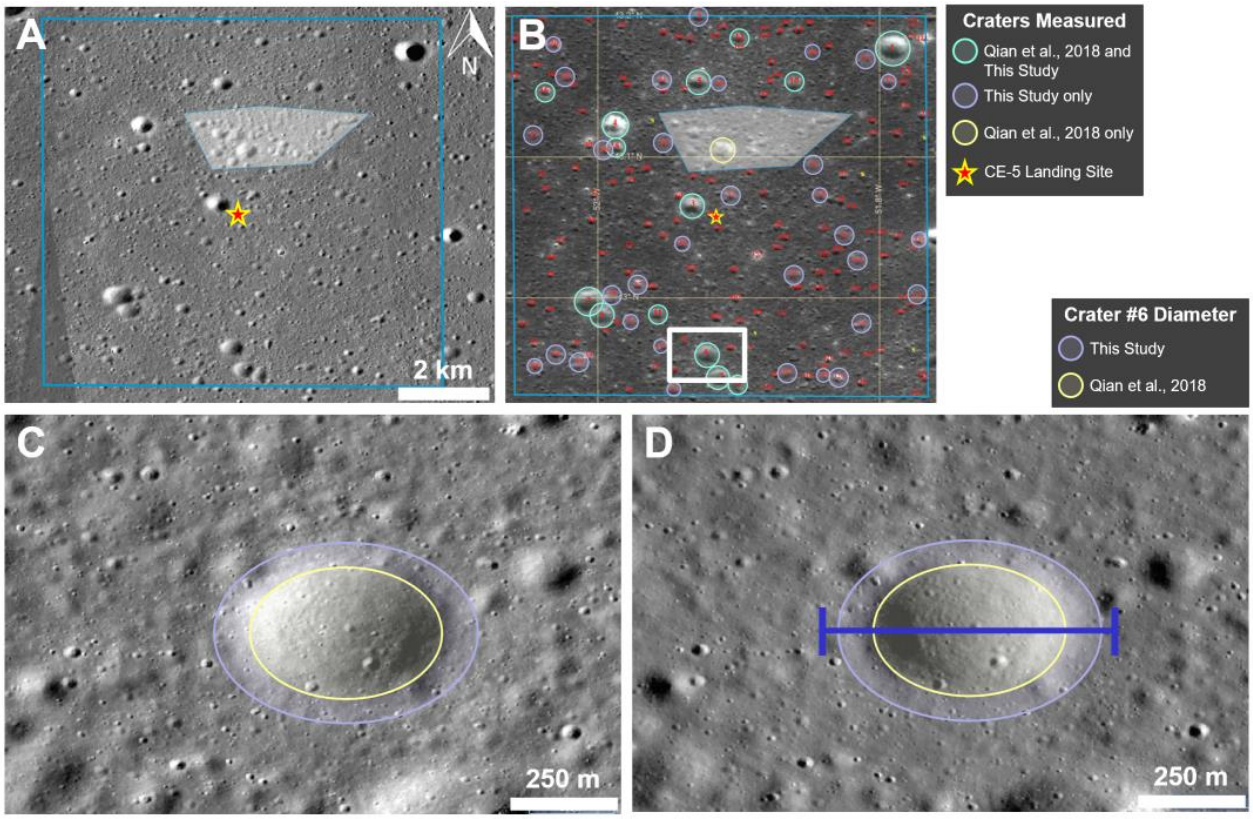

Figure 3.7. A) Overview of count area (#21, blue rectangle) including the Chang'E-5 landing location (red/yellow star). NAC images shown with east illumination. **B)** Count comparison to Qian et al., 2018. Location of comparison crater in C) and D) is designated by the white box. Red numbers are craters identified and counted in this study for CSFD. NAC images shown with medium incidence (~46°). **C)** Diameter of crater #6 (-51.921, 42.961) is 0.446 km (violet ellipse; This Study) and 0.327 km (yellow ellipse; Qian et al., 2018). NAC image M1348581418L with east illumination. **D)** Same as C) with NAC image M1188684210L exhibiting west illumination. Diameter of 0.491 km (blue line) measured with DTM from SLDEM2015 (Barker et al., 2016). LROC NAC images are displayed in a cylindrical projection.

Further rim crest diameter checks were made with a high resolution NAC DTM (~3 m/pixel) for the Chang'E-5 landing site. The NAC DTM, although slightly lower in resolution than the source NAC images (0.91 m/pixel), provided detailed morphology of the comparison craters and allowed precise diameter measurements. Available global DEM datasets have relatively low resolution (GLD100, 100 m/pixel, Scholten et al., 2012; SLDEM2015, 59 m/pixel, Barker et al., 2016). A DTM derived from LROC NAC images has a higher spatial resolution than the global

DEM datasets, however, the area covered is smaller and the DTMs are less frequently available for an area of interest (<<1% of the Moon has NAC DTM coverage).

We converted the NAC DTM (~3 m/pixel) to an aspect image to highlight slope direction. These images clearly show where the rim crest peaks and changes direction (Figure 3.8). The aspect surfaces are color-coded based on the eight compass directions. The crater rim crest is located at the junction of opposing surfaces, i.e. where the crater interior and exterior meet. Unambiguous diameter measurements are made at these junctions. The CE-5 DTM is a small area (<40 Km^2) and does not fully cover count area #21 (Chang'E-5 landing site), however, the image does overlap with eight craters greater than 200 m in diameter. Five of the eight craters are shown in Figure 3.8. We compared the measured CE-5 DTM crater diameters to our measurements and to Qian et al. (2018) (Table 3.3). We averaged the eight crater diameters from each study. Our average using the single NAC image is 1% larger than the NAC DTM diameters; the average for Qian et al. (2018) is systematically 18% smaller than the NAC DTM diameters. Our crater diameter measurements, on average, are closer to those determined from the CE-5 NAC DTM than in Qian et al. (2018).

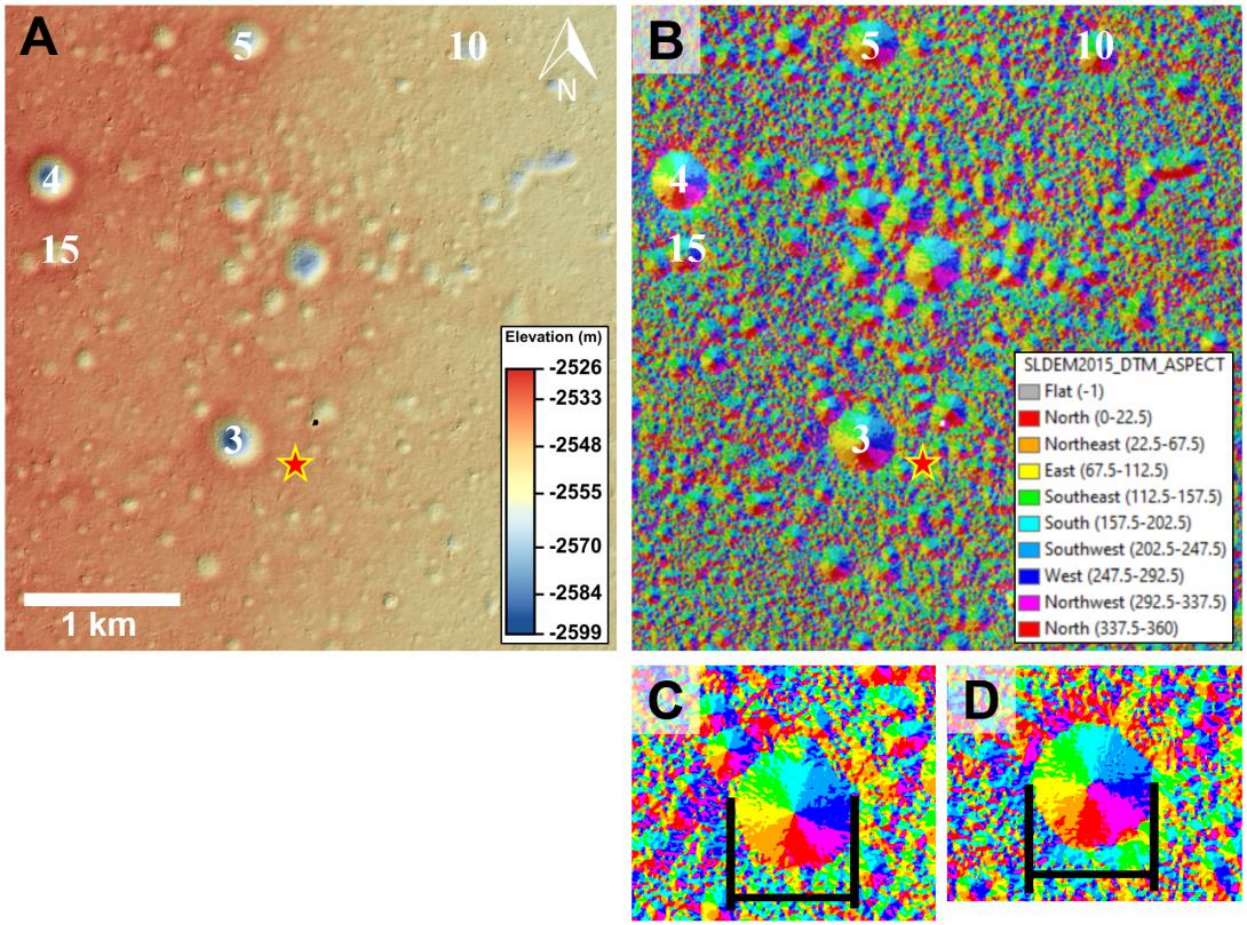

Figure 3.8. Chang'E-5 (red/yellow star) landing site, which is a portion of count area #21 in NE Oceanus Procellarum. Craters are numbered in the sequence counted. A) High-resolution NAC DEM produced with images: M1374407232LE, M1374421274LE (Henriksen et al., 2017). B) Aspect surfaces are color-coded based on azimuth facing direction (see legend) and used to determine the diameter of each numbered crater based on the observed rim crests. C) Crater #03, located just northwest of the Chang'E-5 landing site. D) Crater #04, located northwest of the Chang'E-5 landing site. DEM aspect information assists with locating the crater rim crest (black measurement bars). See B) for the color-coded aspect direction.

Table 3.3: Comparison of measured crater diameters in count area #21 to diameter measurements made on the LROC NAC DTM.

Comparison of measured crater diameters			
Crater Number[1]	**LROC NAC DTM[2] (m)**	**Qian et al., 2018 (m)**	**This Study (m)**
3	445	378	457
4	401	369	406
5	368	282	356
6	413	327	446

7	405	316	402
10	306	219	302
11	273	232	259
15	255	240	258
Average (8 craters)	**358**	**295**	**361**
Compared to NAC DTM	**NA**	**-18%**	**+1%**

[1]See Figure 3.8 for the location of craters

[2]LROC NAC source images: M1374407232LE, M1374421274LE

Another source of inconsistent model ages is the identification of secondary craters. Challenges exist when identifying secondaries in any count area on the Moon. For example, we identified a 3 km^2 area dominated by a cluster of overlapping, irregular shaped craters in count area #21 we interpret as a secondary crater cluster based on these characteristics (Figure 3.7A). No measurements were made in this area and the 3 km^2 was subtracted from the overall area, thus reducing the size of our count area. However, Qian et al. (2018) offered an alternate interpretation and measured a primary crater in this area. The cumulative result of counting fewer craters per area, together with undersized diameter measurements, is a younger mare surface model age than otherwise prescribed by the lunar PF.

Based on the discussion of crater rim crest measurement, secondary crater omission, under counting of degraded craters, and previous comparisons (Robbins et al., 2014), it is clear that a set of standards and procedures for performing crater counts must be developed. Use of these protocols would ensure the production of model age data that is accurate and reproducible. This initiative will take the efforts of crater count researchers and likely will require a workshop on the subject. The focus of such a workshop should include such subjects as: identifying and measuring crater rim crests, recognizing degraded primary craters, dealing with partial, encroached (overlapped) craters, and elimination of secondary craters. We suggest that it will take cooperation within the broader crater counting community to move toward consistent and ultimately, more accurate absolute model ages.

3.4.3 Mare Composition: Distribution of FeO and TiO_2

Here we use FeO and TiO_2 geochemical data and find the same relative compositional uniformity within Hiesinger's et al. (2003) unit P58. However, some minor compositional variations within our 21 count areas are noted. For instance, our area with the lowest FeO and TiO_2 values is #18. Count area #18 is located north of Mons Rümker and its uniformly low FeO and

TiO_2 abundance is consistent with Em3 being spectrally distinct from the eastern portion (Em4) of P58 as suggested by Qian et al. (2018).

Our average geochemical values (FeO 17.2 wt.%, TiO_2 6.2 wt.%) are slightly higher than previous studies (Qian et al., 2018; FeO 16.7 wt.%, TiO_2 4.8 wt.%) as we average only within count areas and exclude the nearby areas that may have had geochemical values lowered by material transported by secondary impact craters. Primary craters identified by other researchers, mainly Aristarchus, Copernicus, Harding, Harpalus, Philolaus, Pythagoras, Sharp B (Xie et al., 2020; Qian et al., 2021a, Xu et al., 2021), may have contributed material that has lower FeO and TiO_2 values than the average found in our study area via their secondary craters.

The mare surfaces in NE-OP, similar to the lava flows on the west side of Mare Imbrium, have an intermediate TiO_2 composition (Taylor et al., 1991; Giguere et al., 2000). Classification terms (very low, low, etc.) describing ranges of TiO_2 values (summarized in Table 1 of Giguere et al., 2000), are designed to allow scientists to identify and classify basalt groups. Basaltic rocks in the current sample collection generally have either very low-Ti (i.e., <1 wt.% TiO_2; Apollo 17 and Luna 24), low TiO_2 (i.e., 1-6 wt.% TiO_2; Apollo 12, 14, 15; Luna 16), or high TiO_2 (>6 wt.% TiO_2; Apollo 11, 17) (Neal and Taylor, 1992). Mare regolith samples collected from the above missions have TiO_2 values that are lower by ~20% on average than the composition of basaltic rocks from the same site, which Gillis et al. (2003) suggests reveals the dilution effect of nonmare components on basaltic soil bulk compositions. For instance, secondary craters, may transport low FeO and low TiO_2 feldspathic material from the highlands via ballistic sedimentation (Oberbeck, 1975). In areas surrounding secondary craters, highlands contamination can reduce mare TiO_2 values by ~1.5 wt.% and FeO by as much as ~3 wt.% in some cases (Korotev and Gillis, 2001). Hence, anomalous compositions from areas with secondaries are excluded.

A basalt sample from this region would help resolve this issue; i.e., whether the basalts from NE-OP are of intermediate TiO_2 composition or a mixture of high- and low-Ti rocks. In either case, the samples chemistry, particularly its trace element composition will provide new information on mantle source composition, amount of fractional melting, and transport processes from the mantle to the surface (Taylor, 1982; Ryder, 1991; Giguere et al., 2000).

The Chang‘E-5 landing site is ~10 km northeast of a highlands kipuka and ~50 km from the nearest mare-highland boundary. Samples will likely contain some feldspathic lithic and mineral material similar to 10084—Apollo 11, which landed ~50 km from the nearest highland exposure

(Li and Mustard, 2005; Huang et al., 2017), and contains up to 28% nonmare material (highlands and KREEP-rich material) (Korotev and Gillis, 2001). Equivalently, we suggest that FeO and TiO_2 values are reduced around the margins of our study area due to the lateral (Li and Mustard, 2000) and vertical (Rhodes, 1977) transport of lower FeO and TiO_2 materials by impact.

3.4.4 Eruption Ages and Compositions

The wide distribution of model ages within our study area indicate that multiple eruptions occurred over an extended period (e.g. between 3.5 and 1.4 Ga). However the geochemistry (FeO & TiO_2) varies only slightly across the NE-OP region. Multiple eruptions in Em4 have previously been suggested (Qian et al., 2021a; Xu et al., 2021) and implied (Wu et al., 2018; Jia et al., 2020). No apparent correlation between mare surface model age and geochemistry is identified in this region.

The eruption duration in NE-OP is approximately 70% of the time the Moon was volcanically active based on estimates from absolute model age studies (~1.1 - 4.0 Ga) (Head, 1976; Boyce, 1976; Hiesinger et al., 2003, 2011). Our model ages, based on crater count data, suggest that individual eruptions continued from the early eruptions (3.5 Ga), waning to ~3.0 Ga, but then resurged around 2.0 – 2.4 Ga, and may have lasted ~2.1 Gyr. These data indicate that the bulk of NE-OP volcanism is younger than the apparent peak of lunar eruption activity, which occurred between 3.4 and 3.7 Ga (see Figure 18 in Hiesinger et al., 2011). The bulk of these older deposits are likely now obscured by younger flows. Our data also suggests that eruptions continued past ~2.0 Ga in west-central NE-OP (i.e., west of 52.3° Lon.) with the youngest flows located in northwest NE-OP (#15).

Zhao et al. (2017) proposed that Mons Rümker, a basaltic edifice with three units >3.51 Ga, could have been a source for these older eruptions. We have identified three areas around Mons Rümker with similar model ages, i.e., #12, #18, #19. However, Mons Rümker, along with area #19, exhibits lower FeO and lower TiO_2 values than the basalts in eastern NE-OP (Figure 3.1 and 3.2). Consequently, we suggest that Mons Rümker is not the source of the nearby flows in areas #12 and #18, but could be for count area #19.

The relative uniformity of composition across the NE-OP region could be due to either a single mantle magma source that did not change with time or multiple magma sources that were similar in composition (Wieczorek et al., 2006). Moreover, the model age and geochemistry of the mare in NE-OP fits with the overall trend for Oceanus Procellarum. Where the younger basalts (<3.0

Ga) (Hiesinger et al., 2011) have intermediate to high TiO_2 values, and the older basalts (>3.0 Ga) have low TiO_2 values (Staid et al., 2011) and abundant olivine (Staid and Pieters, 2001). Early Oceanus Procellarum lava flows apparently were supplied from low TiO_2 mantle material, which either evolved or was supplanted by partial melting of higher TiO_2 mantle material in later eruptions (Gillis et al., 2004); most lava flows in NE-OP are part of this later phase.

Major eruption activity in the study area appears to have ceased by ~1.4 Ga according to our model age determination. We attribute the extended duration and effusion of volcanic activity in NE-OP to its location within the high-thorium (Th) Procellarum KREEP Terrane (PKT). As suggested by Jolliff et al. (2000) and Wieczorek et al. (2013), the concentration of radiogenic elements and thin crust could have promoted partial melting for a longer duration than locations outside of the PKT.

3.5.0 Chang'E-5 Sample Ages and their Implications

Chang'E-5 landed in NE-OP at 43.0584°N, 51.9162°W, (Wang et al., 2021) and returned approximately 1.7 kg of regolith from a depth of up to 1 meter (Zou and Li, 2017; Qian et al., 2021b). The Chang'E-5 samples will likely be physically similar to Apollo and Luna regolith samples, and include material of different radiometric ages and compositions derived from nearby and distant sources. These samples will enable measurements not possible by remote sensing. Information derived from these samples may help us better understand the lunar impact flux history, as well as potentially fill gaps in our knowledge of the lunar geologic history, such as the thermal evolution time scale.

Despite the relatively uniform spectral and morphologic appearance of the region, model age dates indicate that Chang'E-5 landed in a region with a complex eruption history. Based on our new data, we suggest that the dominant sample age will be ~3.0 +0.2/-0.3 Ga (#21), but will also likely include a small fraction of material derived from neighboring flows. For example, small amounts of material from nearby younger flows (e.g., #4, #5, #6, #7 #15, with model ages in the 1.4 – 2.6 Ga range), may have been transported to the site by impact processes. In addition, mare materials with model ages of >3.4 Ga are possible, as vertical and horizontal gardening of older material (e.g., #12, #18, #19) is known to occur (e.g., Rhodes, 1977).

The current lunar impact crater flux curve (Baldwin, 1985; and Neukum et al., 2001; Figure 1 in Hiesinger et al., 2012) is constructed from the relationship between the radiometric age of returned lunar samples (i.e., Apollo and Luna sample) compared with the cumulative number of

craters of a given size at the site where the sample were collected (Section 3.2.0). However, no lunar samples from a known location exist for the time span between Apollo 12 (~3.33 +0.050/-0.069 Ga, Iqbal et al., 2020) and the Copernicus impact (797 +51/-52 Ma, Hiesinger et al., 2012). Moreover, the validity of the Copernicus sample age has been called into question by Stöffler and Ryder (2001). This supposition suggests that there may be no sample age to anchor the young part of the lunar impact cratering chronology.

The uncertainty with the Copernicus age makes determining the radiometric age of the Chang'E-5 samples even more critical. Suppose Chang'E-5's returned sample is as geologically young as some researchers predict from their crater counts. In that case, these samples could provide a valuable calibration point in the young part of the lunar impact cratering chronology. However, there is a broad range in predicted model age for the Chang'E-5 site. These researchers all used the same lunar impact crater flux curve. The only difference are their crater densities measurements and crater rim diameter determination. The differences in these two subjective measurements cast doubt on the accuracy of absolute model age determinations.

Further complicating this situation, our crater count data predicts the model age of the Chang'E-5 site is approximately the radiometric age of the Apollo 12 site. Based on our model age, we infer that the dominant age of the Chang'E-5 samples will be 3.0 Ga, which corresponds to the surface age of the unit. Still, there will be minor components of both younger and older basaltic material mixed in. Hence, if the dominant age is as old as we predict, it would do little to improve calibration of the lunar impact flux curve. However, our determined AMA for different count areas surrounding the Chang'E-5 site may allow us to associate the younger and older rock fragments to nearby surface units. Providing the geologic context for these younger samples by connecting the sample ages to surfaces with determined crater density will improve the calibration of the lunar impact flux curve.

3.6.0 Summary

We examined the NE-OP region with the goal to understand and characterize mare volcanism processes in this area of the Moon. We found that this region exhibits multiple basaltic flows with a wide range of model ages, from 1.4 – 3.5 Ga, spanning 70% of lunar volcanic history. Our data indicate that:

1. Our model age data shows that the maria in NE-OP is comprised of a patchwork of individual flows, which can be as young as 1.4 +0.2/-0.2 Ga to as old as 3.5 +0.1/-0.2 Ga. Our average age for all count areas in NE-OP, and EM4, is 2.3 Ga.
2. The frequency of eruption in NE-OP was bimodal, peaking at ~3.0+ Ga, near the end of the Imbrian period, and the second peak in eruption frequency occurred during the Eratosthenian period (2.2 Ga; Wilhems, 1987).
3. The wide distribution of model ages and the near-uniform FeO and TiO_2 abundance of the basalt within our study area indicate that multiple eruptions occurred over an extended period. This finding contradicts previous assumptions that because this region's composition and spectral properties are similar, it is a unit of a single age.
4. NE-OP basalts are not sourced from Mons Rümker as both the age and geochemistry (FeO, TiO_2) of the basalts are dissimilar.
5. Our NE-OP and Chang‘E-5 count area model ages are in disagreement with model ages determined by other researchers, which are commonly inconsistent with each other. The model ages determined here are systematically older than those calculated by previous workers.
6. The three key reasons our model ages are systematically older are 1) differences in measured rimcrest-to-rimcrest crater diameters, 2) identification of primary versus secondary craters, and 3) detection and counting of degraded craters.
7. Chang’E-5 will likely return basaltic rock and regolith material with a dominant radiometric age of ~3.0 +0.2/-0.3 Ga that reflects the model age of the landing location. Younger (1.4 – 2.6 Ga) and older sample ages will also be found, due to impact mixing from neighboring flows. Our AMAs calculated for different count areas surrounding the Chang’E-5 site may allow us to associate these younger and older rock fragments to nearby surface units. Thus, connecting the sample ages to surfaces with determined crater density, which will improve the calibration of the lunar impact flux curve.
8. A cautionary note: In spite of counting craters in the same area, and using similar supporting data researchers have measured a wide range of crater densities in NE-OP and at the Chang‘E-5 landing site. This is concerning and, without a calibration standard, there appears to be no way of determining which of the counts is most accurate. Hence, the actual crater density at the landing site is unknown and the use of any of these data to calculate a

point on the lunar impact flux is problematic. Thus, even after the absolute age of the sample from the Chang'E-5 site is determined, none of the different crater densities (and their model ages) should be used to calibrate the lunar impact flux curve until a detailed peer review of all data collection methods is conducted. This is especially true if the radiometric age of the Chang'E-5 sample is young (i.e., < 2.5 Ga). In addition, to begin working toward consistent model ages, we recommend that detailed crater count supporting data (i.e., coordinates of the location, diameter of each crater counted, area and edge coordinates of the count area, spacecraft imagery and resolution) be submitted as a required supplement to the publication process.

3.7.0 Acknowledgements

The authors would like very much to thank Zhiyong Xiao, Sun Yat-sen University and anonymous Reviewer 2 for their helpful and constructive comments. We appreciate Scott Rowland, University of Hawaii-Manoa, for his suggestion to use DTM aspect data for crater rimcrest diameter measurements. We would like to acknowledge support from NASA through the LRO/LROC Contract ASU 11-599 with Arizona State University (Mark Robinson, PI) and SSERVI award NNA80NSSC20M0027 (Jeffrey Gillis-Davis, PI). This paper is SOEST Contribution 11450 and HIGP Contribution 2454.

Data Availability Statement

The lunar remote sensing data sets used in this article is publicly available in the Planetary Data System (PDS). All crater count data and CSFDs used to reproduce the results and figures in this work can be accessed online at doi:10.17632/63w48xy5jc.1 (http://dx.doi.org/10.17632/63w48xy5jc.1).

CHAPTER 4: CALIBRATING LOCALIZED AND REGIONAL LAVA FLOW AGES AT CLPS LANDING SITES ON THE MOON

[Manuscript in preparation for publication]

Thomas A. Giguere[a*], Julie D. Stopar[b], Jaclyn D. Clark[c], Joseph M. Boyce[a], and Jeffrey J. Gillis-Davis[d]

[a]Hawai‘i Institute of Geophysics and Planetology, Department of Earth Sciences, University of Hawai‘i at Manoa, 1680 East-West Road, Honolulu, HI, 96822, United States, [b]Lunar and Planetary Institute (USRA), 3600 Bay Area Boulevard, Houston, TX 77058, [c]School of Earth and Space Exploration, Arizona State University, Tempe, AZ 85251, [d]Washington University, Department of Physics, One Brookings Drive, St. Louis, MO 63130.

* Corresponding author: Thomas Giguere

E-mail address: giguere@hawaii.edu

Submitted to **Planetary Science Journal**

Running Head: **Lava flow ages at CLPS landing sites**

Topical Corridor: The Solar System, Exoplanets, and Astrobiology

Keywords: Moon; Cratering; Volcanism; Moon, surface; Impact processes

Key Points:

#1: Three NASA Commercial Lunar Payloads Services (CLPS) landing sites Reiner Gamma, Mare Crisium, and Lacus Mortis were selected for determination of their lava flow ages (absolute model age) and to compare differences in researcher crater counting and measurement techniques.

#2: The mare basalts at all three sites are Imbrian-aged: Reiner Gamma AMA: 3.29 +0.041/-0.054 to 3.78 +0.018/-0.021; Mare Crisium AMA: 3.24 +0.083/-0.14 to 3.63 +0.024/-0.029; and Lacus Mortis AMA: 3.26 +0.082/-0.14 to 3.73 +0.033/-0.043.

#3: The variation in absolute model ages between two of the coauthors is likely due to differences in the number of secondary and degraded craters identified and to a lesser extent crater diameter measurements.

Abstract

We selected three NASA CLPS landing sites in the lunar maria (e.g., Reiner Gamma, Mare Crisium, and Lacus Mortis), for crater counting based determination of their lava flow ages (absolute model age). This study aims to compare differences in researcher measurement techniques and to place the sites in regional context with regards to their lava flow ages. Two researchers performed crater density measurements at the three sites, using identical imagery with the same illumination conditions, and the same software tools. The uniform nature of the analysis environment allowed researchers to use accepted crater counting techniques to determine absolute model ages (AMA), while subsequently allowing the examination of the variations in the personal approaches used by the researchers. Comparisons revealed variations in researcher methodology and resulting AMAs.

Landing sites were subdivided into two or more smaller count areas, and we determined that all areas have mare basalts that are Imbrian in age. Variations in AMAs between researchers were the result of differences in the number of secondary and degraded craters identified and to a lesser extent crater diameter measurements. Building on the legacy work of the crater counting community, we recommend rigorous secondary crater identification and exclusion, DTM aspect-based diameters to calibrate measurements, high-resolution orbital imagery to improve rimcrest location measurements, and surface imagery to verify rimcrest condition.

4.1.0 Introduction

The pace of lunar research and associated missions is accelerating and reaching unprecedented levels of activity. Not since the Apollo era in the 60's and 70's have we seen this level of involvement from multiple countries, research institutions, and the public. A large number of missions are slated for the current decade with about a dozen missions tied to the NASA Commercial Lunar Payloads Services (CLPS), which funds commercial companies to transport NASA and commercial payloads to the Moon, such as small robotic landers and rovers (Bussey et al., 2019). The goals vary between each lunar landing mission and a variety of experiments are planned for each mission. Our science results are intended to support selected experiments that benefit from knowing the mare age on these missions.

We have selected for crater counting analysis three proposed CLPS mare landing sites: Reiner Gamma, Mare Crisium, and Lacus Mortis (Figure 4.1). Our aim is to understand these sites in regional context with regards to their lava flow ages (Table 4.1). These landing sites have not been previously sampled; thus we do not have laboratory determined ages for the basalts. However, remotely acquired high-resolution imagery may be used to estimate lava flow ages at these locations.

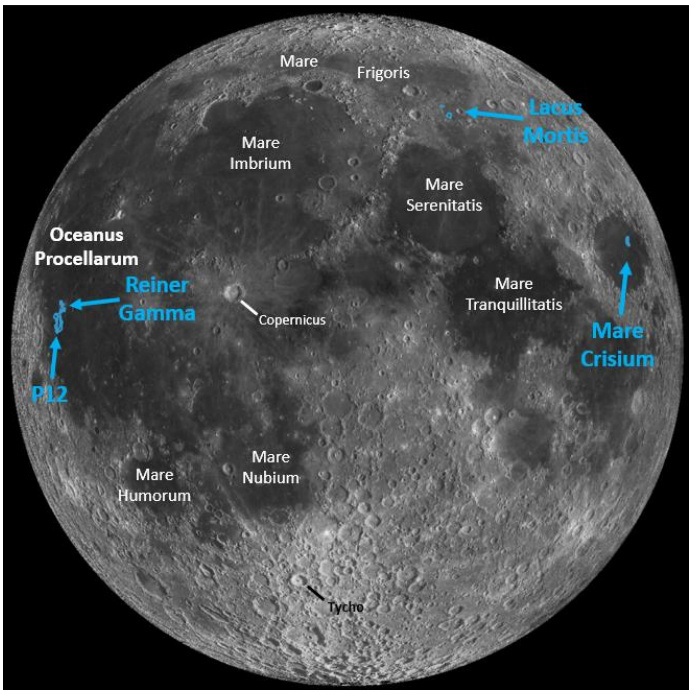

Figure 4.1. Study areas on the nearside of the Moon: Lacus Mortis, Mare Crisium, and Reiner Gamma in Oceanus Procellarum. Comparison count area (P12, Hiesinger et al., 2011), southern Oceanus Procellarum. Basemap: WAC Normalized Reflectance (Albedo) Map (643 nm), bottom image; low-sun WAC Near Side mosaic (643 nm), top image with transparency. Speyerer et al., 2011; orthographic projection, 100 meters/pixel.

Table 4.1. CLPS mission details for three study areas

Target Location	Date	Location (lat/lon)	Task Order	Contractor	Mission	Lander	Rover
Reiner Gamma	2024	7°.585 N, 58°.725 W	CP-11 (PRISM1a)	Intuitive Machines	Lunar Vertex	Nova C Lunar Lander	Yes
Mare Crisium	2024	18°.560 N, 61°.807 E (Crisium Horseshoe)	TO 19D	Firefly Aerospace	Blue Ghost 1	Blue Ghost Lander	NA
Lacus Mortis[1]	TBD	~44 N, 25 E	Future	Future	Future	Future	NA

[1]Mission: TO2-AB, Astrobotic, rerouted to Oceanus Procellarum, near the Gruithuisen Domes.

The general process for determining the relative and absolute model ages of planetary surfaces begins with the assumption that the flux of impacting meteoroids is relatively constant and spatially stochastic, and that crater size is primarily a function of impactor mass and velocity which also influences size, is assumed constant for a given planetary body. Hence, a surface with fewer impact craters is younger than a surface with more craters, which is logical as the older surface accumulates more craters over time. An age relationship is established when the surface with a specific number of craters, in a given size range, has an absolute age-dated sample from the same surface (e.g., the Apollo landing sites). This crater size frequency versus sample age relationship is performed for multiple surfaces. As a result, we have the ability extrapolate this age-crater relation to estimate the absolute age of other locations, even though they have not been directly sampled.

Various approaches for determining ages for unsampled surfaces have been in use in different forms for over 50 years (Trask, 1971; Soderblom & Lebofsky, 1972; Soderblom & Boyce, 1972; Boyce et al., 1974; Boyce and Dial, 1975; Boyce, 1976; Neukum et al., 1975a, 1975b). The need for remotely determined ages continues and is more relevant based on the accelerated pace of lunar exploration. As an example, a previous age study (Hiesinger et al., 2006, 2011a, 2011b) divided up the nearside maria by spectral unit into ~300 mare age units of various sizes, only a small portion of the eight units have been age-verified with returned samples (i.e., Apollo 11, 12, 14, 15,

17; Luna 16 and 24; Change'E-5). Thus, roughly 98% of the Hiesinger "mare age units" have ages determined via remote methods—A much smaller percentage of the area of the mare has been age-verified. The age units in this past study were generally large; thus, there is a need for age studies of smaller mare areas (This Study) and additional samples from unexplored areas.

Each of our CLPS landing sites (Reiner Gamma, Mare Crisium, and Lacus Mortis) are unsampled, so we used crater counting methods to determine absolute ages. Accepted practices, include collecting the primary crater locations and diameters for primary craters in a GIS mapping tool (Kneissl et al., 2011), analyzing the list of craters, calculating statistics, and calculating an absolute model age (AMA) via a crater size-frequency diagram (CSFD) (Michael and Neukum, 2010). This process was performed by two researchers for multiple count areas at each landing site.

We examine the data to identify factors that can cause variations in researcher determined ages. As we have seen in previous studies (Robbins, 2014), independent researchers can arrive at a different absolute model ages for the same study area, despite using the identical imagery, count area location, and software tools. In other cases, the parameters may not be exactly identical as in the situation where image quality has improved or the count area boundaries from a previous study are not available (Iqbal et al., 2020). An additional scenario, involving multiple independent researchers, sought to predict the age of the Oceanus Procellarum mare basalts to the east of Mons Rümker prior to the return of the samples from the Chang'e 5 mission. The variation in predicted ages was substantial (~1.8 Gy) (Giguere et al., 2022, see Figure 6) and indicates that improvements to the method should be identified and implemented.

There are many possible reasons for researchers to determine different ages for the same basalt flow. Hence, as part of this study, we examined variations in AMAs that were calculated by the two researchers who performed crater density measurements using identical imagery with the same illumination conditions and the same software tools. First, we focus on identifying primary versus secondary craters by researchers, as the number of primary craters in a count area has an effect on the AMA. Next, we compare the crater diameter measurements for each researcher. Variations in diameter tend to have a minor effect on the AMA, but a measurable factor nonetheless. Our criteria for comparing these two effects include identifying individual cases where variations occur and documenting examples to illustrate the difference. A complete statistical comparison of individual

craters has previously been provided to the community (Robbins et al., 2014). The goals of this research for the three CLPS study areas is the following:

1) Provide new or updated absolute model ages (AMAs) for small areas at or near each of the three proposed landing sites. Small, distributed count areas can aide in the identification of individual flows or collectively provide improved statistics for the entire area.
2) Determine the AMA variation for each researcher for the count areas within a study area. Age variations between count areas may indicate differences in lava flow ages or the presence of secondary craters.
3) Quantify the AMA differences between researchers for study area count areas. This information can tell us if researchers have an identification or measurement bias in their approach. Identify the possible reasons for variations in researchers AMAs.
4) Place the basalt ages at the CLPS locations in context with both local and regional mare ages.

4.1.1 Background

We review previous work related to the crater measurement and counting processes, and their effects on the AMA. CLPS missions and landing site context is provided for our three study areas.

4.1.1.1 Legacy crater counting issues

Identifying craters for the purpose of determining mare basalt ages has a long history of research aimed at assessing and quantifying the sources of errors to ensure age consistency and also accuracy. Two processes that cause the greatest uncertainty in crater counting are: Crater degradation state (Arthur et al., 1963; Trask, 1971; Robbins, 2014; Riedel et al., 2020) and the identification/rejection of secondary craters (Oberbeck and Morrison, 1974; Pike and Wilhelms, 1978; McEwen and Bierhaus, 2006; Xiao and Strom, 2012). Degraded craters lack sharp definition and are progressively harder to detect as solar elevation angle increases. These craters are more easily missed than fresh craters. Issues with detecting secondary craters come in two forms: first, the morphology of secondary craters may be the same as primary craters (circular shape, raised rim, high depth/diameter ratio) increasing counts; second, researchers have not reached consensus on the number of secondary craters produced from a primary crater impact (McEwen and Bierhaus, 2006), which can have an ambiguous effect on counts.

Additional sources of error in the crater count and measurement process have been previously described (Gault, 1970; Greeley and Gault, 1970; Kirchoff et al., 2011). To remain above the minimum threshold resolution, we used high-resolution imagery for crater rim identification (Wang et al., 2020). Count areas are located in mare locations to minimize variations in the target properties (e.g., density, porosity, and strength) that affect final crater size (van der Bogert et al., 2017), are larger than the minimum recommended count area size (van der Bogert et al., 2015), and are not located near large primary craters (> 10 km) to minimize self or auto secondaries (Shoemaker et al., 1969; Plescia and Robinson, 2011; Williams et al., 2014b; Zanetti et al., 2013, 2014, 2017). Variations in solar incidence was identified as a source of crater count variations (Ostrach et al., 2011), which we mitigated by using imagery with consistent lighting.

4.1.1.2 Reiner Gamma

In 2024, the Intuitive Machines (IM) Nova C lander will visit Reiner Gamma in southern Oceanus Procellarum (7.585 N, 301.275 E) (Blewett et al., 2021b). Reiner Gamma is a prominent swirl of bright albedo material superposed on a vast dark lava plain. Its areal extent and elevated albedo allow it to be viewed with amateur telescopes (Figure 4.1). Although, the IM mission targets the approximate center of the feature, less prominent wispy lobes of bright swirl material extend ~200 km to the south and ~150 km into the Marius Hills to the northwest. The Reiner Gamma swirl, despite being located >150 km from the nearest highlands, may be influenced by the distal impact ejecta of multiple large craters; (Wilhelms, 1987, See Figure 12.10) (Figures 4.1 and 4.2), or could be influence by electrostatic lofted dust (Blewett et al. 2011).

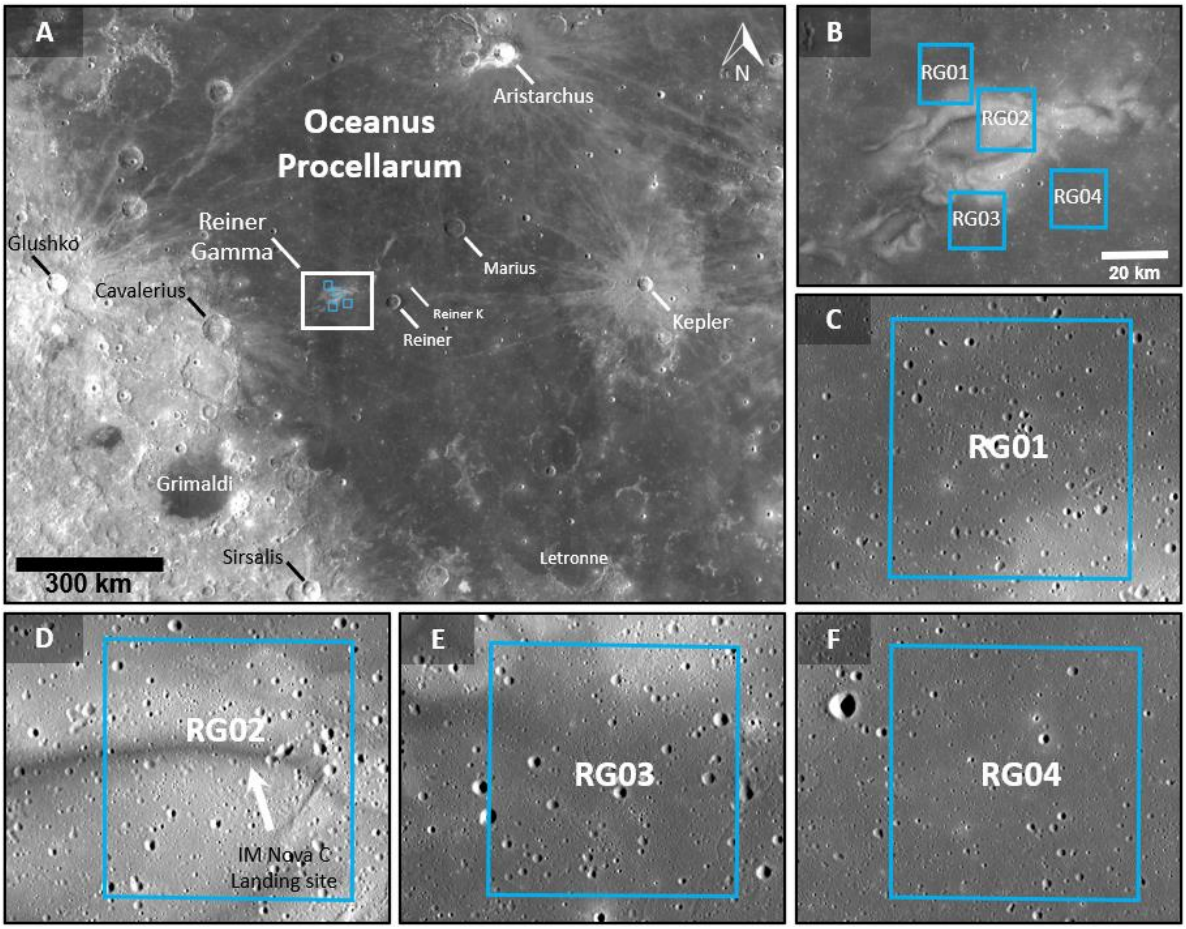

Figure 4.2. Reiner Gamma count areas are located west of Kepler in Oceanus Procellarum. A) The count areas were distributed to identify variations in mare surface ages regardless of albedo difference. Location of detailed count areas in B (white box). WAC Normalized Reflectance (Albedo) Map (643 nm) (Speyerer et al., 2011; cylindrical projection). B) The four count areas include varying amounts of high albedo mare. C) Count area RG01 is located northwest of the main portion of RG, encompasses mainly mare basalt and includes high albedo mare in the southeast corner. D) Count area RG02 encompasses the main portion of RG, including alternating light and dark albedo lanes. This area includes the Intuitive Machines Nova C landing site (white arrow shows the approximate location) for the Lunar Vertex payload (lander and rover). E) Count area RG03 is located south of the main portion of RG and includes high albedo mare at the north end. F) Count area RG04 is located to the east away from RG. Figures C, D, E, and F use Kaguya morning TC imagery (Haruyama et al., 2008b).

4.1.1.3 Mare Crisium

The Firefly Aerospace Blue Ghost lander will land in Mare Crisium (~2024), >100 km northeast of the center of the mare (18.560 N, 61.807 E). The landing site is adjacent to Mons Latreille, the most prominent volcanic cone in the basin (18.47°N, 61.92°E, diam 6.4 km). Mare Crisium (16.18° N, 59.10° E), is a mare-filled impact basin (diameter 555.92 km; ~19,200 sq km; IAU) located on the eastern lunar nearside (Figure 4.1 and 4.3). Although, Mare Crisium is a

prominent basin, the mare basalts were not dated initially in global surveys (Boyce, 1976; Hiesinger et al., 2000, 2003, 2006, 2010), but were dated in other studies: Boyce et al. (1977), Boyce and Johnson (1977) focused on the mare basalts as well as the Luna 24 landing area and published AMAs for all in the range of 2.5 – 3.75 Ga, Hiesinger et al. (2011b) determined AMAs ranging from 2.72 – 3.61 Ga. Lu et al. (2021) likewise performed counts and determined AMAs ranging from 2.49 – 3.74 Ga.

This mare has been visited in the past by two lunar missions. Luna 23, a Soviet sample return mission, landed in southern Mare Crisium (Florenskii et al., 1977; 12.67°N 62.15°E, Robinson et al., 2012) on November 6, 1974. Although the spacecraft survived for three days on the Moon, no samples were returned likely due to damage that occurred during landing. Nearly two years later, Luna 24 landed in Mare Crisium (12.71°N 62.21°E, Robinson et al., 2012), about 2 km northeast of Luna 23, on August 18, 1976. This mission successfully returned a sample of the lunar regolith (170 g) from the ejecta of a 65 m diameter secondary impact crater, which is composed mainly of regolith at depth (not surface), along with distal ejecta from crater Fahrenheit (Barsukov, 1977). Although, the Luna 24 location has been sampled, the Blue Ghost landing site, which is located ~175 km to the north, has been demonstrated to be spectrally distinct (Hiesinger et al., 2011b; Lu et al., 2021) and the lava flows in this area likely have a different composition and age.

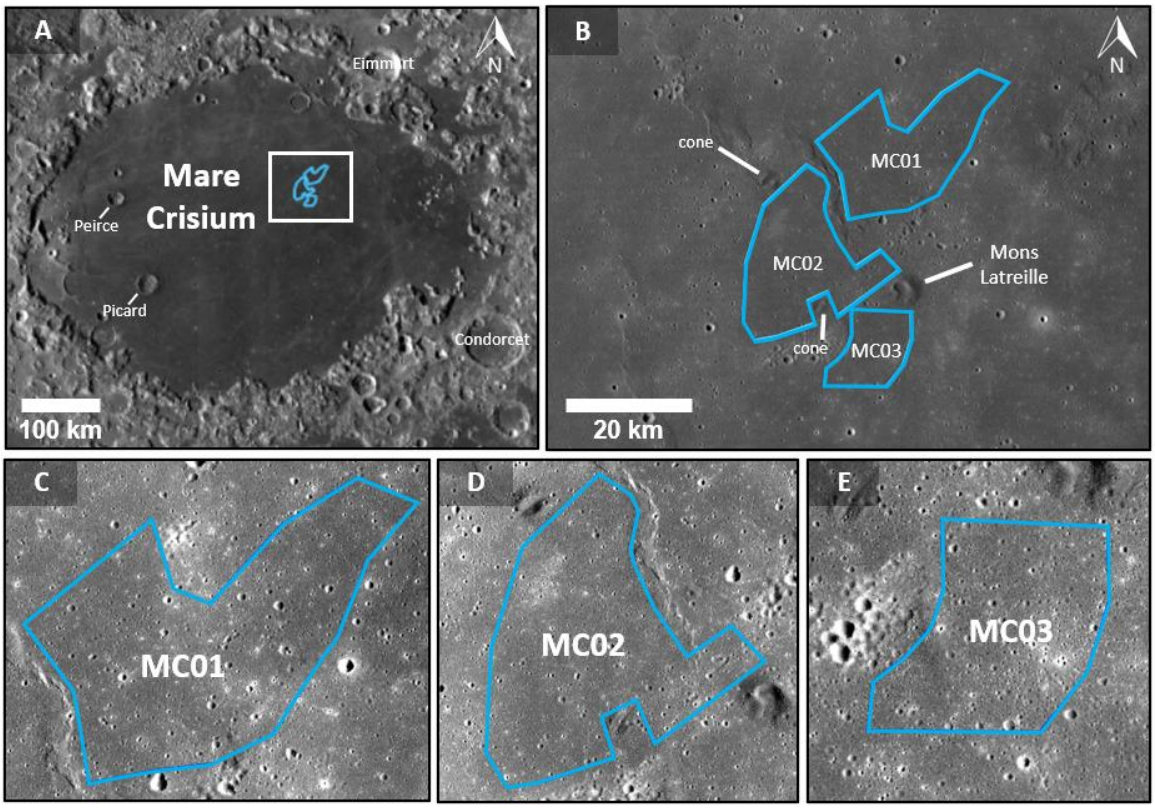

Figure 4.3. Mare Crisium count areas are located northwest of the center of the basin. A) The count areas are distributed to the north, west and south of Mons Latreille. Location of detailed cout areas in B (white box). WAC Normalized Reflectance (Albedo) Map (643 nm) (Speyerer et al., 2011; cylindrical projection). B) Distribution of count areas including locations of Mons Latreille and two unnamed cones. C) Count area MC01, north of Mons Latreille, mapped to exclude secondary crater clusters to the north and south, and a wrinkle ridge to the west. D) Count area MC02 west of Mons Latreille, mapped to exclude secondary craters to the south, the unnamed north and south cones, and the east wrinkle ridge. E) Count area MC03 south of Mons Latreille, mapped to exclude secondary craters on all other sides. Figures C, D, and E use Kaguya morning TC imagery (Haruyama et al., 2008b).

4.1.1.4 Lacus Mortis

Lacus Mortis was the original planned target of Astrobotic Peregrine lander. The Astrobotic mission was recently retargeted for the mare area around Gruithuisen domes. Western Lacus Mortis is a unique geologic destination and is very likely to be the target of a future mission; thus, it will remain a "target" of our research. Lacus Mortis (45.13° N, 27.32° E), is a small mare (diameter 158.78 km; ~19,200 sq km) located on the northeastern lunar nearside (Figure 4.1). Most major mare along with many minor ones have been age dated in lunarwide studies (Boyce, 1976; Hiesinger et al., 2011a); However, Lacus Mortis has been largely overlooked. One recent study

provides basalt model ages of 3.3, 3.5, and 3.8 Ga for the areas around the Lacus Mortis pit (Kushida et al., 2016).

Despite the small size, this mare exhibits characteristics that are noteworthy (Figure 4.4). The relatively large, compared to the diameter of Lacus Mortis, crater Bürg (40 km, 45.0°N 28.2°E) is a Copernican-aged crater that impacted just east of the center of the lacus. It has been identified as a radar dark halo crater with relatively few blocks in the ejecta (Ghent et al., 2005).

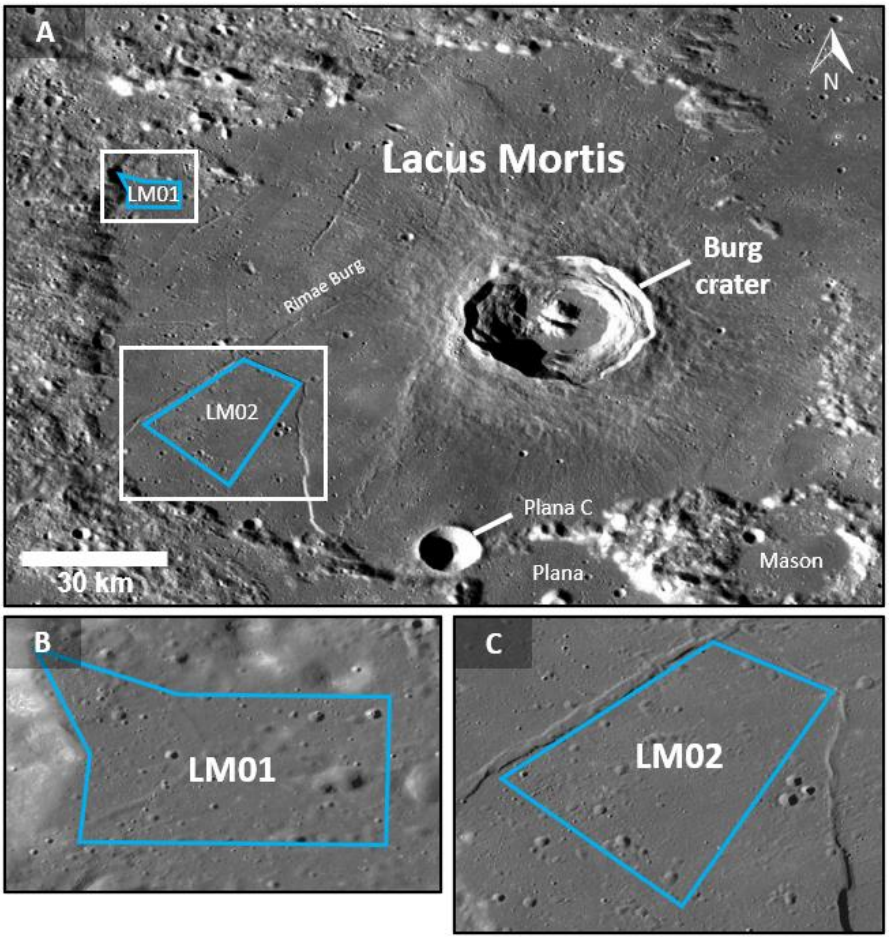

Figure 4.4. Lacus Mortis count areas are located in the western mare to avoid Burg ejecta. A) The smaller count area LM01 is located north of count area LM02. White boxes show the location of detailed cout areas in B and C. WAC Normalized Reflectance (Albedo) Map (643 nm) (Speyerer et al., 2011; cylindrical projection). B) Count area LM01 in the northwest corner of Lacus Mortis. Secondary craters are found in the eastern portion of the count area, despite the distance from Burg crater. C) Count area LM02, located in southwest Lacus Mortis, is bounded by rimae on two sides. Figures B and C use Kaguya morning TC imagery (Haruyama et al., 2008b).

4.2.0 Data and Methods

This investigation used imagery from several instruments on two lunar orbiting spacecraft (Kaguya, LRO), surface photos acquired during two Apollo landings (11, 16), standard tools for

handling crater count data (CraterTools, Craterstats2), and innovative approaches for examining the data.

4.2.1 Spacecraft Imagery

This investigation used Lunar Reconnaissance Orbiter Camera (LROC) Narrow Angle Camera (NAC) and Wide-Angle Camera (WAC) images (Robinson et al., 2010). The WAC imaged the Moon at seven band passes (Table 4.2). A single-band (643 nm) WAC mosaic at 100 m/pixel served as the base map and context for this investigation. The WAC subset image for each study area was cropped from the global WAC morphological mosaic, which was constructed from more than 15,000 individual map-projected images acquired between 2009 and 2011 (Speyerer et al., 2011) with improved geometric accuracy and photometric correction in July 2013. This mosaic, available through the Planetary Data System (PDS), was acquired over a narrow solar incidence range (55-80°) in order to accentuate morphology. Additional single-band WAC imagery with very low-Sun angles (high incidence) at 100 m/pixel, was used to identify subtle topography and degraded crater morphology. WAC imagery with high-Sun angles (solar incidence <40°) emphasizing albedo differences, together with NAC imagery, was used to locate fresh craters. The high-sun imagery highlights the light albedo ejecta of fresh craters against the mature, darker regolith background.

Table 4.2: Instrument Band Passes: LROC/WAC, Clementine, Kaguya/MI.

LROC/WAC			Clementine			Kaguya/MI		
Band (nm)	FWHM (nm)	Resolution (m/px)	Band (nm)	FWHM (nm)	Resolution (m/px)	Band (nm)	FWHM (nm)	Resolution (m/px)
320	32	384	415	40	100	415	20	20
360	15	384	750	10	100	750	10	20
415	36	100	900	30	100	900	20	20
565	20	100	950	30	100	950	30	20
605	20	100	1000	30	100	1000	40	20
645	23	100				1000	30	62
690	39	100				1050	30	62
						1250	30	62
						1550	50	62

The LROC NAC acquires two adjacent frames simultaneously covering an area 5 km wide by up to 26 km long. During the initial nominal orbital altitude of 50 km, the image pixel scale is 0.5

m (Robinson et al., 2010). LRO has undergone a number of orbital adjustments since December 2011 with a periapsis as low as 40 km and an apoapsis as high as 185 km. Hence, the resulting NAC pixel widths range from 0.3 m to 2.2 m. When available for our study areas, the higher resolution NAC images were selected to provide fine details of the smallest geologic features (Speyerer et al., 2016); resolution <5 m is useful for identifying the boulders, impact melt, and the rimcrest of impact craters. The various sun angles described for WAC imagery also applies to NAC imagery, except at much higher resolution. Additionally, sun angles from opposing directions (east, west) are used to verify crater shape and reveal details in shadowed areas.

Image data from the Japanese lunar orbiter spacecraft SELENE (Selenological and Engineering Explorer; also known as "Kaguya") Terrain Camera (TC) (Haruyama et al., 2008a; 2008b) was used for identifying impact craters for crater counts and measuring crater diameters. Imagery resolution for the TC is 7.4 m/pixel (Okumura et al., 2009), which is lower than the LROC WAC camera. The TC camera imagery is available as either of two global mosaics (morning or evening sun) and each have consistent photometric properties (incidence angle >60°, Haruyama et al., 2008b). Our count areas were extracted from the morning global mosaic.

The SELENE 30 m/pixel Multi-band Imager (MI) (Ohtake et al., 2008) visible and near-infrared multispectral camera was used for performing geochemical analyses (Figure 4.5 – 4.7). Lemelin et al. (2015) produced a conversion for the 750 and 950 nm bands (Table 4.2) to match the Clementine ultraviolet-visible (UV-VIS) data allowing for the algorithm developed by Lucey et al. (2000a,b) to be used on Kaguya data. This allowed us to derive the optical maturity parameter (OMAT) (Lemelin et al., 2019) and FeO composition. In addition, following the steps in Lemelin et al. (2015), we converted the Kaguya MI 415 nm band to match Clementine UVVIS data and used Lucey et al. (2000a) to also calculate weight percent TiO_2 (see supplementary materials). The standard deviations for the fit are ±0.43 wt.% for titanium content and ±0.81 wt.% for iron content (Otake et al., 2012). For each study area, maximum FeO and TiO_2 values were determined by averaging 30 m/pixels over a 0.25 km^2 area. LROC WAC UV-VIS derived TiO_2 abundances (Sato et al., 2017) at 400 m/pixel were also used in this study as an independent check on the TiO_2 abundances derived with the SELENE MI imagery (Ohtake et al., 2008).

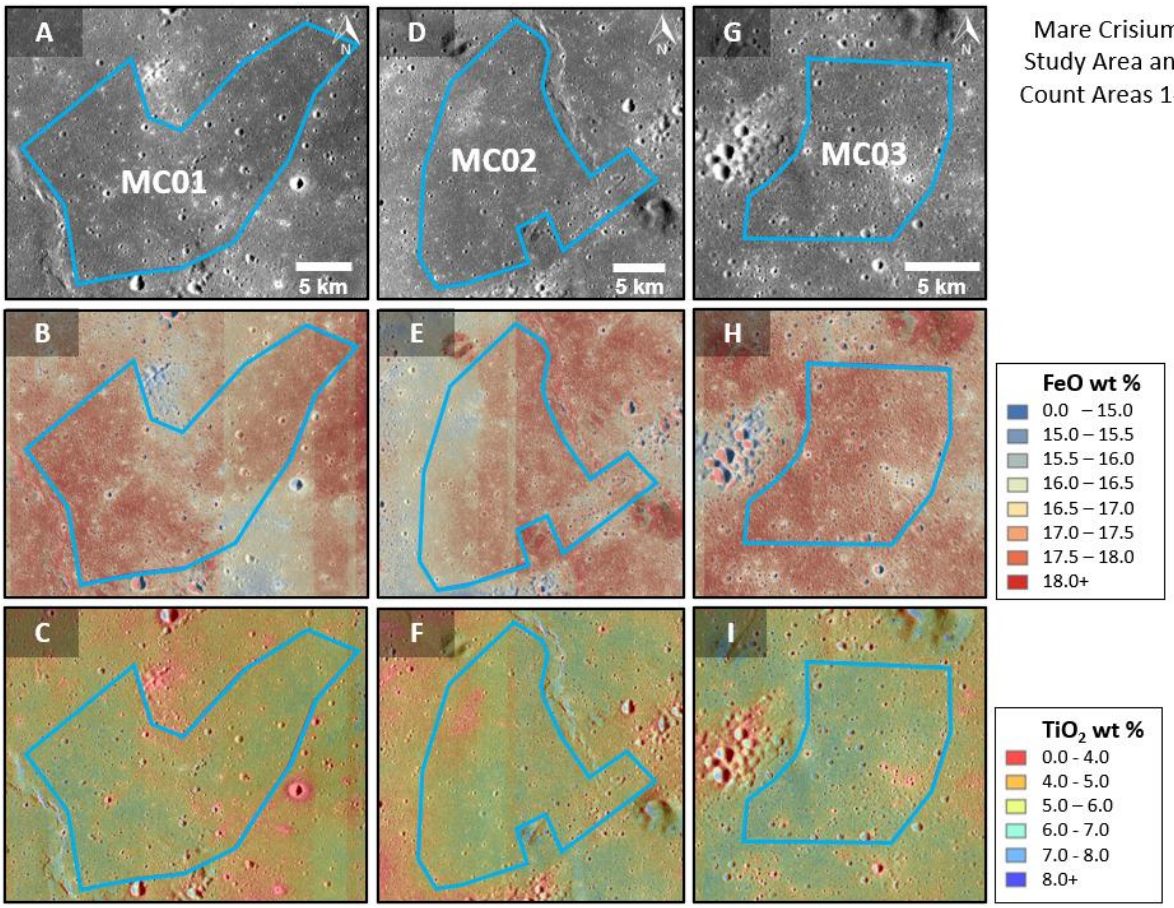

Figure 4.5. Mare Crisium count areas are located northwest of the center of the basin. A) The count areas are distributed to the north, west and south of Mons Latreille. Location of detailed cout areas in B (white box). WAC Normalized Reflectance (Albedo) Map (643 nm) (Speyerer et al., 2011; cylindrical projection). B) Count area Distribution of count areas including locations of Mons Latreille and to unnamed cones. C) Count area #01, north of Mons Latreille, mapped to exclude secondary crater clusters to the north and south, and a wrinkle ridge to the west. D) Count area #02 west of Mons Latreille, mapped to exclude secondary craters to the south, the unnamed north and south cones, and the east wrinkle ridge. E) Count area #03 south of Mons Latreille, mapped to exclude secondary craters on all other sides. Basemap imagery: Kaguya morning TC imagery (Haruyama et al., 2008b) with overlaid MI (Ohtake et al., 2008) FeO (Lemelin et al., 2019) or TiO_2 (Lemelin et al., 2015).

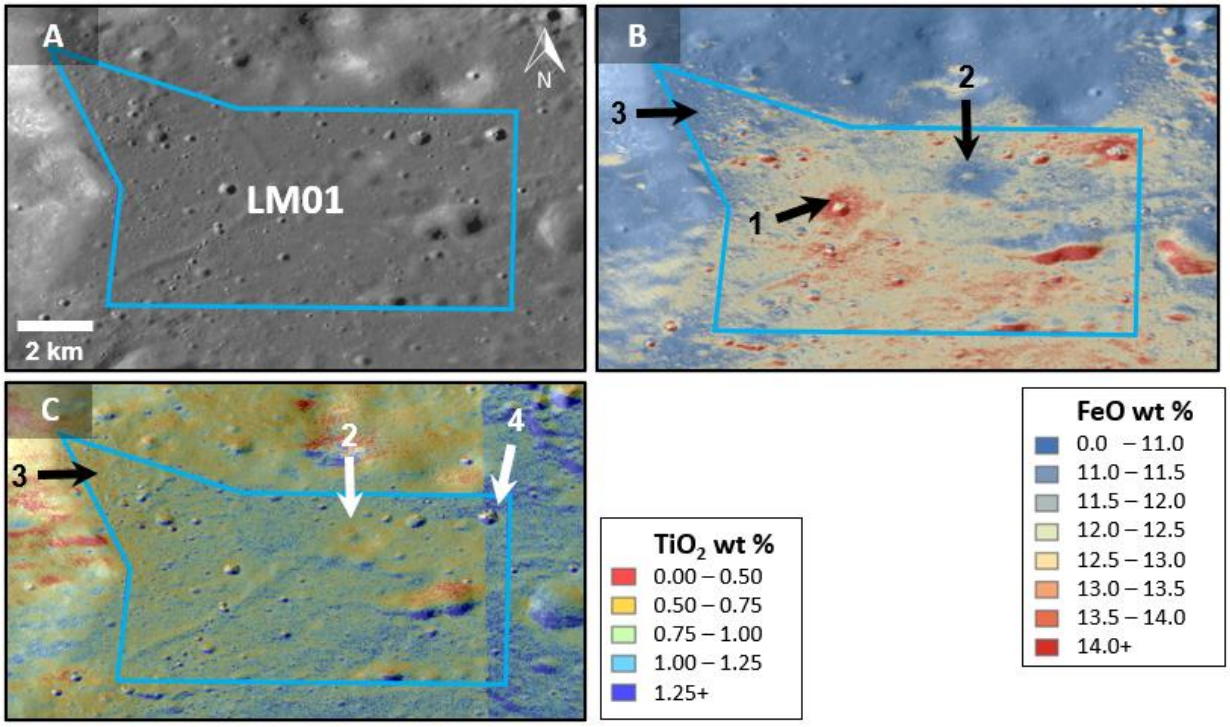

Figure 4.6. Geochemical maps for the Lacus Mortis count area LM01. A) Comparison albedo image. B) FeO concentration values for LM01. Maximum FeO located northwest of 700 m crater (arrow 1). FeO values vary slightly (< 1 wt %) from north to south, with the higher values in the southern portion (~13 wt . Lower than average FeO values (~11 wt %) are found at the lower elevation northwest corner (arrow 3) and the elevated terrain to the east (arrow 2). C) TiO_2 concentration values for LM01. Maximum TiO_2 located northeast of 900 m crater (arrow 4). Basemap imagery: Kaguya morning TC imagery (Haruyama et al., 2008b) with overlaid MI (Ohtake et al., 2008) FeO (Lemelin et al., 2019) or TiO_2 (Lemelin et al., 2015).

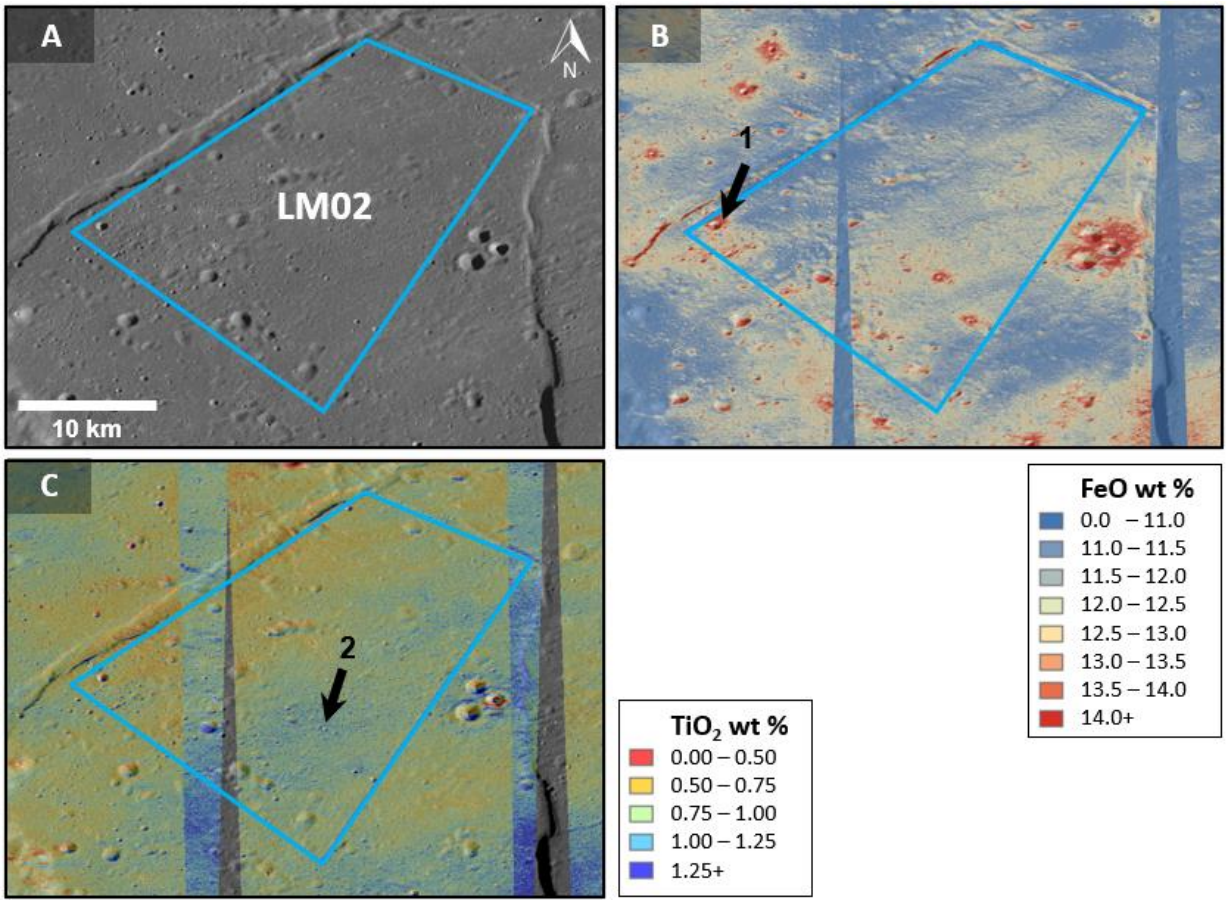

Figure 4.7. Geochemical maps for the Lacus Mortis count area LM02. A) Comparison albedo image. B) FeO concentration values for LM02. The distribution of FeO and TiO_2 exhibits lower values in the north of the area and higher values in the south. Maximum FeO located northeast of a 1.4 km diameter crater (arrow 1). C) TiO_2 concentration values for LM02. Maximum TiO_2 located north of a 700 m crater (arrow 2). Basemap imagery: Kaguya morning TC imagery (Haruyama et al., 2008b) with overlaid MI (Ohtake et al., 2008) FeO (Lemelin et al., 2019) or TiO_2 (Lemelin et al., 2015).

4.2.2 DTM Topography

General topographic data and morphology information were collected for features in the various regions using the global WAC 100 m/pixel topographic model, called the LROC GLD100 (Scholten et al., 2012). Moderate spatial resolution Digital Elevation Model (DEM) data, ~59 m/pixel at the equator, were obtained from the SLDEM2015 (Barker et al., 2016), which was constructed from geodetically-accurate topographic heights from the LRO Lunar Orbiter Laser Altimeter (LOLA) and co-registered stereo-derived DEMs from the Kaguya monochromatic Terrain Camera (TC) (Haruyama et al., 2008a; 2008b). Higher resolution DTM data were obtained for regional scales from the SLDEM2015 (Barker et al., 2016) and the Japanese Space Agency

(JAXA) SELENE “Kaguya” monochromatic Terrain Camera. This data set permits more precise elevation measurements to be made on small features. Kaguya DTMs were produced from geometrically rectified Level-2A data Terrain Camera (TC) images (Haruyama et al., 2008b). The DTMs were then map-projected and mosaicked (Isbell et al., 2014) to bring the data to MAP-form (similar to the PDS archives) and made available from the SELENE online archive (http://l2db.selene.darts.isas.jaxa.jp/, Okumura et al., 2009). The TC DTM has a pixel scale of ~7.4 m (4096 pixel/degree) and a predicted vertical error of 17 m (Haruyama et al., 2008a, 2014).

Very high spatial resolution NAC Digital Terrain Models (DTMs), <= 5 m/pixel, were created by the LROC Team at Arizona State University (Henriksen et al., 2017). These DTMs have partial areal coverage of our count areas and were used for crater diameter measurement confirmation for our study areas, similar to an approach used to measure larger scale craters (Fassett et al., 2012) (Figures 4.8, 4.9; Table 4.3):

1) Study area Reiner Gamma:

   A single NAC DTM was created for Reiner Gamma. This DTM was created from sixteen NAC stereo pairs, is 70 km tall and 60 km wide, and has a post spacing of 2.54 m. The reported precision error from SOCET SET (SOftCopy Exploitation Toolkit developed and published by BAE Systems) is 5.0 m based on a measure of the horizontal and vertical accuracy of LOLA points and the DTM. This large DTM partially covers count area RG04 and covers the majority of count areas RG01, RG02, and RG03 (Figure 4.9A-D).

2) Study area Mare Crisium:

   Two NAC DTMs were created for the Mare Crisium. The first DTM created (named "Horseshoe" by the LROC Team) was created from four NAC stereo pairs has a post spacing of 2.11 m and partially overlaps with count area MC01, MC02, and MC03 (Figure 4.9E, right half of image). The reported precision error from SOCET SET is 4.0 m based on a measure of the horizontal and vertical accuracy of LOLA points and the DTM). The second DTM created ("Horseshoe3") was created from two NAC stereo pairs and has a post spacing of 3.13 m. The reported precision error from SOCET SET is 5.0 m. The DTM overlaps with count area MC02 (Figure 4.9E, left half of image).

3) Study area Lacus Mortis:

   There were three NAC DTMs created for western Lacus Mortis that cover a portion of count area LM02 (Figure 4.9F). Each DTM was created from two NAC stereo pairs, which have post spacing ranging from 1.82 m to 3.46 m. The reported precision error from SOCET SET has a range of 3.0 – 5.0 m.

Additionally, these same NAC DTMs were used to generate aspect images to highlight slope direction (Figure 4.9). Aspect images are raster images, where each pixel has the degree value of the azimuth of the slope direction in degrees, ranging from 0 to 360. The aspect surfaces are color-coded based on compass direction and are assigned a different color for each of the four cardinal and four ordinal directions (e.g., north=red, northwest=pink, west=blue, etc.). Opposing slope faces are clearly visible in aspect imagery. These data are used to identify the rimcrests around selected craters.

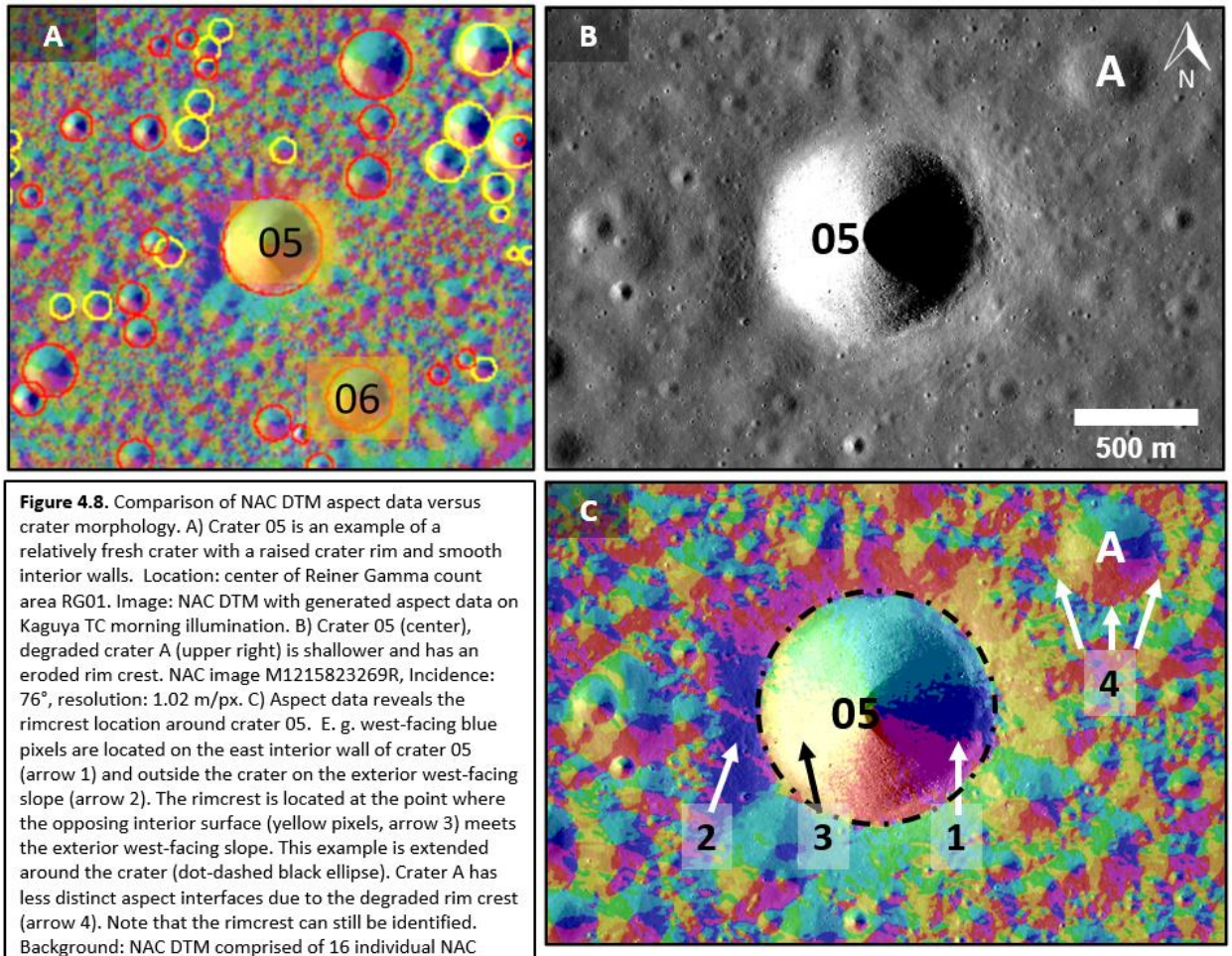

Figure 4.8. Comparison of NAC DTM aspect data versus crater morphology. A) Crater 05 is an example of a relatively fresh crater with a raised crater rim and smooth interior walls. Location: center of Reiner Gamma count area RG01. Image: NAC DTM with generated aspect data on Kaguya TC morning illumination. B) Crater 05 (center), degraded crater A (upper right) is shallower and has an eroded rim crest. NAC image M1215823269R, Incidence: 76°, resolution: 1.02 m/px. C) Aspect data reveals the rimcrest location around crater 05. E. g. west-facing blue pixels are located on the east interior wall of crater 05 (arrow 1) and outside the crater on the exterior west-facing slope (arrow 2). The rimcrest is located at the point where the opposing interior surface (yellow pixels, arrow 3) meets the exterior west-facing slope. This example is extended around the crater (dot-dashed black ellipse). Crater A has less distinct aspect interfaces due to the degraded rim crest (arrow 4). Note that the rimcrest can still be identified. Background: NAC DTM comprised of 16 individual NAC images, resolution 5.0 m/px used for Figure A and C.

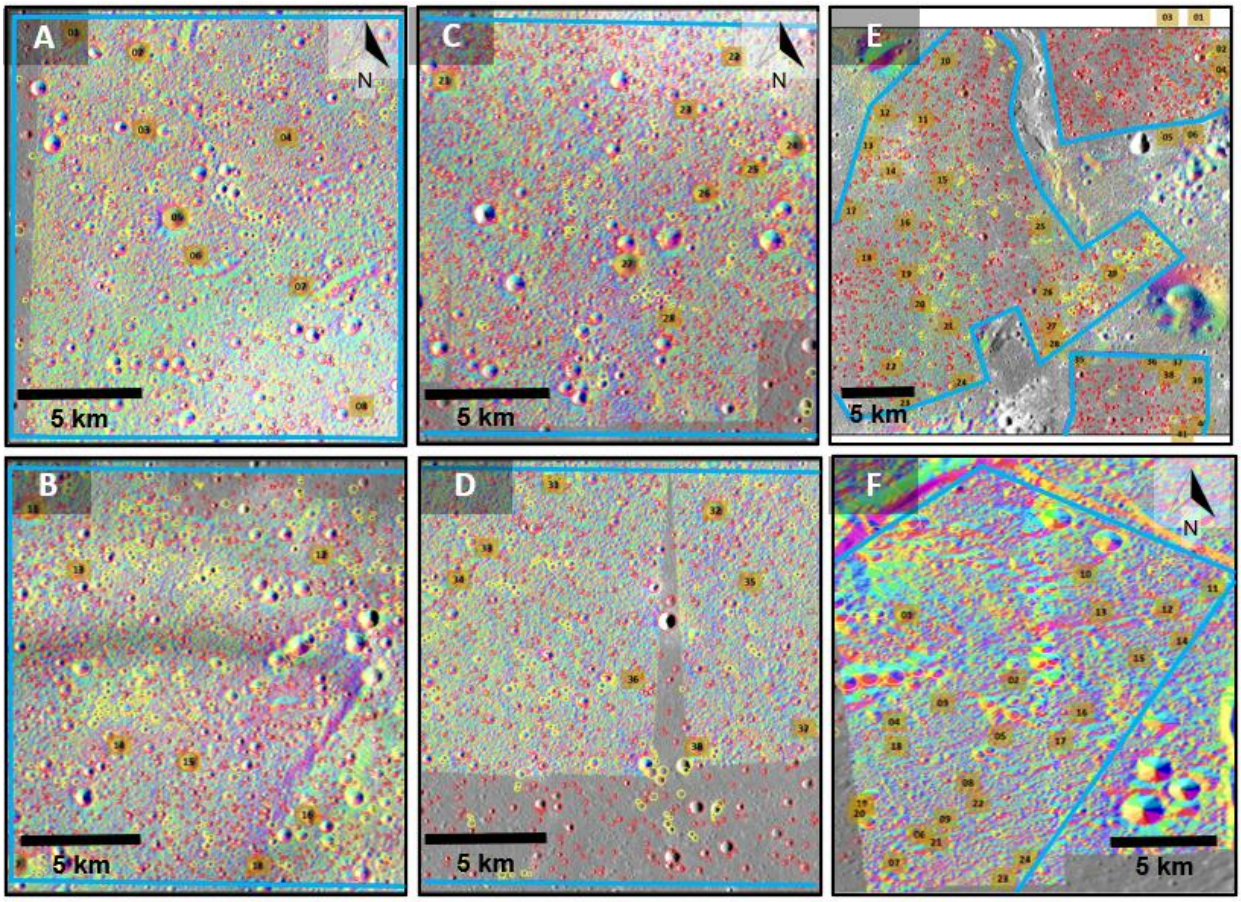

Figure 4.9. Location of NAC DTM aspect craters used for diameter measurements. See **Table 4.8** for diameter comparison. NAC DTM coverage varies with count area. A) Count area RG01. B) Count area RG02. C) Count area RG03. D) Count area RG04. E) Count areas MC01 (top), MC02 (left), MC03 (bottom right). F) Count area LM02. Background: see the Methods section for NAC DTM coverage for each study area, superposed on Kaguya morning TC imagery (Haruyama et al., 2008b).

Table 4.3. Study area NAC SOCET DTMs: Location, NAC images, and resolution.

Target Location	Creation Date	Center Location (lat/lon)	Product Name	NAC Images	Pixel Scale (m)	Post Spacing (m)
Lacus Mortis	2021-08-19	44°.91 N, 25°.53 E	LACUSMORT02	M1105737674, M1105759104	5.0	3.46
	2021-08-19	44°.86 N, 24°.97 E	LACUSMORT03	M1192879954, M1192901040	5.0	2.76
Mare Crisium	2021-01-28	18°.45 N, 61°.73 E	Crisium Horseshoe mosaic	M1356089436, M1356103508, M152472241, M152479025	4.0	2.11

	2021-07-27	18°.51 N, 61°.27 E	Crisium Horseshoe (3)	M1378380928, M1378387965	5.0	3.13
Reiner Gamma	2020-01-09	7°.48 N, 58°.65 W	Reiner Gamma Mosaic (v2)	M129669325, M129676110 M135568741, M135575527 M145006433, M145013219 M102536848, M102551166 M1142816646, M1142830869 M1152250376, M1152264615 M1167539972, M1167554189 M1167547085, M1167561301	5.0[1]	2.54

[1]Mosaic is 5 m/px: created from 8 DTMs of 2 and 5 m/px.

4.2.3 Defining Count Areas

Our crater count approach takes into account issues cited by multiple researchers (Ostrach et al., 2011; Xiao and Strom, 2012; van der Bogert et al., 2017; Robbins et al., 2018). High-resolution imagery (Robinson et al., 2010; Haruyama et al., 2008b; Ohtake et al., 2008) used in this study allowed relatively smaller areas than those used by previous workers to be counted (Stadermann et al., 2018; Hon and Stopar, 2020). Smaller count areas (this study: 85 – 605 km^2) provide a more detailed characterization of the basalts ages in each study area. Very small count areas (<10 km^2) were avoided as AMA accuracy decreases for smaller count areas (van der Bogert et al., 2015) and the likelihood of identifying secondary craters as primary craters increases (Xiao and Strom, 2012).

Determining accurate AMAs for these CLPS missions landing sites requires having count areas that are near to or ideally include each landing site. Assuming that the landing site coordinates are established and do not change, the subsequent challenge was to identify mare surfaces that were uncomplicated and lend themselves to accurate counts. Ideally, the count area should encompass basalt flows of a single age, be devoid of structural features that disrupt the mare surface (e.g., rilles, wrinkle ridges, and pyroclastic deposits), have minimal secondary craters, and resurfacing by crater ejecta deposits (e.g., cryptomare deposits). If secondary craters are present, they should be easy to recognize so that they are not counted.

Multiple count areas were defined in each study area. Count areas were distributed to capture both the age and geochemistry of individual locations within each study area (Figures 4.1 – 4.4). Count area boundaries were expressed as irregular polygons for Mare Crisium and Lacus Mortis;

square count areas were used for Reiner Gamma. The areas were irregular for several reasons: (1) to maximize the crater counting statistics, (2) to minimize the inclusion of secondary impact crater chains identified by their morphology, and (3) to delineate zones of uniform FeO and TiO_2 composition and maturity based on OMAT. As discussed in Giguere et al. (2022), mare surfaces with reduced FeO and TiO_2 values, and relatively higher OMAT values (i.e., less mature) may indicate the presence of secondary craters (Figure 4.5 – 4.7).

The uniform count area shapes for Reiner Gamma were positioned to capture crater counts on the light and dark albedo portions with one count area (RG03) positioned off of the albedo feature to the southeast. Count areas RG01, RG03, and RG04 were placed to avoid secondary impact crater chains, however, count area RG02 was located to include the CLPS Vertex mission planned for a 2025 landing (Blewett et al., 2021b), and includes known secondary crater chains. A control area P12 was included as a comparison count area. The size and location of this count area was determined by Hiesinger et al. (2011a).

4.2.4 Standardized Study Area Projects

We established crater count standardized projects to determine accurate and precise AMAs. This set of standard tools, data, and count areas has eliminated many of the factors that make comparing AMA results between researchers difficult and provides an environment to understand the differences between researcher crater count techniques.

Individual ArcMap projects were established for each study area and all projects were distributed to co-author researchers for counting. We have anonymized the researchers (A, B) performing crater counts to maintain focus on the counts rather than the individuals. Each project contains imagery (SELENE TC-morning/evening, LRO/LROC NAC and NAC DTM) displayed in a simple cylindrical Moon coordinate system with the Plate Carrée projection, which is an equidistant cylindrical projection. Crater diameter measurements can be affected by the map projection (Fassett, 2016). The geographic information system (GIS) software used in this study captures digitized impact craters (location, diameter) and measures the diameter without distortion (Kneissl et al., 2011).

Vector count area boundaries (i.e., AREA_”studyarea”) were included to ensure consistency; the area of each boundary was recorded (Table 4.4 – 4.7). The vector crater layer (CRATER_”studyarea”) was defined and left unpopulated. Researchers used this layer to identify and measure the diameter of primary craters (“standard”) and measure approximate diameters for

secondary craters ("marked"). Diameter measurements for secondary craters are approximate due to their irregular shape.

These standardized projects ensured that each researcher performed counts with identical products and in identical locations under the same illumination conditions. Crater counts were conducted using the ArcMap CraterTools add-in for map-projection-independent crater size-frequency measurements (Kneissl et al., 2011).

Table 4.4: Absolute model ages for study areas: Reiner Gamma.

Reiner Gamma						
Count Area	**Area** (sq km)	**Researcher**	**# Count Craters**	**Diameter range** (m)	**AMA** (Ga)	**N(1) km²**
RG01 8°.04 N, 59°.38 W	268.00	A	128	350 - 1100	3.67 +0.018/-0.02	9.10×10^{-3}
	272.57	B	131	300 - 2000	3.59 +0.021/-0.025	6.38×10^{-3}
RG02 7°.58 N, 58°.78 W	251.00	A	83	450 - 1100	3.78 +0.018/-0.021	1.63×10^{-3}
	282.88	B	158	250 -1000	3.47 +0.028/-0.034	4.47×10^{-3}
RG03 6°.61 N, 59°.06 W	260.00	A	196	300 - 1300	3.68 +0.014/-0.016	9.40×10^{-3}
	276.63	B	579	200 - 1200	3.62 +0.010/-0.010	7.42×10^{-3}
RG04 6°.82 N, 58°.06 W	277.55	A	153	300 - 900	3.55 +0.022/-0.026	5.57×10^{-3}
	277.55	B	302	200 - 900	3.29 +0.041/-0.054	3.20×10^{-3}

Table 4.5: Absolute model ages for study areas: Mare Crisium.

Mare Crisium						
Count Area	**Area** (sq km)	**Researcher**	**# Count Craters**	**Diameter range** (m)	**AMA** (Ga)	**N(1) km²**
MC01 19°.17 N, 61°.97 E	340.00	A	119	350 - 1000	3.57 +0.023/-0.027	6.00×10^{-3}
	364.80	B	553	200 - 900	3.52 +0.013/-0.014	5.06×10^{-3}
MC02 18°.62 N, 61°.37 E	307.00	A	167	300 – 800	3.56 +0.02/-0.024	5.81×10^{-3}
	361.69	B	97	300 – 700	3.24 +0.083/-0.14	3.01×10^{-3}
MC03 18°.10 N, 61°.75 E	115.00	A	77	300 - 800	3.63 +0.024/-0.029	7.69×10^{-3}
	124.46	B	84	300 - 750	3.43 +0.042/-0.058	3.66×10^{-3}

Table 4.6: Absolute model ages for study areas: Lacus Mortis.

Lacus Mortis

Count Area	Area (sq km)	Researcher	# Count Craters	Diameter range (m)	AMA (Ga)	N(1) km^2
LM01 46°.31 N, 24°.22 E	-	A[1]	-	-	-	-
	84.87	B	53	250 - 1000	3.49 +0.043/-0.059	4.66 x 10^{-3}
LM02 44°.15 N, 24°.97 E	88.27	A	26	450 - 800	3.73 +0.033/-0.043	1.25x10^{-2}
	604.74	B[2]	77	350 - 700	3.26 +0.082/-0.14	3.07x10^{-3}
			6	800 – 1500	3.56 +0.08/-0.18	5.89x10^{-3}

[1]Researcher A was unable to determine an AMA for LM01, citing secondary crater contamination.
[2]Researcher B identified two AMAs for LM02.

Table 4.7: Absolute model ages for study areas: P12 (Hiesinger et al., 2011).

P12, Mare count area (Hiesinger et al., 2011)						
Count Area	**Area** (sq km)	**Researcher**	**# Count Craters**	**Diameter range** (m)	**AMA** (Ga)	**N(1) km^2**
P12 4°.53 N, 59°.51 W	1936.2	A	27	700 - 2000	3.44 +0.067/-0.120	4.12 x 10^{-3}
	1936.2	B	55	600 - 2300	3.51 +0.040/-0.054	4.89 x 10^{-3}

4.2.5 Primary Craters and Rimcrest Diameter Measurements

We used a wide range (e.g. 40 – 80°) of illumination incidence angles (Ostrach et al., 2011; Richardson et al., 2021) to identify craters. Using LROC NAC imagery at various incidence angles as a supplement to the Kaguya TC imagery ensures that all craters in a given size range are identified and counted. Questionable craters viewed via the TC imagery were verified in the NAC imagery.

Measurements were performed with either 2-point or 3-point ellipses. Craters were considered to be in the count area if the center point of the ellipse was located within the count area; craters with the center point outside of the count area but that overlapped the count area were not counted. All measured craters within each count area had diameters higher than the minimum conservative pixel threshold diameter, Dmin; the threshold at which crater population can be completely included in the count (diameter > 10 base image pixels) (Wang et al., 2020).

4.2.6 Accounting for Secondary Craters

Researchers removed obvious secondary craters using the Kaguya TC and LROC WAC/NAC images based on methods established by Shoemaker, 1962; Oberbeck and Morrison, 1974; Oberbeck, 1975; Pike and Wilhelms, 1978; McEwen and Bierhaus, 2006; Robbins and Hynek,

2011. The criteria include: crater morphology, occur within a crater cluster or as part of a larger crater's ejecta, and a shallow depth/diameter ratio. The exclusion of secondary craters was done to avoid contamination of the crater counts. Some count areas have a higher number of secondary craters that must be identified (e.g., Reiner Gamma count area RG02, **§4.3.1.1 Reiner Gamma**).

Two basic approaches were employed for secondary crater removal: 1) exclusion areas were defined and all craters within the area were not counted and the area was subtracted from the overall count area; and, 2) individual craters were identified as secondary based on the above criteria and were excluded. Approach 1) not only involved exclusion areas interior to the count boundary, but also involved a trim of the count boundary to avoid secondary craters. Both the "trim" and "exclude" approach reduce the size (km^2) of the count area and were most useful for discrete clusters of secondary craters that were either well inside or near the count boundary. In the second approach, each secondary crater is mapped and measured, but the count area or boundary are not modified. This approach proved useful in several scenarios: e.g., for sparse background secondary craters, for marking the secondary craters of small chains of craters, which avoided the need to establish an excluded area, and when a count area was established that avoided obvious secondary chains, then upon closer examination, one or two craters were identified from an external secondary chain that extended into the count area. An additional case occurs when a primary crater, identified by the depth/diameter ratio (d/D) or morphology, is co-located with a secondary chain (Jia et al., 2020). In some instances, both approaches were used on a count area.

All primary craters were counted within each count area to achieve the completeness diameter, the smallest crater diameter for which all craters of that size and larger are fully counted (Chapman, 2015; Robbins et al., 2018; Singer et al., 2020; Jia et al., 2022). A crater diameter size range that is not fully counted falls short of the Production Function (PF) and cannot be used to determine the AMA. Our typical completeness crater diameter measure is ~300 m; some count areas had completeness crater diameters as low as 200 m. The count areas range in area from 84.9 km^2 to 604.7 km^2.

Nevertheless, key decisions remain as the researcher must evaluate craters and categorize them as primary or secondary. The researcher may then elect to isolate the secondary craters, reducing the size of the count area, or maintain the current count area and measure only the primary craters. AMAs determined from a reduced count area are denoted by the term "subset area". How a researcher decides to deal with primary and secondary craters affect the AMA (Robbins et al.,

2014; Giguere et al., 2022). Characterization of the secondary crater population is provided for each study area (Figure 4.10 – 4.13).

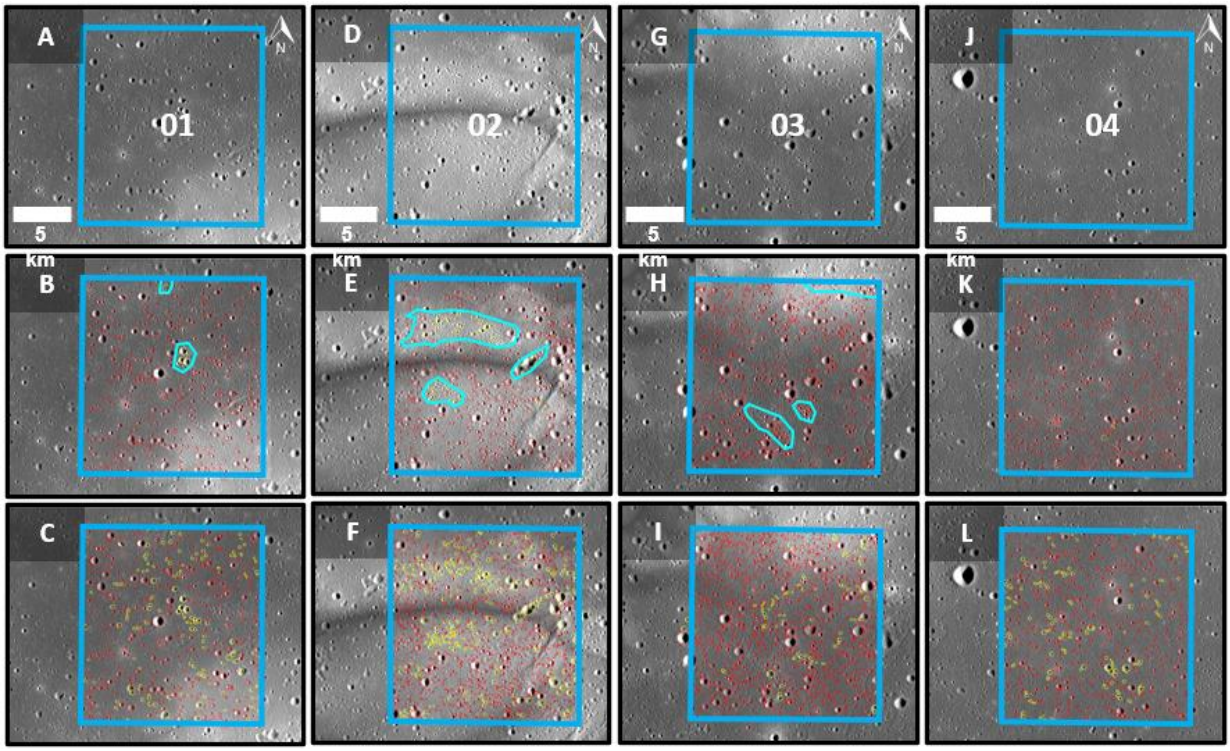

Figure 4.10. Crater count comparison for the Reiner Gamma study area, including count areas: RG01, RG02, RG03, and RG04. Researchers performed counts and indicated primary craters (red) and secondary craters (yellow). Researchers indicate all primary craters and some or all identified secondary craters. Primary craters, not secondary craters, are used to generate the CSFD. A) Count area RG01, B, C) crater type and location for researchers A, B, respectively. D) Count area RG02, E, F) crater type and location for researchers A, B, respectively.G) Count area RG03, H, I) crater type and location for researchers A, B, respectively. J) Count area RG04, K, L) crater type and location for researchers A, B, respectively. All background images are Kaguya morning TC imagery (Haruyama et al., 2008b).

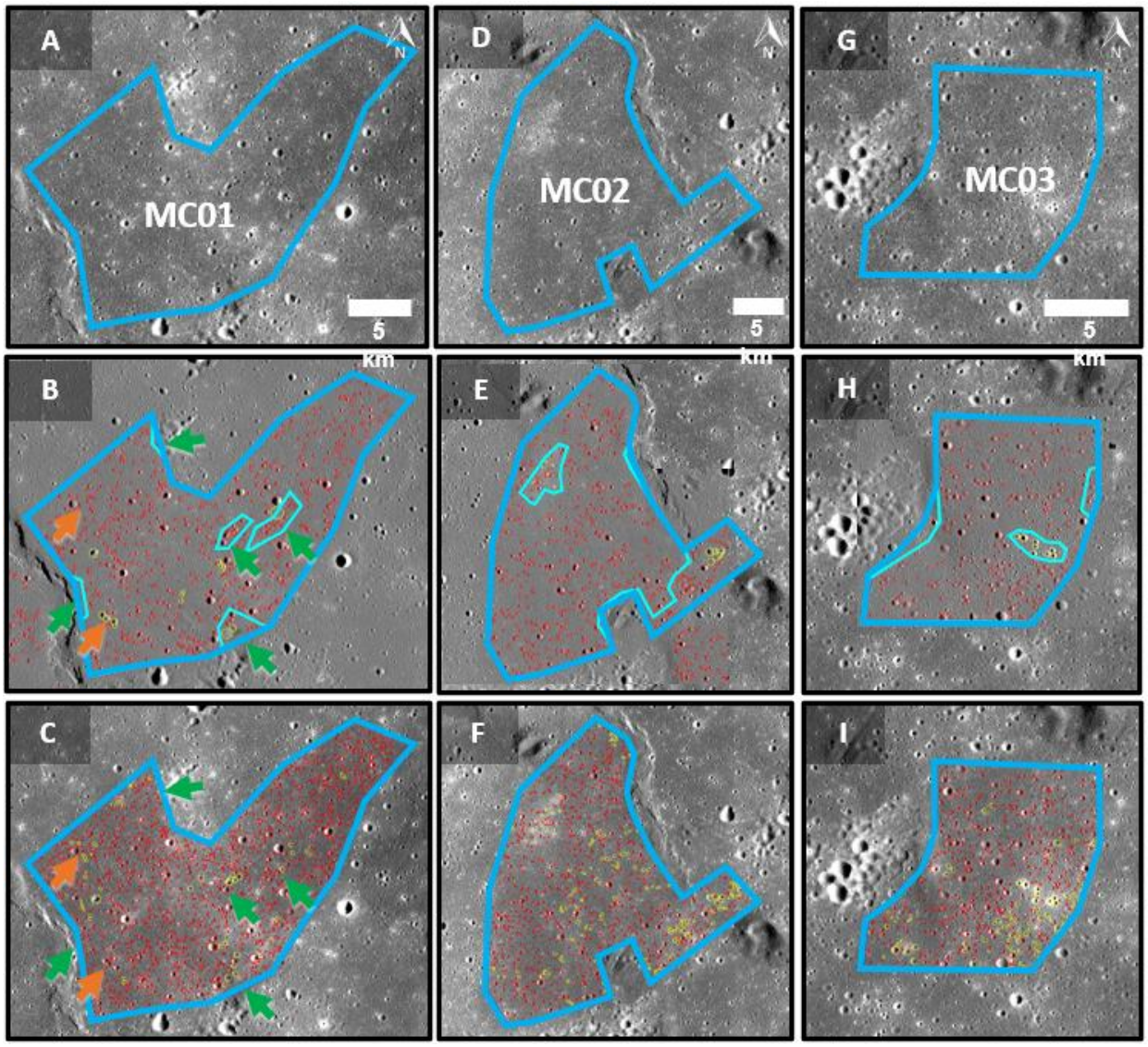

Figure 4.11. Crater count comparison for the Mare Crisium study area, including count areas: MC01, MC02, and MC03. Researchers performed counts and indicated primary craters (red) and secondary craters (yellow). Researchers indicate all primary craters and some or all identified secondary craters. A) Count area MC01, B, C) crater type and location for researchers A, B, respectively. Some secondaries were identified by multiple researchers (green arrows), and other secondaries were identified by one researcher (orange arrows). D) Count area MC02, E, F) crater type and location for researchers A, B, respectively. G) Count area MC03, H, I,) crater type and location for researchers A, B, respectively. All background images are Kaguya morning TC imagery (Haruyama et al., 2008b).

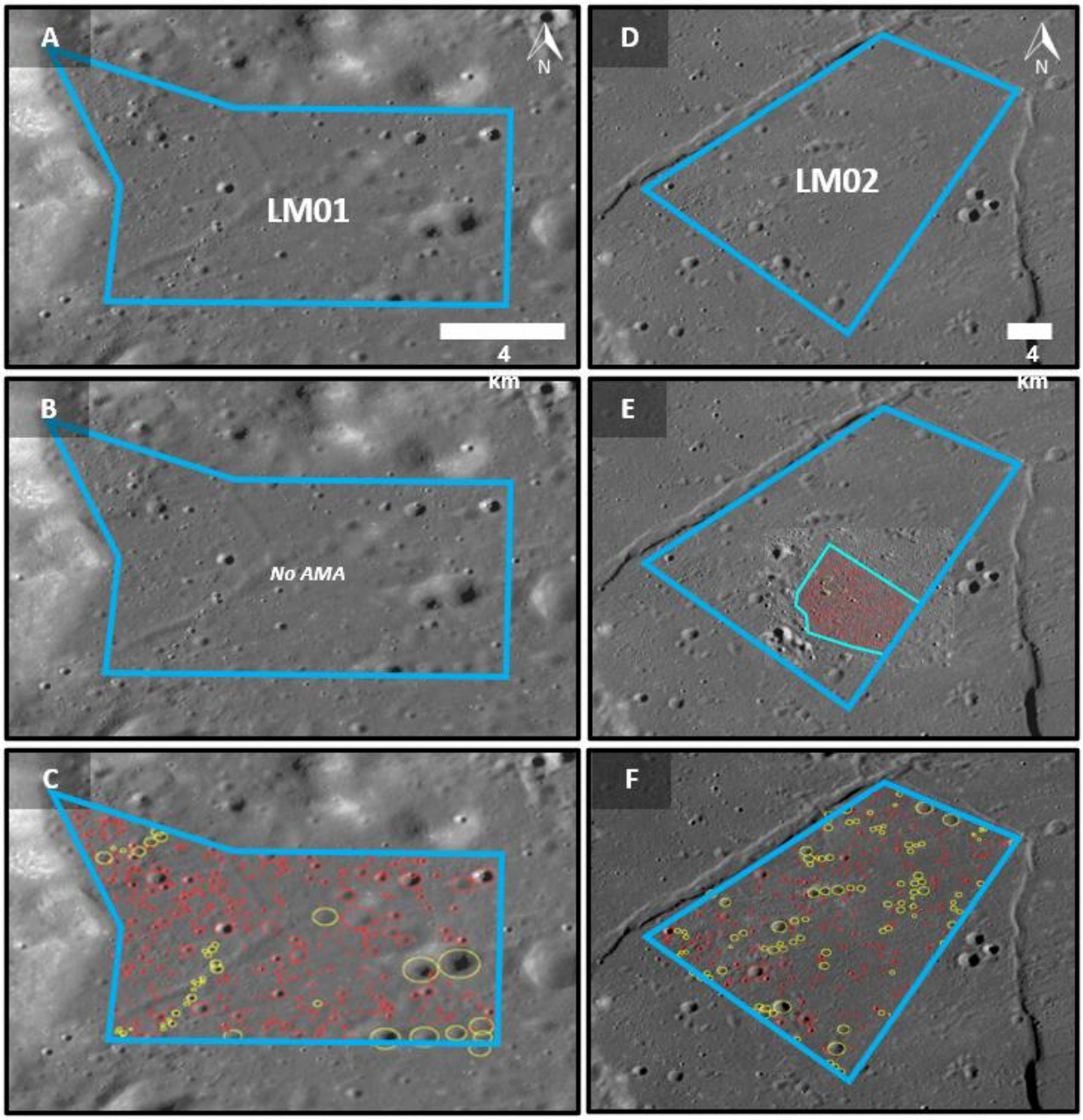

Figure 4.12. Crater count comparison for the Lacus Mortis study area, including count areas: LM01, LM02. Researchers performed counts and indicated primary craters (red) and secondary craters (yellow). Researchers indicate all primary craters and some or all identified secondary craters. Primary craters, not secondary craters, are used to generate the CSFD. A) Count area LM01, B) Researcher A, - no counts or AMA C) Researcher B crater type and locations. D) Count area LM02. E, F, crater type and location for researchers A and B, respectively. All background images are Kaguya morning TC imagery (Haruyama et al., 2008b).

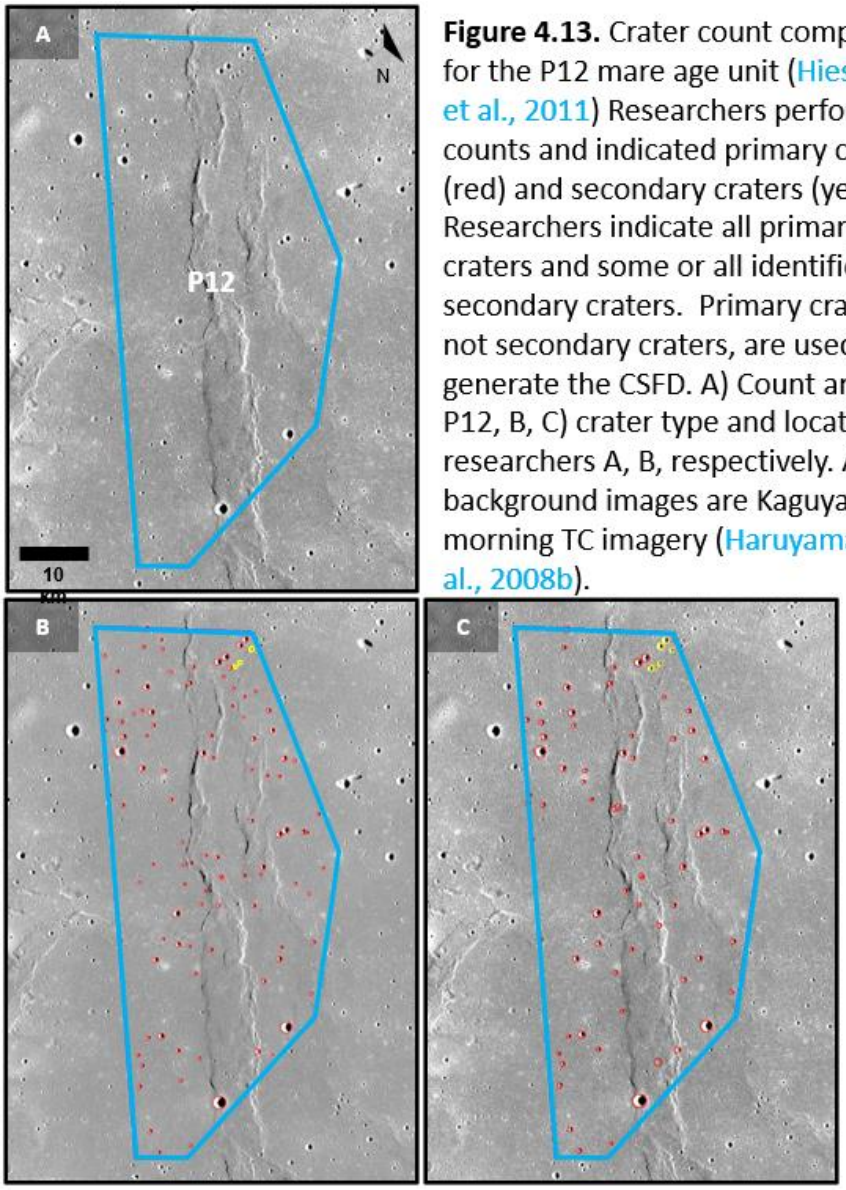

Figure 4.13. Crater count comparison for the P12 mare age unit (Hiesinger, et al., 2011) Researchers performed counts and indicated primary craters (red) and secondary craters (yellow). Researchers indicate all primary craters and some or all identified secondary craters. Primary craters, not secondary craters, are used to generate the CSFD. A) Count area P12, B, C) crater type and location for researchers A, B, respectively. All background images are Kaguya morning TC imagery (Haruyama et al., 2008b).

4.2.7 CSFD Curve Construction

CSFD curves were constructed from the crater count data collected for each of the count areas (Figures 4.10 – 4.13). Primary craters were used to generate the Crater size-frequency distribution (CSFD). Most secondary craters are marked by researchers, but are not used for CSFD generation. Despite not using secondary craters for CSFDs, the location of marked craters are useful for comparison between researchers.

Crater absolute model ages (AMA) were calculated based on the CSFD curve using the Craterstats2 program (Michael and Neukum, 2010) and rounded to two decimal places. The

statistical error was calculated for the craters in each diameter bin based on a Poisson distribution and is represented as error bars on the CSFD (Michael and Neukum, 2010). The lunar chronology function of Neukum et al. (2001) was used to estimate model ages from the CSFD curves. The model ages for the count areas and study areas, by researcher, are plotted in Figures 4.14 – 4.17 and given in Tables 4.4 – 4.7.

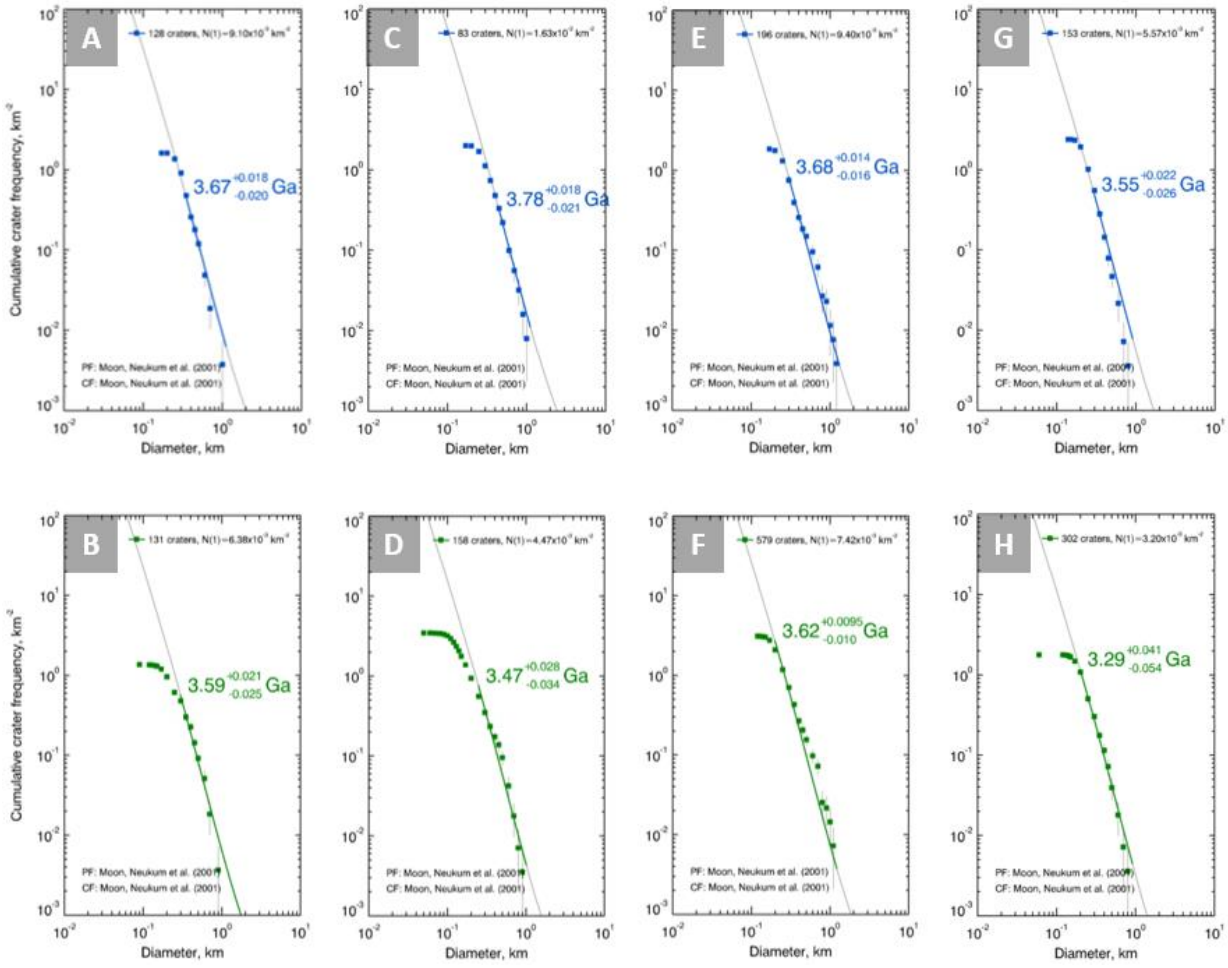

Figure 4.14. CSFDs for Reiner Gamma

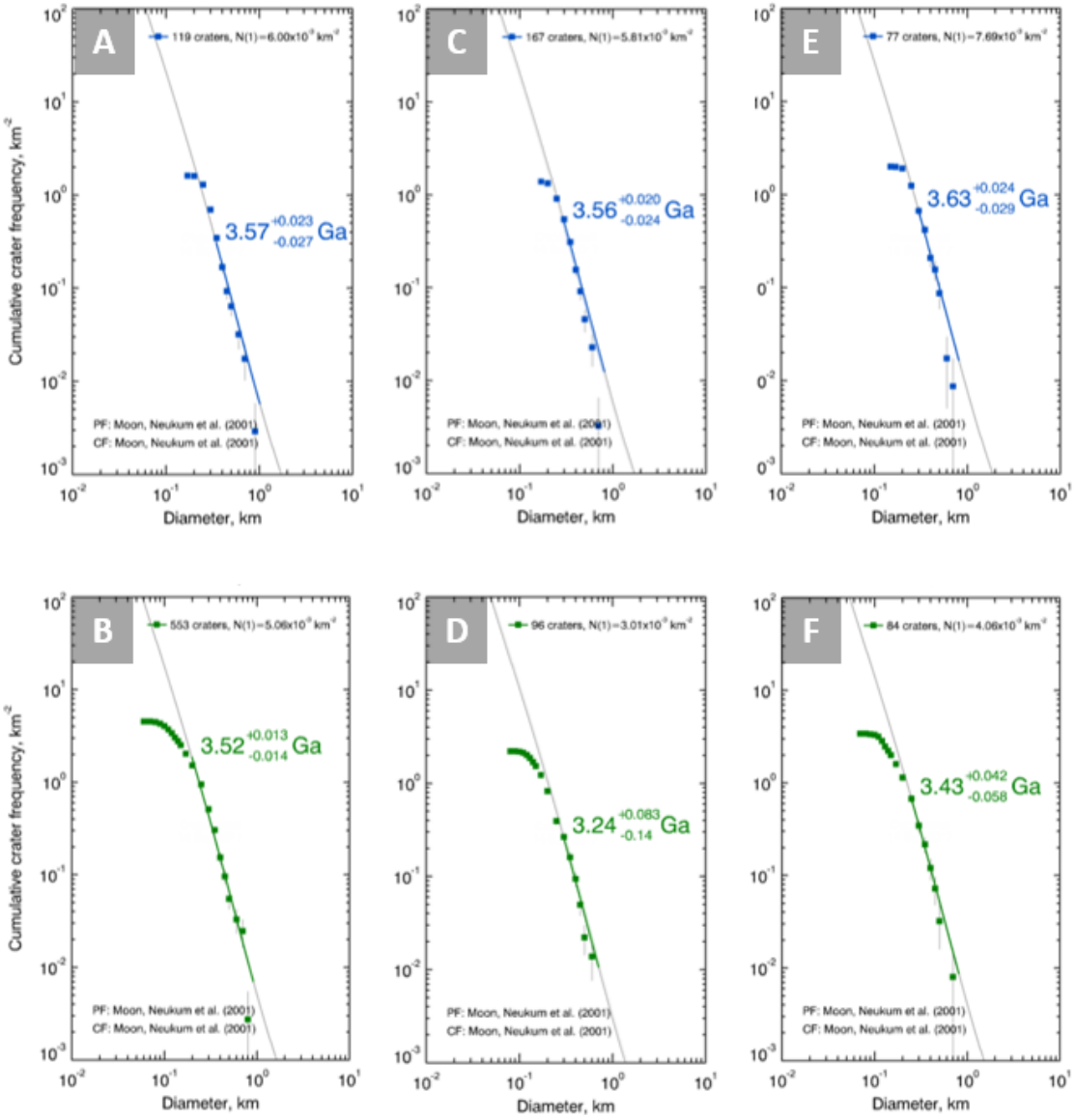

Figure 4.15. CSFDs for Mare Crisium

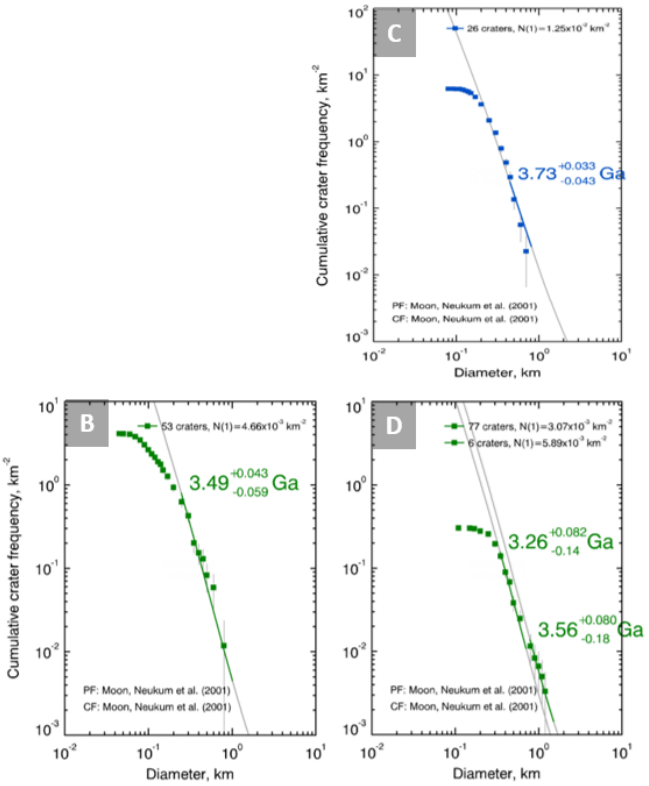

Figure 4.16. CSFDs for Lacus Mortis

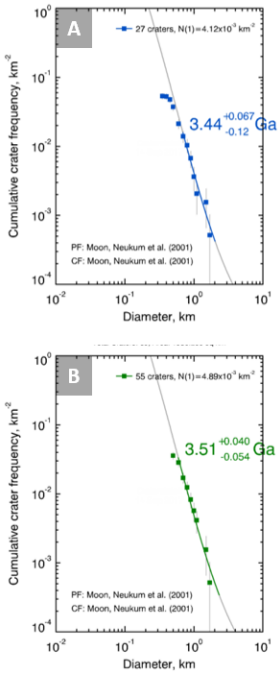

Figure 4.17. CSFDs for P12

4.3.0 Results

We investigated the ages of three landing sites involved in the Commercial Lunar Payload Services (CLPS) program and share our results for Reiner Gamma, Mare Crisium, and Lacus Mortis (Figure 4.1; Table 4.1).

4.3.1 Model ages for study areas

We present our estimated model age results (Tables 4.4 – 4.7) for each of the three study areas and one additional comparison area (area P12, Hiesinger et al., 2011a). The study areas consist of 2 – 4 individual count areas. Researchers identified and measured craters independently using standardized project datasets (e.g., identical imagery, map projection, and measurement software). In return, they have provided their results as CSFDs and supporting count data for comparison. The primary craters measured were used to produce CSFDs for the individual count areas (Figures 4.14 – 4.17). Determining the model age of the basalts at each landing site will provide context for CLPS experiments and serve to place them in age sequence with neighboring maria.

4.3.1.1 Reiner Gamma

The four count areas (Figure 4.2) include varying amounts of high-albedo mare. Count area RG01 is located northwest of the main portion of Reiner Gamma, encompasses mainly mare basalt and includes high-albedo mare in the southeast corner (Figure 4.2C). Count area RG02 encompasses the main portion of RG, including alternating light and dark albedo lanes. This area includes the Intuitive Machines Nova C landing site, carrying the Lunar Vertex payload, which consists of the joint lander and rover. The planned rover traverse is wholly within this count area (Figure 4.2D) (Blewett et al., 2023, see Figure 1). Count area RG03 is located south of the main portion of RG and includes high-albedo mare at the north end (Figure 4.2E). Count area RG04 is located to the east away from RG and is free of high-albedo mare (Figure 4.2F). Count areas (RG01-03) will provide ages for the actual Reiner Gamma feature. Area RG04 will serve as the control as the count. RG04 is adjacent to, but not part of the high albedo portion of Reiner Gamma Formation.

In contrast to Lacus Mortis, the Reiner Gamma study area has previously been age-dated in global studies (Hiesinger et al., 2011a, see Figure 17). Designated “P16”, this mare age unit (5033 km^2) was determined to be a distinctive basalt unit in high-resolution Clementine multispectral color ratio composite imagery. The count area (1108 km^2), encompasses the central portion of

Reiner Gamma, minus the northeast and south west extensions. The absolute model age determined for the count area is 3.33 +0.08/-0.05 Ga. All four of the count areas in this study are contained by or overlap with the mare age unit defined by Hiesinger et al. (2011a). Our count area RG01 has a small overlap with the P16 count area, RG02 is contained in the count area, RG03 partially overlaps with the P16 mare age unit, and RG04 is contained by the mare age unit (Figure 4.18).

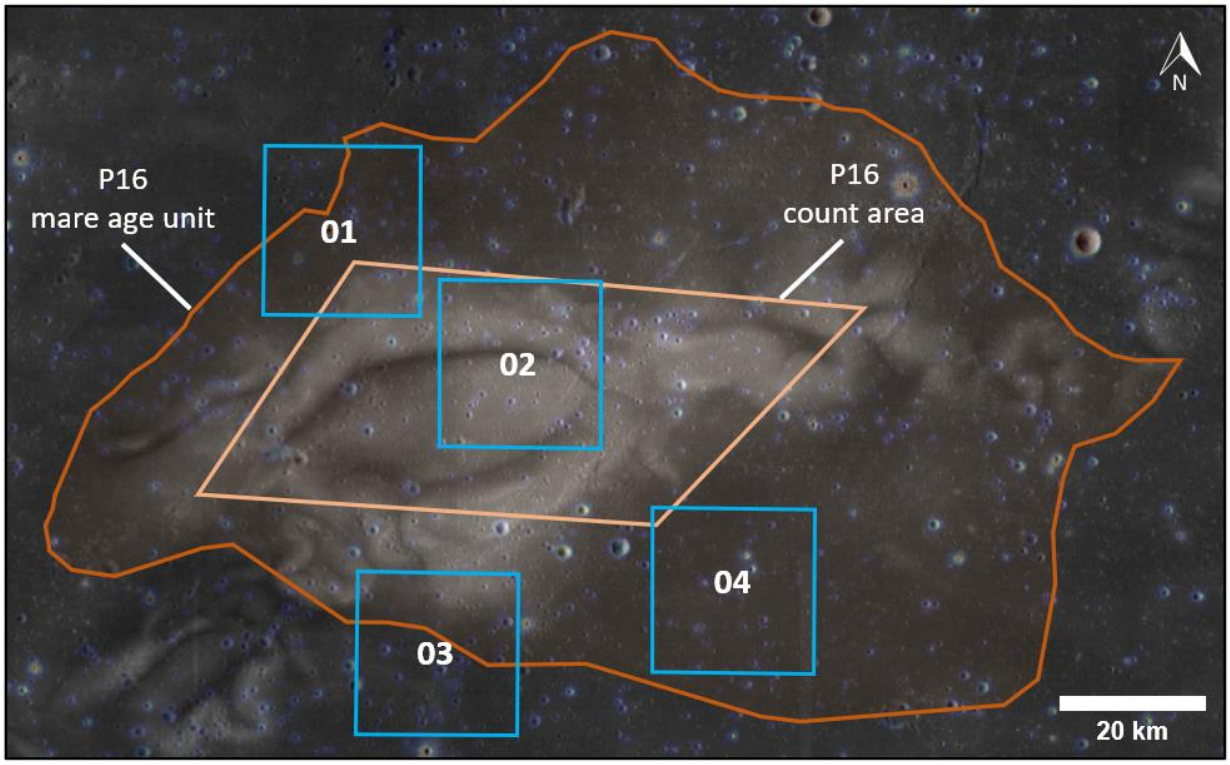

Figure 4.18. Reiner Gamma count area comparison. The four count areas in this study (blue boxes) are overlaid on the P16 count area (lt orange box) and P16 mare age unit (orange bounding polygon). All four of the count areas are contained by or overlap with the larger mare age unit defined by Hiesinger et al. (2011). Background: Diviner rock abundance map (Bandfield et al., 2011) over the WAC Normalized Reflectance (Albedo) Map (643 nm) (Speyerer et al., 2011; cylindrical projection).

Count area RG01 has a small number of disbursed background secondaries (< 500 m diameter), which are distributed in the count area without regard to the high-albedo mare in the southeast corner (Figure 4.10). Researcher A excluded a small area (~14 km^2) of secondaries near the center of this count area; researcher B did not exclude these same secondaries, but instead marked them as secondaries. AMAs for count area RG01 are in Table 4.4; Figure 4.14A, B.

Count area RG02, features contrasting bright and dark albedo terrain along with a wrinkle ridge in the southeast corner that traverses from the northeast to southwest. Large secondary craters

traverse from the east (<1000 m diam) to the west (<900 m diam). Researchers A and B identified several clusters of secondary craters (<300 m diam) located in this count area. Researcher A eliminated secondaries with three exclusion areas, decreasing the count area by ~32 km^2, whereas, researcher B marked secondaries for exclusion (Figure 4.10). AMAs for count area RG02 are in Table 4.4; Figure 4.14C, D.

Count area RG03 contains a small rille (~200 m width) in the southeast corner that traverses from northeast to southwest. Researcher B identified multiple large craters (~800 to 1200 m diam) as primary craters, which increases the surface age. This count area is the oldest of the four count areas. Clusters of small craters (<300 m diam) are located in the northeast, central, and south central areas, which were excluded by researcher A (Figure 4.10). AMAs for count area RG03 are in Table 4.4; Figure 4.14E, F.

Count area RG04 is least affected by the albedo anomaly, has few secondary crater chains (Figure 4.10), and is identified as the youngest of the four count areas by researchers A and B. AMAs for count area RG04 are in Table 4.4; Figure 4.14G, H.

4.3.1.2 Mare Crisium

We mapped three count areas in Mare Crisium, numbered MC01-MC03 from north to south, ranging in size from 124.45 – 364.82 sq km (Figure 4.3). The irregular count areas are positioned around Mons Latreille to the north, west, and south of the cone; secondary craters limit placing a count area to the east of the cone. Count area MC01, was located 12+ km north of Mons Latreille to avoid an obvious secondary cluster, extends northeast and northwest around another secondary cluster (Figure 4.3C). Count area MC02, includes the Firefly Aerospace (Task Order 19D) CLPS landing site approximately 1.5 km to the northwest of the edge of Mons Latreille. The eastern side of the area includes the southern end of a mapped wrinkle ridge (Thompson et al., 2017). The boundaries of this area are defined to exclude the three cones, as well as a large secondary crater complex to the south (Figure 4.3D). Count area MC03 provides mare age information to the south of Mons Latreille. The area was positioned to avoid a dense secondary crater cluster to the west (Figure 4.3E).

Count area MC01, the largest in area, has multiple minor secondary crater chains located in and around the count area (Figure 4.11A-C). Researcher A trimmed three sides of the count area and added two exclusion areas around secondary crater chains. Researcher B left the count area intact and marked secondary craters. As is standard practice, these secondaries are not included in

the CSFD inventory, thus do not affect the AMA. Determined AMAs for count area MC01 are in Table 4.5; Figure 4.15A, B.

Count area MC02 has more secondary craters than count area MC01 (Figure 4.11D-F). Two depressions of possible volcanic origin (< 500-800 m diam) were identified in the southeast corner, they were marked as secondary craters to avoid adding them to the count by researcher B. Additional secondaries identified include a cluster of small (< 500 m diam) craters on the southeast side and groups of smaller craters (~ 10 craters < 200 diam; majority < 50 m diam) in the north central region. Researcher A trimmed the east side of the count area to exclude these secondaries and added an excluded area around the north central secondaries. AMAs for count area MC02 are in Table 4.5; Figure 4.15C, D.

The smallest count area, MC03, exhibits secondary craters recognized by each researcher. Researcher A trimmed a portion of the west side to avoid a ridge and trimmed the east side to avoid secondaries. One excluded area was placed around a secondary crater chain on the southeast side. Researcher B marked secondaries in the southwest (< 400 m diam) and southeast (< 400 m diam) corners (Figure 4.11G-I). AMAs for count area MC03 are in Table 4.5; Figure 4.15E, F. Researcher A used the Kaguya "evening" imagery (sun from the west) to count each of the three count areas.

4.3.1.3 Lacus Mortis

To obtain representative absolute model ages of the mare, our two selected areas needed to avoid the major effects of the 40 km Bürg crater (Figure 4.4). Count areas were especially challenging to map as the continuous ejecta blanket of Bürg obscures at least 20% of the surrounding mare. Every effort was made to avoid the discontinuous ejecta blanket when defining each count area and during the crater selection process. The continuous ejecta blanket typically extends one crater radii from the crater rimcrest (Melosh, 1989), whereas the discontinous ejecta and associated secondary craters can extend well beyond the boundary of Lacus Mortis (Singer et al., 2020). Count area LM01 (Figure 4.4B) was placed in the northwest corner of the mare, as far from Bürg as possible (~85 km from the center of Bürg). The count area showed elevated levels of FeO, indicating that the mare was minimally disturbed by the low-FeO ejecta of Bürg. Count area LM02 (Figure 4.4C) was mapped in the southwest mare, roughly ~58 km from the center of crater Bürg. This area avoids the low-FeO region and rille to the northwest, a rille and secondary craters to the east, and the large rima (1-2 km wide) to the east. The former landing location of the CLPS mission lies outside of our two count areas, approximately ~15-20 km to the north of count

area LM02. Our count area selection precluded this particular part of the mare as having basalts that may be obscured by crater Bürg ejecta; thus, not representative of the typical Lacus Mortis mare and difficult to determine an accurate absolute model age.

We provide model ages for two areas within Lacus Mortis to refine our understanding of eruption ages in this area. Count area LM01 has several large secondaries (< 1.4 km diam) located in the SE corner and a small secondary chain in the NW and the SW corners, two rilles on the west side: trending central NE to SW and central NNW to SSE (Figure 4.12A-C). Independent counts performed by researchers yield the AMAs listed in Table 4.6; Figure 4.16B. Researcher A was unable to obtain a useful count in this count area, citing the large secondary craters.

Count area LM02, similar to area LM01, has secondaries up to 1.5 km in diameter and several chains of secondary crater of smaller diameters (Figure 4.12D-F). Researcher B produced a CSFD plot that exhibits a "knee" in the curve suggesting two ages for this area (Figure 4.16C, D). The knee in the CSFD curve of Area LM02, along with the subdued appearance of craters suggests that the small crater population (<600 m) is more sparsely distributed compared with the larger craters. We obtained AMAs as shown in Table 4.6; Figure 4.16C, D. Researcher A used a reduced count area to avoid the secondary crater clusters and a NAC mosaic composed of eight images to perform the counts.

4.3.1.4 Comparison count area P12

Count area P12 (3.42 Ga, Hiesinger et al., 2011a) is located in southwest Oceanus Procellarum at 4.53°N, 59.51°W (Figure 4.1). P12 was selected because it is a small area, relatively close to Reiner Gamma, and the AMA can be determined by measuring larger craters (>800 m) than the was done for the study area count areas. The count area is 1807 km^2 and is contained within the larger mare age unit, which is 5463 km^2. Each researcher determined AMAs for count area P12. Having AMAs for this standard area along with the AMAs for all study areas allowed us to identify age discrepancies and compare the results for our study areas to the global counts in the literature (Hiesinger et al., 2011a).

One challenge encountered with count area P12 was the presence of a large wrinkle ridge complex that traverses the count area from north to south (Figure 4.19B and C). The wrinkle ridge varies from 0.5 to 7 km in width and has several degraded impact craters on its surface. Researchers were aware of the potential for crater morphology degradation, nonetheless, were able to identify and measure craters on the wrinkle ridge.

Count area P12 was largely devoid of obvious secondary craters, with the exception of a small group in the northeast corner identified by all researchers (Figure 4.13A-C). Researchers identified craters in the AMA diameter range (600 m to 2000+ m) that were slightly degraded but remained measurable. AMAs for count area P12 are in Table 4.7; Figure 4.17A-B. Hiesinger et al. (2011a) determined an AMA of 3.42 +0.10/-0.07 Ga for P12. The AMAs for researcher A and B, although older than reported by (Hiesinger et al., 2011a) fall within a standard deviation of each other.

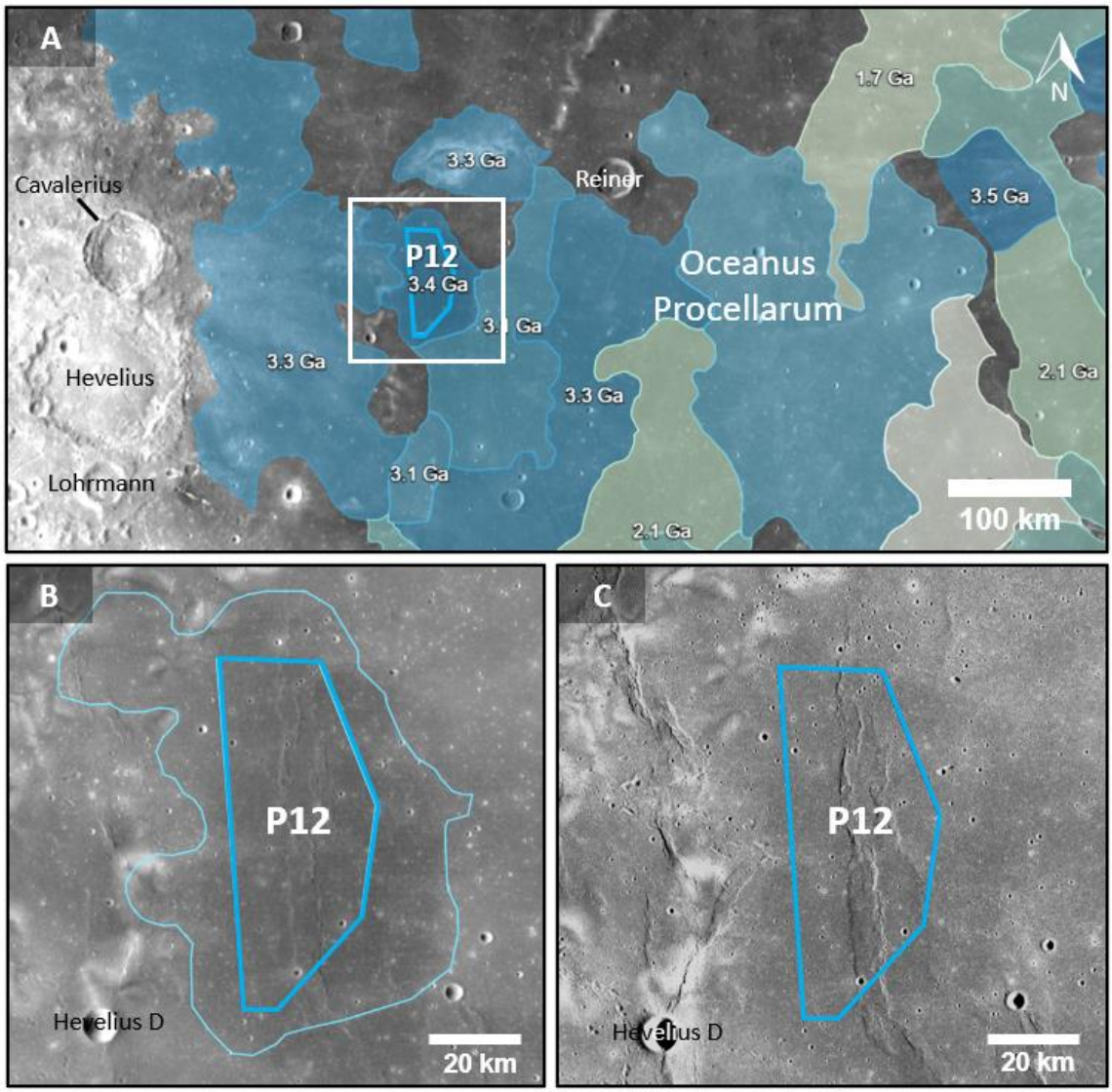

Figure 4.19. A) The P12 count area (blue outline) for the larger mare age unit (light blue bounding polygon), was mapped by Hiesinger et al. (2011) to the east of Cavalerius crater in Oceanus Procellarum. This single count area was selected from the global data set (Hiesinger et al., 2011) and used for AMA calibration. Other mare age units, together with their AMAs are shown. B) Count area P12 (blue outline) for the larger mare age unit (light blue bounding polygon). Figures A, B use WAC albedo map (Speyerer et al., 2011). C) Count area P12 (blue outline) used for crater counts in this study. Note the north-south trending wrinkle ridge in the count area. Kaguya morning TC imagery (Haruyama et al., 2008b).

4.3.2 Crater count summary

We summarize the crater count data for all researchers, for all areas, including the comparison area. Ages are summarized in this section; error information is available herein (Table 4.4 – 4.7). Reiner Gamma has four count areas with a total area of 1110 km^2. The AMAs for Reiner Gamma range from 3.29 +0.041/-0.054 – 3.78 +0.018/-0.021 Ga (2 researchers). The Mare Crisium study area has an AMA range of 3.24 +0.083/-0.14 – 3.63 +0.024/-0.029 Ga (2 researchers) for the three count areas, which have a total area of 851 km^2. Lacus Mortis, with two count areas totaling 690 km^2, have AMAs that range from 3.49 +0.043/-0.059 – 3.73 +0.033/-0.043 Ga. A resurfaced portion of LM02 had a younger age (3.26 +0.082/-0.14 Ga). The age of count area LM01 was determined with 53 craters (1 researcher), whereas the age of LM02 was determined with 162 craters (2 researchers). Comparison area P12 has an area of 1936 km^2, with and AMA range of 3.44 +0.067/-0.12 – 3.51 +0.04/-0.054 Ga (2 researchers). The comparison age determined by Hiesinger et al. (2011a) was 3.42 Ga. Researcher B posted younger ages than researchers A in each count area, with the except of comparison area P12.

Age variations were observed between count areas within study areas. Researcher A found a difference of 0.07 Ga between areas in Mare Crisium and 0.23 Ga between areas in Reiner Gamma (RG02, RG04). Researcher B showed differences of 0.33 Ga, 0.28 Ga, and 0.07 Ga for count areas Reiner Gamma, Mare Crisium, Lacus Mortis, respectively. Count area MC01 showed the closest age agreement between researcher A (3.57 +0.023/-0.027 Ga) and B (3.52 +0.013/-0.014 Ga), with a difference of 0.05 Ga. These ages for MC01 are in near agreement (0.01 Ga) when the error is taken into account. Count area MC02 exhibited the largest age difference. Researcher A (3.56 +0.02/-0.024 Ga) and B (3.24 +0.083/-0.014 Ga), with a difference of 0.32 Ga. These two ages are not in agreement, even when the error is considered. All study areas and the comparison area (3.24 – 3.78 Ga) are Imbrium-aged (3.2 – 3.85 Ga) (Wilhelms, 1987).

4.3.3 DTM aspect diameter comparison

Rimcrest diameter checks were made with high resolution NAC DTMs (~3 - 5m/pixel) for selected primary craters within each count areas. These check were made after the researcher counts were completed. The NAC DTMs provided a higher resolution, 3 – 5 m/pix versus 7.4 m/pix, than the Kaguya TC imagery and other global DEM datasets (GLD100, 100 m/pixel,

Scholten et al., 2012; SLDEM2015, 59 m/pixel, Barker et al., 2016). A DTM derived from LROC NAC images allowed precise diameter measurements, however, the coverage area is small. Although, the DTMs did not provide complete coverage of any of our count areas the partial coverage was sufficient for the comparison.

For the purpose of slope direction, NAC DTMs (~3 - 5 m/pixel) were converted to aspect images. An example crater (#05) with an overlaid aspect image, clearly shows where the rimcrest peaks and changes direction (Figure 4.8). The crater rimcrest is located at the junction of opposing sloped surfaces, i.e., where the crater interior and exterior meet. Unambiguous diameter measurements are made at these junctions. Measurements were made on well-defined primary craters ranging from ~200 – 1100 m in diameter. A sample of between five and twenty craters were measured in each count area; the number measured depended on the DTM coverage of the count area and on whether craters with adequate rimcrest definition could be identified. Well-defined craters are relatively fresh with crisp, identifiable rimcrests (Figure 4.8A, B, crater 05) as opposed to older craters that have been degraded by subsequent impacts of all sizes, which degrades the sharpness of rimcrests and decreases the depth to diameter ratio (Figure 4.8B, C, crater A) (Fassett and Thompson, 2014).

We compared crater DTM aspect diameter measurements and researcher measurements for selected craters and show results for individual count areas, study areas (i.e., combined count areas), and combined study areas (Figure 4.9, Table 4.8). Reiner Gamma has four similarly sized count areas that have varying amounts of coverage by a single 5.0 m/px DTM (Figure 4.9A-D). Eight craters were measured in each count area. Crater diameters in the four areas vary from ~7% larger to ~-14% smaller for researcher A and ~7% larger to ~-13% smaller for researcher B than the DTM measured value. The average for all Reiner Gamma count areas by researcher is -4.4% (researcher A); -2.1% (researcher B). A negative value indicates that the measured diameter was smaller than the DTM aspect diameter.

The three Mare Crisium study areas were partially covered by two NAC DTMs that allowed diameter comparisons (Figure 4.9E). The number of craters measured in each count area varies. Five craters were measured in count area MC01, nineteen in MC02, and six in MC03. Area MC02 featured the largest measurement variation in crater sizes with diameters varying from ~15% to ~-20% when compared to the DTM measured value. Area MC01, had marginally more consistent measurements between researchers with diameters varying from ~18% to -10% in relation to the

DTM diameter. The average researcher diameter measurements for all Mare Crisium count areas are -0.7% (researcher A); -4.6% (researcher B).

Lacus Mortis had DTM coverage for count area LM02 (Figure 4.9F); no DTM coverage was available for count area LM01. Ten craters were measured in count area LM02. Measured diameters for all researchers varied from ~12% larger to ~-21% smaller than the DTM measured value. Measured diameters averaged -4.2% (researcher A); -1.4% (researcher B) when compared to DTM diameters. The average for all researchers is -2.8% smaller diameters.

Overall, researchers measured slightly smaller crater diameters than those obtained from DTM aspect measurements (researcher A: -2.8%; researcher B: -3.0%). The average measured diameter versus DTM diameter for all 72 comparison craters: -2.9%. Individual diameter measurements were variable. All measurement results are listed in Figure 4.9, Table 4.8.

Table 4.8: NAC DTM aspect crater diameter comparison. Diameter measurements of DTM craters were compared to measurements of the same craters made by Researchers.

Count Areas	# of craters	Researcher A Average (%)	Researcher B Average (%)	All Researchers Average (%)
RG01	8	-3.3±6.9	+0.4±3.7	-1.4
RG02	8	-2.5±5.6	-3.7±5.1	-3.1
RG03	8	-4.8±5.3	+0.6±2.4	-2.1
RG04	8	-6.9±4.3	-5.7±4.5	-6.3
MC01	5	-2.3±6.6	2.9±9.8	0.3
MC02	19	-0.0±7.3	-7.5±6.4	-3.8
MC03	6	-1.4±8.5	-1.5±10.7	-1.5
LM01[1]	-	-	-	-
LM02	10	-4.2±8.5	-1.4±9.0	-2.8
Avg All Areas	72	-2.8	-3.0	-2.9

[1]NAC DTM not available for count area LM01.

4.4.0 Discussion

We examine the researcher counts and place the results in context for each landing site and with past work on AMAs. Diameter measurements are verified by comparing to DTM derived diameters, high-resolution rimcrest imagery, and surface photography. The effect of diameter variations and the influence of secondary craters is assessed.

4.4.1 Comparing Model Ages between researchers

We examine the variations in absolute model ages for each study area and count area. Study area projects were defined and distributed to each researcher to ensure uniformity of products with the idea that AMA differences would highlight variations between the count/measurement approach of each researcher. Researchers are creative and typically look for the optimum approach to solving problems, including this crater counting exercise where the goal was to not only to compare approaches but to also determine the most accurate AMA. As a result, researchers endeavored to alter the provided crater count boundaries, inserted areas for excluding secondary craters, and in some cases, used alternative imagery with different illumination and resolution.

As expected, the AMAs vary for each count area. We examine the extent and possible reasons for the variation in determined ages. All results are summarized as crater count maps (Figures 4.10 – 4.13) and CSFD's (Figures 4.14 – 4.17). AMAs, errors, diameter range, and N(1) are presented in Tables 4.4 – 4.7. We select specific count areas in the following sections to illustrate both coherent and divergent count results.

4.4.1.1 Reiner Gamma

The Reiner Gamma study area offered four tightly clustered count areas around the Reiner Gamma albedo feature. Researchers used Kaguya morning imagery for their counts. One challenge for the researchers involved identifying secondary craters in the high-albedo portion of Reiner Gamma. Count areas RG01 and RG03 included some of the high-albedo mare, while, RG02 contained a significant amount of high albedo mare. Previous work on Reiner Gamma has suggested that the regolith is shielded from the maturing effects of space weather, preventing the darkening of the mare in selected areas (Hood and Schubert, 1980; Hood and Williams, 1989; Blewett et al., 2011; Kramer et al., 2011; Glotch et al., 2015). If this is the case, the steep, interior slopes of younger craters would remain albedo bright longer than craters with similar morphology that are not shielded. Bright primary craters in a linear configuration, can be misidentified as secondary craters.

Count areas RG01 and RG03 had good agreement on age as determined by researchers A and B. Final AMAs were 0.08 and 0.06 Ga apart, respectively. The remaining two count areas had a larger difference in AMA, RG02: 0.31 Ga and RG04: 0.26 Ga. Similar to count area MC02, RG02 appears to have an abundance of background secondary craters. Researcher A added three

exclusion areas to remove secondaries from the AMA. Researcher B marked a large number of craters as secondaries with good correlation to researcher A's exclusion area. The discrepancy in ages arise because researcher B marked craters outside of the A's exclusion areas as secondaries. RG04 is southeast of the "eye" of Reiner Gamma and outside of the albedo anomaly. The area is relatively free from secondaries; researcher A did not add any exclusion areas, whereas researcher B marked short secondary crater chains and some individual secondary craters. The marked secondaries contributed to the younger age determined by researcher B (3.29 +0.041/-0.054 Ga) versus researcher A: (3.55 +0.022/-0.026 Ga) (Table 4.4; Figure 4.14G, H).

4.4.1.2 Mare Crisium

The Mare Crisium study area offered three areas for researchers to examine. Researcher A use the "trim" and "exclude" approach for AMA determination. Researcher B counted craters in each count area as presented without modifying the count area boundary nor defining excluded areas. Secondary craters were identified individually and marked for exclusion. There is overlap in the two approaches as researcher A marked some individual secondary craters for exclusion and conversely, researcher B marked multiple secondary craters in groups that correspond to reseacher's A excluded areas.

Count area MC01 had fewer background secondary craters identified by researchers than MC02, MC03. When secondaries were identified, they were excluded using one of the three methods previously mentioned (trim count area, polygon exclusion, individual crater exclusion). Although, not a one-to-one correspondence, researchers A and B excluded many of the same craters (Figure 4.11B, C), just using different approaches, resulting in similar AMAs (0.05 Ga difference). Some secondaries were identified by multiple researchers (green arrows), and other secondaries were identified by one researcher (orange arrows).

Count area MC02 has a >0.3 Ga AMA discrepancy between researchers. Researcher A counted the entire count area and initially determined the AMA to be 3.58 +0.017/-0.019 Ga. A revised count was made after observing the location of secondary craters and trimming the eastern portion of the count area (including the proposed landing site) and adding one excluded area. The final AMA is 3.56 +0.02/-0.024 Ga, an AMA decrease of 0.02 Ga. Because the diameter fit for both CSFDs remained constant (300 – 800 m), the net decrease in age indicates that some primary craters were likely eliminated with the trimming of the count area (Figure 4.11E). Otherwise, the AMA would have increased if the trimmed area only contained secondary craters. The question of

the large AMA difference remains between researchers A and B. The explanation is likely the large number of secondary craters that researcher B identified in this count area (Figure 4.11F). These craters (yellow) are distributed throughout the central and eastern portion of the count area. As some secondary craters are likely included in the Production Function (PF; McEwen and Bierhaus, 2006; Xiao and Strom, 2012; Chapman, 2015), it is possible that researcher B eliminated more background secondaries than are factored into the PF, lowering the AMA. Count area MC03 follows the same trend as area MC02. Namely, the area clearly has numerous secondary craters, which are addressed by the researchers. The gap in ages between researchers A and B (0.20 Ga) is less than for count area MC02.

The imagery used to count craters is another factor that can affect the AMA. Researchers used two forms of Kaguya imagery for Mare Crisium, researcher A used evening imagery and Reseacher B used morning imagery. Previous studies have shown that differences in incidence angle (Wilcox et al., 2005; Ostrach et al., 2011; Liu and Wu, 2021; Richardson et al., 2021) can affect count results; specifically, cratered surfaces illuminated with low sun appear to have more craters that surfaces with high sun. Our inspection of the morning and evening imagery shows that the solar incidence angle is larger (stronger shadows) for the evening imagery in this study area (Figure 4.20), which may have enabled researcher A to see and count more degraded craters than researcher B.

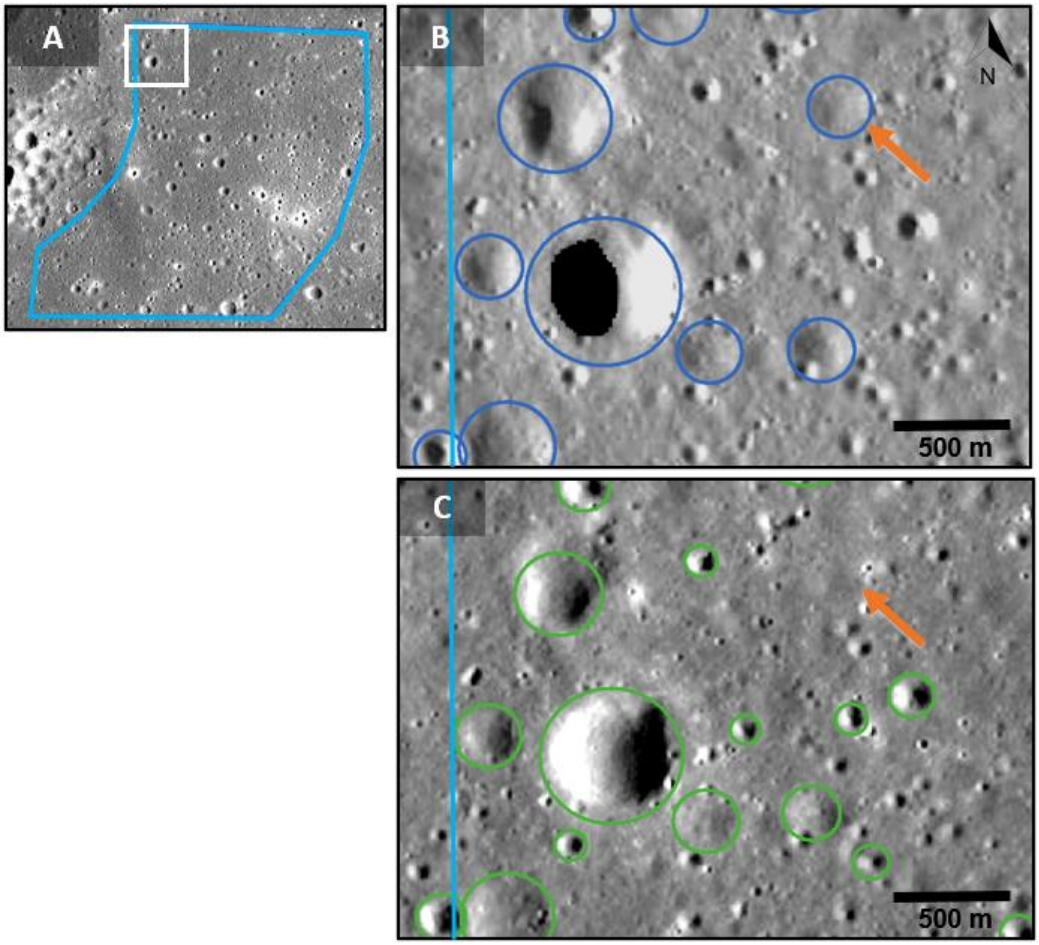

Figure 4.20. A) Northwest portion of count area MC03, superposed on Kaguya morning TC imagery (Haruyama et al., 2008b). Detailed view of panels B) and C) (white box). **B)** Primary craters mapped by Researcher A (blue circles). Degraded crater identifiable in evening sun, but not visible in morning sun (orange arrow). Kaguya TC evening imagery. **C)** Primary craters mapped by Researcher B (green circles). Unidentifed degraded (orange arrow). The number, location, and size of the craters varies with researcher and illumination. Kaguya TC morning imagery.

4.4.1.3 Lacus Mortis

Count area 01 is as far from Bürg as possible while remaining on the lacus, nevertheless the area is affected by secondary craters from the impact. Researcher A was unable to obtain a count. The CSFD for researcher B's counts (Figure 4.16B) exhibits variations along the 3.49 Ga isochron indicating the area is influenced by secondaries, notably at the 450 m and the 600 m bin, which had count values higher than the production function.

The difference between AMAs for LM02 was relatively small (0.17 Ga) despite the different approaches used by researchers A and B (Figure 4.16C, D). Researcher A elected to count a portion of the count area (~17%) using an LROC NAC mosaic with evening sun illumination (Figure

4.12E). The subset area appears to be nearly devoid of secondary craters; only five craters were marked as secondary craters. Four of the five secondary craters were identified by researcher B, illustrating that the two researchers used similar approaches for identifying secondary craters. Although there is general agreement on older ages between researchers (A: 3.73 +0.033/-0.043 Ga, B: 3.56 +0.08/-0.18 Ga), researcher B identified more secondaries and fewer small craters outside of the subset area specified by A. The result is two AMAs for this count area with the younger age at 3.26 +0.082/-0.14 Ga (Table 4.6; Figure 4.16C, D). The younger age is generally regarded as evidence of the partial resurfacing of a mare area where a thin young lava flow superposes an older cratered surface (BVSP, 1981), however, in this unusual mare the most likely scenario is obscuration by distal Bürg impact ejecta. The layer of ejecta would have the same affect as a lava flow, namely reducing the number of smaller craters that are visible. When the number of craters of a given size is reduced in a fixed area; the absolute model age is younger.

4.4.1.4 P12 – Comparison count area

Count area P12 is used as a benchmark to which the AMAs determined in this paper can be compared. This count area, with an age of 3.42 +0.10/-0.07 Ga, is one of 60 defined by Hiesinger et al. (2011a) in Oceanus Procellarum; for reference, neighboring count areas include P18 (3.32 +0.08/-0.06 Ga) to the west, P20 (3.12 +0.18/-0.45 Ga, 3.93 +0.08/-0.03 Ga) to the south and southeast, and P16 (Reiner Gamma, 3.33 +0.08/-0.05 Ga) to the northeast (Figure 4.19). We selected P12 at random as it is just one of many nearside mare count areas whose absolute model was determined with a consistent dataset and measurement approach (Hiesinger et al., 2011a). Researchers in this work counted craters in P12 in the same fashion as they did for the three study areas.

There were differences in the products used to perform the counts that may have affected the identification of craters. The Hiesinger et al. (2011a) counts were performed using Lunar Orbiter IV photographs as a basemap and first acquired in 1967. This high quality product had variable spatial resolution (60 – 150 m), incidence angles of ~60 – 80° (low sun) and good image contrast. The Kaguya TC camera imagery used for our counts had a constant spatial resolution of 7.4 m/pixel (Okumura et al., 2009) and a “morning” sun incidence angle of >60° (low sun) (Haruyama et al., 2008b). In addtion to the Kaguya dataset, the LROC NAC imagery was available for reference when performing crater counts. Although, the NAC imagery was not used for diameter measurements, this high- resolution imagery was useful for inspecting crater morphology.

Researchers determined AMAs for P12 that are slightly older (researchers A: +0.02 Ga; B: +0.09 Ga.) than the AMA determined by Hiesinger et al. (2011a), but are within the standard deviation. This comparison provides an link to previous foundational mare age-dating work (Hiesinger et al., 2011a).

4.4.1.5 Summary of absolute model ages

General observations may be made when all count data are compared. Researcher A produced higher AMAs than researcher B for all areas, with the exception of P12. Researchers used different approaches for removing secondary craters from count areas, resulting in a disparity of ages (0.05 – 0.32 Ga). Excluding secondary craters via exclusion areas versus excluding individual craters resulted in older AMAs, likely due to the larger number of secondary identified via the latter method (Figure 4.21).

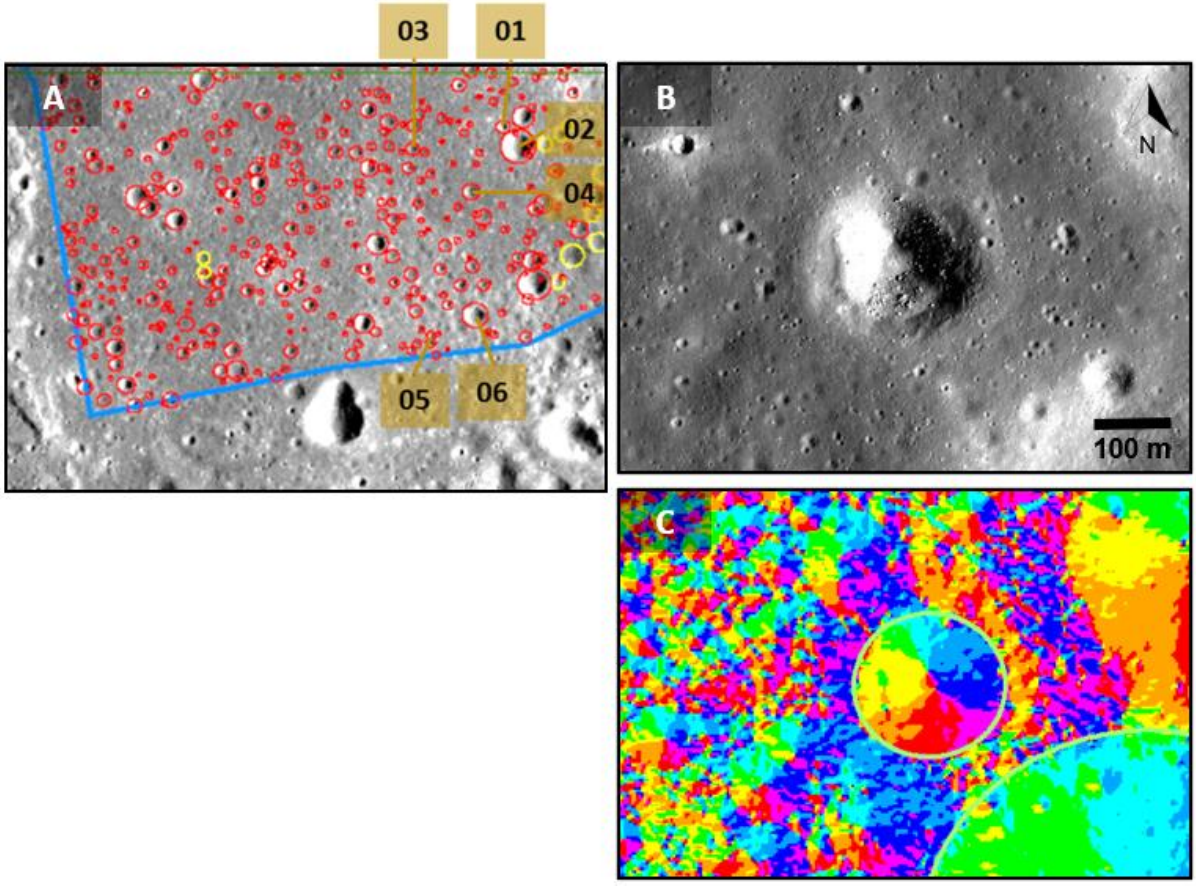

Figure 4.21. Count area age comparison. The AMAs determined by each researcher are compared for each count area. Researcher determined ages vary both by study area (blue and yellow background) and by count area (points). The count areas from left to right: Reiner Gamma (blue background), Mare Crisium (yellow background), Lacus Mortis (blue background), P12 (yellow background). Researcher ages are color coded (A blue, B green).

We average the ages determined by researchers for each count area and study area (Table 4.8-B). Averaging researcher counts for the same count area may or may not minimize identification issues and measurement variations depending on researcher bias. Averaging two or more count areas in a study area may provide a more accurate AMA if the count areas are on the same flow unit.

Table 4.8-B: Average AMAs determined by researchers for each count area and study area**.**

Study Area	All Areas	Researcher A (AMA)	Researcher B (AMA)	Count Area (Avg AMA)	Study Area (Avg AMA)
Reiner Gamma	RG01	3.67	3.59	3.63	3.58
	RG02	3.78	3.47	3.63	
	RG03	3.68	3.62	3.65	
	RG04	3.55	3.29	3.42	
Mare Crisium	MC01	3.57	3.52	3.55	3.49
	MC02	3.56	3.24	3.40	
	MC03	3.63	3.43	3.53	
Lacus Mortis	LM01	-	3.49	3.49	3.59
	LM02	3.73	3.56	3.65	
P12	P12	3.44	3.51	3.48	3.48

4.4.1.6 Mare ages in context

We compare our AMAs to the results of previous work at or near our study area locations.

4.4.1.6.1 Reiner Gamma **–** AMAs for the four count areas range from 3.29 – 3.78 Ga (Table 4.4). Approximately 80% of the total area of our four count areas coincide with mare age unit P16 (Hiesinger et al., 2011a), which has an AMA of 3.33 +0.08/-0.05 Ga. A second age comparison can be made to the actual count area for P16, which is smaller and interior to the larger mare age unit boundary (Figure 4.18). Count area RG02 is smaller (24%) than the Hiesinger et al., (2011a) count area, falls entirely within the area, and has an AMA of 3.47 – 3.78 Ga.

Although Boyce (1976, see Figure 4) excluded the "eye" of Reiner Gamma from his count areas, it is possible to examine the ages for the overlapping areas. Three of four count areas in our study included mare in Oceanus Procellarum and were offset from the main portion of Reiner Gamma. Count areas RG01 (3.59 – 3.67 Ga) and RG03 (3.62 – 3.68) have a small overlap with Boyce (1976) area DL=140 – 190 m (2.6 ±0.3 Ga). Count area RG04 (3.29 – 3.55 Ga) overlaps with Boyce (1976) area DL=211 - 240 m (3.2 ±0.1 Ga). Note that RG04, along with our other

areas, represent a much smaller portion (<300 km^2 versus 90,000+ km^2) of the mare than are represented in the earlier study.

4.4.1.6.2 Mare Crisium – This mare has a comprehensive history of research investigating the age of the basalts. Our AMAs for the study area range from 3.24 to 3.63 Ga (not including error). Boyce and Johnson (1977, 1978) used Apollo and Lunar Orbiter photographs to produce crater density maps for all of Mare Crisium. Four units were mapped for the mare. Unit II covered the majority of Mare Crisium, includes our study area, and was determined to have an absolute age of 3.5 ±0.1 Ga (C_s = 119) (Boyce and Johnson (1977, 1978), see Figure 1). Following the extensive study of nearside basalt ages (Hiesinger et al., 2011a), a subsequent study (Hiesinger et al., 2011b) focused on Mare Crisium using Clementine color ratio imagery to define homogeneous count areas and LRO WAC imagery for crater counts. Although, Hiesinger et al. (2011b) determined AMAs for multiple areas across Mare Crisium, with ages that range from 2.71 to 3.61 Ga, none of the ~22 areas included our study area. However, four Hiesinger et al. (2011b) count areas were located near to and distributed around our count areas (km's between boundaries; MC01 has a ~10% overlap with a Hiesinger et al. (2011b) area that has an AMA of 3.15 Ga) and have ages of 3.00, 3.02, 3.15, and 3.38 Ga. The most recent Mare Crisium mare basalt age analysis (Lu et al., 2021) determined AMAs for four mare units: Im1: 3.74 Ga; Im2: 3.49 Ga; Im3: 3.56 Ga; EIm: 2.49 Ga. Our study area/CLPS site corresponds to count area Im2, with an AMA of 3.49 Ga. Our average age for this study area (3.49 Ga) agrees with Boyce and Johnson (1977, 1978), (0.1 Ga lower in age), is generally older than Hiesinger et al. (2011b, which is 0.11-0.49 Ga higher in age), and agrees with Lu et al., (2021, 0.0 Ga, i.e., same age).

4.4.1.6.3 Lacus Mortis – This lacus, due to its small size and disruptive Bürg crater, has been bypassed in the comprehensive nearside surveys (Boyce, 1976; Hiesinger et al., 2011a). A recent survey (Kushida et al., 2016) focused on the area around a lunar pit that lies west of crater Bürg (Wagner and Robinson, 2014) as a site for future exploration. Kushida et al. (2016) mapped two count areas (M-1, M-2) in the vicinity of the pit; area M-1 included the pit and M-2 is north of M-1. These count areas are northeast and adjacent to our count area LM02. AMAs for area M-1 are 3.5 and 3.8 Ga; AMAs for area M-2 are 3.3, 3.5, and 3.8 Ga (Kushida et al., 2016, see Table 1). Our AMAs are in general agreement (Table 4.6) with the AMAs produced by Kushida et al. (2016) and researchers from both groups identified two ore more ages, that we interpret as a resurfacing event, likely from the Crater Bürg impact. Kushida et al. (2016) identified the transition in ages

for craters with diameters of 500+ m, whereas, our work specified the transition for craters with diameters at 700+ m. This difference may reflect variations within the complicated floor of Lacus Mortis. Although, our count area LM01 lies to the northwest of LM02, M-1, and M-2, the LM01 AMA is bracketed by the AMAs determined by Kushida et al. (2016).

4.4.2 DTM aspect diameters comparison

We compared our measured diameters to DTM aspect diameters (§**4.3.3 DTM aspect diameter comparison**) to ascertain the accuracy and precision of our measurements. Although, a subset of craters was analyzed, the craters were distributed between all count areas (with the exception of LM01 for which no NAC DTM data was available) to eliminate variations in the location of the DTM and to provide a representative sample across study areas. Comparing our measurements against an objective measurement provides more confidence in the results. There are, however, limitations to using DTM aspect diameter measurements. The aspect faces and boundary can be ambiguous if the rimcrest has been degraded or has superposed impacts that disturb the rimcrest. This sample of DTM aspect diameters provides a base for the analysis.

The Reiner Gamma measurement comparison was more precise than for the other two study areas. Researchers had less variation in their measurements with researcher A at 4-7%, researcher B with 2-5% (Table 4.8). All researchers used the Kaguya Morning imagery, which demonstrates the importance of using the identical imagery when comparing crater counts and AMAs. Researcher B showed the largest difference between average DTM aspect diameter and measured diameter for RC04 (-6%) when compared to the other three RG count areas, which would contribute to the younger age determined for this count area.

Reported count diameters for Mare Crisium were smaller than DTM aspect diameters, with the exception of researcher B's slightly positive MC01 average (Table 4.8). This is due to a positive value for crater 01, which had a larger diameter also reported by researcher A. Two researchers reported a larger diameter for this ~250 m crater. A closer look reveals that this impact crater has unusual morphology and may either be a crater within an existing crater (two impacts in the same location at different times) or an impact into stratified regolith (Figure 4.22). Determining an accurate diameter can be problematic for craters with atypical morpohology. We use the researcher measurements for all three MC count areas to assess the precision of their measurements. Researcher A was most precise with a standard deviation of 7-9%, followed by researcher B with

6-11%**.** Researcher A used Kaguya evening imagery to perfom all Mare Crisium count, unlike researcher B, which suggests that this imagery offers an advantage over the morning data set.

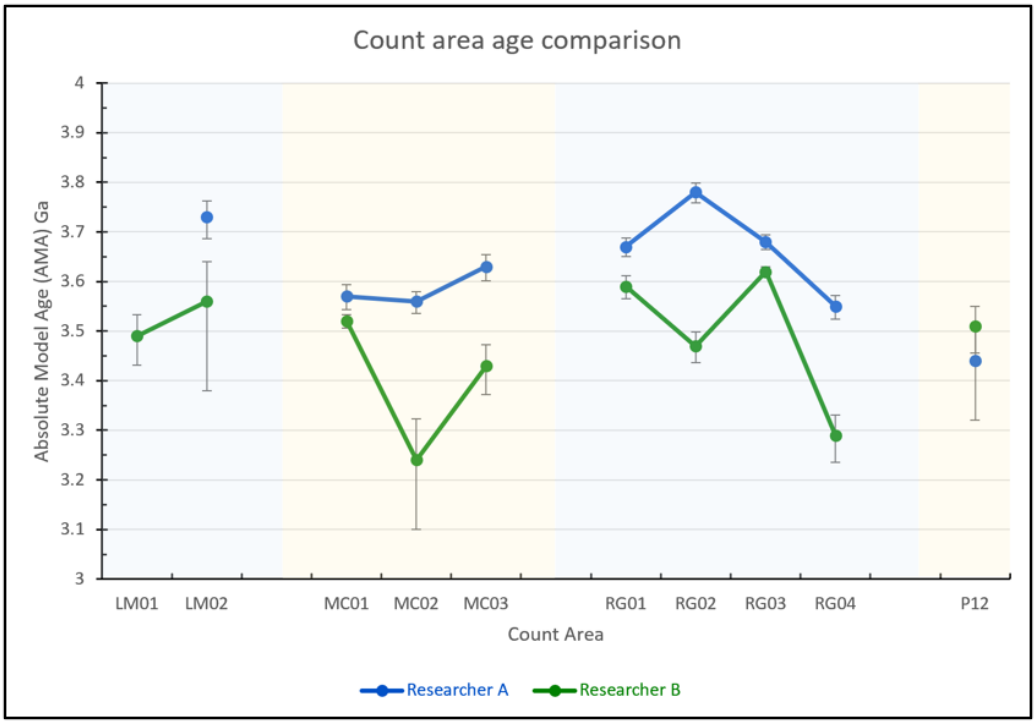

Figure 4.22. A) Crater 01 in count area MC01. Two researchers reported a larger diameter for this crater. B) A closer look reveals that this impact crater has unusual morphology and may either be a crater within a crater (two impacts in the same location at different times) or an impact into stratified regolith. C) NAC DTM aspect image for diameter comparison.

Lacus Mortis diameter averages had a small variation, despite the use of different imagery for the counts. Researcher A had concerns about secondary craters and used a small area of a LROC NAC mosiaic to perform counts. Researcher B counted with Kaguya morning imagery. Diameters were 2-4% smaller than DTM aspect diameters (Table 4.8). The higher NAC mosaic resolution (2 m/px) did not provide a measurement advantage over the lower resolution TC imagery (7.4 m/px) for detecting the rimcrest.

The resolution of the DTMs used in this comparison have similar resolutions (4.0 m/px for the eastern Mare Crisium study area and 5.0 m/px for the other DTMs) and are a potential source of diameter measurement error. However, the researcher diameter measurements, which involve at least two measurements on opposite sides of the crater, have a larger affect on the accuracy of the diameter (Table 4.8). Diameter measurements are more accurate for large craters (smaller % of the diameter) than for small craters (Table 4.9).

Table 4.9: The affect of DTM resolution on a range of crater diameter measurements. The NAC DTM mosaics that were used to measure the diameter of based on the DTM aspect imagery had resolutions of 4 m/px and 5 m/px. Diameter measurements are more accurate for large craters (smaller % of the diameter) than for small craters.

Diameter (m)	Crater diameter percent	
	±4 m[a]	±5m[b]
100	8.00%	10.00%
200	4.00%	5.00%
300	2.67%	3.33%
400	2.00%	2.50%
500	1.60%	2.00%
600	1.33%	1.67%
700	1.14%	1.43%
800	1.00%	1.25%
900	0.89%	1.11%
1000	0.80%	1.00%
2000	0.40%	0.50%
3000	0.27%	0.33%
4000	0.20%	0.25%
5000	0.16%	0.20%

[a]DTM for Mare Crisium (east)
[b]DTM for: Lacus Mortis, Mare Crisium (west), Reiner Gamma

Overall, researchers posted consistent results with diameter measurements averaging ~3% smaller than DTM aspect diameters (Table 4.8) and this finding is in line with observations of smaller diameter measurements with optical imagery versus topography-based measurements (Jia et al., 2022).

Although, the average diameter percentages were small and the precision averaged 7% for all researchers, there were substantial variations in some of the individual crater measurements (researcher A: -21 to 15%; researcher B: -20 to 18%) (Supplemental Data). These anomalous measurements , if representative of the crater counting community, may be reviewed and used as training examples to improve researcher measurement technique.

This 3% difference in diameter has a small but measurable affect on the AMA. Crater morphology affects diameters measured by researchers with unusual morphology creating the most significant variation. Craters with poor morphology are more likely to be secondary craters and should be eliminated from counts.

4.4.3 Affect of diameter variations on AMA

We examine the affect that variations in crater diameter measurements have on the AMA. Previous research demonstrates that measurements and crater recognition varies between researchers (Robbins et al., 2014, 2018; Giguere et al., 2022; Jia et al., 2022) from the average diameter. In the Robbins et al. (2014) study, crater counters measured craters in identical areas, similar to this study. Representative craters that ranged from fresh to mature were selected from the full set of craters. The diameter varied ±3-4% for the fresh crater example, which was measured by eight experts (Robbins et al., 2014, Figure 1A, B). Six experts measured the degraded crater example; the diameter varied by ±10-11% (Robbins et al., 2014, Figure 1C, D). When crater diameters were measured by non-experts, the dispersion increased (±13-15%) for fresh craters (Robbins et al., 2014, Figure 1A, B) and was higher for degraded craters (±16-17%) (Robbins et al., 2014, Figure 1C, D). In another study, diameters were compared for 14 craters. The diameters measured by two researchers varied by an average of 13% (Giguere et al., 2022). Finally, our study showed the least average variation between researchers (~3%) (Table 4.8).

We selected Mare Crisium, count area MC02, for analysis of the affect of diameter variation on AMA. We start with the AMA determined by researcher B (3.24 +0.083/-0.14 Ga) (Figure 4.15D) for this area and generate new AMAs based on calculated oversized diameter measurements (larger crater) and undersized diameter measurements (smaller crater). The new model crater diameters were generated by increasing or decreasing the diameter of all 800 craters in the original survey by 10% increments. The factors applied to enlarge the craters were 10% and 20%, additionally 7.47% and -7.47% is plotted as this is the largest difference in measured crater diameters between researchers in this study (Fig 9, Table 4.10). The factors applied to decrease the diameter was -10% and -20%. We used a fixed diameter range of 300 m – 1000 m to calculate the new AMA with the Craterstats2 program (Michael and Neukum, 2010). The factors were applied to all craters measured so that craters that were originally outside of the diameter range but now fell within the range had factors applied. We find that the increased diameters of 7.47%, 10%, 20% resulted in higher AMAs of 3.40 Ga, 3.43, and 3.54 Ga, respectively. The decreased diameters of -7.47%, -10% and -20%, resulted in younger AMAs of 2.65, 2.37 and 1.39 Ga, which is significantly younger than the original AMA of 3.24 Ga (Figure 4.23, Table 4.5).

Table 4.10: Crater diameter AMA comparison for increased diameters of 7.47%, 10%, 20% and decreased diameters of -7.47%, -10%, -20% compared to the original Mare Crisium count area MC02. Diameters ranging from -20% to +20% result in a significant variantion in AMA.

Diameter Variation	AMA diameter 300 m - 1 km	# of craters	N(1) km^{-2}
+20%	3.54 +0.024, -0.028	142	$5.36x10^{-3}$
+10%	3.43 +0.038, -0.049	115	$4.01x10^{-3}$
+7.47%	3.40 +0.042, -0.057	111	$3.80x10^{-3}$
Orig MC02[1]	3.24 +0.083, -0.14	96	$3.01x10^{-3}$
-7.47%	2.65 +0.27, -0.30	76	$2.22\ x10^{-3}$
-10%	2.37 +0.27, -0.28	71	$1.98x10^{-3}$
-20%	1.39 +0.22, -0.22	41	$1.17x10^{-3}$

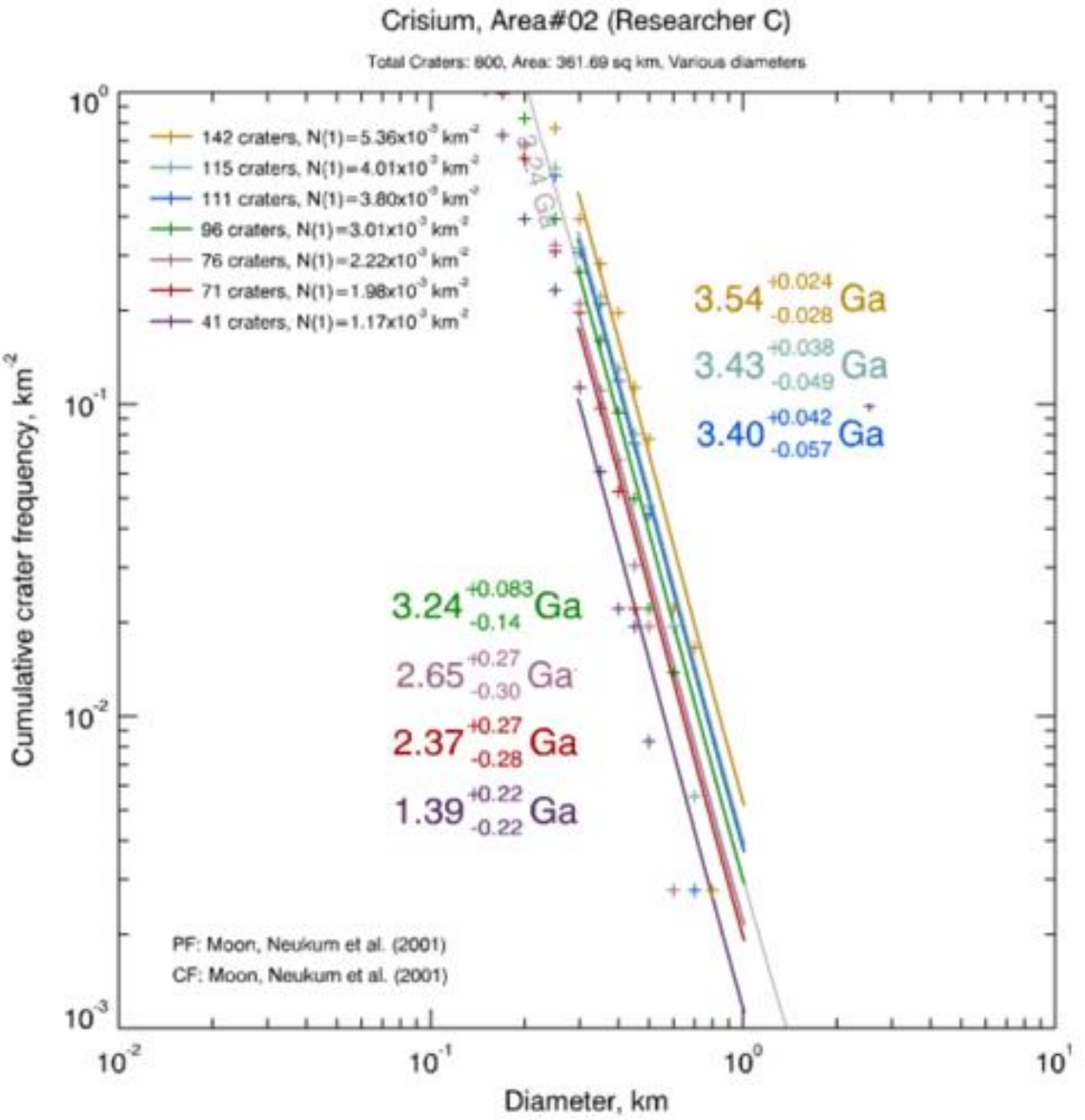

Figure 4.23. The AMA determined by Researcher B (3.24 +0.083/-0.14 Ga) is used to generate new AMAs based on oversized diameter measurements (larger crater) and undersized (smaller crater). The new model crater diameters were generated by increasing or decreasing the diameter of all 800 craters in the original survey by 10% increments. The factors applied to enlarge the craters was 10% and 20%, additionally ~7.47% is plotted as this is the largest difference in measured crater diameters between researchers in this study. The factors applied to decrease the diameter was -10% and -20%. We used a fixed diameter range of 300 m – 1000 m to calculate the new AMA with the Craterstats2 program (Michael and Neukum, 2010). The increased diameters of ~7.47%, 10%, 20% resulted in higher AMAs of 3.40 Ga, 3.43, and 3.54 Ga, respectively. The decreased diameters of -7.47%, -10% and -20%, resulted in younger AMAs of 2.65, 2.37 and 1.39 Ga.

Current (this study) and past (Robbins et al., 2014, 2018; Giguere et al., 2022; Jia et al., 2022) examinations on crater work, show that variations in crater diameter measurements have a measureable affect of determined AMAs. Steps taken to reduce variation in measurements, such as calibrating to a standardized crater field, will serve to reduce AMA differences between researchers.

4.4.4 Crater rimcrest location

We focus on the measurement of crater diameters, with specific attention on the location of the crater rimcrest, as a key component directly responsible for determining the AMA (i.e. Crater diameter is the x-axis of the CSFD plot). Measuring accurate crater diameters is a learned skill that requires knowledge of crater morphology.

There are multiple reasons for variations in diameter measurements. Post impact modification effects such as mass wasting of the crater wall or superposed craters (most common) from later impacts can alter the rimcrest. Degradation mutes the rimcrest and makes identification more difficult. Illumination inside of crater interiors changes with solar incidence angle, which can affect the apparent location of the rimcrest.

We examined Copernican-aged Reiner K crater (8.1° N, 53.9° W, ~3 km diam.), Northeast of crater Reiner and east of the Reiner Gamma albedo anomaly (Figure 4.24A). The crater rimcrest is the highest elevation, continuous terrain encircling the crater. The rimcrest may be visually identified by observing a subtle change in albedo from the sunfacing side to the opposing side. Melosh (1989) provides both a model (see Figure 7.1) and an image (see Figure 2.2) of an idealized crater and a typical fresh crater for comparison(also Stoffler et al., 2006, see Figure 5.5). We selected fresh crater Reiner K for study with its crisp morphology as the rimcrest is progressively more difficult to identify in older, degraded craters [Wilhelms, 1987, see Figure 7.2]. Following our visual identification of the rimcrest we made measurements based on the SLDEM2015 Digital Elevation Model (DEM) at eight points around the crater (Barker et al., 2016) (Figure 4.24A). The 3.186 km diameter of Reiner K was measured between points X and X', which are located at the rimcrest on the east and west sides (Figure 4.24B). Note that the rimcrest on the east side of the crater (X') is located some distance away from the high contrast transition between the shadow in the interior of the crater and the upper part of the crater wall (Y'). Similarly, the rimcrest on the west side (X) is offset from the sunlit western wall (Y) and the upper crater wall. The location at Y is not identifiable via the shadow location, thus is projected based on the location of Y' and the

partial circle defined by the shadow (yellow). The diameter of the high-contrast areas on the crater wall is 3.087 km measured between Y and Y' (Figure 4.24A). The total offset between the rimcrest (blue dash-dot, Figure 4.24B) and the high contrast area (yellow dash-dot, Figure 4.24B) is ~100m (3% diameter) for this 3 km crater. The offset between these diameter measurements are shown for the east rimcrest (Figure 4.24C). The percentage difference in diameter may increase for smaller craters; a future study will quantify the amount.

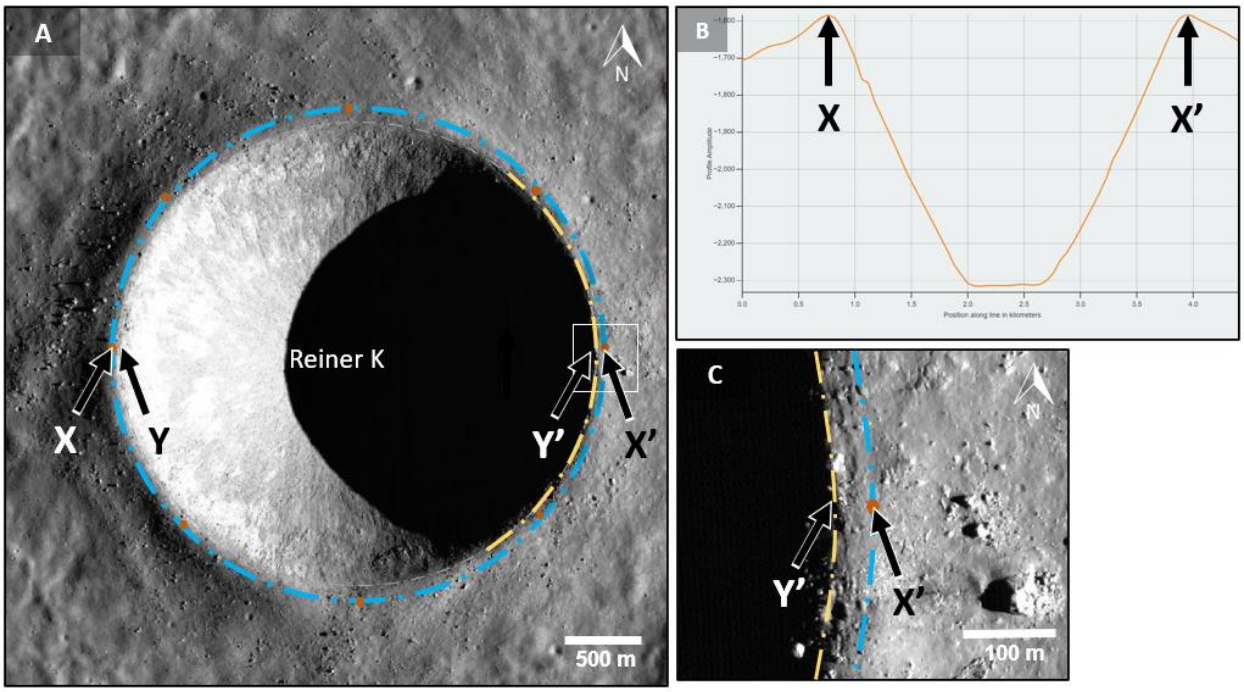

Figure 4.24. A) Crater Reiner K (8.1° N, 53.9° W, ~3 km diam). Diameter measurements for Reiner K through eight points (orange dots) around the crater. True diameter X–X' is 3.186 km (blue). Interior high-contrast smaller diameter, 3.087 km (Y-Y') (yellow and gray (projected)). East rimcrest location of panel C) (white box). LROC NAC image M1200481033LC, res: 0.91 m/px, inc: 71.1°. B) Reiner K diameter 3.186 km measured from rimcrest of digital elevation model, SLDEM2015 (Barker, et al., 2016). C) Rimcrest terrain on the east side of Reiner K. Separation between rimcrest diameter (blue) and interior high-contrast zone (yellow), ~50 m. NAC: M1200481033LC.

Typically, hundreds of craters are measured in an AMA study, and the tendency is to move quickly from crater to crater with measuring tools. The human eye will most easily pick up the contrasting shadow (Y') and sunlight areas (Y) for the measurement, however, this is not necessarily the location of the rimcrest. Measuring at the high contrast locations near the crater rimcrest (Y to Y') will result in a smaller diameter (and a younger AMA).

Crater measurements at the rimcrest provide accurate diameter measurements. A quantitative, repeatable approach is preferred to locate the rimcrest (Mahanti et al., 2014), however, these

approaches must be improved to handle degraded craters. Meantime, several techniques can be used to calibrate diameter measurment at the beginning of a crater count project. These include: comparing diameters to existing databases (IAU.org; Robbins and Hynek, 2012; Robbins, 2019; Fairweather et al., 2023), verifying diameters with DTM and derived aspect data (Giguere et al., 2022), averaging diameters with multiple researchers, and comparing orbital images to surface images to understand the detailed morphology and the effect of superposed craters on the rimcrest. A combination of these steps to verify the rimcrest location, although a relatively small factor in relation to all components that can affect age determination, will contribute to more accurate and consistent AMAs.

4.4.5 Rimcrest verification with Apollo surface photography

All analysis of the crater counting process up to this point has been via orbital imagery, which uses imagery acquired via the nadir view (e.g., Robinson et al., 2010; Kato et al., 2010). The nadir view of craters is logical as it provides the least amount of distortion and most accurate diameter measurements when compared to an oblique view.

Despite having the correct perspective, measurements of crater diameters may not be accurate. This researcher induced error can arise if the location of the rimcrest in misidentified. Incorrect crater diameter measurements have been observed to systematically affect the resulting AMAs (Robbins et al., 2014; Giguere et al., 2022). Viewing a small set of craters in both the nadir view and the surface view provides information about the rimcrest appearance in relation to the crater degradation process.

A surface-level perspective of crater morphology provides a close-up view and can result in a better understanding of the shape of the impact crater. Identification of the crater rimcrest under varying conditions (superposed craters, slumping, degradation over time) results in more accurate diameter measurements.

We use this “ground truth” approach to further our understanding of crater morphology. The examination of individual craters on the surface of the Moon provides a scale that shows very high resolution imagery details, while the disadvantage is that only a small set of craters can be reviewed and the views are usually limited to one side of the crater. We examined one crater from two separate Apollo missions: Little West crater was photographed by Neil Armstrong during Apollo 11 and South Ray crater was photographed by Charlie Duke during Apollo 16.

Images were captured by the Apollo astronauts with film using a Hasselblad 500EL camera. A Zeiss Planar f-2.8/80 mm lens was used to acquire a panoramic view of Apollo 11 Little West crater (Figure 4.25) composed of eight individual 70 mm color frames using type SO-368 film (Kitmacher and Garber). A Hasselblad 500EL camera with an f-8/500 mm lens was used to capture South Ray crater from Apollo 16 station 4 on Stone Mountain (Figure 4.26). The 10 frame panorama was taken with 70 mm black and white type 3401 film. These surface images were compared to imagery acquired by the the Lunar Reconnaissance Orbiter (LRO) Narrow Angle Camera (NAC) (Robinson et al., 2010).

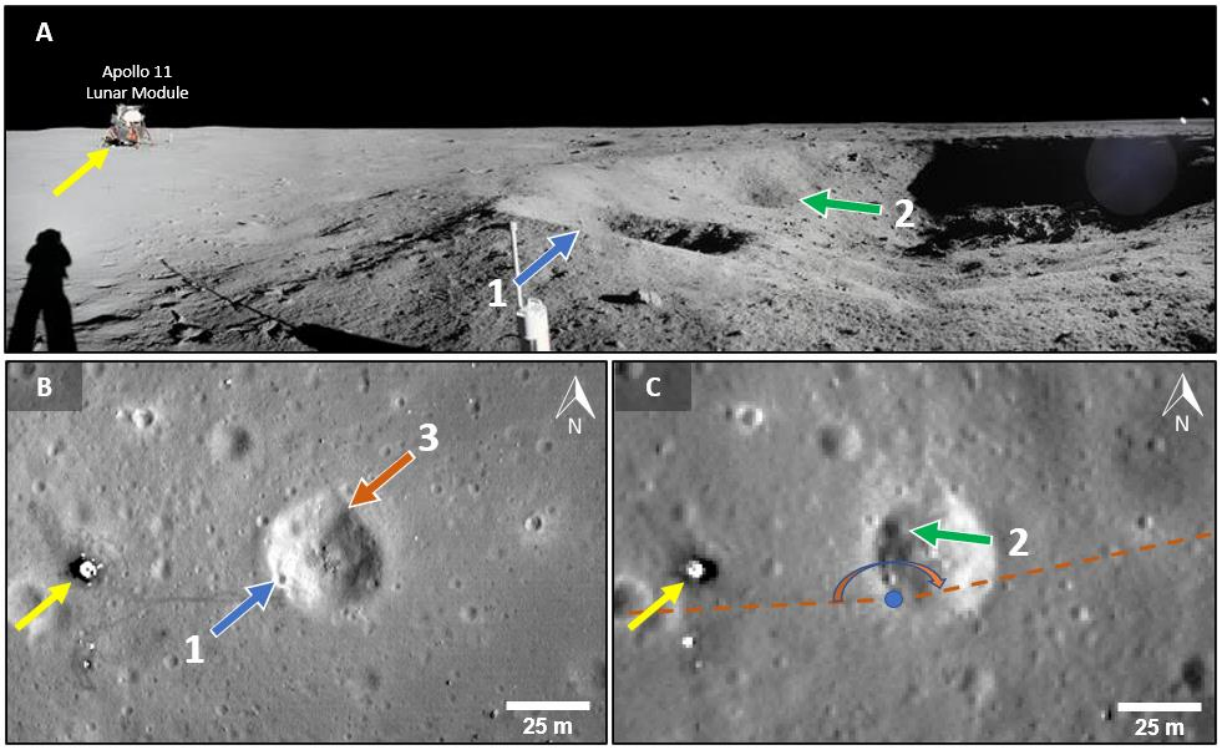

Figure 4.25. Apollo 11, station 5 surface panorama compared to LROC NAC nadir imagery. A) Apollo 11 surface panorama: Lunar Module (LM) yellow arrow, Little West crater (right) is located 60 m east of the LM and is the largest crater (~30 m) with superposed smaller craters. Panorama taken by Neil Armstrong is centered approximately north-northwest and is constructed from multiple images (AS11-40-5954 to AS11-40-5961), NA: JSC2008e040725 (Lunar and Planetary Institute (LPI)'s Regional Planetary Image Facility (RPIF)). B) Little West crater (centered) at the Apollo 11 landing site has a superposed crater on the southwest rimcrest (1, blue arrow; 3, orange arrow). Sun from the east. NAC image M175124932RE, resolution: 0.4 m/px, incidence angle: 41°. C) Little West crater (centered) has a superposed crater just inside the northwest rimcrest (2, green arrow). Approximate location where images taken (blue spot) and field of view of panoramic image (orange line and arrow) (McInall, 2015). Sun from the west. NAC image M1114014396RE, resolution: 0.98 m/px, incidence angle: 44°.

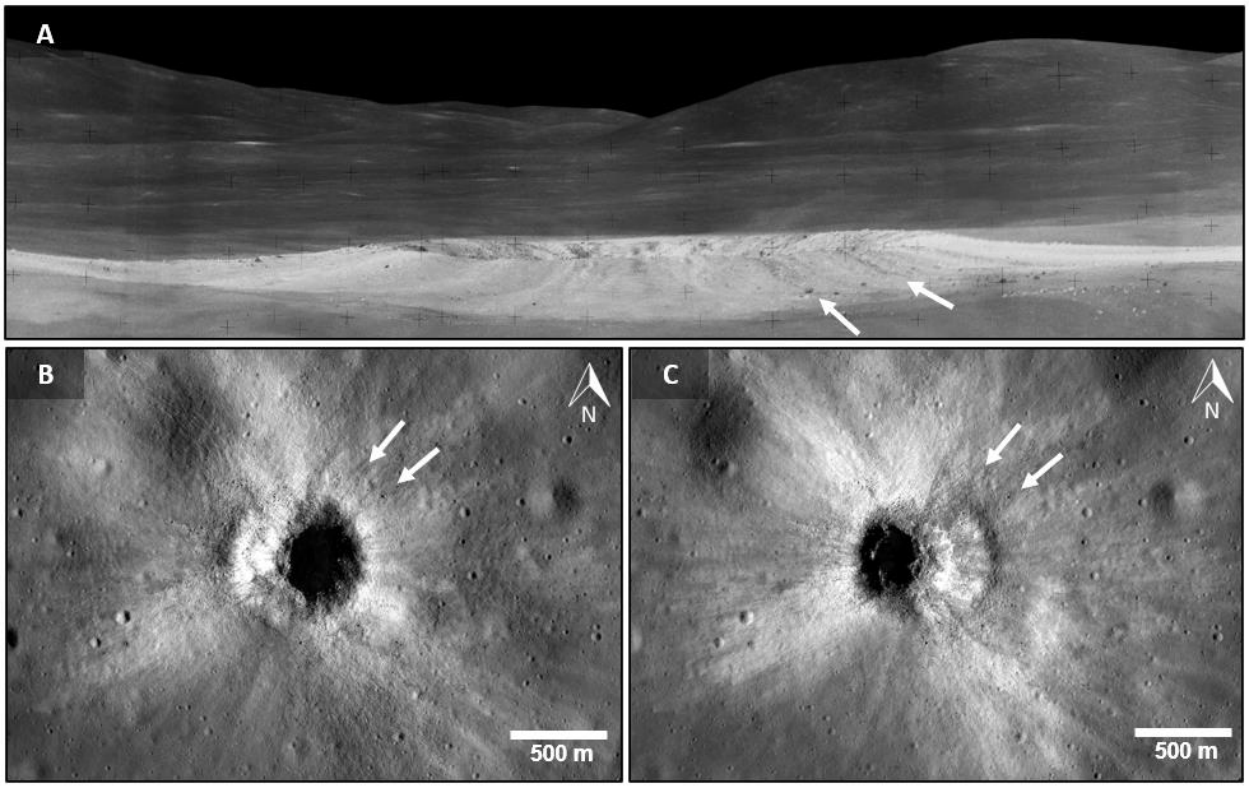

Figure 4.26. Apollo 16 panorama view of South Ray crater from Stone Mountain (station 4) along with LROC NAC nadir imagery. A) Apollo 16 surface panorama of South Ray crater is located 6+ km south-southeast of the LM and is ~700 m in diameter. Panorama taken by Charlie Duke is facing approximately southwest and is constructed from ten images (AS16-112-18243 – AS16-112-18252), NASA File Number: JSC2007e045383 (LPI RPIF). B) South Ray crater is a fresh impact that features alternating light and dark striations in the ejecta blanket. Two dark streaks are identified in each image (white arrows). Sun from the east. NAC image M192853222LE, resolution: 0.9 m/px, incidence angle: 71°. C) South Ray crater with Sun illumination from the west. Many of the details (ejecta rays, rimcrest variations, boulders, etc.) visible in the Apollo image may be seen in this NAC image. NAC image M181065865RE, resolution: 0.96 m/px, incidence angle: 68°.

The Apollo 11 view of Little West crater reveals information about the rimcrest morphology that we do not see from orbit (Figure 4.25). Figure 4.25A is looking approximately N-NW. Two smaller superposed craters are visible on the southwest rimcrest (blue arrow 1) and just inside the northwest rimcrest (green arrow 2). Crater 1 impacted into the southwest rimcrest of Little West. Although crater 1 is small and distributed a minor amount of ejecta the location of the impact disrupted the rimcrest of the larger crater. Likewise, the larger and comparatively degraded crater 2 impacted towards the interior, however, still may have altered the rimcrest of Little West on the northwest side. The altered rimcrest is not discernible on the surface image due to the perspective, but is visible from orbit (Figure 4.25B). The most significant modification is from the degraded

crater on the north rim (orange arrow 3). This small crater (~8 m dia) distorts the overall shape of Little West, creating the appearance of an out of round, larger crater. A diameter measurement of the larger, distorted shape would not reflect the true size of the crater.

We next examined South Ray crater in this SW looking view taken at station 4 in the Descartes highlands, Apollo 16 (Figure 4.26). Immediately obvious are the light and dark albedo variations in the ejecta visible in both the orbital and surface images (Figure 4.26, white arrows). Actually, this was observed by Charlie Duke prior to taking the photos, exclaiming, "it's got black streaks and white streaks coming out of the wall right over the rim". These albedo variations may be attributable to the light and dark lithologic units penetrated by South Ray crater (Ulrich et al., 1981). Variations in the target site (density, porosity, strength) can affect the size of the crater (van der Bogert et al., 2017). South Ray crater is young (AMA 1.07 +0.26 Ma (Gebbing et al., 2021); hence, there are no superposed, meter-sized craters that disrupt the rimcrest. Despite this, the complete rimcrest is difficult to trace due to the high-albedo ejecta. The surface image may be used as an additional aide, marking boulders and albedo feature locations in relation to the rimcrest prior to making diameter measurements.

We compare published diameter measurements for Little West crater and also for South Ray crater (Table 4.11). In the case of Little West crater there is nearly a 20% difference between the smallest diameter measurement (33 m, Shoemaker et al., 1969) and largest measurement (40 m, IAU diameter). Although, a smaller diameter was measured in the Apollo 11 preliminary science report (Aldrin et al., 1969), we consider this value to be an anomaly and therefore not considered in our comparison. A 20% difference in diameter measurement values has a significant affect on the AMA **(§4.4.3 Affect of diameter variations on AMA**). Since the two most recent measurements for Little West crater, 40 m (IAU) and 36 m from this study are closer in value (~10%), it is possible that the earlier measurements were either estimated from low resolution photos or the superposed craters affected the earlier work and the measurements were made inside of the actual rim crest. We see less variation between all diameter measurements for South Ray crater (difference 16%). Again, the earlier Apollo measurements show the largest variation from the measurement made in this study. It is unclear as to why there are two South Ray crater measurements in the Apollo 16 Preliminary Science Report (Muehlberger et al., 1972). The measurement appears to have been refined in the USGS Professional Paper, 680 m (Ulrich et al.,

1981). The diameter difference for the more recent measurements, 700 m (IAU) and 704 m (This study) is small (<1%).

Table 4.11: Diameter measurements for Apollo 11 – Little West crater and Apollo 16 – South Ray crater.

Apollo 11			**Apollo 16**		
Little West crater Lat, Lon: 0.67°, 23.48°			**South Ray crater** Lat, Lon: -9.15°, 15.38°		
Source	Diameter	Reference or Measurement	Source	Diameter	Reference or Measurement
Ap11 Prelim Sci Rpt	"33 ft" (~10 m)	Aldrin, et al., 1969[1]	Ap16 Prelim Sci Rpt	600 m 650 m	Muehlberger, et al., 1972[3] Muehlberger, et al., 1972[4]
Ap11 Prelim Sci Rpt	33 m	Shoemaker, et al., 1969[2]	Geol of Ap16 area	680 m	Ulrich et al., 1981[5]
IAU	40 m	IAU.org	IAU	700 m	IAU.org
This Study	36 m	NAC M175124932R, CraterTools[6]	This Study	704 m	NAC M102057602R, CraterTools[6]

[1]Aldrin, et al., 1969, figure 1-32 and p. 36. The units in "ft" may be a typo in the PSR and should probably be meters.
[2]Shoemaker, et al., 1969, figure 3-3, p. 44.
[3]Muehlberger, et al., 1972, figure 4-24, p. 4-14.
[4]Muehlberger, et al., 1972, figure 29-148, p. 29-111.
[5]Ulrich et al., 1981, figure 3, p. 88, 161.
[6]Kneissl et al., 2010.

Comparison of surface imagery to high-resolution remote imagery provide insights on the variation of impact morphology from a ground level perspective. Additional comparisons can further our understanding of the relationships between the two perspectives. Identifying superposed craters, slumping, or other degradation that modify the rimcrest can inform crater measurements, i.e., where to position diameter measurements. Additionally, surface imagery can help identify secondary craters based on their morphology (shallow bowl, irregular rimcrest, etc) not visible from orbit.

4.4.6 Primary vs Secondary crater comparison

Our work, as well as the work of others (Robbins et al., 2014; Giguere et al., 2022) show substantial variations in the identification of primary and secondary craters between researchers that count craters in identical areas (Figure 4.27). Although the majority of craters are marked with the same designation (i.e., primary), there are deviations. For example, researcher B identified primaries that researcher A marked as secondaries (Figure 4.27B) as the secondaries were thought

to be members of a chain. A second example has researcher A identifying primaries that researcher B characterized as irregularly shaped secondary craters (Figure 4.27C). Similar differences were quantified between "expert" crater counters (Robbins et al., 2014, see Table 1). The Robbins et al. (2014) data indicate there is ~21 – 28% dispersion among researchers in the number of craters found at any given diameter in the NAC data. The dispersion was greatest for larger craters. One possible cause was the use of different tools by researchers to display the NAC imagery and identify craters, however, the study also showed variations when researchers used the same tool to perform counts. We see variations in this study with the number of craters counted using identical tools.

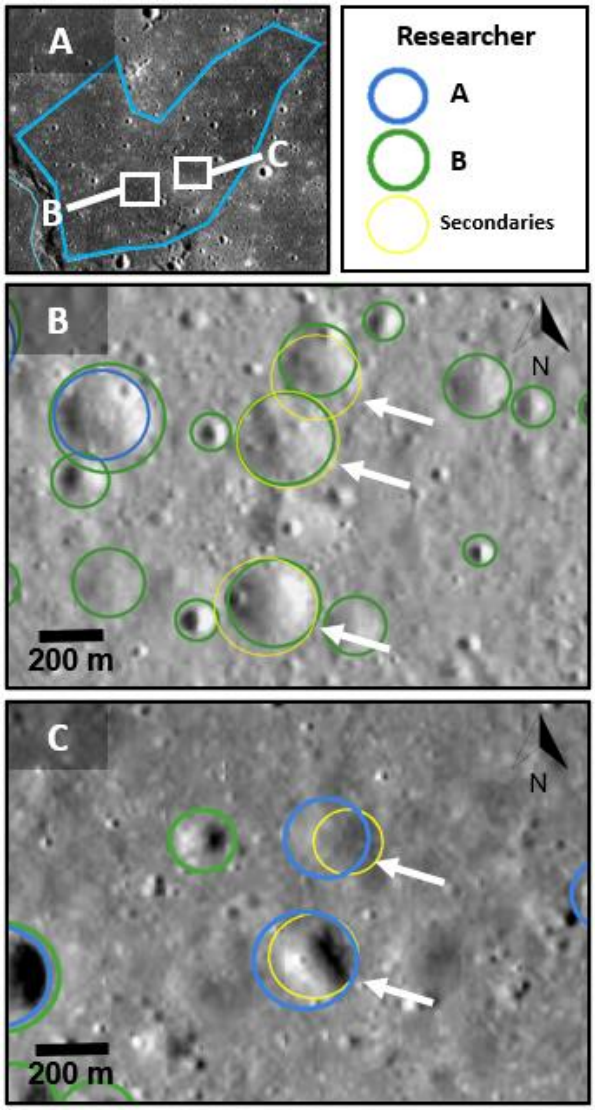

Figure 4.27. Variations occur in the identification of primary and secondary craters between researchers for identical areas. We examing the Mare Crisium study area MC01, which features two examples shown

in panels B and C (white boxes). Researcher A identified three craters in a line as secondary craters (yellow), where Researcher B measured the same craters as primary craters (white arrows). Researcher B identified two craters as secondary craters (yellow), where Researcher A measured the same craters as primary craters (white arrows).

We suggest that crater degradation is a major factor in the ability to recognize both primary and secondary craters. Degradation can be described generally as in the gradual change that occurs to the crater over time (item A) and in more specific event driven terms (items B – D).

A – Crater preservation state classification system. A four-class system ranging (Robbins et al., 2014, see Table 3) from class 1-pristine to class 4-barely distinguishable evolved from earlier gradation scales (Arthur et al., 1963; Trask, 1971). States of degradation are described for the shape, rim, ejecta, walls, and floor.

B – Superposed craters. Impact craters of various sizes that impact the subject crater at any point in time following the original impact and at any location on the rim, ejecta, walls, and floor.

C – Encroached craters. Impact craters that occur after the subject crater has formed and alter the shape of the subject crater. These impact craters can be of any size, however, craters that are proximal and larger than the subject crater are most disruptive.

D – Overshadowed craters. Prominent craters in the vicinity of the subject crater can act as a distraction causing the subject crater to be overlooked.

Each of the degradation types occur in our relatively small data set (Figure 4.28) and in some cases directly affects a researchers crater counts. We find axiomatic (Robbins et al., 2014) that fresh, crisp looking craters are easier to distinguish than older, degraded craters and note that degraded craters were not identified in some cases (Figure 4.28A). Following preservation state, superposed craters are likely the second most common reason for missed craters (Figure 4.28B). Encroached craters have been documented in previous studies (Giguere et al., 2022) and are observed in our study areas (Figure 4.28C). Overshadowed craters, although not strictly a physical event, are interesting as they touch on potential biases in recognizing craters (Figure 4.28D). Past studies on visual perception (Helson & Fehrer, 1932; Bridgen, 1933; Yarbus, 1967; Navon, 1977) posit that perception proceeds from global analysis of a visual scene to more fine-grained analysis, which may explain why larger craters may be perceived more readily than adjacent smaller craters. The perception experiments were performed on a timed basis, thus the simpliest solution to prevent

this potential bias from affecting crater counts is to examine imagery multiple times and for longer periods of time.

The are multiple ways in which craters can vary in appearance and be difficult to distinguish, but with the goal of identifying all primary craters in a given count area and knowledge of the various ways that craters can be obfuscated, crater counts can be maximized.

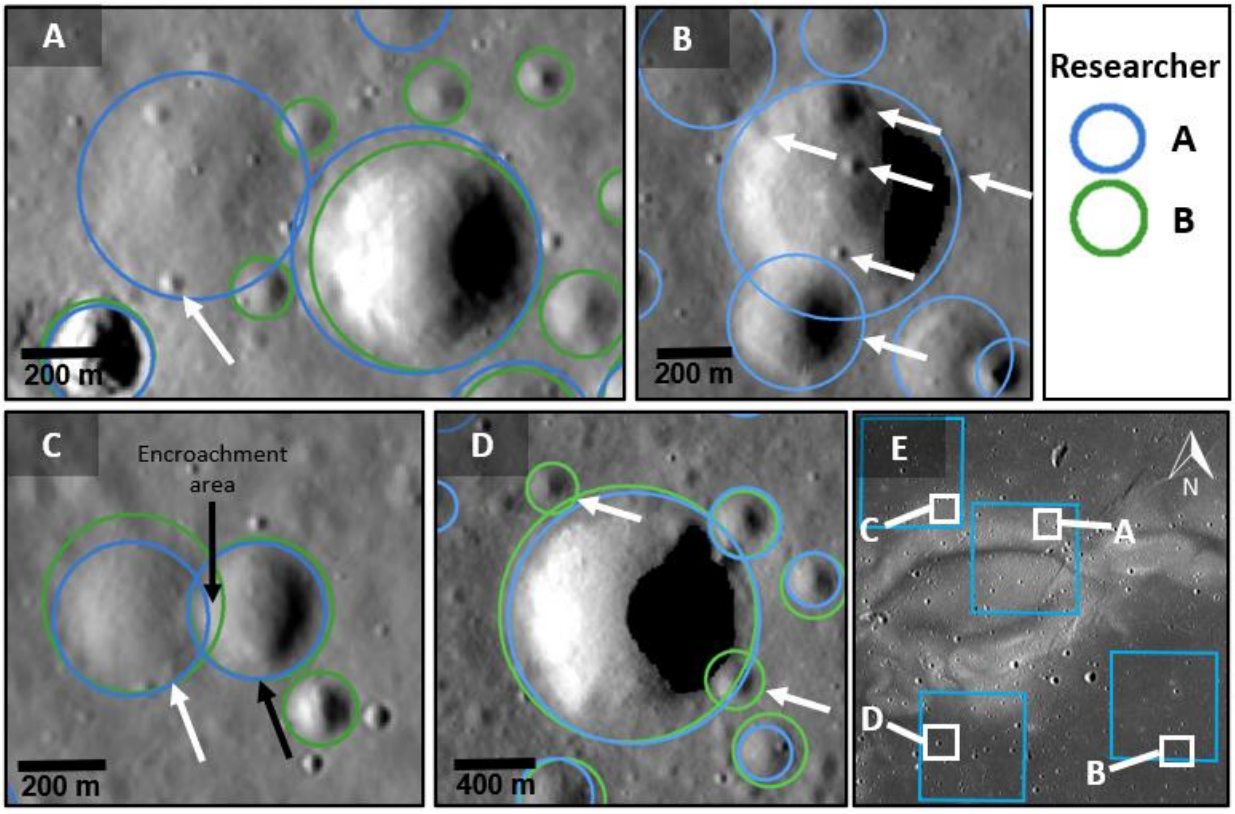

Figure 4.28. Crater degrations states - example craters. Some craters were not counted as a result of the crater degration state. A) A degraded crater (white arrow) in area RG02 was identified by Researcher A (blue), but not measured by Researcher B. This crater is a class 4 – "barely distinguishable" on the Crater preservation state classification system (Arthur et al., 1963; Robbins et al., 2014, see Table 3). B) Superposed craters (white arrows) of various sizes in RG04 that impact the subject crater at any point in time after the original impact and at any location on the rim, ejecta, walls, and floor. Modifications of the rimcrest can make diameter measurements difficult. C) Encroached craters (white arrow) occur when a subsequent crater (black arrow) alters the shape of the earlier crater. These subsequent impact craters can be of any size, however, craters that are proximal and larger than the subject crater are most disruptive. Area RG01. D) Overshadowed craters (white arrows) in RG03 may be missed on an expedited count. A careful reexamination of the count area will reveal these overlooked craters. E) All crater degradation examples are located in the Reiner Gamma study area. The location of each panel A, B, C, and D (white boxes) is shown in relation to each count area (blue).

4.4.7 Production Function (PF) qualities

Multiple production functions (PF) are available for the Moon (Neukum et al., 1983, 1984; Neukum et al., 2001; Hartmann, 2005; Marchi et al., 2009) that describe the cumulative number of craters of a given size for a period of time. The PF used for our measurements (Neukum et al., 2001) was selected as the function has continuous coverage without breaks, is valid for craters diameters larger (~100 km) and smaller (~10 m) than the diameters measured in our study, is the default PF in available tools (Michael and Neukum, 2010) and is an improvement over previous methods (Neukum et al., 2001).

In order to account for the cratering rate over lunar history the PF must not only inventory the primary craters but must also account for multiple factors to arrive at the impactor flux rate at any given point in time. The factors are familiar and include at a minimum: counting a statistically adequate number of craters in a fixed area, selecting a uniform count surface, using optimum solar illumination, measuring craters accurately, and identifying secondary craters. There is more agreement on some factors (e.g., uniform count surface) that there is on other factors (e.g., secondary craters), which has a history of healthy disparate perspectives (e.g., McEwen et al., 2003; McEwen, 2003, 2004; Hartmann, 2005; McEwen and Bierhaus, 2006; Xiao and Strom, 2012; Robbins & Hynek, 2014).

Commonly used PFs and associated CFs are serving their general purpose of providing comparable relative and absolute model ages for this study and the community at large. However, technology has improved and the imagery available has higher resolution and offers additional illumination perspectives since the PF/CFs were defined (Neukum et al., 2001; Hartmann, 2005; Marchi et al., 2009). These improvements actually can be both beneficial and also can have adverse affects on the crater counting process. Several of the beneficial aspects (consistent illumination, high resolution) were used to suggest improvements to the lunar crater-age chronology (Robbins, 2014). Interestingly, the benefit of multiple illumination options (incidence angle, various solar azimuths) for recently available imagery has the net effect of revealing more craters than could be seen on the imagery originally used to produce the PF (Neukum et al., 2001). This is especially true for degraded craters or when the crater diameters approach saturation. The recommended approach to produce consistent results between researchers requires that counts to be performed in conditions that reproduce the original conditions used to derive the PF (i.e., generally a single illumination geometry for a given count area). Naturally, an alternative illumination geometry may

be used if the study area is large and the first illumination geometry is not available. The effect of using imagery with multiple illumination on the PF can be examined in a future study.

5.0 Summary

We contribute age and context for the mare basalts at the three CLPS landing sites: Reiner Gamma, Mare Crisium, and Lacus Mortis. Researchers used accepted crater counting techniques with documented variations to identify and measure craters in our study areas, while using identical tools. Based on this comparative crater count exercise and subsequent analysis of our three CLPS study areas we conclude the following:

1. We determined the AMA of each of our study areas: Reiner Gamma, Mare Crisium, and Lacus Mortis. Each study area was subdivided into two or more smaller count area. All study areas have mare basalts that are Imbrian in age.
    a. Reiner Gamma AMA: 3.29 +0.041/-0.054 to 3.78 +0.018/-0.021 Ga
    b. Mare Crisium AMA: 3.24 +0.083/-0.14 to 3.63 +0.024/-0.029 Ga
    c. Lacus Mortis AMA: 3.26 +0.082/-0.14 to 3.73 +0.033/-0.043 Ga
2. Variations occurred within researcher AMAs.
    a. Researcher A found a difference of 0.07 Ga between count areas in Mare Crisium (MC02, MC03) and 0.23 Ga between areas in Reiner Gamma (RG02, RG04).
    b. Researcher B showed differences of 0.33 Ga for count areas in Reiner Gamma (RG03, RG04), 0.28 Ga for Mare Crisium (MC01, MC02), and 0.07 Ga Lacus Mortis (LM01, LM02).
3. Variations occurred between researcher AMAs.
    a. Count area MC01 showed the closest age agreement between researcher A (3.57 +0.023/-0.027 Ga) and B (3.52 +0.013/-0.014 Ga), with a difference of 0.04 Ga. The ages for MC01 are in near agreement (0.01 Gyr) when the error is taken into account.
    b. Count area MC02 exhibited the largest age difference. Researcher A (3.56 +0.02/-0.024 Ga) and B (3.24 +0.083/-0.014 Ga), with a difference of 0.32 Ga. These ages are not in agreement, even when the error is considered.
    c. Although current CSFD tools allow the calculation of AMA to the second decimal place (Michael and Neukum, 2010), we recommend presenting AMAs with single decimal precision.

4. Variations in AMAs between researchers for the same count areas were the result of differences in the number of secondary and degraded craters identified and to a lesser extent crater diameter measurements. An additional factor was the use of Kaguya imagery with differing illumination (e.g., researcher A, evening; researcher B, morning).
5. An average absolute model age was determined for all researchers for each study area. Averaging the individual count areas for a study area assumes that the basalt flows were contemporaneous.
    a. Reiner Gamma AMA: 3.58 Ga
    b. Mare Crisium AMA: 3.49 Ga
    c. Lacus Mortis AMA: 3.59 Ga

Our work builds on the legacy work of the crater counting community, strives to incorporated previous lessons learned (Crater Analysis Techniques Working Group, 1979; Planetary Crater Consortium (PCC), etc.) and adds new approaches to improve the accuracy of remotely determined absolute model ages of lunar and planetary surfaces.

In summary, crater count practices shall include:

- Accurate locating of count boundaries to exclude secondary craters
- Exclusion of secondary craters interior to count boundaries with exclusionary polygons (excluded area shall deducted from the overall count area).
- Identification single secondary craters for exclusion from AMA determination.
- Diameter measurements
    - Use of high-resolution DTM aspect diameters to calibrate measurements
    - Inspection of high-resolution orbital imagery to improve rimcrest location measurements
    - Leverage surface imagery to verify rimcrest conditon
- When working in a project setting with multiple researchers we recommend
    - Establish standardized crater count projects that use the same imagery (solar azimuth and incidence, pixel resolution)
    - Leverage identical tools to capture craters and perform AMA calculations
    - Comparison of diameter measurement results to a set of standard craters in each of the four degradation states

We recommend that researchers in the community strive to understand crater counting mechanics, verification aids, and personal biases in order to determine more consistent and accurate AMAs. Data sharing between community members by all available means (cratering conference/meetings, supplemental section of publications, data sharing portals) promotes confidence in the results and promotes openness and further discussion of the various subtleties that affect the crater counting process.

CHAPTER 5: CONCLUSIONS AND FUTURE WORK

Our research uses multiple instruments, resolution, and spectral coverage from various spacecraft missions to understand lunar volcanic processes and the age of mare flows. We adopted new data and processing techniques as our research progressed.

In the second chapter, we explored the volcanic processes in the Gassendi region begun by previous researchers (e.g., Schultz, 1976; Hawke et al., 1991). The diverse volcanic history and morphology is likely due to the major lunar terranes that meet in southern oceanus procellarum, including the mare/highlands boundary, southeast periphery of the PKT (high thorium) region (Jolliff et al., 2000), boundary between the thicker highlands crust to the south and the thinner crust associated with the mare region to the north (Zuber et al., 2013). Mare Humorum, a 425 km impact basin adjacent to study area, exerted a major influence on the volcanic processes in the region.

New volcanic features identified include cryptomaria, pyroclastic deposits, mare basalts, and lava lake structures. A Nectarian-aged cryptomare was identified at a shallow depth in the highlands to the west of Gassendi crater. A previously unmapped pyroclastic was identified in the highlands northeast of Gassendi crater. The deposit is in the glassy pyroclastic group and erupted in a vulcanian-style eruption where the juvenile glass material cooled quickly in an optically thin gas cloud. The deposit had a different eruption style (more glass, less blocks), mineralogy, and source region than the Mersenius eruptions to the southwest.

Our examination of Gassendi crater revealed additional cryptomaria located on the fractured floor based on the spectral and geochemical data for small dark-haloed impact craters. The cryptomaria are colocated with the surfaces of three lava lakes that were identified on the northeast, northwest, and southwest floor. The constructs are depressions with bounding curvilinear scarps of uniform elevations. Interior scarps were formed as lake levels lowered. The lava lakes occurred over floor fractures, which allowed lava to enter and drain. The surfaces of the lava lakes exhibit higher mafic values (FeO 12-15 wt. %) than the floor of Gassendi (10-12 wt. %). The spectral data confirm mare basalt mineral assemblages (i.e., high-Ca pyroxene).

The Gassendi region was volcanically active beginning in the Nectarian with two episodes of mare emplacement from two different sources or a single source that evolved in composition between eruptions formed these deposits. Subsequently, Gassendi crater volcanism was widespread and of short duration. The lava lake eruption events have a model age of ~3.6 ± 0.03

Ga and occurred ~300 Ma after the floor was emplaced. The presence of lava lakes suggests that, at least in some instances, magmas stall near the surface. The relation between lava lakes and floor-fractured craters may result from the crustal structure (e.g., an impervious or a low-density layer beneath the crater) and lack of mare flooding that floor-fractured craters provide.

In the future the criteria developed to identify lava lakes in the Gassendi region may be used to search for lava lakes within other floor-fractured craters. We examined just 16% of all known floor-fractured craters and located subsidence morphology in mare basalts on the floors of multiple floor-fractured craters. Initial mapping suggests that lava lakes occur globally but preferentially occur in floor-fractured craters. As a result, lava lakes may signal a unique class of floor-fractured crater worthy of further investigation.

In the third chapter we examined the north-eastern Oceanus Procellarum (NE-OP) region with the goal to understand the composition and timing of mare volcanism processes in this area of the Moon. This region exhibits multiple basaltic flows with a wide range of model ages, from 1.4 – 3.5 Ga, spanning 70% of lunar volcanic history. Our model age data from 21 distinct count areas shows that the maria in NE-OP is comprised of a patchwork of individual flows, which can be as young as 1.4 ±0.2 Ga to as old as 3.5 +0.1/-0.2 Ga. Our average age for all count areas in NE-OP (spectral area EM4) is 2.3 Ga. The frequency of eruption in NE-OP was bimodal, peaking at ~3.0+ Ga, near the end of the Imbrian period, and the second peak in eruption frequency occurred during the Eratosthenian period (2.2 Ga; Wilhems, 1987). Chang'E-5 will likely return basaltic rock and regolith material with a dominant radiometric age of ~3.0 +0.2/-0.3 Ga that reflects the model age of the landing location. Younger (1.4 – 2.6 Ga) and older sample ages will also be found, due to impact mixing from neighboring flows.

We compare our count results directly with a previous researchers' count results and generally to all previous count work performed in the region. Our NE-OP and Chang'E-5 count area model ages are in disagreement with model ages determined by other researchers, which are commonly inconsistent with each other. The model ages determined here are systematically older than those calculated by previous workers. The three key reasons our model ages are older are 1) differences in measured rimcrest-to-rimcrest crater diameters, 2) identification of primary versus secondary craters, and 3) detection and counting of degraded craters.

Generally, the wide distribution of model ages and the near-uniform FeO and TiO_2 abundance of the basalt within our study area indicate that multiple eruptions occurred over an

extended period. This finding contradicts previous assumptions that because this region's composition and spectral properties are similar, it is a unit of a single age.

In the fourth chapter we build on the absolute model age work begun in chapter 3 by contributing age and context for the mare basalts at the three CLPS landing sites: Reiner Gamma, Mare Crisium, and Lacus Mortis. Previously, we compared our count results to earlier researchers; this updated effort used experienced researchers under controlled conditions. Researchers used accepted crater counting techniques with documented variations to identify and measure craters in our study areas, while using identical tools.

We determined the AMA of each of our study areas, which were subdivided into two or more smaller count areas. All study areas have mare basalts that are Imbrian in age, specifically: Reiner Gamma AMA: 3.29 +0.041/-0.054 to 3.78 +0.018/-0.021 Ga, Mare Crisium AMA: 3.24 +0.083/-0.14 to 3.63 +0.024/-0.029 Ga, and Lacus Mortis AMA: 3.26 +0.082/-0.14 to 3.73 +0.033/-0.043 Ga.

Variations were documented between researcher AMAs. Count area MC01 showed the closest age agreement between researcher A (3.57 +0.023/-0.027 Ga) and B (3.52 +0.013/-0.014 Ga), with a difference of 0.04 Ga. The ages for MC01 are in near agreement (0.01 Gyr) when the error is taken into account. The largest variation was observed for count area MC02. Researcher A (3.56 +0.02/-0.024 Ga) and B (3.24 +0.083/-0.014 Ga), with a difference of 0.32 Ga. These ages are not in agreement, even when the error is considered.

Variations in AMAs between researchers for the same count areas were the result of differences in the number of secondary and degraded craters identified and to a lesser extent crater diameter measurements. We recommend that researchers in the community strive to understand crater counting mechanics, verification aids, and personal biases in order to determine more consistent and accurate AMAs. Data sharing between community members by all available means (cratering conference/meetings, supplemental section of publications, data sharing portals) promotes confidence in the results and promotes openness and further discussion of the various subtleties that affect the crater counting process.

Our crater counting research builds on the legacy work of the crater counting community, strives to incorporated previous lessons learned (Crater Analysis Techniques Working Group, 1979; Planetary Crater Consortium (PCC), etc.) and adds new approaches to improve the accuracy of remotely determined absolute model ages of lunar and planetary surfaces. While working

toward consistent model ages, we recommend that detailed crater count supporting data (i.e., coordinates of the location, diameter of each crater counted, area and edge coordinates of the count area, spacecraft imagery and resolution) be submitted as a required supplement in the publication process.

REFERENCES

Aldrin, E.E., Armstrong Jr., N.A., Collins, M., 1969. Crew observations. In: Apollo 11 Preliminary Science Report. NASA Manned Spacecraft Center, Houston, Texas, pp. 35–40.

Antonenko, I., Head, J.W., Mustard, J.F., Hawke, B.R., 1995. Criteria for the detection of lunar cryptomaria. Earth, Moon Planets 69, 141–172.

Arthur, D.W.G., Agnieray, A.P., Horvath, R.A., Wood, C.A., Chapman, C.R., 1963. The system of lunar craters, quadrant I. Comm. Lunar Planet. Lab. 2, #30.

Arvidson, R. et al., Crater Analysis Techniques Working Group, 1979. Standard techniques for presentation and analysis of crater size-frequency data. Icarus, 37(2), pp.467-474.

Baldwin, R.B., 1985. Relative and absolute ages of individual craters and the rate of infalls on the Moon in the post-Imbrium period. Icarus, 61(1), pp.63-91.

Bandfield, J.L., Ghent, R.R., Vasavada, A.R., Paige, D.A., Lawrence, S.J. and Robinson, M.S., 2011. Lunar surface rock abundance and regolith fines temperatures derived from LRO Diviner Radiometer data. Journal of Geophysical Research: Planets, 116(E12).

Barker, M.K., Mazarico, E., Neumann, G.A., Zuber, M.T., Haruyama, J. and Smith, D.E., 2016. A new lunar digital elevation model from the Lunar Orbiter Laser Altimeter and SELENE Terrain Camera. Icarus, 273, pp.346-355.

Barsukov, V.L., 1977. Preliminary data for the regolith core brought to earth by the automatic lunar station Luna 24. In Lunar and Planetary Science Conference Proceedings (Vol. 8, pp. 3303-3318).

Beaty, D.W., Albee, A.L., 1980. The geology and petrology of the Apollo 11 landing site. Proc. Lunar Planet. Sci. Conf. 11, 23–35.

Bell, J.F. and Hawke, B.R., 1984. Lunar dark-haloed impact craters: Origin and implications for early mare volcanism. Journal of Geophysical Research: Solid Earth, 89(B8), pp.6899-6910.

Besse, S., Sunshine, J., Staid, M., Boardman, J., Pieters, C., Guasqui, P., Malaret, E., McLaughlin, S., Yokota, Y. and Li, J.Y., 2013. A visible and near-infrared photometric correction for Moon Mineralogy Mapper (M3). Icarus, 222(1), pp.229-242.

Besse, S., Sunshine, J.M. and Gaddis, L.R., 2014. Volcanic glass signatures in spectroscopic survey of newly proposed lunar pyroclastic deposits. Journal of Geophysical Research: Planets, 119(2), pp.355-372.

Blewett, D.T., Hawke, B.R., Lucey, P.G., Taylor, G.J., 1995. Remote sensing and geological studies of the Schiller–Schickard region of the Moon. J. Geophys. Res. 100(E8), 16959–16977. doi:10.1029/95JE01409.

Blewett, D.T., Coman, E.I., Hawke, B.R., Gillis-Davis, J.J., Purucker, M.E. and Hughes, C.G., 2011. Lunar swirls: Examining crustal magnetic anomalies and space weathering trends. Journal of Geophysical Research: Planets, 116(E2).

Blewett, D.T., Denevi, B.W., Cahill, J.T. and Klima, R.L., 2021a. Near-UV and near-IR reflectance studies of lunar swirls: Implications for nanosize iron content and the nature of anomalous space weathering. Icarus, 364, p.114472.

Blewett, D.T., Halekas, J., Ho, G., Greenhagen, B.T., Anderson, B.J., Regoli, L., Vines, S.K., Jahn, J.M., Kollmann, P., Denevi, B.W. and Meyer, H.M., 2021b, August. Lunar Vertex: A PRISM Mission to a Magnetic Anomaly. In 2021 Annual Meeting of the Lunar Exploration Analysis Group (Vol. 2635, p. 5016).

Blewett, D.T., Meyer, H.M., Kinczyk, M.J., Halekas, J., Ho, G., Greenhagen, B.T., Denevi, B.W., Klima, R.L., Cahill, J.T.S., Anderson, B.J., Vines, S.K., Waller, C.D., Regoli, L., Jahn, J.M., Kollmann, P., Hood, L.L., and others, 2023, Selection and Characterization of the Landing Site for Nasa CLPS Prism1 Lunar Lander Mission CP-11, LPSC54, #1780.

Boardman, J.W., Pieters, C.M., Green, R.O., Lundeen, S.R., Varanasi, P., Nettles, J., Petro, N., Isaacson, P., Besse, S. and Taylor, L.A., 2011. Measuring moonlight: An overview of the spatial properties, lunar coverage, selenolocation, and related Level 1B products of the Moon Mineralogy Mapper. Journal of Geophysical Research: Planets, 116(E6).

Boroughs, L.L. and Spudis, P.D., 2001, March. The stratigraphy of lava flows in northern Oceanus Procellarum, Moon. In Lunar and Planetary Science Conference (p. 1192).

Boyce, J.M., Dial, A.L. and Soderblom, L.A., 1974. Ages of the lunar nearside light plains and maria. In Lunar and Planetary Science Conference Proceedings (Vol. 5, pp. 11-23).

Boyce, J.M. and Dial Jr, A.L., 1975. Relative ages of flow units in Mare Imbrium and Sinus Iridum. In In: Lunar Science Conference, 6th, Houston, Tex., March 17-21, 1975, Proceedings. Volume 3.(A78-46741 21-91) New York, Pergamon Press, Inc., 1975, p. 2585-2595. (Vol. 6, pp. 2585-2595).

Boyce, J.M., 1976, April. Ages of flow units in the lunar nearside maria based on Lunar Orbiter IV photographs. In Lunar and Planetary Science Conference Proceedings (Vol. 7, pp. 2717-2728).

Boyce, J.M., Schaber, G.G. and Dial, A.L., 1977. Age of Luna 24 mare basalts based on crater studies. Nature, 265(5589), pp.38-39.

Boyce, J.M. and Johnson, D.A., 1977. Ages of flow units in Mare Crisium based on crater density. In Lunar and Planetary Science Conference Proceedings (Vol. 8, pp. 3495-3502).

Boyce, J.M. and Johnson, D.A., 1978. Ages of flow units in the far eastern maria and implications for basin-filling history. In Lunar and Planetary Science Conference Proceedings (Vol. 9, pp. 3275-3283).

Bridgen, R.L., 1933. The basis of directional orientation. Journal of Comparative Psychology, 16(2), p.159.

Burns, K., Robinson, M. S., Speyerer, E., and LROC Science Team, 2011. Two years of digital terrain model production using the Lunar Reconnaissance Orbiter Narrow Angle Camera. In AGU Fall Meeting Abstracts 43, abstract 1706, http://adsabs.org/2011AGUFM.P43D1706B.

Bussey, B., Clarke, S.W., Jenkins, J. and Bailey, B.E., 2019, December. NASA's Lunar Discovery And Explorartion Program. In AGU Fall Meeting Abstracts (Vol. 2019, pp. PA54B-11).

Cahill, J.T.S., Martin, A.C., Hayne, P.O., Patterson, G.W., Greenhagen, B.T., Wieczorek, M.A. and Bhiravarasu, S.S., 2022. A Comparison of the Atlas/Hercules Thermophyiscal Anomaly and Radar-Dark Halo Craters. LPI Contributions, 2678, p.2797.

Campbell, B.A., Hawke, B.R. and Thompson, T.W., 1997. Regolith composition and structure in the lunar maria: Results of long-wavelength radar studies. Journal of Geophysical Research: Planets, 102(E8), pp.19307-19320.

Campbell, B.A. and Hawke, B., 2005. Radar mapping of lunar cryptomaria east of Orientale basin. Journal of Geophysical Research: Planets, 110(E9).

Campbell, B.A., Campbell, D.B., Margot, J.L., Ghent, R.R., Nolan, M., Carter, L.M. and Stacy, N.J.S., 2007. Focused 70-cm wavelength radar mapping of the moon. IEEE Transactions on Geoscience and Remote Sensing.

Campbell, B.A., Carter, L.M., Hawke, B.R., Campbell, D.B. and Ghent, R.R., 2008. Volcanic and impact deposits of the Moon's Aristarchus Plateau: A new view from Earth-based radar images. Geology, 36(2), pp.135-138.

Campbell, B.A., Hawke, B.R., Carter, L.M., Ghent, R.R. and Campbell, D.B., 2009. Rugged lava flows on the Moon revealed by Earth-based radar. Geophysical research letters, 36(22).

Campbell, B.A., Carter, L.M., Campbell, D.B., Nolan, M., Chandler, J., Ghent, R.R., Hawke, B.R., Anderson, R.F. and Wells, K., 2010. Earth-based 12.6-cm wavelength radar mapping of the Moon: New views of impact melt distribution and mare physical properties. Icarus, 208(2), pp.565-573.

Casella, C.J. and Binder, A.B., 1972. Geologic map of the Cleomedes quadrangle of the Moon: US Geol. Survey Misc. Geol. Inv. Map I-707.

Chapman, C.R., 2015. A critique of methods for analysis of crater size-frequency distributions. Issues in Crater Studies and the Dating of Planetary Surfaces, 1841, p.9039.

Chevrel, S. and Pinet, P., 1990. Near-infrared multispectral images for Gassendi crater-Mineralogical and geological inferences. Lunar and Planetary Science Conference Proceedings 20, 187-194.

Chevrel, S. and Pinet, P.C., 1992. Revisited geology of Gassendi crater from Earth-based near-infrared multispectral solid state imaging. Lunar and Planetary Science Conference Proceedings 22, 249-258.

Clark, R.N., Pieters, C.M., Green, R.O., Boardman, J.W. and Petro, N.E., 2011. Thermal removal from near-infrared imaging spectroscopy data of the Moon. Journal of Geophysical Research: Planets, 116(E6).

Colwell, R.N., 1966. Uses and limitations of multispectral remote sensing.

Delano, J.W., 1986. Pristine lunar glasses: Criteria, data, and implications. Journal of Geophysical Research: Solid Earth, 91(B4), pp.201-213.

Dombard, A. J., Gillis, J. J., 2001. Testing the viability of topographic relaxation as a mechanism for the formation of lunar floor-fractured craters. J. Geophys. Res. 106, 27,901-27,910.

Eaton, J.P., and Murata, K.J., 1960. How volcanoes grow. Science 132, 3432, 925-938.

Eaton, J.P., Richter, D.H. and Krivoy, H.L., 1987. Cycling of magma between the summit reservoir and Kilauea Iki lava lake during the 1959 eruption of Kilauea volcano. US Geol. Surv. Prof. Pap, 1350, pp.1307-1335.

Elger, T.G., 1895. The Moon: a full description and map of its principal physical features. G. Philip & son.

Eliason, E.M., McEwen, A.S., Robinson, M.S., Lee, E.M., Becker, T., Gaddis, L., Weller, L.A., Isbell, C.E., Shinaman, J.R., Duxbury, T. and Malaret, E., 1999. Digital processing for a global multispectral map of the Moon from the Clementine UVVIS imaging instrument. Lunar and Planetary Science Conference 30, 1933.

Elphic, R.C., Lawrence, D.J., Feldman, W.C., Barraclough, B.L., Gasnault, O.M., Maurice, S., Lucey, P.G., Blewett, D.T. and Binder, A.B., 2002. Lunar Prospector neutron spectrometer constraints on TiO2. J. Geophys. Res. 107, E4.

Fairweather, J.H., Lagain, A., Servis, K., Benedix, G.K., 2023, Lunar Surface Model Age Derivation-Comparing Automatic and Human Crater Counting Across LRO-NAC & Kaguya TC Images, LPSC54, #1234.

Fassett, C.I., Head, J.W., Kadish, S.J., Mazarico, E., Neumann, G.A., Smith, D.E. and Zuber, M.T., 2012. Lunar impact basins: Stratigraphy, sequence and ages from superposed impact crater populations measured from Lunar Orbiter Laser Altimeter (LOLA) data. Journal of Geophysical Research: Planets, 117(E12).

Fassett, C.I. and Thomson, B.J., 2014. Crater degradation on the lunar maria: Topographic diffusion and the rate of erosion on the Moon. Journal of Geophysical Research: Planets, 119(10), pp.2255-2271.

Fassett, C.I., 2016. Analysis of impact crater populations and the geochronology of planetary surfaces in the inner solar system. Journal of Geophysical Research: Planets, 121(10), pp.1900-1926.

Florenskii, K.P., Basilevskii, A.T., Ivanov, A.V., Pronin, A.A. and Rode, O.D., 1977. Luna 24-Geologic setting of landing site and characteristics of sample core/Preliminary data. In In: Lunar Science Conference, 8th, Houston, Tex., March 14-18, 1977, Proceedings. Volume 3.(A78-41551 18-91) New York, Pergamon Press, Inc., 1977, p. 3257-3279. (Vol. 8, pp. 3257-3279).

Florenskii, C.P., Basilevskii, A.T., Bobina, N.N., Burba, G.A., Grebennik, N.N., Kuzmin, R.O., Polosukhin, B.P., Popovich, V.D., Pronin, A.A., Ronca, L.B. 1978. The floor of crater Le Monier - A study of Lunokhod 2 data, Lunar and Planetary Science Conference Proceedings 9, 1978LPSC....9.1449F.

Flynn, L.P. and Mouginis-Mark, P.J., 1992. Cooling rate of an active Hawaiian lava flow from nighttime spectroradiometer measurements. Geophysical Research Letters, 19(17), pp.1783-1786.

Francis, P. (1993) Volcanoes. A planetary perspective, Clarendon Press, Oxford (UK), 452 p., ISBN 0-19-854452-9.

Gaddis, L.R., Pieters, C.M., Hawke, B.R., 1985. Remote sensing of lunar pyroclastic mantling deposits. Icarus, 61(3), 461-489.

Gaddis, L.R., Staid, M.I., Tyburczy, J.A., Hawke, B.R., Petro, N.E., 2003. Compositional analyses of lunar pyroclastic deposits. Icarus, 161(2), 262-280.

Gault, D.E., 1970. Saturation and equilibrium conditions for impact cratering on the lunar surface: Criteria and implications. Radio Science, 5(2), pp.273-291.

Gault, D., Hörz, F., Brownlee, D., Hartung, J., 1974. Mixing of the lunar regolith. Lunar and Planetary Science Conference Proceedings, Vol. 5, pp. 2365-2386.

Gebbing, T., Hiesinger, H., Iqbal, W. and van der Bogert, C.H., 2021, March. New Geologic Map of the Apollo 16 Landing Site: Implications for Crater Size-Frequenzies of the Lunar Chronology. In 52nd Lunar and Planetary Science Conference (No. 2548, p. 1986).

Ghent, R.R., Leverington, D.W., Campbell, B.A., Hawke, B.R. and Campbell, D.B., 2005. Earth-based observations of radar-dark crater haloes on the Moon: Implications for regolith properties. Journal of Geophysical Research: Planets, 110(E2).

Giguere, T.A., Taylor, G.J., Hawke, B., Lucey, P.G., 2000. The titanium contents of lunar mare basalts. Meteoritics & Planetary Science, 35(1), 193-200.

Giguere, T.A., Hawke, B., Blewett, D.T., Bussey, D.B.J., Lucey, P.G., Smith, G.A., Spudis, P.D., Taylor, G.J., 2003. Remote sensing studies of the Lomonosov-Fleming region of the Moon. J. Geophys. Res., 108(E11).

Giguere, T.A., Boyce, J.M., Gillis-Davis, J.J. and Stopar, J.D., 2020. Lunar Mare Basalt Age and Composition in Northeastern Oceanus Procellarum. LPI Contributions, 2251, p.2070.

Giguere, T.A., Boyce, J.M., Gillis-Davis, J.J. and Stopar, J.D., 2021, March. Determination of Lunar Lava Flow Ages in Northeastern Oceanus Procellarum: The Need for Calibrating Crater Counting Procedures Across the Field. In Lunar and Planetary Science Conference (No. 2548, p. 1091).

Giguere, T.A., Boyce, J.M., Gillis-Davis, J.J., Trang, D. and Stopar, J.D., 2022. Lava flow ages in northeastern Oceanus Procellarum: The need for calibrating crater counting procedures. Icarus, 375, p.114838.

Gillis, J.J. and Spudis, P.D., 2000. Geology of the Smythii and Marginis region of the Moon: Using integrated remotely sensed data. Journal of Geophysical Research: Planets, 105(E2), pp.4217-4233.

Gillis, J. J., Jolliff, B. L., Elphic, R. C., 2003. A revised algorithm for calculation TiO_2 concentrations from Clementine UVVIS data: A synthesis of rock, soil, and remotely sensed TiO_2 concentrations. J. Geophys. Res. 108, 5009, doi:10.1029/2001JE001515.

Gillis, J. J., Jolliff, B. J., Korotev, R. L., 2004. Lunar surface geochemistry: Global concentrations of Th, K, and FeO as derived from Lunar Prospector and Clementine data. Geochim. Cosmochim. Acta. 68, 3791-3805.

Glotch, T.D., Bandfield, J.L., Lucey, P.G., Hayne, P.O., Greenhagen, B.T., Arnold, J.A., Ghent, R.R. and Paige, D.A., 2015. Formation of lunar swirls by magnetic field standoff of the solar wind. Nature communications, 6(1), p.6189.

Greeley, R. and Gault, D.E., 1970. Precision size-frequency distributions of craters for 12 selected areas of the lunar surface. The Moon, 2(1), pp.10-77.

Greeley, R., 1971. Lava tubes and channels in the lunar Marius Hills. The Moon, 3(3), pp.289-314.

Greeley, R., 1976. Modes of emplacement of basalt terrains and an analysis of mare volcanism in the Orientale Basin. In Lunar and Planetary Science Conference Proceedings (Vol. 7, pp. 2747-2759).

Greeley, R., Spudis, P.D., 1978. Mare volcanism in the Herigonius region of the Moon. Lunar and Planetary Science Conference Proceedings 9, 3333-3349.

Green, R.O., Pieters, C., Mouroulis, P., Eastwood, M., Boardman, J., Glavich, T., Isaacson, P., Annadurai, M., Besse, S., Barr, D. and Buratti, B., 2011. The Moon Mineralogy Mapper (M^3) imaging spectrometer for lunar science: Instrument description, calibration, on-orbit measurements, science data calibration and on-orbit validation. Journal of Geophysical Research: Planets, 116(E10).

Gustafson, J.O., Gaddis, L.R., Hawke, B.R., Giguere, T.A., 2014. Pyroclastic Deposits Within Floor-Fractured Mersenius Crater. Lunar and Planetary Science Conference 45, 2044.

Hackwill, T., Guest, J., Spudis, P., 2006. Stratigraphy and evolution of basalts in Mare Humorum and southeastern Procellarum. Meteoritics & Planetary Science, 41(3), 479-488.

Hall, J.L., Solomon, S.C. and Head, J.W., 1981. Lunar floor-fractured craters: Evidence for viscous relaxation of crater topography. Journal of Geophysical Research: Solid Earth, 86(B10), 9537-9552.

Hallowes, G., 1916. Report of the Lunar Section, Gassendi. British Astronomical Association, 20, doi:1916MmBAA..20T.106.

Hamilton, C.W., Scheidt, S.P., Bleacher, J.E., Irwin, R.P. and Garry, W.B., 2015, March. "Fill and Spill" Lava Emplacement Associated with the December 1974 Flow on Kilauea Volcano, Hawaii, USA. In Lunar and Planetary Science Conference (Vol. 46, p. 1072).

Harris, A.J.L., Flynn, L.P., Rothery, D.A., Oppenheimer, C.,Sherman, S.B., 1999. Mass flux measurements at active lava lakes: implications for magma recycling. J. Geophys. Res. 104, 7117–7136.

Hartmann, W.K. and Davis, D.R., 1975. Satellite-sized planetesimals and lunar origin. Icarus, 24(4), pp.504-515.

Hartmann, W.K., 2005. Martian cratering 8: Isochron refinement and the chronology of Mars. Icarus, 174(2), pp.294-320.

Haruyama, J., T. Matsunaga, M. Ohtake, T. Morota, C. Honda, Y. Yokota, M. Torii, Y. Ogawa, and LISM Working Group, 2008a. Global lunar surface mapping experiment using the Lunar Imager/Spectrometer on SELENE, Earth Planets Space, 60, 243– 256.

Haruyama, J., Ohtake, M., Matsunaga, T., Morota, T., Yokota, Y., Honda, C., Hirata, N., Demura, H., Iwasaki, A., Nakamura, R. and Kodama, S., 2008b. Planned radiometrically calibrated and geometrically corrected products of lunar high-resolution terrain camera on SELENE. Adv. Space Res 42(2), 310–316. doi: 10.1016/j.asr.2007.04.062.

Haruyama, J., Ohtake, M., Matsunaga, T., Otake, H., Ishihara, Y., Masuda, K., Yokota, Y. and Yamamoto, S., 2014, March. Data products of SELENE (Kaguya) terrain camera for future lunar missions. In Lunar and Planetary Science Conference (Vol. 45, p. 1304).

Hawke B., Spudis P., 1980. Geochemical anomalies on the eastern limb and farside of the moon. Proc.Conf. Lunar Highlands Crust, 467.

Hawke, B.R. and Bell, J.F., 1981, March. Spectral Studies of Lunar Dark-Halo Craters: Preliminary Results. Lunar and Planetary Science Conference 12, 412-414. 1981LPI....12..412H.

Hawke, B.R. and Bell, J.F., 1983, March. Spectral Reflectance studies of dark-haloed impact craters: implications for the composition and distribution of ancient lunar basalts. In Lunar and Planetary Science Conference (Vol. 14, pp. 287-288).

Hawke, B.R., Spudis, P.D., Clark, P.E., 1985. The origin of selected lunar geochemical anomalies: Implications for early volcanism and the formation of light plains. Earth, Moon, and Planets, 32(3), 257-273.

Hawke, B.R., Coombs, C.R. and Clark, B., 1990. Ilmenite-rich pyroclastic deposits: An ideal lunar resource. In Lunar and Planetary Science Conference Proceedings (Vol. 20, pp. 249-258).

Hawke, B. R., Peterson, C. A., Lucey, P. G., Taylor, G. J., Blewett, D. T., Campbell, B. A., Coombs, C. R., Spudis, P. D., 1993. Remote sensing studies of the terrain northwest of Humorum basin. Geophysical Research Letters, 20, 10.1029/92GL02921.

Hawke, B. R., Gillis, J. J., Giguere, T. A., Blewett, D. T., Lawrence, D. J., Lucey, P. G, Smith, G. A., Spudis, P. D., Taylor, G. J., 2005. Remote sensing and geologic studies of the Balmer-Kapteyn region of the Moon. J. Geophys. Res., 110, doi:10.1029/2004JE002383.

Hawke, B.R., Giguere, T.A., Gillis-Davis, J.J., Lucey, P.G., Peterson, C.A., Lawrence, S.J., Stopar, J.D., Robinson, M.S., 2013. An Investigation of Cryptomare and Pyroclastic Deposits in the Gassendi Region of the Moon. Lunar and Planetary Science Conference 44, 1894.

Hawke, B.R., Giguere, T.A., Peterson, C.A., Lawrence, S.J., Stopar, J.D., Gaddis, L.R., 2015. Cryptomare, lava lakes, and pyroclastic deposits in the Gassendi region of the moon: Final Results. Lunar and Planetary Science Conference 46, 1310.

Head III, J.W., 1976. Lunar volcanism in space and time. Reviews of Geophysics, 14(2), pp.265-300.

Head, J.W., Wilson, L., 1979. Alphonsus-type dark-halo craters: morphology, morphometry and eruption conditions. Proc. Lunar and Planet. Sci. Conf. 10th, 10, pp. 2861–2897.

Head, J. W., Wilson, L., 1992. Lunar mare volcanism: Stratigraphy, eruption conditions, and the evolution of secondary crusts, Geochim. Cosmochim. Acta, 56, 2144–2175.

Head, J.W., Murchie, S., Mustard, J.F., Pieters, C.M., Neukum, G., McEwen, A., Greeley, R., Nagel, E., Belton, M.J., 1993. Lunar impact basins: New data for the western limb and far side (Orientale and South Pole-Aitken basins) from the first Galileo flyby. J. Geophys. Res. 98(E9), 17149-17181.

Helson, H. and Fehrer, E.V., 1932. The role of form in perception. The American Journal of Psychology, 44(1), pp.79-102.

Henriksen, M.R., Manheim, M.R., Burns, K.N., Seymour, P., Speyerer, E.J., Deran, A., Boyd, A.K., Howington-Kraus, E., Rosiek, M.R., Archinal, B.A. and Robinson, M.S., 2017. Extracting accurate and precise topography from LROC narrow angle camera stereo observations. Icarus, 283, pp.122-137.

Hicks, M.D., Buratti, B.J., Nettles, J., Staid, M., Sunshine, J., Pieters, C.M., Besse, S. and Boardman, J., 2011. A photometric function for analysis of lunar images in the visual and infrared based on Moon Mineralogy Mapper observations. Journal of Geophysical Research: Planets, 116(E6).

Hiesinger, H., Jaumann, R., Neukum, G. and Head, J.W., 2000. Ages of mare basalts on the lunar nearside. J. Geophys. Res. 105(E12), 29239-29275.

Hiesinger, H., Head III, J.W., Wolf, U., Jaumann, R. and Neukum, G., 2002. Lunar mare basalt flow units: Thicknesses determined from crater size-frequency distributions. Geophysical Research Letters, 29(8), pp.89-1.

Hiesinger, H., Head III, J.W., Wolf, U., Jaumann, R. and Neukum, G., 2003. Ages and stratigraphy of mare basalts in oceanus procellarum, mare nubium, mare cognitum, and mare insularum. Journal of Geophysical Research: Planets, 108(E7).

Hiesinger, H., Head, J.W., Wolf, U., Jaumann, R. and Neukum, G., 2006. New ages for basalts in Mare Fecunditatis based on crater size-frequency measurements. Lunar and Planetary Science XXXVII, 1303, pp.abstract-1151.

Hiesinger, H., Head III, J.W., Wolf, U., Jaumann, R. and Neukum, G., 2010. Ages and stratigraphy of lunar mare basalts in Mare Frigoris and other nearside maria based on crater size-frequency distribution measurements. Journal of Geophysical Research: Planets, 115(E3).

Hiesinger, H., Head, J.W., Wolf, U., Jaumann, R. and Neukum, G., 2011a. Ages and stratigraphy of lunar mare basalts: A synthesis. Recent Advances and Current Research Issues in Lunar Stratigraphy, 477, pp.1-51.

Hiesinger, H., van der Bogert, C.H., Reiss, D. and Robinson, M.S., 2011b, March. Crater size-frequency distribution measurements of Mare Crisium. In Lunar and Planetary Science Conference (No. 1608, p. 2179).

Hiesinger, H.V., van der Bogert, C.H., Pasckert, J.H., Funcke, L., Giacomini, L., Ostrach, L.R. and Robinson, M.S., 2012. How old are young lunar craters?. Journal of Geophysical Research: Planets, 117(E12).

Holcomb, R., 1971. Terraced depressions in lunar maria. Journal of Geophysical Research, 76(23), 5703-5711.

Hon, E. and Stopar, J., 2020. Dating Young Mare Flows: Lichtenberg and Flamsteed Regions. LPI, (2326), p.1081.

Hood, L.L. and Schubert, G., 1980. Lunar magnetic anomalies and surface optical properties. Science, 208(4439), pp.49-51.

Hood, L.L. and Williams, C.R., 1989. The lunar swirls-Distribution and possible origins. In Lunar and planetary science conference proceedings (Vol. 19, pp. 99-113).

Huang, Y.H., Minton, D.A., Hirabayashi, M., Elliott, J.R., Richardson, J.E., Fassett, C.I. and Zellner, N.E., 2017. Heterogeneous impact transport on the Moon. Journal of Geophysical Research: Planets, 122(6), pp.1158-1180.

Hulme, G. and Fielder, G., 1977. Effusion rates and rheology of lunar lavas. Philosophical Transactions of the Royal Society of London. Series A, Mathematical and Physical Sciences, 285(1327), pp.227-234.

Hurwitz D. M., Fassett C. I., Head J. W. and Wilson L. (2010) Formation of an eroded lava channel within an Elysium Planitia impact crater: distinguishing between a mechanical and thermal origin. Icarus 210, 626–634.

International Astronomical Union (IAU.org) for crater diameters

Iqbal, W., Hiesinger, H. and van der Bogert, C.H., 2020. Geological mapping and chronology of lunar landing sites: Apollo 12. Icarus, 352, p.113991.

Isbell, C.E., Eliason, E.M., Adams, K.C., Becker, T.L., Bennett, A.L., Lee, E.M., McEwen, A.S., Robinson, M.S., Shinaman, J.R., Weller, L.A., 1999. Clementine: A multi-spectral digital image model archive of the Moon. Lunar and Planetary Science Conference 30, 1812.

Isbell, C., Gaddis, L., Garcia, P., Hare, T. and Bailen, M., 2014, March. Kaguya terrain camera mosaics. In 45th Annual Lunar and Planetary Science Conference (No. 1777, p. 2268).

Jia, M., Yue, Z., Di, K., Liu, B., Liu, J. and Michael, G., 2020. A catalogue of impact craters larger than 200 m and surface age analysis in the Chang'e-5 landing area. Earth and Planetary Science Letters, 541, p.116272.

Jia, B., Fa, W., Zhang, M., Di, K., Xie, M., Tai, Y. and Li, Y., 2022. On the provenance of the Chang'E-5 lunar samples. Earth and Planetary Science Letters, 596, p.117791.

Jolliff, B.L., Gillis, J.J., Haskin, L.A., Korotev, R.L., Wieczorek, M.A., 2000. Major lunar crustal terranes: Surface expressions and crust-mantle origins. J. Geophys. Res. 105, 4197–4216.

Jozwiak, L.M., Head, J.W., Zuber, M.T., Smith, D.E., Neumann, G.A., 2012. Lunar floor-fractured craters: Classification, distribution, origin and implications for magmatism and shallow crustal structure. J. Geophys. Res. 117, E11005. doi:10.1029/2012JE004134.

Jozwiak, L.M., Head, J.W., Wilson, L., 2015. Lunar floor-fractured craters as magmatic intrusions: Geometry, modes of emplacement, associated tectonic and volcanic features, and implications for gravity anomalies. Icarus 248, 424–447.

Kato, M., Sasaki, S., Takizawa, Y. and Kaguya Project Team, 2010. The Kaguya mission overview. Space science reviews, 154, pp.3-19.

Kaula, W.M., Head III, J.W., Merrill, R.B., Pepin, R.O., Solomon, S.C., Walker, D. and Wood, C.A., 1981. Basaltic volcanism on the terrestrial planets. Basaltic volcanism on the terrestrial planets.

Kesson, S.E. and Ringwood, A.E., 1976. Mare basalt petrogenesis in a dynamic moon. Earth and Planetary Science Letters, 30(2), pp.155-163.

Kirchoff, M., Sherman, K. and Chapman, C., 2011, Examining lunar impactor population evolution: Additional results from crater distributions on diverse terrains. In EPSC-DPS Joint Meeting (Vol. 1587).

Kitmacher, G.H and Garber, S., https://www.history.nasa.gov/apollo_photo.html.

Kneissl, T., van Gasselt, S. and Neukum, G., 2011. Map-projection-independent crater size-frequency determination in GIS environments—New software tool for ArcGIS. Planetary and Space Science, 59(11-12), pp.1243-1254.

Korotev, R.L., Gillis, J.J., 2001. A new look at the Apollo 11 regolith and KREEP. Journal of Geophysical Research-Planets 106, 12339-12353.

Kramer, G. Y., Besse, S., Dhingra, D., Nettles, J., Klima, R., Garrick–Bethell, I., … McCord, T. B. (2011). M3 spectral analysis of lunar swirls and the link between optical maturation and surface hydroxyl formation at magnetic anomalies. Journal of Geop, pp. 1–20, 2011, doi: 10.1029/2010JE003729.

Kushida et al. (2016) Japan Aerospace Exploration Agency, ISSN 1349-1121, JAXA-RM-15-007.

Lawrence, D.J., Feldman, W.C., Elphic, R.C., Little, R.C., Prettyman, T.H., Maurice, S., Lucey, P.G. and Binder, A.B., 2002. Iron abundances on the lunar surface as measured by the Lunar Prospector gamma-ray and neutron spectrometers. J. Geophys. Res. 107(E12).

Lawrence, D.J., Elphic, R.C., Feldman, W.C., Prettyman, T.H., Gasnault, O., Maurice, S., 2003. Small-area thorium features on the lunar surface. J. Geophys. Res. 108(E9).

Lawrence, S.J., Stopar, J.D., Hawke, B.R., Greenhagen, B.T., Cahill, J.T., Bandfield, J.L., Jolliff, B.L., Denevi, B.W., Robinson, M.S., Glotch, T.D., Bussey, D.B.J., Spudis, P.D., Giguere, T.A., and Garry, W.B., 2013. LRO observations of morphology and surface roughness of volcanic cones and lobate lava flows in the Marius Hills. Journal of Geophysical Research: Planets, 118(4), pp.615-634.

Lemelin, M., Lucey, P.G., Song, E. and Taylor, G.J., 2015. Lunar central peak mineralogy and iron content using the Kaguya Multiband Imager: Reassessment of the compositional structure of the lunar crust. Journal of Geophysical Research: Planets, 120(5), pp.869-887.

Lemelin, M., Lucey, P.G., Miljković, K., Gaddis, L.R., Hare, T. and Ohtake, M., 2019. The compositions of the lunar crust and upper mantle: Spectral analysis of the inner rings of lunar impact basins. Planetary and Space Science, 165, pp.230-243.

Li, L. and Mustard, J.F., 2000. Compositional gradients across mare-highland contacts: Importance and geological implication of lateral transport. Journal of Geophysical Research: Planets, 105(E8), pp.20431-20450.

Li, L. and Mustard, J.F., 2005. On lateral mixing efficiency of lunar regolith. Journal of Geophysical Research: Planets, 110(E11).

Lillesand, T.M. and Kiefer, R.W., 1979. Remote sensing and image interpretation(Book). New York, John Wiley and Sons, Inc., 1979. 624 p.

Liu, W.C. and Wu, B., 2021. Influence of solar incidence angle on single-image photoclinometry for precision lunar topographic mapping. ISPRS Journal of Photogrammetry and Remote Sensing, 182, pp.208-227.

Lu, X., Cao, H., Ling, Z., Fu, X., Qiao, L. and Chen, J., 2021. Geomorphology, Mineralogy, and Geochronology of Mare Basalts and Non-Mare Materials around the Lunar Crisium Basin. Remote Sensing, 13(23), p.4828.

Lucey, P. G., Bruno, B. C., Hawke, B. R., 1991. Preliminary results of imaging spectroscopy of the Humorum Basin region of the moon. Proceedings Lunar and Planetary Science Conference 21, 391-403. doi:1991LPSC...21..391L.

Lucey, P. G., Blewett, D. T., Jolliff, B. L., 2000a. Lunar iron and titanium abundance algorithms based on final processing of Clementine UV-VIS data, J. Geophys. Res. 105(E8), 20,297 – 20,305.

Lucey, P. G., Blewett, D. T., Taylor, G. J., Hawke, B. R., 2000b. Imaging of lunar surface maturity, J. Geophys. Res. 105(E8), 20,377 – 20,386.

Macdonald, G. A., Eaton, J. P., 1955. The 1955 eruption of Kilauea volcano. Volcano Letter, no. 529-30, 1-10.

Mahanti, P., Robinson, M.S., Humm, D.C. and Stopar, J.D., 2014. A standardized approach for quantitative characterization of impact crater topography. Icarus, 241, pp.114-129.

Malaret, E., Guasqui, P., McLaughlin, S., Sunshine, J., Besse, S., Clark, R. and Isaacson, P., 2011. CH1-ORB Moon M3 4 L2 reflectance near-IR spectral images V1. 0. Ch1-Orb-L-M3-4-L2-Reflectance-V1. 0, NASA Planetary Data System.

Marchi, S., Mottola, S., Cremonese, G., Massironi, M. and Martellato, E., 2009. A new chronology for the Moon and Mercury. The Astronomical Journal, 137(6), p.4936.

Marshall, C.H., 1963. Geologic map and sections of the Letronne region of the Moon, scale 1: 1,000,000. Map I-385, USGS, Department of the Interior, Washington, DC.

Mattson, S., Ojha, L., Ortiz, A., McEwen, A. S., Burns, K., 2012. Regional digital terrain model production with LROC-NAC. 43rd Lunar and Planetary Science Conference, abstract 2630.

McEwen, A.S., Robinson, M.S., Eliason, E.M., Lucey, P.G., Duxbury, T.C. and Spudis, P.D., 1994. Clementine observations of the Aristarchus region of the Moon. Science, 266(5192), pp.1858-1862.

McEwen, A., Turtle, E., Burr, D., Milazzo, M., Lanagan, P., Christensen, P., Boyce, J. and THEMIS Science Team, 2003, March. Discovery of a Large Rayed Crater on Mars: Implications for Recent Volcanicand Fluvial Activity and the Origin of Martian Meteorites. In Lunar and Planetary Science Conference (p. 2040).

McEwen, A.S., 2003, July. Secondary cratering on Mars: Implications for age dating and surface properties. In Sixth International Conference on Mars (p. 3268).

McEwen, A.S., 2004, March. New Age Mars. In Lunar and Planetary Science Conference (p. 1756).

McEwen, A.S. and Bierhaus, E.B., 2006. The importance of secondary cratering to age constraints on planetary surfaces. Annu. Rev. Earth Planet. Sci., 34, pp.535-567.

Mee, M., Brenner, H., 1895. Report of the Lunar Section, Gassendi. British Astronomical Association, 3, p. 163-164, doi:1895MmBAA...3..163.

Melosh, H. J., 1984. Impact ejection, spallation, and the origin of meteorites, Icarus 59, 234-260.

Melosh, H.J., 1989. Impact cratering: A geologic process. Research supported by NASA. New York, Oxford University Press (Oxford Monographs on Geology and Geophysics, No. 11), 1989, 253 p., 11.

Michael, G.G. and Neukum, G., 2010. Planetary surface dating from crater size–frequency distribution measurements: Partial resurfacing events and statistical age uncertainty. Earth and Planetary Science Letters, 294(3-4), pp.223-229.

Moore, P., 2001. Patrick Moore on the Moon. Cassell.

Morota, T., Haruyama, J., Ohtake, M., Matsunaga, T., Honda, C., Yokota, Y., Kimura, J., Ogawa, Y., Hirata, N., Demura, H. and Iwasaki, A., 2011. Timing and characteristics of the latest mare eruption on the Moon. Earth and Planetary Science Letters, 302(3-4), pp.255-266.

Muehlberger, W.R., Batson, R.M., Boudette, E.L., Duke, C.M., Eggleton, R.E., Elston, D.P., England, A.W., Freeman, V.L., Hait, M.H., Hall, T.A. and Head, J.W., 1972. Preliminary geologic investigation of the Apollo 16 landing site.

Murase, T., McBirney, A. R., 1970. Viscosity of Lunar Lavas, Science, 167, 3924, 1491-1493.

Navon, D., 1977. Forest before trees: The precedence of global features in visual perception. Cognitive psychology, 9(3), pp.353-383.

Neal, C.R., Taylor, L.A., 1992. Petrogenesis of mare basalts: A record of lunar volcanism. Geochim. Cosmochim. Acta 56, 2177-2211.

Needham, D.H., Hamilton, C.W., Bleacher, J.E., Whelley, P.L., Young, K.E., Scheidt, S.P., Richardson, J.A. and Sutton, S.S., 2017. Lava Eruption and Emplacement: Using Clues from Hawaii and Iceland to Probe the Lunar Past.

Neukum, G., König, B. and Arkani-Hamed, J., 1975a. A study of lunar impact crater size-distributions. The moon, 12(2), pp.201-229.

Neukum, G., König, B., Fechtig, H. and Storzer, D., 1975b. Cratering in the Earth-Moon system-Consequences for age determination by crater counting. In Lunar and Planetary Science Conference Proceedings (Vol. 6, pp. 2597-2620).

Neukum, G., 1983. Meteoritenbombardement und datierung planetarer oberflachen. Habilitation Dissertation for Faculty Membership, Ludwig-Maximilians-Univ.

Neukum, G., 1984. Meteorite bombardment and dating of planetary surfaces (No. NASA-TM-77558).

Neukum, G., Ivanov, B.A., Hartmann, W.K., 2001. Cratering records in the inner Solar System in relation to the lunar reference system. Space Sci. Rev. 96, 55–86.

Nozette, S., Rustan, P., Pleasance, L.P. and Horan, D.M., et al., 1994. The Clementine mission to the Moon: Scientific overview, Science, 266(5192), 1835– 1839.

Oberbeck, V.R. and Morrison, R.H., 1974. Laboratory simulation of the herringbone pattern associated with lunar secondary crater chains. The Moon, 9(3-4), pp.415-455.

Oberbeck, V.R., 1975. The role of ballistic erosion and sedimentation in lunar stratigraphy. Reviews of Geophysics, 13(2), pp.337-362.

Ohtake, M., Haruyama, J., Matsunaga, T., Yokota, Y., Morota, T. and Honda, C., 2008. Performance and scientific objectives of the SELENE (KAGUYA) Multiband Imager. Earth, planets and space, 60(4), pp.257-264.

Okumura, H., S. Sobue, H. Hoshino, A. Yamamoto and T. Fujita (2009), Data archive and visualization for Lunar Orbiter Kaguya (SELENE), Lun. Planet. Sci., abstract #1518, see https://www.soac.selene.isas.jaxa.jp/archive.

Okumura, H., Sasaki, S., Kato, M., Maejima, H., Minamino, H., Nakazawa, S., Otake, H., Tateno, N., Konishi, H., Yonekura, K. and Hirokazu, H., 2009. The Project Highlight of Japan's Lunar Explorer Kaguya (Selene). Shin-ichi Sobue1.

Ostrach, L.R., Robinson, M.S., Denevi, B.W. and Thomas, P.C., 2011, March. Effects of incidence angle on crater counting observations. In Lunar and Planetary Science Conference (No. 1608, p. 1202).

Otake, H., Ohtake, M. and Hirata, N., 2012, March. Lunar iron and titanium abundance algorithms based on SELENE (Kaguya) Multiband Imager data. In Lunar and Planetary Science Conference (No. 1659, p. 1905).

Paige, D.A., Foote, M.C., Greenhagen, B.T., Schofield, J.T., Calcutt, S., Vasavada, A.R., Preston, D.J., Taylor, F.W., Allen, C.C., Snook, K.J. and Jakosky, B.M., 2010. The lunar reconnaissance orbiter diviner lunar radiometer experiment. Space Science Reviews, 150(1-4), pp.125-160.

Pieters, C.M., Head, J.W., Sunshine, J.M., Fischer, E.M., Murchie, S.L., Belton, M., McEwen, A., Gaddis, L., Greeley, R., Neukum, G. and Jaumann, R., 1993. Crustal diversity of the Moon: Compositional analyses of Galileo solid state imaging data. Journal of Geophysical Research: Planets, 98(E9), pp.17127-17148.

Pieters, C.M., Staid, M.I., Fischer, E.M., Tompkins, S. and He, G., 1994. A sharper view of impact craters from Clementine data. Science, 266(5192), p.1844.

Pieters, C. M., Boardman, J., Buratti, B., Clark, R., Combe, J.-P., Green, R., Head, J. W., Hicks, M., Isaacson, P., Klima, R., Kramer, G., Lundeen, S., Malaret, E., McCord, T. B., Mustard, J., Nettles, J., Petro, N., Runyon, C., Staid, M., Sunshine, J., Taylor, L., Tompkins, S., Varanasi, P., 2009. Characterization of Lunar Mineralogy: The Moon Mineralogy Mapper (M^3) on Chandrayaan-1, LPI Contributions, 1483, 86-87. 2009LPICo1483...86P.

Pike, R.J. and Wilhelms, D.E., 1978, March. Secondary-impact craters on the Moon: Topographic form and geologic process. In Lunar and planetary science conference (Vol. 9, pp. 907-909).

Plescia, J.B. and Robinson, M.S., 2011, March. New constraints on the absolute lunar cratering chronology. In 42nd Annual Lunar and Planetary Science Conference (No. 1608, p. 1839).

Plescia, J.B., 2012. Uncertainties in the< 3 Ga lunar impact cratering chronology. LPI, (1659), p.1614.

Prettyman, T. H., et al., 2006. Elemental composition of the lunar surface: Analyses of gamma ray spectroscopy data from Lunar Prospector J. Geophys. Res. 111, doi:10.1029/2005JE002656, 2006.

Qiao, L., Head, J., Wilson, L., Xiao, L., Kreslavsky, M. and Dufek, J., 2017. Ina pit crater on the Moon: Extrusion of waning-stage lava lake magmatic foam results in extremely young crater retention ages. Geology, 45(5), pp.455-458.

Qian, Y.Q., Xiao, L., Zhao, S.Y., Zhao, J.N., Huang, J., Flahaut, J., Martinot, M., Head, J.W., Hiesinger, H. and Wang, G.X., 2018. Geology and scientific significance of the Rümker region in Northern Oceanus Procellarum: China's Chang'E-5 landing region. Journal of Geophysical Research: Planets, 123(6), pp.1407-1430.

Qian, Y.Q., Xiao, L., Head, J.W., van der Bogert, C.H., Hiesinger, H. Wilson, L., 2021a. Young lunar mare basalts in the Chang'e-5 sample return region, northern Oceanus Procellarum. Earth and Planetary Science Letters, 555(2021) 116702.

Qian, Y.Q., Xiao, L., Head, J.W., van der Bogert, C.H., Hiesinger, H., Wilson, L., Yuan, Y., 2021b. China's Chang'e-5 Landing Site: An Overview. Lunar and Planetary Science Conference 52, abstract 1306.

Qian, Y.Q., Xiao, L., Wang, Q., Head, J.W., Yang, R., Kang, Y., van der Bogert, C.H., Hiesinger, H., Lai, X., Wang, G., Pang, Y., Zhang, N., Yuan, Y., He, Q., Huang, J., Zhao, J., Wang, J., Zhao, S., 2021c. China's Chang'e-5 landing site: Geology, stratigraphy, and provenance of materials. Earth and Planetary Science Letters, 561(2021) 116855.

Rhodes, J.M., 1977. Some compositional aspects of lunar regolith evolution. Phil. Trans. Roy. Soc. London A285, 293-301.

Richardson, M., Malagón, A.A.P., Lebofsky, L.A., Grier, J., Gay, P., Robbins, S.J. and Team, T.C., 2021. The CosmoQuest Moon Mappers Community Science Project: The Effect of Incidence Angle on the Lunar Surface Crater Distribution. arXiv preprint arXiv:2110.13404.

Richter, D.H., Eaton, J.P., Murata, K.J., Ault, W.U., Krivoy, H.L., 1970, Chronological narrative of the 1959-60 eruption of Kilauea Volcano, Hawaii: U.S. Geological Survey Professional Paper 537-E, 73 p.

Riedel, C., Michael, G., Kneissl, T., Orgel, C., Hiesinger, H. and van der Bogert, C.H., 2018. A new tool to account for crater obliteration effects in crater size-frequency distribution measurements. Earth and Space Science, 5(6), pp.258-267.

Riedel, C., Minton, D.A., Michael, G., Orgel, C., van der Bogert, C.H. and Hiesinger, H., 2020. Degradation of small simple and large complex lunar craters: Not a simple scale dependence. Journal of Geophysical Research: Planets, 125(4), p.e2019JE006273.

Robbins, S.J. and Hynek, B.M., 2011. Secondary crater fields from 24 large primary craters on Mars: Insights into nearby secondary crater production. Journal of Geophysical Research: Planets, 116(E10).

Robbins, S.J. and Hynek, B.M., 2012. A new global database of Mars impact craters≥ 1 km: 1. Database creation, properties, and parameters. Journal of Geophysical Research: Planets, 117(E5).

Robbins, S.J. and Hynek, B.M., 2014, March. The Population of Secondary Impact Craters on Mars. In 45th Annual Lunar and Planetary Science Conference (No. 1777, p. 1666).

Robbins, S.J., 2014. New crater calibrations for the lunar crater-age chronology. Earth and Planetary Science Letters, 403, pp.188-198.

Robbins, S.J., Antonenko, I., Kirchoff, M.R., Chapman, C.R., Fassett, C.I., Herrick, R.R., Singer, K., Zanetti, M., Lehan, C., Huang, D. and Gay, P.L., 2014. The variability of crater identification among expert and community crater analysts. Icarus, 234, pp.109-131.

Robbins, S.J., Riggs, J.D., Weaver, B.P., Bierhaus, E.B., Chapman, C.R., Kirchoff, M.R., Singer, K.N. and Gaddis, L.R., 2018. Revised recommended methods for analyzing crater size-frequency distributions. Meteoritics & Planetary Science, 53(4), pp.891-931.

Robbins, S.J., 2019. A new global database of lunar impact craters> 1–2 km: 1. Crater locations and sizes, comparisons with published databases, and global analysis. Journal of Geophysical Research: Planets, 124(4), pp.871-892.

Robinson, M.S., McEwen, A.S., Eliason, E., Lee, E.M., Malaret, E., Lucey, P.G., 1999. Clementine UVVIS global mosaic: A new tool for understanding the lunar crust. Lunar and Planetary Science Conference 30, 1931.

Robinson, M. S., Brylow, S. M., Tschimmel, M., Humm, D., Lawrence, S. J., Thomas, P. C., Denevi, B. W., Bowman-Cisneros, E., Zerr, J., Ravine, M. A., Caplinger, M. A., Ghaemi, F. T., Schaffner, J. A., Malin, M. C., Mahanti, P., Bartels, A., Anderson, J., Tran, T. N., Eliason, E. M., McEwen, A. S., Turtle, E., Jolliff, B. L., Hiesinger, H., 2010. Lunar Reconnaissance Orbiter Camera (LROC) instrument overview. Space Science Reviews 150(1-4), 81–124.

Robinson, M.S., Plescia, J.B., Jolliff, B.L. and Lawrence, S.J., 2012. Soviet lunar sample return missions: Landing site identification and geologic context. Planetary and Space Science, 69(1), pp.76-88.

Ryder, G., 1991. Lunar ferroan anorthosites and mare basalt sources: The mixed connection. Geophysical Research Letters, 18(11), pp.2065-2068.

Sato, H., Robinson, M.S., Lawrence, S.J., Denevi, B.W., Hapke, B., Jolliff, B.L. and Hiesinger, H., 2017. Lunar mare TiO2 abundances estimated from UV/Vis reflectance. Icarus, 296, pp.216-238.

Schaber, G. G., Thompson, T. W., Zisk, S. H., 1975. Lava flows in Mare Imbrium - an evaluation of anomalously low earth-based radar reflectivity, The Moon, vol. 13(4), 395-423. 10.1007/BF02626384.

Schaber, G.G., Boyce, J.M., Moore, H.J., 1976. The scarcity of mappable flow lobes on the lunar maria: Unique morphology of the Imbrium flows. Proc. Lunar Sci. Conf. 7th, 2783-2800.

Scholten, F., Oberst, J., Matz, K.D., Roatsch, T., Wählisch, M., Speyerer, E. J., Robinson, M. S., 2012. GLD100: The near-global lunar 100 m raster DTM from LROC WAC stereo image data. J. Geophys. Res. 117(E12). doi:10.1029/2011JE003926.

Schultz, P.H., 1976a. Moon Morphology, 626 pp. Univ. of Texas.

Schultz, P.H., 1976b. Floor-fractured lunar craters. The Moon, 15(3-4), pp.241-273.

Schultz, P.H., Spudis, P.D., 1979. Evidence for ancient mare volcanism. Lunar and Planetary Science Conference Proceedings 10, 2899-2918.

Shearer, C.K. and Papike, J.J., 1993. Basaltic magmatism on the Moon: A perspective from volcanic picritic glass beads. Geochimica et Cosmochimica Acta, 57(19), pp.4785-4812.

Shoemaker, E.M., 1962. Interpretation of lunar craters. Physics and Astronomy of the Moon, pp.283-359.

Shoemaker, E.M., Bailey, N.G., Batson, R.M., Dahlem, D.H., Foss, T.H. and Grolier, M.J., 1969. 3. Geologic Setting of the Lunar Samples Returned by the Apollo Il Mission. Apollo 11: Preliminary Science Report, 214, p.41-84.

Shylaja, B.S., 2005. Determination of lunar surface ages from crater frequency—size distribution. Journal of earth system science, 114(6), pp.609-612.

Singer, K.N., Jolliff, B.L. and McKinnon, W.B., 2020. Lunar secondary craters and estimated ejecta block sizes reveal a scale-dependent fragmentation trend. Journal of Geophysical Research: Planets, 125(8), p.e2019JE006313.

Smith, E.I., 1973. Identification, distribution and significance of lunar volcanic domes. The moon, 6(1), pp.3-31.

Soderblom, L.A. and Boyce, J.M., 1972. Photogeology: Part A: relative ages of some near-side and far-side terra plains based on Apollo 16 metric photography.

Soderblom, L.A. and Lebofsky, L.A., 1972. Technique for rapid determination of relative ages of lunar areas from orbital photography. Journal of Geophysical research, 77(2), pp.279-296.

Speyerer, E. J., Robinson, M. S., Denevi, B. W., LROC Science Team, 2011. Lunar Reconnaissance Orbiter Camera global morphological map of the Moon. Lunar and Planetary Science Conference 42, 2387.

Speyerer, E.J., Povilaitis, R.Z., Robinson, M.S., Thomas, P.C. and Wagner, R.V., 2016. Quantifying crater production and regolith overturn on the Moon with temporal imaging. Nature, 538(7624), p.215.

Stadermann, A.C., Zanetti, M.R., Jolliff, B.L., Hiesinger, H., van der Bogert, C.H. and Hamilton, C.W., 2018. The age of lunar mare basalts south of the Aristarchus Plateau and effects of secondary craters formed by the Aristarchus event. Icarus, 309, pp.45-60.

Staid, M.I., Pieters, C.M., 2001. Mineralogy of the last lunar basalts: Results from Clementine. J. Geophys. Res. 106, 27,887-827,900.

Staid, M.I., Pieters, C.M., Besse, S., Boardman, J., Dhingra, D., Green, R., Head, J.W., Isaacson, P., Klima, R., Kramer, G. and Mustard, J.M., 2011. The mineralogy of late stage lunar volcanism as observed by the Moon Mineralogy Mapper on Chandrayaan-1. Journal of Geophysical Research: Planets, 116(E6).

Stöffler, D. and Ryder, G., 2001. Stratigraphy and isotope ages of lunar geologic units: Chronological standard for the inner solar system. Chronology and evolution of Mars, pp.9-54.

Stöffler, D., Ryder, G., Ivanov, B.A., Artemieva, N.A., Cintala, M.J. and Grieve, R.A., 2006. Cratering history and lunar chronology. Reviews in Mineralogy and Geochemistry, 60(1), pp.519-596.

Stopar, J.D., Robinson, M.S., van der Bogert, C.H., Hiesinger, H., Ostrach, L.R., Giguere, T.A. and Lawrence, S.J., 2017. Young Lunar Volcanism: Irregular Mare Patches as Drained Lava Ponds and Inflated Flows.

Stovall, W.K., Houghton, B.F., Harris, A.J.L., Swanson, D.A., 2009a. A frozen record of density-driven crustal overturn in lava lakes: the example of Kīlauea Iki 1959. Bulletin of volcanology, 71(3), 313-318. doi:10.1007/s00445-008-0225-y.

Stovall, W.K., Houghton, B.F., Harris, A.J., Swanson, D.A., 2009b. Features of lava lake filling and draining and their implications for eruption dynamics. Bulletin of volcanology, 71(7), pp.767-780. doi:10.1007/s00445-009-0263-0.

Swanson, D.A., Duffield, W.A., Jackson, D.B., Peterson, D.W., 1979. Chronological narrative of the 1969-71 Mauna Ulu eruption of Kilauea volcano, Hawaii (No. 1056). US Govt. Print. Off.

Taylor G. J., Warren P., Ryder G., Delano J, Pieters C. And Lofgren G. (1991) Lunar Rocks-Appendix: Chemical Data for Lunar Rocks. In Lunar Sourcebook, G. H. Heiken, D. T. Vaniman and B. M. French eds., Cambridge Univ. Press, Cambridge, U.K., pp. 183–284.

Taylor, S.R., 1982. Planetary science: A lunar perspective (Vol. 3303). Houston: Lunar and Planetary Institute.

Thompson, T.J., Robinson, M.S., Watters, T.R. and Johnson, M.B., 2017, March. Global lunar wrinkle ridge identification and analysis. In Lunar and Planetary Science Conference (No. 1964, p. 2665).

Thorey, C., & Michaut, C. (2014). A model for the dynamics of crater-centered intrusion: Application to lunar floor-fractured craters. Journal of Geophysical Research: Planets, 119(1), 286-312.

Tilling, R.I., 1987. Fluctuations in surface height of active lava lakes during 1972–1974 Mauna Ulu eruption, Kilauea volcano, Hawaii. Journal of Geophysical Research: Solid Earth, 92(B13), pp.13721-13730.

Titley, S.R., 1967. Geologic map of the Mare Humorum region of the Moon, I-495. US Geological Survey.

Tran, T., Howington-Kraus, E., Archinal, B., Rosiek, M., Lawrence, S.J., Gengl, H., Nelson, D., Robinson, M.S., Beyer, R., Li, R. and Oberst, J., 2010. Generating digital terrain models from LROC stereo images with SOCET SET. Lunar and Planetary Science XLI, 1533, p.2515.

Trang, David, Gillis-Davis, Jeffrey J., Hawke, B. Ray, (2016) The origin of lunar concentric craters, Icarus, Volume 278, p. 62-78, 10.1016/j.icarus.2016.06.001.

Trang, D., Gillis-Davis, J.J., Lemelin, M., Cahill, J.T., Hawke, B.R., Giguere, T.A., 2017. The compositional and physical properties of localized lunar pyroclastic deposits, Icarus 283C, pp. 232-253, doi:10.1016/j.icarus.2016.09.025.

Trask, N.J., 1971. Geologic comparison of mare materials in the lunar equatorial belt, including Apollo 11 and Apollo 12 landing sites. US Geol. Surv. Prof. Pap., 750D, pp.2645-2662.

Ulrich, G.E., Hodges, C.A. and Muehlberger, W.R. eds., 1981. Geology of the Apollo 16 area, Central Lunar Highlands: prepared on behalf of the National Aeronautics and Space Administration (USGS Professional Paper No. 1048). US Government Printing Office.

van der Bogert, C.H., Michael, G., Kneissl, T., Hiesinger, H. and Pasckert, J.H., 2015, March. Effects of count area size on absolute model ages derived from random crater size-frequency distributions. In Lunar and Planetary Science Conference (No. 1832, p. 1742).

van der Bogert, C.H., Hiesinger, H., Dundas, C.M., Krüger, T., McEwen, A.S., Zanetti, M. and Robinson, M.S., 2017. Origin of discrepancies between crater size-frequency distributions of coeval lunar geologic units via target property contrasts. Icarus, 298, pp.49-63.

Wagner, R.V. and Robinson, M.S., 2014. Distribution, formation mechanisms, and significance of lunar pits. Icarus, 237, pp.52-60.

Wang, Y., Xie, M., Xiao, Z. and Cui, J., 2020. The minimum confidence limit for diameters in crater counts. Icarus, 341, p.113645.

Wang, J., Zhang, Y., Di, K., Chen, M., Duan, J., Kong, J., Xie, J., Liu, Z., Wan, W., Rong, Z. and Liu, B., 2021. Localization of the Chang'e-5 Lander Using Radio-Tracking and Image-Based Methods. Remote Sensing, 13(4), p.590.

West, M. N, 1972. Orbital Science Investigation, Part L, Selected Volcanic Features. Apollo 15 Preliminary Science Report, NASA SP-289.

Whitford-Stark, J.L., 1982. Factors influencing the morphology of volcanic landforms: An Earth-Moon comparison. Earth-Science Reviews, 18(2), pp.109-168.

Whitten, J.L. and Head, J.W., 2015. Lunar cryptomaria: Physical characteristics, distribution, and implications for ancient volcanism. Icarus, 247, pp.150-171.

Wichman, R.W. and Schultz, P.H., 1995. Floor-fractured craters in Mare Smythii and west of Oceanus Procellarum: Implications of crater modification by viscous relaxation and igneous intrusion models. Journal of geophysical research, 100(E10), 21-201.

Wieczorek, M.A., Zuber, M.T. and Phillips, R.J., 2001. The role of magma buoyancy on the eruption of lunar basalts. Earth and Planetary Science Letters, 185(1-2), pp.71-83.

Wieczorek et al., 2006. The Constitution and Structure of the Lunar Interior, Rev. Mineral. Geochem., 60, 221–364, Walter de Gruyter GmbH & Co KG.

Wieczorek, M.A., Neumann, G.A., Nimmo, F., Kiefer, W.S., Taylor, G.J., Melosh, H.J., Phillips, R.J., Solomon, S.C., Andrews-Hanna, J.C., Asmar, S.W. and Konopliv, A.S., 2013. The crust of the Moon as seen by GRAIL. Science, 339(6120), pp.671-675.

Wilcox, B.B., Robinson, M.S., Thomas, P.C. and Hawke, B.R., 2005. Constraints on the depth and variability of the lunar regolith. Meteoritics & Planetary Science, 40(5), pp.695-710.

Wilhelms, D. E., 1987. The geologic history of the Moon (US Geol. Surv. Prof. Paper 1348). United States Government Printing Office, Washington, DC.

Wilhelms, D.E. and Byrne, C.J., 2009. Stratigraphy of Lunar Craters, Image Again Online: http://www. imageagain.com/Strata.

Wilhelms, D.E. and El-Baz, F., 1977. Geologic map of the east side of the Moon, I-948. Reston: US Geological Survey.

Williams, J.P., Pathare, A.V. and Aharonson, O., 2014. The production of small primary craters on Mars and the Moon. Icarus, 235, pp.23-36.

Witham, F. and Llewellin, E.W., 2006. Stability of lava lakes. Journal of Volcanology and Geothermal Research, 158(3), pp.321-332.

Witter, J. B., Kress, V. C., Delmelle, P., Stix, J., 2004. Volatile degassing, petrology and magma dynamics of the Villarrrica Lava Lake, Journal of Volcanology and Geothermal Research 134(4), 303– 337.

Wu, B., Huang, J., Li, Y., Wang, Y. and Peng, J., 2018. Rock Abundance and Crater Density in the Candidate Chang'E-5 Landing Region on the Moon. Journal of Geophysical Research: Planets, 123(12), pp.3256-3272.

Xiao, Z. and Strom, R.G., 2012. Problems determining relative and absolute ages using the small crater population. Icarus, 220(1), pp.254-267.

Xiao, Z. and Werner, S.C., 2015. Size-frequency distribution of crater populations in equilibrium on the Moon. Journal of Geophysical Research: Planets, 120(12), pp.2277-2292.

Xie, M., Xiao, Z., Zhang, X. and Xu, A., 2020. The provenance of regolith at the Chang'e-5 candidate landing region. Journal of Geophysical Research: Planets, 125(5), p.e2019JE006112.

Xu, Z.; Guo, D.; Liu, J. Maria Basalts Chronology of the Chang'E-5 Sampling Site. Remote Sens. 2021, 13, 1515. https://doi.org/10.3390/rs13081515

Yarbus, A.L. and Yarbus, A.L., 1967. Eye movements during perception of complex objects. Eye movements and vision, pp.171-211.

Yue, Z., Michael, G.G., Di, K. and Liu, J., 2017. Global survey of lunar wrinkle ridge formation times. Earth and Planetary Science Letters, 477, pp.14-20.

Yue, Z., Di, K., Liu, Z., Michael, G., Jia, M., Xin, X., Liu, B., Peng, M. and Liu, J., 2019. Lunar regolith thickness deduced from concentric craters in the CE-5 landing area. Icarus, 329, pp.46-54.

Zanetti, M., Jolliff, B.L., van der Bogert, C.H. and Hiesinger, H., 2013, March. New determination of crater size-frequency distribution variation on continuous ejecta deposits: Results from Aristarchus crater. In 44th Annual Lunar and Planetary Science Conference (No. 1719, p. 1842).

Zanetti, M., Stadermann, A., Krüger, T., van der Bogert, C., Hiesinger, H. and Jolliff, B.L., 2014, March. Mapping crater density variation on Copernican ejecta blankets: Evidence for auto-

secondary cratering at Tycho and Aristarchus. In 45th Annual Lunar and Planetary Science Conference (No. 1777, p. 1528).

Zanetti, M., Stadermann, A., Jolliff, B., Hiesinger, H., Van der Bogert, C.H. and Plescia, J., 2017. Evidence for self-secondary cratering of Copernican-age continuous ejecta deposits on the Moon. Icarus, 298, pp.64-77.

Zeng, X., Zuo, W., Zhang, Z., Liu, Y. and Li, C., 2017. Topographic and geologic analysis of the Pre-selection landing sites for Chang‘E 5 (CE-5) lunar sample returning mission of China. EGUGA, p.2026.

Zhao, J., Xiao, L., Qiao, L., Glotch, T.D. and Huang, Q., 2017. The Mons Rümker volcanic complex of the Moon: A candidate landing site for the Chang'E-5 mission. Journal of Geophysical Research: Planets, 122(7), pp.1419-1442.

Zhong, Z., Yan, J. and Xiao, Z., 2020. Lunar Regolith Temperature Variation in the Rümker Region Based on the Real-Time Illumination. Remote Sensing, 12(4), p.731.

Zou, Y.L. and Li, W., 2017. Scientific visions of lunar research-station from China. LPI, (1964), p.1730.

Zuber, M.T., Smith, D.E., Watkins, M.M., Asmar, S.W., Konopliv, A.S., Lemoine, F.G., Melosh, H.J., Neumann, G.A., Phillips, R.J., Solomon, S.C. and Wieczorek, M.A., 2013. Gravity field of the Moon from the Gravity Recovery and Interior Laboratory (GRAIL) mission. Science, 339(6120), pp.668-671.